Eco-Friendly Surface Engineering of Magnesium Alloys for Resorbable Implant Applications: Experimental, Computational, and Data-Driven Optimization Approaches

Thesis submitted by

BINOD BARAI

Doctor of Philosophy

(Engineering)

Department of Mechanical Engineering

Faculty Council of Engineering & Technology

Jadavpur University

Kolkata

2026

THESIS DETAILS & LIST OF PUBLICATIONS

INDEX NO: 12/22/E

REGISTRATION NUMBER: 1022211006

1. Title of Thesis

Eco-Friendly Surface Engineering of Magnesium Alloys for Resorbable Implant Applications: Experimental, Computational, and Data-Driven Optimization Approaches

2. Name, Designation & Institution of the Supervisors:

Dr. Buddhadeb Oraon

Professor, Department of Mechanical Engineering

Jadavpur University, Kolkata-700032

Dr. Tapendu Mandal

Assistant Professor, Department of Metallurgy and Materials Engineering

Indian Institute of Engineering Science and Technology Shibpur, Howrah- 711103

Dr. Subhasish Sarkar

Assistant Engineer, Department of PHE. Dte.

Government of West Bengal, Kolkata- 700091

Binod Barui 06.04.2026

06/4/2026

Professor

Dept. of Mechanical Engineering

Jadavpur University, Kolkata-32

Subhasish Sarkar 06/04/2026

Dr. SUBHASISH SARKAR

Assistant Engineer I

Electrical Division, PHE Dte.

Govt. of West Bengal

Tapendu 06.04.2026

Tapendu Mandal

Assistant Professor

Metallurgy and Materials Engineering

IIEST Shibpur

3. List of Publications (Journals)

I. **Barai, B.**, Ojha, A., Sarkar, S., Kundu, S., Oraon, B., & Mandal, T. (2024). Enhancing corrosion resistance of biodegradable magnesium alloys through hydrophobic surface modification: experimental analysis and ANN modeling. **Surface Review and Letters**, doi.org/10.1142/S0218625X24500938.

II. **Barai, B.**, Boorgula, K., Begam, H., Sarkar, S., Barui, A., Kundu, S., ... & Mandal, T. (2025). Multiphysics simulation and experimental investigation of HA and Zn-doped HA coatings on magnesium alloys for resorbable implant applications. **Materials Today Communications**, 42, 111241, doi.org/10.1016/j.mtcomm.2024.111241

III. **Barai, B.**, Kumar, V., Das, P., Sarkar, S., Basak, P., Oraon, B., & Mandal, T. (2025). A hybrid multi-objective optimization framework for designing superhydrophobic coatings on magnesium alloys for biomedical applications. **Biomaterials advances**, 214469., doi.org/10.1016/j.bioadv.2025.214469

IV. Influence of Post-Deposition Heat Treatment on the Performance of Chitosan/Zn-doped Hydroxyapatite Composite Coatings for Bioresorbable Magnesium Alloys: Modelling and Experimental approach, **Journal of Materials Science, (Under review)**

4. Number of Chapters Contributed in Edited Volumes Published by National/International Publishers:

I. **Barai, B.**, Ojha, A., Boorgula, K., Sarkar, S., Mandal, T., & Oraon, B. (2023, June). Synthesis, Characterization, and Studies of the Properties of Low-Cost Eco-friendly Hydrophobic Coating on Magnesium Alloy. **In National Conference on Advancement in Materials Processing Technology (pp. 61-68). Singapore: Springer Nature Singapore.**

5. List of Patents: NIL

Biswajit Barai 06.04.2026

06/4/2026

Professor
Dept. of Mechanical Engineering
Jadavpur University, Kolkata-32

Subhasish Sarkar 06/04/2026

Dr. SUBHASISH SARKAR
Assistant Engineer, I
Electrical Division, PHE Dte.
Govt. of West Bengal

Tapendu Mandal
Assistant Professor
Metallurgy and Materials Engineering
IIEST Shibpur

6. List of presentation in National/International Conferences/ Workshops:

I. August 6-7, 2025, "International Conference on Frontiers in Engineering, Science and Technology: Global Perspective (FESTGP-2025)", Elitte College of Engineering, Sodepur, Kolkata.

II. March 28-29, 2025, "International Conference on Advanced Materials for Sustainable Future (ICAMSF-2025)", Chitkara University, Punjab.

III. January 23-34, 2025, "Indo-Austrialian Symposium on Light weight Metals and alloys for Bioengineering Applications", IIEST Shibpur, Howarh & IIT KGP, Kharagpur

IV. July 18, 2023, "International Conference on Advancement in Materials Processing Technology (AMPT) 2023", National Institute of Technology Jamshedpur

Binod Barui
06.04.2026

06/4/2026

Professor
Dept. of Mechanical Engineering
Jadavpur University, Kolkata-32

Subhasish Sarkar
06/04/2026

Dr. SUBHASISH SARKAR
Assistant Engineer-I
Electrical Division, PHE Dte.
Govt. of West Bengal

Tapendu
06.04.2026

Tapendu Mandal
Assistant Professor
Metallurgy and Materials Engineering
IIEST Shibpur

STATEMENT OF ORIGINALITY

I **BINOD BARAI**, registered on 31.03.2022, do hereby declare that this thesis entitled "Eco-Friendly Surface Engineering of Magnesium Alloys for Resorbable Implant Applications: Experimental, Computational and Data-Driven Optimization Approaches" contains literature survey and original research work done by the undersigned candidate as part of Doctoral studies. All information in this thesis have been obtained and presented in accordance with existing academic rules and ethical conduct. I declare that, as required by these rules and conduct, I have fully cited and referred all materials and results that are not original to this work. I also declare that I have checked this thesis as per the "Policy on Anti Plagiarism, Jadavpur University, 2019", and the level of similarity as checked by iThenticate software is 8 %.

Signature of Candidate: Binod Barai

BINOD BARAI

Date:

Certified by Supervisor(s):

(Signature with date, seal)

1. 06/4/2026

Dr. Buddhadeb Dhaon
Professor
Dept. of Mechanical Engineering
Jadavpur University, Kolkata-32

2. Tapendu 06.04.2026

Dr. Tapendu Mandal

Tapendu Mandal
Assistant Professor
Metallurgy and Materials Engineering
IIEST Shibpur

3. Subhasish Sarkar 06/04/2026

Dr. Subhasish Sarkar

Dr. SUBHASISH SARKAR
Assistant Engineer-I
Electrical Division, PHE Dte.
Govt. of West Benga.

Tapendu Mandal
Assistant Professor
Metallurgy and Materials Engineering
IIEST Shibpur

CERTIFICATE FROM THE SUPERVISORS

This is to certify that the thesis entitled **"Eco-Friendly Surface Engineering of Magnesium Alloys for Resorbable Implant Applications: Experimental, Computational, and Data-Driven Optimization Approaches"** submitted by Shri BINOD BARAI, who got his name registered on 31.03.2022 for the award of Ph.D. (Engineering) degree of Jadavpur University is absolutely based upon his own work under our supervision and that neither his thesis nor any part of the thesis has been submitted for any degree/diploma or any other academic award anywhere before.

1. 06/4/2026

Dr. Buddhadeb Oraon
Professor
Dept. of Mechanical Engineering
Jadavpur University, Kolkata-32

2. 06.04.2026

Dr. Tapendu Mandal

Tapendu Mandal
Assistant Professor
Metallurgy and Materials Engineering
IIEST Shibpur

3. 06/04/2026

Dr. Subhasish Sarkar

SUBHASISH SARKAR
Assistant Engineer I
Electrical Division, PHE Dte.
Govt. of West Bengal

ACKNOWLEDGEMENT

I come from a humble background in a small village, where my parents faced numerous challenges in providing for our family. Despite these hardships, they supported my education selflessly and unconditionally throughout my academic journey. Their sacrifices, perseverance, and unwavering belief in me are beyond words. I dedicate this achievement to my parents, my family, and my friends, whose encouragement and blessings have been my greatest strength.

I express my deepest gratitude to my supervisor, Prof. Buddhadeb Oraon sir, for his constant guidance, encouragement, and unwavering support throughout my Ph.D. journey. It has been a true privilege to pursue my doctoral research under his mentorship. His patience in addressing my numerous queries, his accessibility, and his disciplined approach particularly toward documentation and research ethics have profoundly influenced my academic development.

I am sincerely thankful to my co-supervisor, Dr. Tapendu Mandal sir, for his invaluable contributions to my research work. A major portion of my research was carried out in the Department of Materials and Metallurgy Engineering, IIEST Shibpur, and I owe much of my research knowledge and confidence to his guidance. His support in understanding advanced characterization techniques, manuscript preparation, research presentations, and overall academic development has significantly strengthened my research capabilities and professional growth.

I would also like to express my heartfelt gratitude to another co-supervisor, Dr. Subhasish Sarkar, for his mentorship and encouragement. He was instrumental in motivating me to pursue research with sincerity and dedication, and his continued inspiration has played an important role throughout this journey.

My sincere thanks go to Dr. Howa Begam Di, who guided and supported me as a mentor in the CHST Department at IIEST Shibpur. I am also grateful to Dr. Ananya Barui mam and all the research scholars of the CHST Department for their cooperation and for providing laboratory facilities and a supportive research environment. I extend my appreciation to Dr. Ishita Koley Di, Dr. Avinash Kumar bhaiya, Kesava,

Rishikesh, Sayantan and Abhisek Gupta Da for their valuable contributions to my research work.

I am deeply grateful to the esteemed members of my Research Advisory Committee (RAC), Prof. Rajat Subhra Sen sir and Prof. Partha Sarathi Chakraborty sir, and I also want to thanks Prof. Gautam Majumdar sir, Prof. Goutam Nandi sir, and Dr. Abhisek Mandal Sir for their valuable suggestions, critical insights, and constructive feedback, which have helped refine and strengthen this research work.

A heartfelt thank you to my lab mates Biplab Da, Chandra Sekhar bhaiya, Sovan Da, Ambikesh Da, Soumyabrata Da, Srinath Da, Krishnendu da and to my friends Rupam, Sovan, Arnab and Nabin for their constant moral and emotional support. I am especially thankful to Dr. Vikash Kumar bhaiya, who, though initially my senior, has become one of my closest friends. His continuous encouragement and support have helped me remain focused, resilient, and motivated throughout this journey.

Finally, I sincerely acknowledge all the professors and staff members of Jadavpur University for their support, guidance, and encouragement throughout my academic life.

Binod Barai 06.04.2026

(Binod Barai)

ABSTRACT

Magnesium (Mg) alloys have emerged as promising candidates for resorbable implant applications due to their favorable mechanical compatibility with natural bone and inherent biodegradability. However, their rapid corrosion in physiological environments restricts their clinical translation. This thesis presents a comprehensive and eco-friendly surface engineering strategy integrating experimental development, computational modeling, and data-driven multi-objective optimization to enhance the corrosion resistance and biofunctional performance of Mg alloys for biomedical applications. The study initially focuses on the development of environmentally benign hydrophobic coatings based on stearic acid to mitigate early-stage corrosion. Systematic variation of the coating temperature enabled the formation of metal–stearate protective layers exhibiting improved surface hydrophobicity and reduced corrosion kinetics in simulated body fluid. Building upon this foundation, a hybrid multi-objective optimization framework was implemented to convert hydrophobic surfaces into superhydrophobic coatings using stearic acid and $ZnCl_2$. Response Surface Methodology (RSM-CCD), Artificial Neural Networks (ANN), and evolutionary optimization algorithms (NSGA-II, TLBO, and MOPSO) were integrated to simultaneously optimize the surface roughness, surface free energy, and corrosion resistance. The optimized coating achieved a water contact angle of 152° ± 1°, a corrosion inhibition efficiency exceeding 92%, and a significant reduction in degradation rate, demonstrating the effectiveness of data-driven material design. Subsequently, bioactive ceramic coatings consisting of hydroxyapatite (HA) and Zn-doped HA were developed via dip coating to further regulate the degradation behavior and enhance the biological response. Multiphysics simulations were employed to model flow-induced shear stress under dynamic simulated physiological conditions and correlate mechanical stimuli with corrosion behavior. Experimental electrochemical analysis confirmed substantial reductions in the corrosion rate, while comprehensive surface characterization and in vitro biological evaluations validated improved cytocompatibility and cellular adhesion. The influence of post-deposition heat treatment on chitosan/Zn-doped HA composite coatings was systematically

investigated in this study. Controlled thermal processing optimized microstructural consolidation, phase purity, and interfacial integrity, leading to enhanced corrosion resistance and superior cellular response. Finally, finite element simulations further elucidated the relationship between surface stiffness, morphology, and mechanobiological interactions. Overall, this thesis establishes a scalable, eco-friendly, and data-integrated surface-engineering framework for Mg-based resorbable implants.

Contents

THESIS DETAILS & LIST OF PUBLICATIONS ii
STATEMENT OF ORIGINALITY v
CERTIFICATE FROM THE SUPERVISORS vi
ACKNOWLEDGEMENT vii
ABSTRACT ix
List of Figures xvi
List of Tables xxiv
Chapter 1 1
Introduction 1
1.1 Magnesium alloys: An overview 1
1.2 Emergence of Magnesium Alloys in Biomedical Implants 2
1.3 Challenges Associated with Magnesium-Based Implants 3
1.3.1 Accelerated Corrosion in Physiological Environments 4
1.3.2 Hydrogen Gas Evolution and Local Alkalization 4
1.3.3 Biocompatibility and Cytotoxicity Concerns 5
1.3.4 Localized Corrosion and Micro-galvanic Effects 5
1.3.5 Stress Corrosion Cracking and Mechanical Instability 6
1.4 Strategies to overcome the limitations of Magnesium Alloys 6
1.4.1 Bulk Engineering 6
1.4.2 Surface Engineering Approaches 8
1.5 Optimization and Modeling in Surface coating of Mg Alloys 13
1.5.1 Traditional Optimization Techniques 13
1.5.2 Response Surface Methodology (RSM) 14
1.5.3 Artificial Neural Networks (ANNs) 15
1.5.4 Metaheuristic Algorithms 16
1.5.5 Hybrid Approaches 17
1.6 Cell-Surface interaction simulation 18
1.7 Motivation and Scope of the Present Research 18
1.8 Contribution and Outline of the Thesis 19
Chapter 2 21

Literature review 21
2.1 Magnesium Alloys for Biomedical Applications 21
2.1.1 Mechanical Compatibility with Bone Tissue 21
2.1.2 Common Alloy Systems and Compositions 22
2.1.3 Essential Alloying Elements and Biocompatibility 23
2.1.4 Current Biomedical Applications 23
2.2 Corrosion Mechanisms of Magnesium in Physiological Media 24
2.2.1 General Corrosion Processes 24
2.2.2 Role of Serum Proteins, pH, and Surface Interactions in Corrosion 26
2.2.3 Localized and Stress Corrosion Cracking: Microstructural Influence 27
2.3 Surface Engineering Strategies for Magnesium Alloys 29
2.3.1 Superhydrophobic Coatings on Magnesium Alloys 29
2.3.2 Bioactive Coatings for Magnesium-Based Implants 31
2.4 Dynamic Corrosion and Flow-Induced Shear Stress (FISS) 34
2.5 Optimization Techniques in Surface Engineering 37
2.6 Post deposition treatment and cell-surface Interactions 40
2.7 Summary of Literature Gaps 42
2.8 Research Objectives 44
Chapter 3 47
Development of Hydrophobic Coatings on Magnesium Alloys 47
3.1 Experimental procedure 47
3.1.1 Materials and Pretreatment of Magnesium Alloys 47
3.1.2 Hydrophobic coating construction process 47
3.1.3 Characterization methodology 48
3.1.4 Corrosion study (Potentiodynamic Polarization test) 48
3.2 Result and analysis 49
3.2.1 Surface morphology and EDS analysis 49
3.2.2 Elemental analysis 51
3.2.3 Wettability 52
Chapter 4 55
Multi-Objective Optimization of Superhydrophobic Coatings on Magnesium Alloys 55
4.1 Experimental procedure 55
4.1.1 Design of experiment, data processing and optimization flowchart 55

4.1.2 Experimental design through RSM-CCD 56
4.1.3 Prediction and Optimization Framework 58
4.1.4 Preparation of the coated surface 66
4.1.5 Characterization methods 67
4.1.6 Surface roughness and Surface-free energy measurement 67
4.1.7 Potentiodynamic polarization test 68
4.1.8 In vitro biocompatibility test 69
4.2 Results and dissuasion 70
4.2.1 Experimental data of Corrosion rate and Surface roughness according to RSM-CCD design 70
4.2.2 Analysis of RSM Results 71
4.2.3 ANN results 80
4.2.4 NSGA II results 83
4.2.5 Refine with TLBO, and MOPSO and compare with the experimental and prediction results 84
4.2.6 Sensitivity analysis 89
4.2.7 Analysis of Coating Characterizations 90
4.2.8 Assessment of electrochemical properties 98
4.2.9 Optical after and before corrosion of the coated surface 101
4.2.10 Assessment of the MTT and live dead cell assay of the coated sample 102
Chapter 5 **107**
Bioactive HA and Zn-Doped HA Coatings on Magnesium Alloys: Degradation Assessment in Simulated Physiological Conditions **107**
5.1 Materials and methodology 107
5.1.1 Preparation of coating materials and substrate 107
5.1.2 Dip coating process 108
5.1.3 Computational Framework 109
5.1.4 Structural Characterization 110
5.1.5 Potentiodynamic Polarization 111
5.1.6 Dynamic immersion test 112
5.1.7 Biological characterization 112
5.2 Results and discussion 115
5.2.1 Simulation of FISS distribution 115
5.2.2 Dynamic Immersion test and assessment of degraded surface 117
5.2.3 Assessment of Potentiodynamic Polarization 119

5.2.4 Evaluation of Electrochemical Impedance Spectroscopy 121
5.2.5 Surface morphology after Potentiodynamic Polarization 123
5.2.6 Analysis of Structural Characterization 124
5.2.7 Assessment of Surface roughness 130
5.2.8 Surface morphology and Elemental analysis of substrate and coated samples 131
5.2.9 Cross-sectional view and Elemental Mapping of MgZnHA 134
5.2.10 Adhesion strength of coated sample 136
5.2.11 Assessment of biological characteristics 137
5.2.12 Hemocompatibility 137
5.2.13 Antimicrobial Activity 138
5.2.14 MTT Assay and DAPI Imaging 139
Chapter 6 **141**
Post-Deposition Heat Treatment of Chitosan/Zn-HA Coatings on Mg Alloys: Experimental and Modeling Study **141**
6.1 Experimental procedure 141
6.1.1 Sample preparation 141
6.1.2 Coating Characterization 141
6.1.3 Electrochemical Corrosion Characterization 142
6.1.4 Biological characterization 142
6.1.5 Finite element (FE) analysis 143
6.1.6 FE modelling of cell and substrate 144
6.1.7 Boundary condition and solution method 147
6.2 Result and discussion 147
6.2.1 TGA analysis 147
6.2.2 Optical microscopy and coating thickness 148
6.2.3 Surface morphology and roughness analysis 150
6.2.4 Phase and elemental analysis by XRD, EDS and FTIR 152
6.2.5 Adhesion strength of coated sample (relation with degradation and surface energy, interface energy) 156
6.2.6 Assessment of potentiodynamic test 158
6.2.7 Invitro biocompatibility test 160
6.2.8 Evaluation of Cellular responses through FE simulation 162
Chapter 7 **165**
Conclusions and Future Perspectives **165**

7.1 Conclusion 165
7.1.1 Evolution of Surface Functionalization: From Hydrophobicity to Bioactivity 165
7.1.2 Rational Design through Hybrid Data-Driven Optimization 166
7.1.3 Synergistic Role of Bioactive and Polymeric Components: HA, Zn, and Chitosan 166
7.1.4 Performance under Dynamic Physiological Conditions 167
7.1.5 Tailoring Coating Performance through Post-Deposition Heat Treatment 168
7.1.6 Key Achievements of the Thesis 168
7.1.7 Limitations of the Present Study 169
7.2 Future Perspectives 169
References **171**
APPENDICES **211**

List of Figures

Figure 1.1 Various applications of Mg alloy 2

Figure 1.2 Schematic representation of the applications of magnesium (Mg)-based bioimplants in the human body [9] 3

Figure 1.3 Challenges Associated with Magnesium-Based Implants 6

Figure 1.4 Strategies to Overcome the Limitations of Magnesium Alloys 13

Figure 1.5 Schematic of the Response Surface Methodology (RSM) workflow showing the integration of coating variables, experimental design, statistical optimization, and graphical analysis to determine optimal coating parameters and performance outcomes 15

Figure 1.6 Architecture of the artificial neural network (ANN) model illustrating coating parameters as inputs, nonlinear feature learning through hidden layers, and performance prediction at the output layer 16

Figure 2.1 Schematic representation of corrosion mechanisms in Mg-based alloys under simulated body fluid (SBF) conditions [70] 25

Figure 2.2 (a) Albumin increases solubility via metal-ion chelation. (b) In normal saline, albumin both inhibits corrosion through surface adsorption and promotes it via ion chelation. (c) In Hank's solution, albumin accelerates corrosion by disrupting the Ca/P passivation layer and reducing free Ca^{2+} [71] 27

Figure 2.3 SCC behaviour of Mg–Zn–Zr alloy: (a) fine grains–intergranular cracking; (b–c) bimodal grains–mixed intergranular and transgranular cracking; (d) coarse grains – transgranular cracking [75] 28

Figure 2.4 Network visualization among different keywords in Mg-related papers [124] 42

Figure 3.1 Experimental set up for coating 48

Figure 3.2 SEM images of (a) base and (b–d)coated samples at different temperatures 50

Figure 3.3 Surface profile of base and coated sample at different temperatures 51

Figure 3.4 Comparison of surface roughness value of base and coated samples 51

Figure 3.5 EDS spectra and corresponding atomic compositions of (a) bare magnesium alloy and (b) hydrophobically coated sample prepared at 70 °C for 2 h 52

Figure 3.6 Contact angle measurements of the bare Mg alloy and coated samples .. 53

Figure 3.7 Contact angle testing with droplets of different liquid for time = 0 second and after 20 min respectively 53

Figure 4.1. Schematic of the process flow chart from the design of the experiment to optimization and experimental validation 56

Figure 4.2 Schematic of flow chart NSGA II algorithm [140]..... 61

Figure 4.3 Schematic of flow chart TLBO algorithm [145]..... 63

Figure 4.4 Schematic of flow chart MOPSO algorithm [149] 65

Figure 4.5 Schematic of Coating Process..... 66

Figure 4.6 Response optimization plot obtained using Response Surface Methodology (RSM), showing the optimization of Stearic acid, $ZnCl_2$, and Coating concentrations for maximizing composite desirability (D), corrosion resistance, and surface characteristics 72

Figure 4.7 Surface plot of Surface roughness with different process parameters 78

Figure 4.8 Surface plots of Surface free energy with different input parameters 78

Figure 4.9 surface plots of corrosion resistance efficiency with the different input parameters..... 79

Figure 4.10 ANN results with performance plot, training state plot, error histogram, and regression plot..... 81

Figure 4.11 ANN results after data augmentations with performance plots, training state plots, error histograms, and regression plot 83

Figure 4.12 Diverse Pareto front achieved by NSGA-II, illustrating the trade-offs between multiple objectives in the optimization process 84

Figure 4.13 Refined Pareto front: (a) TLBO optimization and (b) MOPSO optimization, demonstrating improved convergence and solution refinement compared to the initial Pareto front..... 86

Figure 4.14 Individual response convergence plot: (a) TLBO and (b) MOPSO, showing the progression of convergence for each optimization method across the responses..... 86

Figure 4.15 Comparison between actual and predicted values for TLBO, MOPSO, and CCD methods across key performance indicators: (a) Surface roughness (μm), (b) Surface free energy (mN/m), and (c) Corrosion resistance efficiency (%) 88

Figure 4.16 Sensitivity analysis of the optimization results using the TLBO algorithm, showing the impact of various parameters on the objective functions..... 89

Figure 4.17 Sensitivity analysis of the optimization results using the MOPSO algorithm, illustrating the influence of different parameters on the objective functions 90

Figure 4.18 Digital images of magnesium alloy samples: (a) after superhydrophobic coating, displaying a uniformly white surface indicating the formation of Zn/Mg-stearate layer; (b) before coating, showing the bare metallic surface 91

Figure 4.19 Water droplet on the coated Mg alloy surface showing super hydrophobicity. Inset: Goniometer measurement confirms a contact angle of 152.2° 91

Figure 4.20 Surface morphology of (a) Bare polished Mg alloy showing linear grinding marks; (b) Coated surface at low magnification showing rough and hierarchical morphology; (c) High-magnification SEM image revealing densely packed, micro/nano flake-like structures..... 92

Figure 4.21 3D surface profilometry images showing surface roughness topography of (a) uncoated substrate Mg alloy and (b) coated Mg alloy. Clear contrast in surface morphology demonstrates the formation of micro/nano hierarchical structures post-coating 92

Figure 4.22 X-ray Diffraction (XRD) patterns of (a) bare Mg alloy (base) and (b) Zn stearate-coated Mg alloy, showing phase composition and crystallinity of the samples 93

Figure 4.23 Energy Dispersive X-ray Spectroscopy (EDS) spectra of (a) bare Mg alloy and (b) Zn stearate-coated Mg alloy, illustrating the elemental composition and distribution of key elements 94

Figure 4.24 (a) Fourier Transform Infrared (FTIR) spectra of bare and coated Mg alloy, highlighting the functional groups and bonding characteristics. (b) Raman spectra of bare and coated Mg alloy, revealing insights into the chemical bonding of the samples 95

Figure 4.25 Electrochemical characterization of the coated and uncoated Mg alloys: (a) Potentiodynamic polarization curves for substrate and coated samples. (b) Nyquist plot from EIS showing impedance data with fitted curves. (c) Equivalent circuit model with R1, R2, and R3 representing solution resistance, coating resistance, and charge transfer resistance, respectively..... 100

Figure 4.26 Optical images before and after corrosion of coated (a&b) and substrate (c&d)..... 101

Figure 4.27 Cell viability percentage of control and coated sample after 24 hours and 48 hours 102

Figure 4.28 Live dead cell assay of coated sample after 24 hours 104

Figure 4.29 Live dead cell assay of coated sample after 48 hours 104

Figure 5.1 Schematic of flow process of dip coating 108

Figure 5.2. (a) Velocity profile of MgHA sample at 2 ml/min flow rate. (b), (c), (d) Shear Stress profiles along the bisector of the top surface in the flow direction for bare Mg, MgHA, and MgZnHA samples respectively 115

Figure 5.3. (a) Body shear stress profile of the MgZnHA sample at 9 ml/min flow rate, (b) Top surface shear stress profile of bare Mg sample at 5 ml/min, (c) Top surface shear stress average for the three samples w.r.t. flow rate, (d) Range of shear stress on the top surface for the three samples as a function of flow rate. 116

Figure 5.4. Corrosion rate of MgZnHA sample under varying flow rates 117

Figure 5.5. Image of immersion test of the MgZnHA coated sample in two different flow conditions 118

Figure 5.6. Image of SEM micrograph of MgZnHA sample after immersion test in (a) static flow condition, (b) 2 ml/min flow rate, (c) 5 ml/min flow rate, (d) 9 ml/min flow rate, and (e), (f) higher magnification image at 9 ml/min flow rate 119

Figure 5.7. Potentiodynamic polarization curve of Mg, MgHA, and MgZnHA samples 120

Figure 5.8. Equivalent circuit for EIS data fitting 122

Figure 5.9. Nyquist plot of Mg, MgHA, and MgZnHA samples 122

Figure 5.10. SEM and EDS image of (a), (c) MgHA and, (b), (d) MgZnHA 124

Figure 5.11 XRD pattern of substrate Mg, MgHA, and MgZnHA samples 125

Figure 5.12. (a) FTIR and (b) Raman spectrum of substrate Mg, MgHA, and MgZnHA samples 126

Figure 5.13. XPS analysis of base Mg alloy showing (a) survey spectra, (b) Mg 1s, (c) Al 2p, (d) Mn 2p, (e) C 1s, and (f) O1s peaks 127

Figure 5.14 XPS analysis of Zn-doped HA coated Mg alloy (MgZnHA) showing (a) survey peak, (b) C1s, (c) N1s, (d) Ca2p, (e) P2p, (f) Zn2p, (g) O1s 130

Figure 5.15. Surface morphology by 3d profilometer: (a) Bare Mg, (b) Mg after etching, (c) MgHA sample, and (d) MgZnHA sample 131

Figure 5.16. SEM image of (a) base (b) etched (c) HA, (d) Zn HA, (e) HA in higher magnification 132

Figure 5.17. EDS spectra of (a) Base, (b) Etched, (c)HA coated, (d) Zn doped HA-coated, and, (e) their Corresponding EDS spectra plot 133

Figure 5.18. (a) Bare sample before coating and after coating, (b) optical cross-sectional view of the coated sample 134

Figure 5.19 Elemental mapping of MgZnHA 135

Figure 5.20 Tape scratch test to evaluate bonding strength between coating and substrate: (a) sample before scratch test, (b) and (c) samples after scratch test 136

Figure 5.21. Hemolysis analysis of Bare, MgHA, and MgZnHA samples 137

Figure 5.22. Images of (a) Antimicrobial test results, and (b) corresponding inhibition zone..... 138

Figure 5.23. Comparison of cell viability percentages among control, base Mg, MgHA, and MgZnHA samples 139

Figure 5.24. (a), (b), (c) Image of MC3T3 cell nucleus after 5 days of culture of Mg, MgHA, MgZnHA, and, (d) Quantitative cell attachment results for different samples 140

Figure 6.1. (a) Microscopic image of transfected mesenchymal stem cell; (b) 3D FE model and internal components of the cell model; (c) Top view of cell model; (d) Geometric properties used for designing the cell model. 145

Figure 6.2. (a) Average roughness of untreated and heat-treated substrates; (b) Schematic of static cell culture condition indicating cell position on petri dish; (c) Boundary condition on cellular model by applying hydrostatic pressure on cell face (red contour) and keeping bottom face of substrate fixed 146

Figure 6.3. Thermogravimetric analysis (TGA) curve of the Zn-doped hydroxyapatite (HAp) and chitosan composite coated sample. 148

Figure 6.4. Optical micrographs of Zn-doped hydroxyapatite (HAp) and chitosan composite coatings on Mg alloy: (a) as-coated (before heat treatment), and after heat treatment at (b) 120 ℃, (c) 240 ℃, and (d) 360 ℃. 149

Figure 6.5. Cross-sectional optical micrographs of Zn-doped hydroxyapatite (HAp) and chitosan composite coatings on Mg alloy: (a) as-coated (before heat treatment), and after heat treatment at (b) 120 ℃, (c) 240 ℃, and (d) 360 ℃ 150

Figure 6.6. SEM micrographs of Zn-doped hydroxyapatite (HAp) and chitosan composite coatings on Mg alloy: (a) as-coated (before heat treatment), and after heat treatment at (b) 120 ℃, (c) 240 ℃, and (d) 360 ℃ 151

Figure 6.7. 3D surface profilometry images of Zn-doped hydroxyapatite (HAp) and chitosan composite coatings on Mg alloy: (a) as-coated (before heat treatment), and after heat treatment at (b) 120 ℃, (c) 240 ℃, and (d) 360 ℃ 151

Figure 6.8. X-ray diffraction (XRD) patterns of Zn-doped hydroxyapatite (HAp) and chitosan composite coatings on Mg alloy: as-coated (ZnHA) and heat-treated samples at 120 ℃ (S|120), 240 ℃ (S|240), and 360 ℃ (S|360) 153

Figure 6.9. FTIR spectra of Zn-doped hydroxyapatite (HAp) and chitosan composite coatings on Mg alloy: as-coated (ZnHA) and heat-treated samples at 120 ℃ (S|120), 240 ℃ (S2|240), and 360 ℃ (S|360) 155

Figure 6.10. Elemental composition (EDS analysis) of Zn-doped hydroxyapatite (HAp) and chitosan composite coatings on Mg alloy: as-coated (ZnHA) and heat-treated samples at 120 ℃ (S|120), 240 ℃ (S|240), and 360 ℃ (S|360) 156

Figure 6.11 Scratch test images of Zn-doped hydroxyapatite (HAp) and chitosan composite coatings on Mg alloy for adhesion analysis: (a) as-coated (before heat treatment) sample and (b) heat-treated samples at 120 ℃, 240 ℃, and 360 ℃. Optical micrographs of the scratch regions are shown for (c) the as-coated surface and (d–f) coatings after heat treatment at 120 ℃, 240 ℃, and 360 ℃, respectively 157

Figure 6.12. Corrosion test results: (a) Tafel plot, (b) Nyquist plot, (c) & (d) Equivalent circuits 159

Figure 6.13. Cell viability results by MTT test for (a) as-coated (before heat treatment), and after heat treatment at (b) 120 °C, (c) 240 °C, and (d) 360 °C 161

Figure 6.14. Cell attachment results by DAPI for (a) as-coated (before heat treatment), and after heat treatment at (b) 120 °C, (c) 240 °C, and (d) 360 °C 162

Figure 6.15. Maximum principle strain contours at cell interface for (a) untreated coated sample surface and (b), (C), (d) coated sample surface heat treated at 120 °C, 240 °C and 360 °C respectively 163

List of Tables

Table 2.1 Comparison of properties of Mg alloy with other implant materials 22

Table 2.2 Recent Mg-based biomedical devices 24

Table 2.3. Chemical substances and their associated hazard statements in accordance with Regulation (EC) No 1272/2008 [80] 31

Table 2.4 Summary of ceramic and ceramic-polymer composite coatings on magnesium-based alloys 33

Table 2.5 Summary of Dynamic Corrosion behavior and FISS in Mg-Based Alloys 36

Table 2.6 Optimization approaches in Mg alloy surface engineering for resorbable implants: algorithms, applications, outcomes, and key references 39

Table 4.1 The range of input process parameters, including the design summary of RSM-CCD, has been represented below 57

Table 4.2 Experimental data sheet of input process parameters and corresponding responses 70

Table 4.3 Regression coefficient for different response 72

Table 4.4 Analysis of Variance (ANOVA) for surface roughness, showing the significance of different factors on the surface texture 74

Table 4.5 Analysis of Variance (ANOVA) for surface free energy, highlighting the contribution of various factors to the surface energy characteristics 75

Table 4.6 Analysis of Variance (ANOVA) for corrosion resistance efficiency, illustrating the impact of different factors on the corrosion performance 76

Table 4.7 Comparison of predicted responses from different algorithms, including TLBO, MOPSO, and CCD, highlighting the accuracy of predictions for the responses 88

Table 4.8 Corrosion parameters for the coated and uncoated Mg alloy samples, including corrosion current density (I_{corr}), corrosion potential (E_{corr}), and corrosion rate 100

Table 4.9 EIS parameters, including R1, R2, R3, and constant phase elements (CPE n, CPE p), for both substrate and coated samples 100

Table 5.1. The physical attributes of the Mg alloy base material and the coated specimens 110

Table 5.2. Parameter's summary computed from potentiodynamic polarization observations for different samples..... 120

Table 5.3. Impedance parameters for different samples..... 122

Table 6.1. Number of elements used for substrate models..... 145

Table 6.2. Material parameters of cellular components. 146

Table 6.3 Corrosion parameters from Tafel plot 159

Table 6.4 EIS parameters from Nyquist plot..... 160

Table 6.5. Average Strain and Strain energy density (SED) oberved at cell interace for different substrate roughness..... 163

Chapter 1

Introduction

1.1 Magnesium alloys: An overview

Magnesium (Mg) is the lightest structural metal, with a density of approximately 1.74 g cm^{-3}, making it highly attractive for modern engineering applications where weight reduction is critical. Its unique combination of low density, high specific strength, excellent vibration damping capacity, and good thermal conductivity has positioned magnesium alloys as promising materials across automotive, aerospace, electronics, and biomedical sectors. The development of magnesium alloys reflects a continuous interaction between scientific advancements, industrial demands, and strategic requirements, highlighting both their potential and inherent limitations [1].

Elemental magnesium was first isolated by Sir Humphry Davy in 1808, with large-scale industrial production emerging in the late 19th and early 20th centuries. Its strategic importance became evident during World Wars I and II, particularly in lightweight aircraft and military applications. Early milestones include its use in racing engine pistons by Dow Chemical in 1921, engine blocks in the Volkswagen Beetle in the 1930s, and structural components in aircraft such as the Focke-Wulf 200C-3 Condor. By the mid-20th century, magnesium was extensively utilized in military aircraft, including the B-36 bomber, underscoring its engineering significance [2].

In modern engineering practice, magnesium alloys have found wide industrial applications in the automotive, aerospace, and electronics sectors. The automotive industry accounts for approximately 70% of the global magnesium consumption, with applications encompassing body systems, chassis systems, powertrain components, and interior and exterior trim structures [3]. In electronics and consumer products, magnesium alloys are increasingly replacing polymers due to superior electromagnetic shielding, heat dissipation, dimensional stability, recyclability, and vibration damping. Compared with aluminum and steel, they offer a higher strength-to-weight ratio, excellent castability, and outstanding damping capacity. However, industrial adoption

remains limited, with magnesium accounting for only ~0.4 wt. % of an average vehicle in 2022. Its high cost, supply constraints, poor room-temperature formability, low corrosion resistance, sustainability concerns, and limited manufacturing familiarity continue to hinder its widespread implementation. Beyond structural applications, magnesium alloys have emerged as promising materials for biodegradable biomedical implants because of their bone-like elastic modulus and resorbability [4,5].

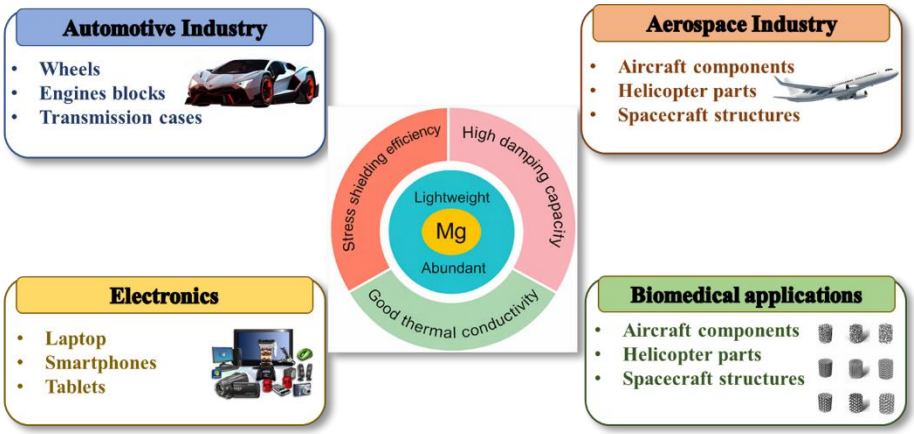

Figure 1.1 Various applications of Mg alloy

1.2 Emergence of Magnesium Alloys in Biomedical Implants

The development of advanced biomaterials is critical for improving implant performance and patient outcomes, particularly in orthopedic and cardiovascular applications. Conventional metallic implants, such as stainless steel and titanium alloys, provide high strength and biocompatibility but suffer from permanent implantation–related limitations, including stress shielding, chronic inflammation, and the need for secondary removal surgeries. These drawbacks have driven interest in biodegradable materials that offer temporary mechanical support while actively participating in tissue healing processes. Magnesium and its alloys have emerged as leading candidates for resorbable implants due to their favorable mechanical compatibility and biodegradability, with an elastic modulus (40–45 GPa) closer to that of cortical bone than titanium or stainless steel, thereby reducing stress shielding. Magnesium is also an essential biological element that is predominantly stored in the bone and involved in cellular metabolism [6]. Although early clinical use was hindered by excessively rapid corrosion and hydrogen evolution, advances in alloy design,

processing, and additive manufacturing have reduced degradation rates to 0.02–0.36 mm·year^{-1} while achieving tensile strengths of up to 365 MPa, enabling the successful clinical translation of devices such as MAGNEZIX and Magmaris [7]. In addition to providing mechanical support, magnesium implants exhibit bioactive degradation, releasing Mg^{2+} ions that promote osteogenesis, and their complete resorption eliminates the need for implant removal [8]. Nevertheless, challenges related to rapid and non-uniform corrosion, hydrogen evolution, and discrepancies between in vitro and in vivo degradation rates persist, highlighting the need for advanced surface engineering and precise control of the degradation kinetics.

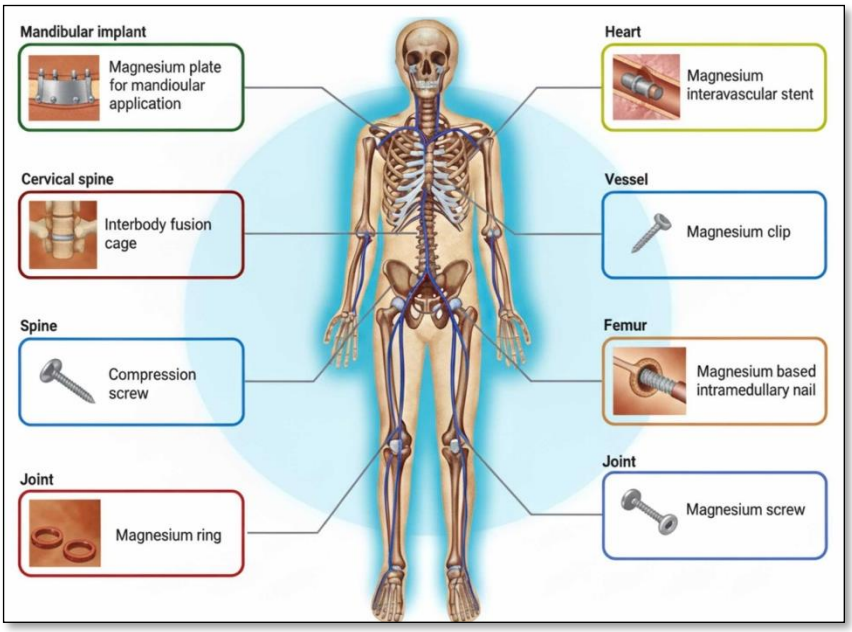

Figure 1.2 Schematic representation of the applications of magnesium (Mg)-based bioimplants in the human body [9]

1.3 Challenges Associated with Magnesium-Based Implants

The principal barrier to the clinical translation of magnesium-based implants is their uncontrolled and excessively rapid degradation in physiological environments. Owing to the highly negative standard electrode potential of magnesium (~−2.37 V), it is extremely susceptible to corrosion in aqueous media [10]. While bone remodeling typically requires 24–32 weeks, most magnesium implants degrade within 6–12 weeks, leading to premature loss of mechanical integrity and compromised load-

bearing capability well before the completion of tissue regeneration. This mismatch between the degradation rate and healing time remains a critical limitation of magnesium-based biomedical devices [11].

1.3.1 Accelerated Corrosion in Physiological Environments

The rapid deterioration of mechanical integrity arises from the complex interactions between magnesium and the physiological environment. Bodily fluids contain a high concentration of chloride ions (approximately 96–106 mEq/L) and maintain a near-neutral pH of 7.4–7.6, conditions that significantly accelerate magnesium corrosion compared with conventional aqueous solutions [12]. Although a magnesium hydroxide layer initially forms on the implant surface, in the absence of any protective layer, this film becomes unstable in the presence of chloride ion concentrations exceeding ~30 mM and is converted into highly soluble magnesium chloride, thereby accelerating corrosion. Given that physiological fluids typically contain ~150 mM chloride ions, far exceeding this threshold, the rapid degradation of magnesium implants becomes inevitable. Consequently, the ideal degradation rate of approximately 0.17 $mm \cdot year^{-1}$ required for bone-supporting implants is rarely achieved in practice [13].

1.3.2 Hydrogen Gas Evolution and Local Alkalization

A particularly problematic consequence of magnesium degradation is hydrogen gas evolution, governed by the overall reaction in Equation 1.1 below [14]:

$$Mg + 2H_2O = Mg(OH)_2 + H_2 \uparrow \quad (1.1)$$

The rapid generation of hydrogen gas negatively impacts the surrounding tissues because gas bubbles can accumulate at the implant–tissue interface and form cavities that separate tissue layers, leading to subcutaneous swelling and delayed healing. Hydrogen evolution rates as high as 0.01 $mL \cdot cm^{-2} \cdot day^{-1}$ have been reported for magnesium alloys containing zinc, aluminum, and manganese. Simultaneously, magnesium corrosion produces hydroxide ions that locally increase pH levels [15].

Surface alkalization can adversely affect cellular activities and induce cytotoxic responses or cell death. Unlike transition metal implants, such as titanium or stainless steel, which often produce acidic corrosion environments, magnesium degradation shifts the local environment toward alkalinity, creating an unfavorable microenvironment for tissue integration and regeneration.

1.3.3 Biocompatibility and Cytotoxicity Concerns

Although magnesium is an essential element in human physiology and is inherently biocompatible, excessive corrosion can generate high concentrations of degradation products that compromise its biological compatibility. Rapid degradation releases large amounts of Mg^{2+}, OH^{-}, and alloying element ions, which may negatively affect cell viability. According to the ISO 10993-5:2009 standards, cytotoxicity is defined as a reduction in cell viability exceeding 30%, and numerous magnesium alloys have been reported to exhibit cell viability below 75% in in vitro studies [16]. Biocompatibility concerns are further exacerbated by the alloy composition. Aluminum, when present in large quantities, may cause adverse effects, including neurotoxicity and impaired osteoblast function, and has been linked to neurological disorders such as dementia and Alzheimer's disease (AD). Similarly, certain rare-earth elements, such as cerium, holmium, and praseodymium, have demonstrated hepatotoxic effects. In addition, impurity elements, including iron, nickel, and copper, act as strong cathodic sites, accelerating galvanic corrosion and further degrading implant performance [17].

1.3.4 Localized Corrosion and Micro-galvanic Effects

Magnesium implants experience multiple corrosion modes simultaneously, with surface and pitting corrosion being the most prevalent. Pitting corrosion is particularly destructive because it initiates the localized breakdown of the surface film and rapidly propagates into the magnesium matrix. The corrosion resistance of magnesium alloys strongly depends on the uniformity and compactness of the surface film; defects in this layer promote localized attacks and accelerated dissolution [18]. The presence of second phases, precipitates, and impurity particles introduces

electrochemical heterogeneity, influence the grain size leading to the formation of micro-galvanic cells. These cells accelerate localized corrosion by creating potential differences between the magnesium matrix and secondary phases, ultimately causing a rapid loss of load-bearing capability [19].

1.3.5 Stress Corrosion Cracking and Mechanical Instability

Under physiological loading conditions, such as walking and running, magnesium-based implants are susceptible to stress corrosion cracking (SCC), a particularly dangerous failure mechanism resulting from the combined action of mechanical stress and corrosive environments [20]. SCC is characterized by the initiation and propagation of fine cracks that may not be readily visible on the surface but can lead to catastrophic, brittle failure. In vivo studies have shown that corrosion-assisted cracking significantly reduces the lifetime and reliability of implants, making mechanical performance prediction extremely challenging [21].

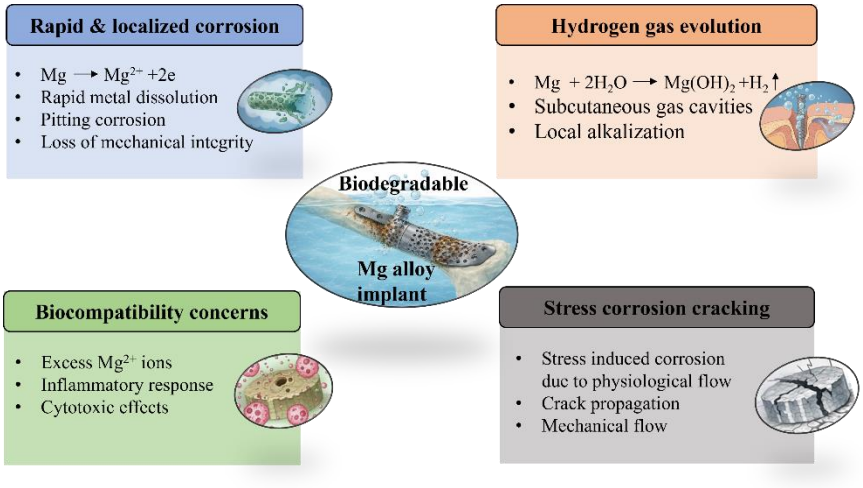

Figure 1.3 Challenges Associated with Magnesium-Based Implants

1.4 Strategies to overcome the limitations of Magnesium Alloys

1.4.1 Bulk Engineering

Bulk engineering enhances the intrinsic properties of magnesium alloys via compositional modification and thermomechanical processing. By refining the grain structure, optimizing the phase distribution, and strengthening the matrix, the

mechanical integrity is improved, and the corrosion behavior is moderated without relying on the surface layers.

1.4.1.1 Bulk Alloying

Bulk alloying is an effective strategy for improving the mechanical properties and corrosion resistance of Mg alloys without complex surface treatments. The addition of selected alloying elements, particularly rare earth elements such as Ce, Y, Gd, and Nd, promotes grain refinement and the formation of stable oxide layers, resulting in enhanced strength and passivation. Grain refinement is the dominant strengthening mechanism in magnesium alloys, which exhibit a high Hall-Petch coefficient (200–300 $MPa \cdot \mu m^{-1/2}$), indicating a strong sensitivity to grain size reduction [22]. Multicomponent alloying enables synergistic strengthening through solid solution and precipitation mechanisms, whereas elements such as Zn, Ca, Sr, and Mn offer cost-effective and biocompatible alternatives to rare-earth additions. When combined with thermomechanical processing, bulk alloying can produce magnesium alloys with a superior strength–ductility balance, outperforming commercial alloys such as WE43 in some cases [23].

1.4.1.2 Thermomechanical Processing

Thermomechanical processing is a powerful approach for enhancing the mechanical and corrosion performance of magnesium alloys by exploiting their improved deformability at high temperatures. Controlled deformation refines the grains, homogenizes the microstructure, fragments the secondary phases, and increases the dislocation density, thereby addressing the intrinsic limitations of as-cast Mg alloys. Conventional processes such as hot extrusion, rolling, and forging-often used sequentially-enable the simultaneous optimization of strength, corrosion resistance, and biocompatibility, with hot extrusion being particularly effective for biomedical Mg alloys. Severe plastic deformation techniques offer further refinement but are limited by the component size. Consequently, the integration of optimized alloy compositions with tailored thermomechanical processing is essential for developing high-performance magnesium alloys for biomedical applications [24].

1.4.2 Surface Engineering Approaches

Surface engineering plays a crucial role in enhancing magnesium alloys for biodegradable implants by mitigating rapid corrosion and premature mechanical failures. The objective is to control the degradation kinetics while maintaining the mechanical integrity and biocompatibility during tissue healing. These strategies are broadly categorized into surface modification, which alters the substrate without forming a distinct layer, and surface coating, which deposits protective layers with tailored properties. Both approaches are often integrated to create a controlled interface between the magnesium substrate and the physiological environment, ensuring regulated degradation and improved biological performance.

1.4.2.1 Surface Modification

Surface modification techniques are commonly employed as preliminary or intermediate steps to tailor the surface chemistry, morphology, and reactivity without significantly altering the bulk properties. These methods improve the initial corrosion resistance, suppress early hydrogen evolution, and enhance the adhesion of subsequent coatings, making them particularly relevant for biodegradable magnesium implants.

Anodization

Anodization is a cost-effective and environmentally compatible surface modification technique for magnesium alloys that forms $MgO/Mg(OH)_2$ layers in alkaline electrolytes, reducing early hydrogen evolution and surface alkalization while improving initial implant stability and cell attachment [25]. The coating morphology and roughness can be tuned via anodization parameters, and the intrinsic porosity supports controlled ion release for biodegradable applications. Fluoride-containing electrolytes generate MgF_2-rich layers with enhanced corrosion resistance, whereas higher voltages induce plasma-assisted anodic oxidation, producing thicker, harder, and more adherent ceramic-like coatings with improved bioactivity. However, the inherent porosity and limited thickness of the anodic layers permit electrolyte ingress over time. Consequently, anodization is often used as an interfacial or anchoring layer

in hybrid coating systems to enable sealing treatments and achieve sustained corrosion control and tailored degradation [26].

Chemical and physical treatments

Beyond electrochemical oxidation, chemical and physical treatments offer complementary approaches to tailor magnesium alloy surfaces. These include solution-based reactions and physical methods such as laser processing, thermal treatment, and ion implantation [3]. Although they provide limited standalone corrosion protection, they effectively modify the surface chemistry, morphology, and surface energy, thereby enhancing the corrosion resistance and improving the adhesion of subsequent coatings.

Chemical Treatments

Chemical treatments modify magnesium surfaces via spontaneous reactions in alkaline or acidic solutions, forming thin protective layers without an external current. NaOH produces $Mg(OH)_2$ films with limited durability, while fluoride treatments form MgF_2 layers that restrict chloride ingress but may reduce long-term bioactivity of the coating. Phosphate coatings offer good insolubility and biocompatibility but are brittle, whereas rare-earth (e.g., cerium) treatments generate thicker and more stable corrosion-resistant layers through insoluble compound formation. Phytic acid provides a biofriendly alternative, forming chelated surface networks that enhance the adhesion of subsequent coatings. Although insufficient for long-term protection alone, chemical treatments are effective as pretreatment layers in hybrid systems [27].

Physical and Laser-Based Treatments

Physical treatments alter the surface morphology and microstructure to influence the degradation behavior. Laser surface modification refines grains, increases dislocation density, and tailors electrochemical activity through rapid thermal cycling without causing bulk distortion. Laser texturing improves coating adhesion by enhancing the roughness, surface energy, and mechanical interlocking. When combined with micro-arc oxidation or chemical functionalization, synergistic improvements in oxide uniformity, superhydrophobicity, and corrosion resistance are achieved. However, an

increased surface area may accelerate degradation, and long-term biocompatibility data remain limited, underscoring the need for integrated surface engineering approaches [28].

1.4.2.2 Surface Coating

While surface modification alters intrinsic surface properties, surface coatings introduce distinct protective layers that act as physical and chemical barriers against aggressive physiological environments. Coatings reduce corrosion kinetics by hindering diffusion of corrosive species and can be engineered to promote bioactivity, controlled degradation, and mechanical compatibility. For biodegradable magnesium implants, coating strategies increasingly rely on multilayer and composite architectures, often deposited by hydrothermal or dip-coating techniques.

Conversion coatings

Conversion coatings are chemically or electrochemically formed layers created by the in-situ transformation of the magnesium substrate into adherent oxide or compound phases, offering strong interfacial bonding and cost-effective corrosion protection for industrial and biomedical applications. Phosphate-based coatings are environmentally benign and widely applied. They are formed via magnesium dissolution in phosphoric media and the precipitation of insoluble phosphates. They typically exhibit a duplex structure with a dense inner layer and a porous outer barrier. Zinc phosphate systems provide corrosion resistance comparable to chromates, while calcium phosphate coatings yield biocompatible phases such as hydroxyapatite; however, high processing temperatures, long treatment times, and brittleness may limit their durability [29,30].

Polymer, Ceramic and composite coating

Polymer, ceramic, and composite coatings represent advanced surface engineering strategies for magnesium alloys, offering greater flexibility in tailoring corrosion resistance, bioactivity, and degradation behavior compared to single-phase conversion or oxide coatings. These coatings are typically deposited by dip coating, spin coating, layer-by-layer assembly, or hydrothermal routes, enabling controlled thickness, composition, and interfacial properties [10]. Their primary function is to form an

effective physical and chemical barrier that limits corrosive ion transport while supporting biological integration of the stent.

Polymer-Based Coating

Polymer coatings offer biocompatible and biodegradable barriers for magnesium implants and can incorporate bioactive and therapeutic agents. Their effectiveness is strongly governed by coating–substrate adhesion, which arises from hydrogen bonding, chemical interactions, and, most critically, mechanical interlocking enabled by surface roughness. Surface pretreatments, such as conversion coatings, enhance polymer adhesion by increasing roughness and generating oxide species capable of strong interfacial bonding [31]. For biodegradable implants, polymer degradation must be synchronized with magnesium corrosion; however, the acidic degradation products from common polyesters can locally alter the pH and accelerate corrosion. Hybrid polymer–ceramic coatings address this limitation by combining corrosion resistance with controlled degradation [32]. For example, dual-layer Poly-trimethylene carbonate (PTMC–MAO) systems significantly reduce the corrosion current density, maintain a near-neutral pH, and degrade uniformly while offering additional functionalities such as drug delivery, highlighting the promise of polymer–ceramic architectures for multifunctional biodegradable implants [33].

Ceramic-Based Coating

Ceramic coatings provide high hardness, chemical stability, and bioactivity, with hydroxyapatite (HA) and calcium phosphate systems being particularly attractive for orthopedic applications due to their similarity to bone mineral. HA coatings deposited on magnesium by plasma spraying or hydrothermal methods enhance bioactivity but suffer from an elastic modulus mismatch with magnesium, leading to interfacial stress, coating fracture, and reduced corrosion protection [34]. To address this limitation, intermediate organic or hybrid interlayers have been introduced into the device structure. Multilayer architectures incorporating polymers or silica-based interlayers improve stress redistribution, enhance interfacial bonding, and buffer hydrogen evolution during magnesium degradation, thereby improving the durability of the coating. Alternative ceramic systems, such as calcium silicate and bioactive glass,

offer similar biocompatibility and enable therapeutic ion incorporation, supporting multifunctional coating designs [35].

Hydrothermal Coating Deposition

Hydrothermal coating techniques offer distinct advantages for producing dense and well-adhered ceramic and composite coatings on magnesium alloys. Conducted in sealed autoclaves under elevated temperature and pressure, hydrothermal processing promotes in situ crystal growth and strong interfacial bonding, resulting in coatings with superior density and corrosion resistance compared to conventional chemical deposition methods. Advanced hydrothermal strategies have enabled fabrication of multilayer calcium phosphate-based coatings. For instance, zinc phosphate conversion coatings followed by hydrothermal treatment produced dense phosphate/ZnO multilayer systems with sealed microcracks and significantly enhanced corrosion resistance on the AZ61 magnesium alloy. Such systems demonstrate the effectiveness of hydrothermal processing as a post-treatment or secondary deposition route in composite coating architectures [36]

Layer-by-Layer and Smart Coating Systems

Layer-by-layer (LBL) assembly enables precise control over coating thickness and composition through sequential deposition, allowing tailored functionality on Mg alloys. LBL architectures combining ceramic and polymer layers provide controlled degradation, improved biocompatibility, antibacterial performance, and enhanced mechanical stability by distributing stress across multiple interfaces. Advanced smart coatings further incorporate self-healing functionality using inhibitor-loaded microcapsules. For example, gelatin–chitosan microcapsules containing lanthanum nitrate embedded in magnesium–cerium conversion coatings release inhibitors upon crack formation, effectively suppressing localized corrosion and extending the coating service life [37].

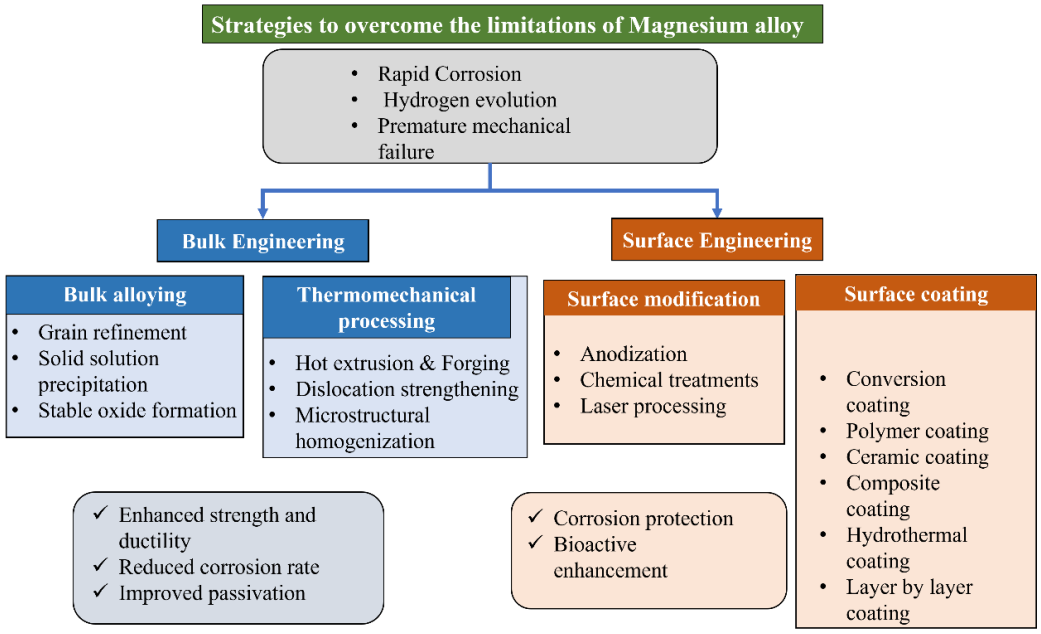

Figure 1.4 Strategies to Overcome the Limitations of Magnesium Alloys

1.5 Optimization and Modeling in Surface coating of Mg Alloys

The performance of surface coatings on magnesium alloys is governed by a complex interplay of multiple processing parameters, including precursor concentration, pH, temperature, deposition time, surface pretreatment, and post-deposition treatments. These parameters collectively influence the coating morphology, thickness, adhesion strength, corrosion resistance, mechanical integrity, and biocompatibility. Due to the strong interdependence and nonlinearity among these variables, systematic optimization and predictive modeling have become essential tools for designing high-performance coatings for biomedical and engineering applications. Over the past few decades, optimization strategies have evolved from empirical trial-and-error approaches to advanced data-driven and hybrid modeling frameworks.

1.5.1 Traditional Optimization Techniques

Early efforts to optimize the surface coating processes on magnesium alloys were predominantly empirical. Researchers typically employed a one-factor-at-a-time (OFAT) strategy, wherein a single processing parameter was varied while all others

were held constant to evaluate its influence on coating characteristics. Although conceptually straightforward, this approach is inherently inefficient, time-consuming, and resource-intensive. More importantly, it fails to capture interaction effects between process variables, which are often significant in coating systems involving coupled chemical reactions, diffusion processes, and interfacial phenomena. As a result, OFAT-based optimization frequently leads to suboptimal parameter selection and an incomplete mechanistic understanding. These limitations highlight the need for more statistically rigorous and systematic methodologies capable of evaluating multiple variables simultaneously, thereby motivating the adoption of formal design of experiments (DoE) techniques [38].

1.5.2 Response Surface Methodology (RSM)

Response surface methodology (RSM) represents a major advancement in the statistical modeling and optimization of coating processes characterized by multiple interacting parameters. RSM integrates mathematical modeling with structured experimental designs to establish quantitative relationships between independent variables (process parameters) and dependent responses (such as corrosion rate, hardness, coating thickness and surface roughness). Common experimental designs employed in RSM include the central composite design (CCD) and Box–Behnken design (BBD), which are selected for their efficiency in exploring multidimensional parameter spaces while minimizing experimental runs. The resulting datasets are typically fitted using second-order polynomial models, enabling the prediction of response trends, identification of significant interaction effects, and determination of optimal parameter combinations. RSM has been extensively applied in surface coating studies to optimize electroless, sol-gel, hydrothermal, and polymer-based coatings on magnesium alloys. Despite its effectiveness, RSM relies on predefined polynomial assumptions and may struggle to accurately represent highly nonlinear systems or complex physicochemical interactions beyond second-order behavior [39,40]. The schematic of the RSM workflow has been shown in Figure 1.5.

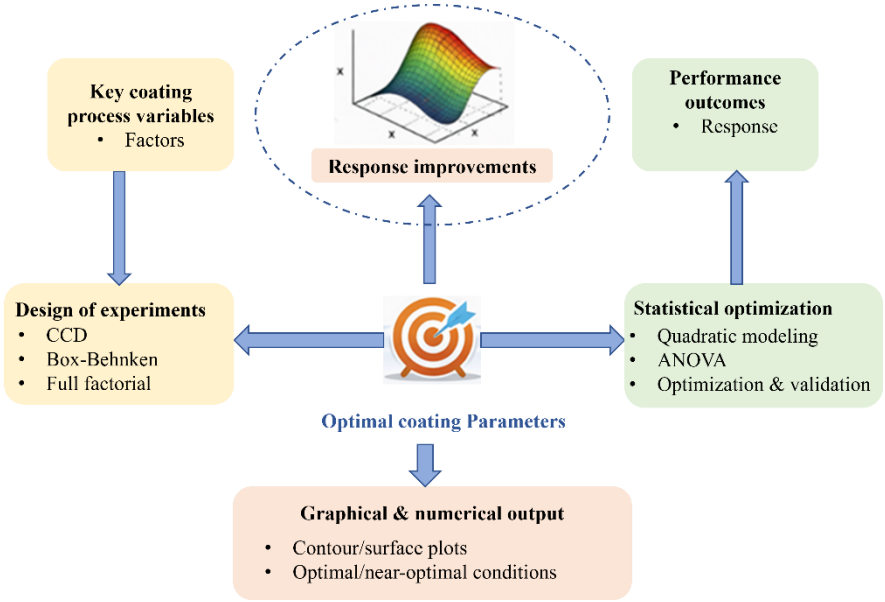

Figure 1.5 Schematic of the Response Surface Methodology (RSM) workflow showing the integration of coating variables, experimental design, statistical optimization, and graphical analysis to determine optimal coating parameters and performance outcomes

1.5.3 Artificial Neural Networks (ANNs)

Artificial neural networks (ANNs) have emerged as powerful data-driven modeling tools capable of capturing complex, nonlinear relationships between coating parameters and performance outcomes. Unlike regression-based approaches, ANNs do not require explicit functional assumptions and can learn directly from experimental data through adaptive weight optimization. In the context of surface coatings on magnesium alloys, ANNs have been successfully used to predict the corrosion behavior, microhardness, surface roughness, and adhesion strength based on multiple input variables. However, a key limitation of ANN-based models is their dependence on sufficiently large and diverse datasets for stable training and reliable generalization. Experimental coating studies often generate limited datasets due to practical constraints. To address this challenge, data augmentation strategies, such as interpolation between experimental points, stochastic perturbation within experimental uncertainty, and synthetic sample generation, have been increasingly explored. These techniques enhance dataset diversity, reduce overfitting, and improve predictive robustness, thereby extending the applicability of ANN models for coating optimization [39,40]. The schematic of an ANN has been shown in Figure 1.6.

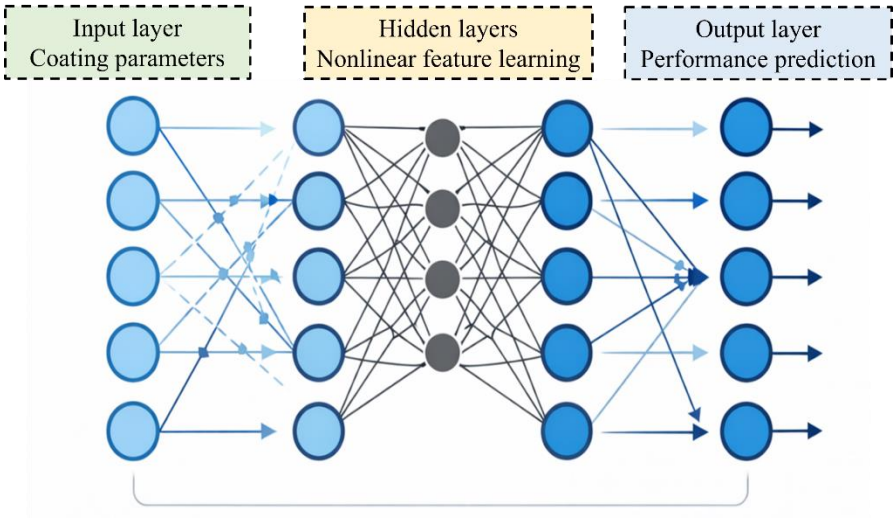

Figure 1.6 Architecture of the artificial neural network (ANN) model illustrating coating parameters as inputs, nonlinear feature learning through hidden layers, and performance prediction at the output layer

1.5.4 Metaheuristic Algorithms

Metaheuristic optimization algorithms have gained increasing attention for solving complex multi-objective optimization problems associated with surface coating design. Algorithms such as genetic algorithms (GA), particle swarm optimization (PSO), grey wolf optimizer (GWO), and differential evolution (DE) are particularly well suited for navigating high-dimensional, nonlinear, and multimodal search spaces. In coating optimization, metaheuristic algorithms are often employed to identify optimal process parameters that simultaneously satisfy competing objectives, such as maximizing corrosion resistance while minimizing surface roughness and degradation rate. These algorithms are population-based, do not require gradient information, and are less prone to convergence at local optima compared to traditional optimization techniques. Nevertheless, their performance depends strongly on algorithm parameter tuning and the quality of the underlying predictive models.

Among the various metaheuristic approaches, the Teaching–Learning-Based Optimization (TLBO) algorithm has gained attention due to its parameter-light structure and fast convergence characteristics. TLBO mimics the pedagogical interaction between a teacher and learners, where population improvement occurs through teacher and learner phases without requiring algorithm-specific control

parameters, making it computationally efficient and robust for coating parameter optimization. For multi-objective problems, the Multi-Objective Particle Swarm Optimization (MOPSO) algorithm extends the conventional PSO by incorporating Pareto dominance and external archive mechanisms to obtain a diverse set of non-dominated solutions. MOPSO is particularly effective in balancing conflicting objectives, such as corrosion rate, surface roughness, and coating thickness, through dynamic particle movement guided by personal and global best solutions. Similarly, the Non-Dominated Sorting Genetic Algorithm II (NSGA-II) is a widely adopted evolutionary algorithm for multi-objective optimization. It employs fast non-dominated sorting, crowding distance mechanisms, and elitism to maintain the solution diversity and convergence toward the true Pareto front. NSGA-II is especially suitable for complex coating optimization problems involving nonlinear interdependencies among process parameters and performance responses

1.5.5 Hybrid Approaches

Hybrid optimization frameworks represent the most advanced stage in the evolution of coating process optimization. These approaches combine the strengths of statistical methods, machine learning models, and metaheuristic algorithms to overcome the limitations of individual techniques. Common hybrid strategies include RSM-ANN, ANN-GA, and ANN-PSO models, where predictive models are integrated with global optimization algorithms to efficiently identify optimal parameter sets.

In surface coating applications for magnesium alloys, hybrid approaches have demonstrated superior predictive accuracy, enhanced optimization efficiency, and improved reliability in multi-objective decision-making. By coupling data-driven learning with evolutionary optimization, these frameworks enable robust coating designs tailored to specific functional requirements, making them particularly attractive for biomedical implant applications, where performance constraints are stringent.

1.6 Cell-Surface interaction simulation

Cell-surface interactions critically regulate cellular adhesion, spreading, migration, proliferation, and differentiation, thereby governing osseointegration and long-term implant performance. Although experimental studies have confirmed that surface chemistry, stiffness, and topography influence cell behavior, the direct quantification of the mechanical stimuli experienced by cells at the cell-substrate interface remains challenging. Mechanotransduction depends on local stress, strain, and deformation transmitted through focal adhesions of the cytoskeleton. Variations in substrate properties, such as elastic modulus, surface roughness, and post-processing treatments, alter the mechanical microenvironment sensed by adhered cells. Finite element (FE)-based computational modeling provides a powerful complementary approach by enabling spatially resolved analysis of stress, strain, and strain energy density (SED) within cellular components, parameters closely linked to mechanosensitive cellular responses. Image-based FE models incorporating realistic cell morphology, nucleus, and cytoskeletal structures further enhance predictive capability, allowing systematic investigation of how surface modifications affect intracellular mechanical stimulation. Coupling such cell models with substrates of varying roughness or stiffness enables isolation of substrate-induced effects under physiologically relevant loading conditions. In this work, FE-based cell–surface interaction simulations are employed to elucidate how heat-treatment-induced surface modifications influence the mechanical microenvironment of an adhered mesenchymal stem cell. Analysis of strain and SED distributions provides mechanistic insight into substrate-driven cellular stimulation, supporting the rational design of surface-engineered bioactive and resorbable implant materials.

1.7 Motivation and Scope of the Present Research

Magnesium and its alloys have emerged as promising biodegradable materials for temporary biomedical implants due to their favorable mechanical properties, biocompatibility, and elastic modulus close to that of natural bone, enabling gradual resorption and eliminating the need for secondary removal surgeries. However, their high chemical reactivity in physiological environments necessitates effective surface

modification to control degradation and preserve mechanical integrity during healing. Bioactive ceramic, polymeric, and hybrid composite coatings offer versatile routes to enhance corrosion resistance, surface stability, and biological compatibility, while enabling tailored surface chemistry and morphology for improved cellular response. Motivated by these challenges, the present research focuses on the development and optimization of functional surface coatings on magnesium alloys through systematic control of coating composition, processing parameters, and post-deposition treatments to improve adhesion, corrosion resistance, and surface performance. The study evaluates coating behavior under both static and dynamic conditions, investigates cell–surface interactions, and integrates statistical optimization and multiphysics simulations to elucidate degradation mechanisms under physiologically relevant environments. Overall, this work aims to establish a comprehensive framework for designing durable, biocompatible, and controllably degradable coatings for magnesium-based implants.

1.8 Contribution and Outline of the Thesis

The thesis entitled "**Eco-Friendly Surface Engineering of Magnesium Alloys for Resorbable Implant Applications: Experimental, Computational and Data-Driven Optimization Approaches**" has been divided into seven chapters, excluding the APPENDICES. An overview of the remainder of this thesis is summarized below:

Chapter 2 presents a comprehensive literature review focusing on magnesium alloys for biodegradable implant applications and the role of surface engineering in controlling their degradation behavior. This chapter discusses various surface modification techniques, including inorganic, organic, polymer-ceramic composite, and superhydrophobic coatings, along with their influence on corrosion resistance, surface properties, and biological response. The review also covers statistical optimization approaches, machine learning models, and computational simulations applied to coating design and performance evaluation.

Chapter 3 presents the initial phase of this research, focusing on the development of a hydrophobic coating on magnesium alloy via a hydrothermal process using zinc chloride and stearic acid. This chapter establishes the fundamental coating formation mechanism and evaluates its wettability, surface morphology, and corrosion behavior in simulated physiological environments.

Chapter 4 builds upon this initial work by optimizing the developed coating system. A structured design of experiments based on central composite design (CCD) within response surface methodology (RSM) was implemented, followed by hybrid multi-objective optimization using artificial neural networks combined with data augmentation and metaheuristic algorithms. Through this optimization framework, the coating performance was significantly enhanced, achieving a transition from hydrophobic to superhydrophobic behavior while simultaneously improving surface roughness, surface energy, and corrosion resistance.

Chapter 5 extends the study toward enhancing biofunctionality by introducing bioactive composite coatings. Chitosan–hydroxyapatite (HAp) and chitosan-Zn-doped HAp coatings were deposited on magnesium alloy using dip coating. Detailed characterization (SEM, XRD, EDS, XPS) and dynamic degradation studies under simulated physiological flow conditions were conducted, with results correlated to fluid–implant–structure interaction simulations using COMSOL Multiphysics, thereby integrating experimental and computational insights.

Chapter 6 further advances the coating system by investigating post-deposition heat treatment as a strategy to enhance coating performance. The effects of heat treatment on adhesion, surface characteristics, corrosion resistance, and biological response were systematically analyzed. Additionally, finite element simulations were employed to understand the influence of surface roughness on cell migration behavior, linking surface engineering modifications with biological performance.

Finally, **Chapter 7** presents a consolidated summary of the research work carried out in this thesis and provides recommendations for future research directions. The references cited in this study are listed at the end of the thesis.

Chapter 2

Literature review

2.1 Magnesium Alloys for Biomedical Applications

Magnesium and its alloys have emerged as transformative candidates for biodegradable orthopedic implants due to their unique combination of mechanical compatibility with bone and complete resorption capabilities, as demonstrated by Aikin et al. [7]. These materials address persistent issues associated with permanent metallic implants, including stress shielding and the necessity for secondary removal surgeries. The utilization of Mg-based biomedical devices eliminates the need for biomaterial removal surgery post-healing and mitigates adverse effects associated with permanent biomaterial implantation, as noted by Amukarimi et al. [41]. As promising biodegradable materials with nontoxic degradation products, magnesium alloys have received increasing attention in the biomedical field due to their excellent biocompatibility and unique mechanical properties.

2.1.1 Mechanical Compatibility with Bone Tissue

A distinguishing characteristic of magnesium alloys is their bone-mimetic elastic modulus ranging from 10 to 30 GPa, which closely matches that of cortical bone, as reviewed by Chaudhari et al. [42]. This similarity significantly reduces the stress-shielding effect commonly observed with traditional metallic implants such as titanium and stainless steel. Magnesium alloy AZ31 is highly valued for aerospace components, medical implants, and prosthetics due to its exceptional mechanical properties, with density and elastic modulus closely matching those of cortical bone, according to Singh et al. [43]. The biodegradability further enhances its potential by eliminating the need for secondary surgeries. The mechanical properties of natural bone, Mg alloy and other candidate materials have been summarizing in the Table 2.1.

Table 2.1 Comparison of properties of Mg alloy with other implant materials

Materials / Alloys		Density (g/cc)	Elastic modulus (GPa)	YS (MPa)	TS (MPa)	Elongation (%)	Ref.
Natural bone		1.7–2.0	3–20	60–90	80–150	1–6	[44]
Permanent implant materials	SS-alloys	7.9–8.1	190–205	180–250	350–620	30–40	[45]
	Ti-alloys	4.4–4.5	110–117	270–400	460–900	8–15	[46]
	Co-Cr alloys	8.3–9.2	210–230	290–410	530–950	30–40	[47]
Potential temporary implant materials	Mg-based alloys	1.74–2.0	41–45	120–180	140–290	1–11	[44]
	Zn-based alloys	7.14–7.3	90–100	115–205	160–390	3–15	[48]
	Fe-based alloys	7.8–8.1	200–205	140–260	210–360	30–45	[49]
	PLA	_	1.9	_	27–41	3–10	[50]

2.1.2 Common Alloy Systems and Compositions

Several magnesium alloy systems have been extensively investigated for biomedical applications. The AZ series (Mg-Al-Zn), particularly AZ31 and AZ91, represents the most widely studied systems due to their favorable mechanical properties. The WE series alloys, especially WE43 (Mg-4Y-3RE), are among the most extensively studied and widely utilized magnesium alloys in clinical applications, as reported by Dong et al [51]. Research outcomes have suggested that ZEK100, WE43, and EW62 (Mg-6% Nd-2% Y-0.5% Zr) alloys are effectively used for biomedical applications, having preferable biodegradable, biocompatible, bioactive implant materials with a lower corrosion rate, according to Sharma et al. [52]. The ZK series

(Mg-Zn-Zr), particularly ZK60, has also gained attention for cardiovascular and orthopedic applications.

2.1.3 Essential Alloying Elements and Biocompatibility

The selection of alloying elements is critical for achieving the desired balance between mechanical properties, corrosion resistance, and biocompatibility. Zinc is considered the best candidate to improve the corrosion response and biocompatibility of magnesium, as demonstrated in studies by Shuai et al. [53] Calcium additions have been shown to improve mechanical properties and biocompatibility, with Mg-Zn-Ca alloys being added to enhance these characteristics, according to Kim et al. [54]. The hot-rolled Mg2.5Zn-0.3Ca alloy exhibits the lowest corrosion rate along with the highest basal texture, where increasing the Zn/Ca atomic ratio intensifies the basal texture and enhances corrosion resistance, as reported by Zhou et al. [55]. Rare earth elements, while beneficial for corrosion resistance, require careful consideration regarding their long-term safety and cost-effectiveness.

2.1.4 Current Biomedical Applications

Current biomedical applications of magnesium alloys encompass a broad spectrum of clinical fields, reflecting their unique combination of biodegradability, biocompatibility, and mechanical properties comparable to natural bone. In orthopedic and trauma surgery, Mg-based fixation devices such as plates, screws, intramedullary nails, spinal cages, and joint treatment rings have been extensively developed and evaluated, with long-term clinical studies reporting excellent functional outcomes, low complication rates, and the elimination of secondary implant removal procedures [56]. Systematic reviews and meta-analyses further confirm that absorbable magnesium screws exhibit complication rates comparable to conventional titanium implants, supporting their clinical feasibility in bone surgery [57]. In cardiovascular applications, magnesium-based bioresorbable stents offer superior mechanical performance over polymeric counterparts and address limitations associated with permanent metallic stents, demonstrating controlled degradation, positive vascular remodeling, and minimal long-term inflammatory response in preclinical studies [58–

60]. In maxillofacial and dental surgery, Mg alloys-often combined with surface treatments such as plasma electrolytic oxidation-are increasingly recognized as promising alternatives to non-degradable metals for fixation structures, as reported by Giavaresi et al. [61]. Recent Mg-based devices for biomedical applications have been presented in the Table 2.2.

Table 2.2 Recent Mg-based biomedical devices

Device Name	Application	Ref
RemeOs™ screws	Bone fracture fixation, deformity correction	[62]
MAGNEZIX® screws	Hallux valgus surgery, orthopedic fixation	[63]
Magmaris (DREAMS 2G), (DREAMS 3G)	Coronary artery stent	[64,65]
JDBM-2	Cardiovascular stenting	[66]
AMS-1 stents	Peripheral arteries stent	[67]

2.2 Corrosion Mechanisms of Magnesium in Physiological Media

2.2.1 General Corrosion Processes

Magnesium alloys undergo complex corrosion in physiological environments due to their high chemical reactivity. Wei and Gao et al. [12] identified multiple corrosion mechanisms in these media, including general corrosion, localized corrosion, pitting corrosion, and degradation influenced by body fluid environments. The electrochemical corrosion reactions of magnesium in physiological solutions are fundamentally driven by the inherent electrochemical potential of the metal, which undergoes anodic dissolution while simultaneously supporting cathodic hydrogen evolution at the surface. The corrosion behavior exhibits crystallographic anisotropy-a phenomenon investigated by Merson et al. [68] wherein different crystal planes degrade at significantly different rates in physiological solutions. For instance, in a 0.9% NaCl physiological solution, corrosion rates vary substantially from 0.51

mm/year on the basal (0001) plane to 0.98 mm/year on pyramidal planes, demonstrating the critical influence of material microstructure on degradation kinetics. The electrochemical corrosion process is significantly accelerated by the presence of chloride ions in physiological media. Yang et al. [69] demonstrated that chloride ions fundamentally alter the corrosion mechanism of magnesium alloys, shifting from hydrogen embrittlement dominance in deionized water to anodic dissolution dominance in chloride-containing solutions. Chloride ions penetrate and destabilize the protective oxide/hydroxide layer on the magnesium surface, facilitating localized corrosion initiation and accelerating overall degradation rates. Building on this mechanism, Xu et al. [70] demonstrated, as illustrated in Figure 2.1, that Mg corrosion in physiological media involves the formation of intermediate hydroxide and phosphate-based layers, where Mg^{2+} reacts with OH^- and HPO_4^{2-} to form $Mg(OH)_2$ and $MgHPO_4$ deposits. However, chloride ion ingress disrupts these protective layers, converting them into soluble $MgCl_2$ and sustaining continuous anodic dissolution. This interplay between deposition and Cl^--induced breakdown further reinforces the dominant role of chloride ions in accelerating Mg degradation.

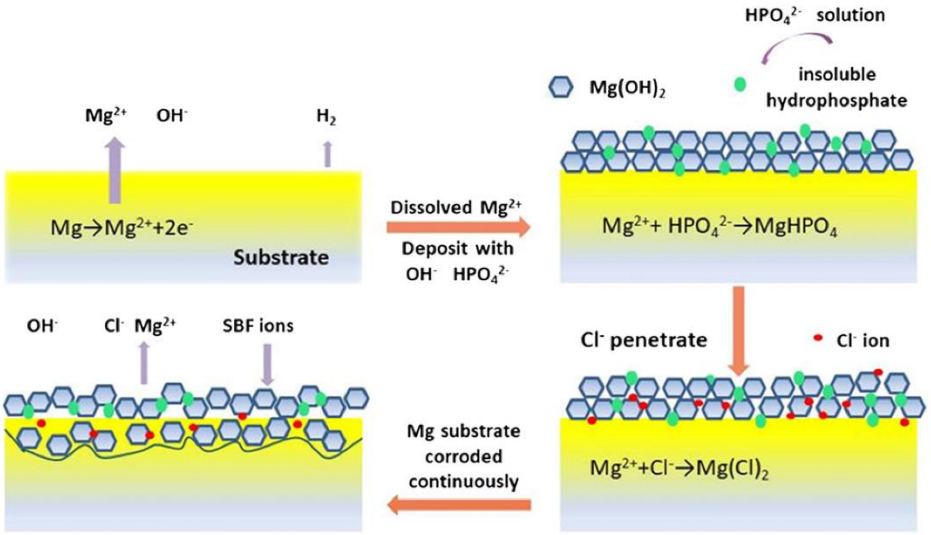

Figure 2.1 Schematic representation of corrosion mechanisms in Mg-based alloys under simulated body fluid (SBF) conditions [70]

2.2.2 Role of Serum Proteins, pH, and Surface Interactions in Corrosion

One critical factor affecting magnesium corrosion is the presence of serum proteins and the pH of the physiological environment. Zhang et al. [71] demonstrated that albumin, an abundant macromolecule in blood, significantly influences both corrosion rates and the solubility of corrosion products in physiological systems. The key mechanism involves albumin's interference with the calcium-phosphate passivation layer that forms on the magnesium surface. This passivation layer is crucial for slowing degradation; its disruption leads to accelerated corrosion. pH plays a fundamental role in controlling the stability of the protective oxide/hydroxide films on magnesium surfaces. Kuznetsov and Frumkin (2021) et al. [72] showed that at higher pH values (pH 10), protective hydroxide films such as $Mg(OH)_2$ form more readily and remain stable, significantly reducing corrosion rates. Conversely, lower pH values in physiological environments can dissolve these protective layers, promoting hydrogen evolution and accelerating the electrochemical dissolution process. Gnedenkov et al. [73] observed that magnesium-calcium alloys exhibit lower corrosivity in mammalian cell culture media compared to simple saline solutions, suggesting that microstructural elements and corrosion products formed during degradation collectively influence the overall corrosion trend. The surface condition and composition of corrosion products directly affect the hydrogen evolution kinetics during the cathodic reaction, influencing the overall degradation rate and the risk of hydrogen-induced embrittlement. Zhang et al. [71] reported that albumin significantly modifies Mg corrosion behavior by increasing the solubility of corrosion products through metal–protein complexation, thereby enhancing bioresorbability. As schematically illustrated in Figure 2.2, albumin adsorption in saline media can initially suppress corrosion via barrier formation, whereas in Ca/P-containing environments it destabilizes protective passivation layers through Ca^{2+} chelation, resulting in accelerated degradation.

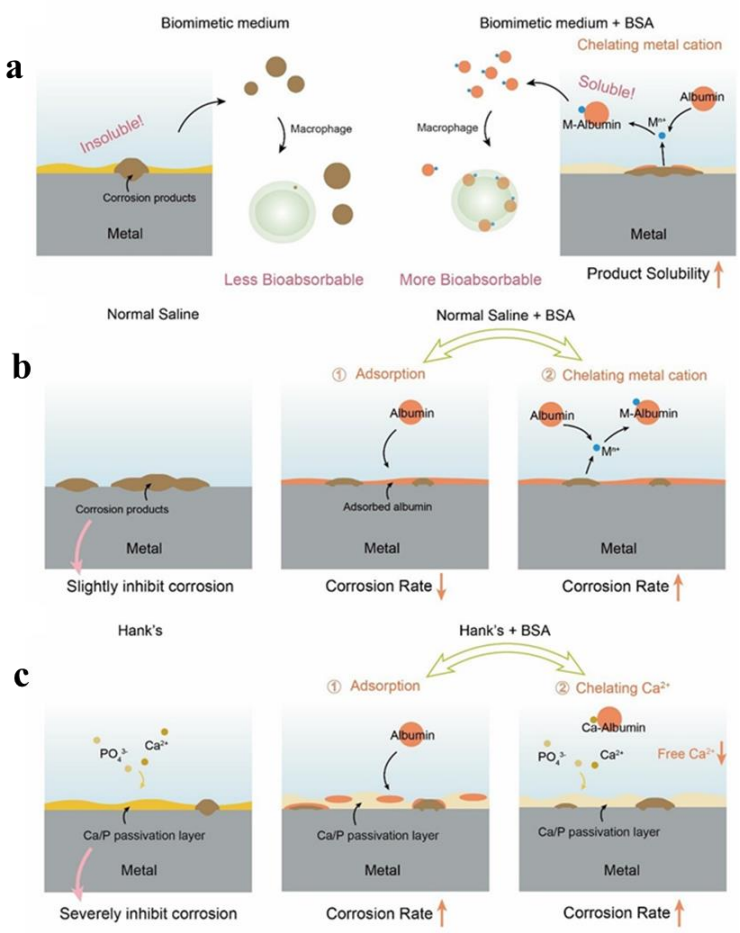

Figure 2.2 (a) Albumin increases solubility via metal-ion chelation. (b) In normal saline, albumin both inhibits corrosion through surface adsorption and promotes it via ion chelation. (c) In Hank's solution, albumin accelerates corrosion by disrupting the Ca/P passivation layer and reducing free Ca^{2+} [71]

2.2.3 Localized and Stress Corrosion Cracking: Microstructural Influence

The microstructure of magnesium alloys significantly affects their corrosion susceptibility, a critical aspect of the surface condition and its electrochemical response. Li et al. [74] investigated the coupling effect of grain size and residual stress on intergranular corrosion behavior, demonstrating that these factors work synergistically to determine corrosion susceptibility. In areas with residual tensile stress (characterized by larger grains), the electrochemical corrosion reaction rate accelerates, and corrosion cavities preferentially expand along grain boundaries, allowing corrosive media and hydrogen ions to penetrate deeper into the material. Conversely, regions with residual compressive stress and fine grains show reduced electrochemical corrosion reaction rates at grain boundaries, resulting in a more

uniform corrosion surface. This microstructural variation directly influences the hydrogen evolution kinetics, as areas of high electrochemical activity experience enhanced hydrogen generation and absorption. Yang et al. [69] further elucidated that magnesium alloys face challenges from stress corrosion cracking in physiological environments through two distinct electrochemical mechanisms: hydrogen embrittlement and anodic dissolution. The influence of surface condition and microstructure on these mechanisms is profound in pure water, hydrogen embrittlement dominates as the primary failure mode due to enhanced hydrogen evolution at cathodic sites. Jiang et al. [75] demonstrated that SCC propagation in Mg–Zn–Zr alloys is strongly governed by grain structure, with fine grains promoting predominantly intergranular cracking, as also can be shown in Figure 2.3. In contrast, bimodal structures exhibit mixed intergranular and transgranular modes, while coarse-grained microstructures favor transgranular crack propagation. These observations highlight the critical role of grain size distribution in controlling crack path evolution.

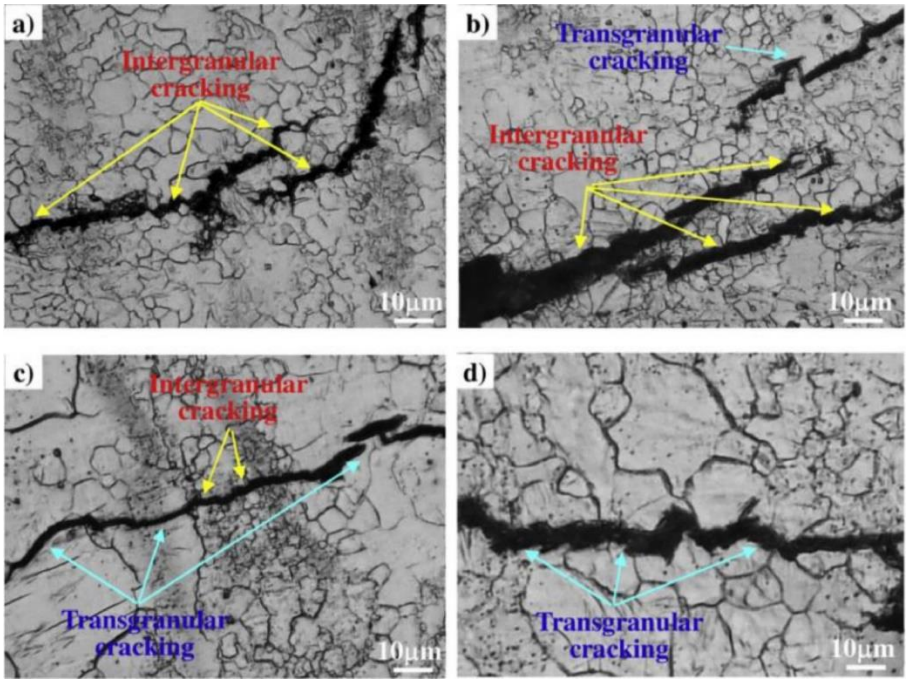

Figure 2.3 SCC behaviour of Mg–Zn–Zr alloy: (a) fine grains–intergranular cracking; (b–c) bimodal grains–mixed intergranular and transgranular cracking; (d) coarse grains – transgranular cracking [75]

2.3 Surface Engineering Strategies for Magnesium Alloys

Surface engineering represents a transformative approach to address the fundamental limitations of magnesium alloys for resorbable orthopedic implants by modifying surface chemistry, topography, and reactivity while preserving the bulk mechanical properties essential for load-bearing applications. Two principal strategies have emerged as particularly promising: superhydrophobic coatings that leverage hierarchical surface architecture and low-energy materials for exceptional corrosion suppression, and bioactive coatings incorporating hydroxyapatite, bioactive glass, and biocompatible polymers to directly stimulate bone regeneration and biological integration. This section critically evaluates these complementary approaches, examining their mechanistic principles, fabrication methodologies, performance in physiological environments, and remaining barriers to clinical translation for biodegradable implant applications.

2.3.1 Superhydrophobic Coatings on Magnesium Alloys

Superhydrophobic coatings are an effective strategy to improve the corrosion resistance of magnesium alloys by combining hierarchical surface roughness with low surface energy. Such surfaces incorporate micro- and nano-scale features that entrap air at the solid–liquid interface, thereby significantly reducing electrolyte contact with the magnesium substrate. An et al. [76] reported that deep eutectic solvent pretreatment followed by electrodeposition of cerium stearate on AZ31B magnesium alloy produced a coral-like micro/nano architecture with a water contact angle of 154.7°, achieving a protection efficiency of 99.68% and decreasing the corrosion current density from 1.79×10^{-4} to 5.57×10^{-7} $A \cdot cm^{-2}$.

Recent advances have shifted toward environmentally benign surface modification techniques that eliminate toxic fluorinated compounds without compromising performance. Stearic acid and palmitic acid-based coatings represent a paradigmatic eco-friendly approach, where Kalmoni et al. [77] successfully fabricated robust fluorine-free superhydrophobic films using a mixture of two fatty acids, silica nanoparticles, and polydimethylsiloxane via aerosol-assisted chemical vapor

deposition. These coatings maintained superhydrophobicity following ultraviolet exposure, heat treatment, 300 tape peel cycles, and organic solvent immersion, demonstrating exceptional environmental stability without relying on per- and polyfluoroalkyl substances. The scalability of such approaches was further validated through inverse vulcanization polymer technology, where sulfur-based polymers combined with carbon nanofibers and silica nanoparticles produced durable superhydrophobic coatings that retained superhydrophobicity for 150 tape peeling cycles, up to 250°C, and 6 hours of ultraviolet C exposure [78].

The corrosion protection afforded by superhydrophobic coatings on magnesium alloys arises from multiple synergistic mechanisms. Hierarchical hybrid coatings composed of polystyrene and zirconium dioxide have shown that air entrapment within micro-nano surface features increase roughness by nearly four-fold, leading to a 90% reduction in Mg^{2+} release and an 85% decrease in pitting corrosion depth compared to uncoated substrates, as reported by Luis et al [79]. This enhanced performance is attributed to the formation of a tortuous diffusion pathway for aggressive ions, reduced wettability due to low surface energy, and the presence of entrapped air pockets that interrupt continuous electrolyte contact with the magnesium surface. Although extensive research has been conducted on magnesium alloy surfaces to develop superhydrophobic coatings, many of the chemicals and methods employed are either toxic in nature or comparatively expensive.

The toxicity levels and hazard statements of the chemical compounds were compiled in Table 2.3 based on information provided in their respective Safety Data Sheets (SDS), following the guidelines set by Regulation (EC) No 1272/2008. The SDS documents were obtained from the websites of the respective chemical suppliers. According to this regulation, chemicals are classified into four toxicity categories, with Category 1 indicating the highest level of toxicity and irritation, and Category 4 representing substances that are considered practically non-toxic and non-irritant [80].

Table 2.3. Chemical substances and their associated hazard statements in accordance with Regulation (EC) No 1272/2008 [80]

Chemical	Toxicity level	Hazard statement
HF	Category 1	H300, H310, H330, H314, H318, H319, H300+H310+H330
CrO_3	Category 1	H301, H312, H314, H271, H350, H318, H311, H361F, H330, H317, H272, H334, H335, H372, H400, H410, H340
$PdCl_2$	Category 1	H317, H410, H290, H400, H302, H318
HNO_3	Category 1, Category 3	H331, H290, H272, H314
H_2SO_4	Category 1	H314, H290
$NiCl_2$	Category 1, Category 3	H301, H317, H319, H331, H334, H341, H350i, H372, H410
$NiSO_4$	Category 1	H334, H315, H302, H372, H319, H360D, H317, H332, H341, H350i
NH_4HF_2	Category 3	H301, H314, H318, H331, H335
KF	Category 3, Category 2, Category 4	H301, H311, H315, H319, H373

2.3.2 Bioactive Coatings for Magnesium-Based Implants

2.3.2.1 Hydroxyapatite-Based Coating Systems

Hydroxyapatite (HAp) coatings are widely regarded as the gold-standard bioactive surface modification for magnesium implants due to their compositional similarity to bone mineral and strong osteoconductive behavior. Chaudhari et al. [42] reported that HAp coatings reduce magnesium corrosion rates to ~0.25 mm·year^{-1}

compared to >2 mm·year^{-1} for bare Mg, while significantly enhancing osteoblast adhesion and bone formation. These benefits arise from combined barrier protection, controlled release of Ca^{2+} and PO_4^{3-} ions, and biomimetic surface chemistry that promotes protein adsorption and integrin-mediated cell signaling.

2.3.2.2 Chitosan/Hydroxyapatite Composite Coatings

Polymer–ceramic composites have emerged as multifunctional coatings with improved adhesion, mechanical compliance, and biological performance. Groza et al. [81] investigated Mg-doped HAp/chitosan coatings fabricated by RF magnetron sputtering and modified via electron beam irradiation. The coatings promoted formation of carbonated, B–type substituted apatite layers, enhanced MG63 osteoblast attachment, and increased proliferation, with nanoscale surface features (60–200 nm) effectively tuning cell responses without compromising crystallinity. Iconaru et al. [81] further demonstrated that Mg-doped HAp/chitosan composites exhibited dose-dependent antifungal activity against Candida albicans while maintaining excellent cytocompatibility with MG63 cells. Optimal Mg concentrations (0.08–0.3 mol fraction) provided simultaneous antimicrobial efficacy and biocompatibility through synergistic electrostatic interactions and controlled Mg^{2+} release. A more complex multifunctional design was reported by He et al. [82], who developed a vancomycin-loaded PLGA/HAp/chitosan coating system. This ternary composite achieved low corrosion rates (0.27 ± 0.03 mg·cm^{-1}·day^{-1}), near-physiological pH (~7.2), sustained antibacterial release against resistant strains, enhanced alkaline phosphatase activity, and improved cell viability, simultaneously addressing corrosion, infection, and osseointegration.

2.3.2.3 Zinc-Doped Hydroxyapatite Coatings and Dopant Effects

Zinc incorporation into hydroxyapatite significantly enhances osteogenic and antimicrobial performance. Ullah et al. [83] synthesized Mg/Zn co-doped HAp coatings and showed that 5 wt% Mg and 5 wt% Zn promoted osteoblast proliferation while exhibiting strong antibacterial activity against S. aureus and E. coli . Structural modifications induced by Ca-site substitution increased ion release kinetics and

bioactivity, supported by first-principles calculations. Hou et al. [84] developed Zn-SrMg multidoped HAp coatings using atmospheric plasma spraying, achieving superior osteogenic gene expression and antibacterial activity against periodontal pathogens. In vivo rat studies confirmed enhanced bone formation along implant threads, demonstrating the synergistic benefits of combining osteogenic (Mg, Sr) and antimicrobial (Zn) dopants. Mechanistic insights into Zn antimicrobial action were provided by Hamza et al. [85] who showed that Zn-doped HAp nanoparticles disrupt bacterial membranes and DNA in a dose-dependent manner. High Zn^{2+} content produced inhibition zones exceeding 25 mm against Klebsiella and S. aureus, while careful compositional control-maintained osteoblast compatibility. A summary of ceramic and ceramic-polymer composite coatings on magnesium-based alloys, compiled from recent literature, is presented in Table 2.4.

Table 2.4 Summary of ceramic and ceramic-polymer composite coatings on magnesium-based alloys

Alloy	Compounds	Coating	Application	Key	Ref.
ZK60	Ceramic (MgO and Mg2SiO4) + Gallic acid	Micro-arc oxidation (MAO)	Orthopedic implants	Enhanced corrosion resistance and osteoblast activity	[86]
Mg-Mn-Ce	Mg_2SiO_4 + Polytetrafluoroethylene (PTFE)	Plasma electrolytic oxidation (PEO)	biomedical applications	Corrosion current reduced by >3 orders; 27× less wear;	[87]

AZ31	Hydroxyapatite (HA) + Chitosan-metformin (CS-MF)	Hydrothermal treatment	Orthopaedic implants	Improved corrosion resistance, Osteogenic activity	[88]
ZK41	Hydroxyapatite (HA, CaP-based)	Anodization + electrochemical deposition	Implant material	Better corrosion resistance than uncoated	[89]
Mg_{20}-Zn	Calcium phosphate (CaP) + Chitosan Water glass	Spin-coating method	Biodegrada-ble implants	Reduced corrosion rate in Hank's solution, Formation of protective Magnesium/Calcium silicate	[90]

2.4 Dynamic Corrosion and Flow-Induced Shear Stress (FISS)

Flow-induced shear stress (FISS), defined as the product of fluid viscosity and velocity gradient at the solid–liquid interface, significantly influences magnesium degradation behavior. Ferroni et al. quantified physiologically relevant ocular shear stresses (0.01 and 0.032 Pa) using CFD-coupled bioreactor systems and demonstrated a pronounced acceleration of magnesium corrosion under dynamic conditions

compared to static immersion [91]. Zhang et al. [92] reported that vascular environments experience substantially higher and spatially heterogeneous shear stresses, typically 1–6 Pa under normal arterial flow and up to 10–20 Pa in pathological conditions, resulting in enhanced mass transport and diffusion boundary layer disruption at implant surfaces. Ren et al. [93] identified flow erosion, corrosion fatigue, and stress–corrosion coupling as dominant degradation mechanisms governing magnesium alloy performance under physiological conditions. Similarly, Shang et al. [94] observed significantly accelerated corrosion of pure Mg, AZ31, and WE43 alloys under dynamic flow, with implications for both endothelial response and premature implant failure in vascular applications.

Juan Wang et al. [95] employed computational fluid dynamics (CFD) simulations to predict the distribution of flow-induced shear stress (FISS) on MgZnCa alloy surfaces in a vascular bioreactor. Using COMSOL Multiphysics, DMEM at 37 °C was modeled as an incompressible Newtonian fluid (viscosity = 0.78 mPa·s, density = 0.99 g cm^{-3}), with laminar flow conditions applied over inlet flow rates of 0–40 mL min^{-1}. The simulations showed that surface shear stress increased monotonically with flow rate, ranging from 0 to 0.62 Pa, with higher flow producing more localized shear stress distributions. By coupling shear stress to mass transfer using the Chilton–Colburn analogy, the authors demonstrated that increased FISS enhanced corrosion product removal, promoting relatively uniform corrosion at low shear and localized corrosion at higher shear stresses. The Table 2.5 presents the flow-induced shear stress (FISS) values of magnesium and magnesium-based alloys across different flow rate or velocity ranges, along with their respective application areas and the key findings reported in each study. While previous studies have provided valuable insights into flow-induced corrosion of Mg alloys, they are often limited to simplified flow conditions and narrow FISS ranges, with insufficient consideration of coating stability and long-term degradation behavior. Therefore, the integration of surface engineering approaches with dynamic corrosion studies should be considered a significant focus for future research.

Table 2.5 Summary of Dynamic Corrosion behavior and FISS in Mg-Based Alloys

Alloy / Material	Application Area	Flow Velocity / Flow Rate	FISS Range (Pa)	Key Observations	Ref
AZ31	Cardiovascular stents	0–40 ml/min	0–0.62 Pa	Corrosion increases with FISS; pitting severity and depth increase; corrosion products removed under flow	[96]
MgZnCa alloy	In vitro vascular simulation	5–40 ml/min	0.07–0.62 Pa	Higher FISS leads to higher localized corrosion coverage (up to ~59%)	[97]
Porous Mg (30–55% porosity)	Bone scaffold (cancellous bone)	0.025 – 0.8 ml/min	~10^{-5} order (very low Pa range)	Higher flow accelerates degradation and reduces mechanical strength	[98]
Pure Mg, AZ31, WE43	Cardiovascular stents	0.1 m/s–0.6 m/s	~0.68 Pa	Dynamic flow significantly accelerates corrosion; AZ31 shows best corrosion resistance	[94]
Coated Mg-based alloys	Biodegradable implant	100 ml/min–2000 ml/min	1.86 ×10^{-3} pa to 2.71 pa	Coatings reduce corrosion under flow	[99]

2.5 Optimization Techniques in Surface Engineering

Design of Experiments (DoE) and Response Surface Methodology (RSM) are widely employed in surface engineering to systematically model the relationships between coating process parameters and performance responses while minimizing experimental effort. Sathiyamoorthy et al. [100] utilized a Central Composite Design-based RSM approach to optimize porosity and hardness of HVOF-sprayed TiO_2 coatings on magnesium alloys, demonstrating strong agreement between predicted and experimental results and confirming RSM's effectiveness in identifying optimal spray conditions. Similarly, Bukhari et al. [101] integrated RSM with finite element analysis to optimize dental implant coatings, identifying coating thickness as the dominant factor influencing mechanical stability. The strong agreement between RSM predictions and simulations ($R^2 > 0.95$) underscores its reliability as an efficient multi-parameter optimization tool.

Complex coating design often requires balancing conflicting objectives, such as minimizing porosity while maximizing hardness or corrosion resistance with bioactivity. RSM addresses this using desirability functions, converting multiple responses into a single objective to identify optimal compromise conditions. Hernández et al. [102] applied RSM with desirability function analysis to optimize machining parameters, simultaneously minimizing surface roughness and maximizing tool life. By incorporating weighted objectives, the approach enabled systematic trade-off analysis and identification of balanced optimal conditions.

A critical strength of RSM resides in its integrated statistical framework providing quantitative assessment of model reliability through Analysis of Variance (ANOVA), coefficient of determination (R^2) values, and lack-of-fit tests. Aristizbal-Alzate et al. [103] highlighted that integrating DOE, ANOVA, and RSM in catalysis effectively quantifies relationships between variables and responses. Analysis of ANOVA and R^2 values identifies significant factors and ensures statistically reliable optimization, distinguishing true effects from random variation.

Machine learning (ML), particularly deep neural networks and ensemble models, has emerged as a powerful tool for materials and coating design by capturing complex non-linear relationships beyond the capability of conventional statistical methods. Jain et al. [104] reviewed ML pipelines for solid-state electrolyte discovery, demonstrating that graph-based and transformer neural networks achieve high predictive accuracy for ionic conductivity across large chemical spaces without manual feature engineering. Sun et al. [105] developed an integrated ML framework combining feature extraction, selection, and deep learning to predict thermoelectric performance, achieving high predictive accuracy ($R^2 \approx 0.90–0.95$) and identifying candidate materials later validated by density functional theory.

Recent advances also emphasize model interpretability through feature-importance analysis. Wu et al. [106] applied SHAP analysis to ML-based phase stability prediction, identifying key compositional and thermodynamic descriptors governing phase formation. Fu et al. [107] and Nandurkar et al. [108] showed that explainable ML models using SHAP and LIME achieve high accuracy ($R^2 \approx 0.91–0.94$) while identifying key factors influencing performance. For Mg coatings, such approaches can pinpoint critical variables governing corrosion, bioactivity, and mechanical properties, enabling targeted optimization over exhaustive experimentation.

Chen et al. [109] used machine learning to predict density and volume of Mg-containing phases, with Random Forest achieving the highest accuracy for volume ($R^2 > 0.96$) and SVM for density ($R^2 = 0.885$). Feature analysis showed volume depends on atomic count, while density is governed by atomic mass and stoichiometry, highlighting ML's role in uncovering structure-property relationships. Similarly, Wu et al. [106] combined deep neural networks with density functional theory validation to predict the structural stability of layered oxide cathode materials, highlighting the effectiveness of ML-driven screening supported by first-principles verification.

Metaheuristic algorithms, including genetic algorithms (GA) and particle swarm optimization (PSO), are widely applied in surface engineering for multi-objective optimization due to their ability to avoid local optima and efficiently search high-dimensional parameter spaces. Mohankumar et al. [110] integrated RSM with PSO to

optimize AA2024/Al_2O_3 coatings, where PSO achieved lower wear loss than RSM, demonstrating its advantage in parameter refinement. Advanced variants like MOPSO and GA-PSO hybrids further enable simultaneous optimization of competing objectives through Pareto-optimal solutions. Wu et al. [111] demonstrated that GAPSO significantly outperformed conventional design strategies by achieving substantial performance improvements unattainable through parameter sweeps.

Multi-objective formulations using Pareto fronts are particularly relevant for coating systems requiring trade-offs between corrosion resistance, mechanical integrity, cost, and bioactivity. Shao et al. [112] proposed an improved MOIPSO incorporating non-dominated sorting, crowding distance, and adaptive mutation, which outperformed existing algorithms on benchmark and real engineering problems. Recent studies increasingly employ hybrid metaheuristic frameworks, leveraging GA's global exploration and PSO's fast convergence; Hu et al. [113] showed that GA-PSO hybrids consistently outperform standalone algorithms in multi-objective optimization tasks. Beyond classical methods, emerging algorithms such as the Slime Mould Algorithm and adaptive metaheuristics further enhance optimization performance by dynamically balancing exploration and exploitation, achieving superior results in complex engineering systems [114]. Some of the other studies of application of prediction and optimization algorithms have been represented in the Table 2.6 below.

Table 2.6 Optimization approaches in Mg alloy surface engineering for resorbable implants: algorithms, applications, outcomes, and key references

Algorithm/Method	Application	Key Outcomes	Ref.
Design of Experiments (DoE)/RSM (Response Surface Methodology)	MAO coatings on Mg for corrosion control; turning of AZ31 Mg alloy	Reduced corrosion rate; Ra minimized to ~0.28 μm under cryogenic conditions with optimal Vc=150 m/min, f=0.10 mm/rev	[115]
Statistical Optimization (e.g.,	develop and optimize a magnetic field-	Surface roughness (Ra) was reduced from 450 nm to 70 nm (84.5% improvement),	[116]

RSM-CCD in coatings)	assisted finishing process (MFAFP) on for Co-Cr-Mo biomaterial alloys	alongside a robust RSM model with only 1.92% prediction error validated experimentally	
ANN/Fuzzy	Design of biodegradable Mg alloys for vascular stent systems	accurately predicted alloy compositions with excellent mechanical properties (UTS ≈ 346 MPa, YS ≈ 231 MPa, ductility ≈ 15%)	[117]
Metaheuristic Algorithms (ABC, GBA, TLBO)	Optimization of end-milling parameters for AZ31–Si_3N_4 alloy	Significantly reduced surface roughness (13.36%), cutting force (15.35%), and temperature (35.91%), with high prediction reliability (~95%)	[118]

Collectively, these studies demonstrate the growing effectiveness of metaheuristic and hybrid optimization strategies for addressing multi-objective challenges in advanced coating and magnesium alloy design.

2.6 Post deposition treatment and cell-surface Interactions

Post-deposition treatments play a decisive role in tailoring the surface properties of magnesium (Mg) alloys, directly influencing corrosion behavior, bioactivity, and cell-material interactions in resorbable implant applications. Among various strategies, plasma electrolytic oxidation (PEO) followed by polymeric or composite top-coatings has emerged as an effective route to overcome the inherent rapid degradation of Mg alloys while promoting cytocompatibility.

Usmaniya et al. [119] demonstrated that post-treatment of PEO-coated Mg alloys with biodegradable polymers such as polycaprolactone (PCL) and polylactic acid (PLA)

markedly enhances corrosion resistance and cellular response. A PLA top-coat on PEO-treated AZ31 reduced corrosion current density by over two orders of magnitude relative to PEO alone, demonstrating effective electrolyte sealing. Incorporation of hydroxyapatite (HA) into polymer matrices further enhanced both corrosion resistance and biocompatibility. Chitosan coatings are particularly promising due to their biodegradability, antibacterial activity, and hydrogen-bonding interaction with $MgO/Mg(OH)_2$, which improves coating stability and supports apatite nucleation. The addition of bioactive glass (BG) to chitosan increased coating thickness and adhesion strength, achieving more than a 300-fold improvement in corrosion resistance. Si-O groups in BG further promoted calcium adsorption and hydroxyapatite formation, enhancing biomineralization and cell adhesion. Beyond surface chemistry, post-deposition treatments also modify surface topography and wettability, both of which are critical determinants of cellular behavior. Wang et al. [120] showed that micro- and nano-scale surface geometries influence cell adhesion through mechanisms that extend beyond conventional roughness parameters. The concept of "stereo coverage" was introduced to describe the effective cell-surface contact on complex topographies, highlighting the importance of geometric design in regulating adhesion density and spreading. Cell-surface interactions are further governed by mechanotransduction mechanisms, wherein cells sense substrate stiffness and topographical cues through integrin-mediated focal adhesions. Ingber et al. [121] established those cellular responses such as adhesion, proliferation, and differentiation are regulated by cytoskeletal tension and mechanical coupling between the extracellular matrix and intracellular structures. Substrate stiffness has been shown to direct lineage-specific differentiation, with Chen [122] reporting stiffness-dependent regulation of focal adhesion maturation and signaling pathways. At the nanoscale, surface modifications such as nanorods and nanotubes have been shown to significantly enhance cell migration and osteogenic potential. Gupta et al. [123] demonstrated that TiO_2 nanorod-modified surfaces induce higher local strain energy densities at the cell–substrate interface, facilitating cell migration and improving osteogenic response compared to flat surfaces. These findings underscore the importance of post-deposition nano-engineering in optimizing cell-material interactions.

Overall, post-deposition treatments combining polymer sealing, bioactive ceramic incorporation, and controlled micro-/nano-topography effectively regulate corrosion behavior, biomineralization, and mechanobiological responses. Such strategies are essential for designing next-generation resorbable Mg implants with predictable degradation and enhanced biological performance. Figure 2.4 illustrates the 150 most significant keywords identified in recent research papers concerning magnesium and its alloys, ranked by their thematic relevance.

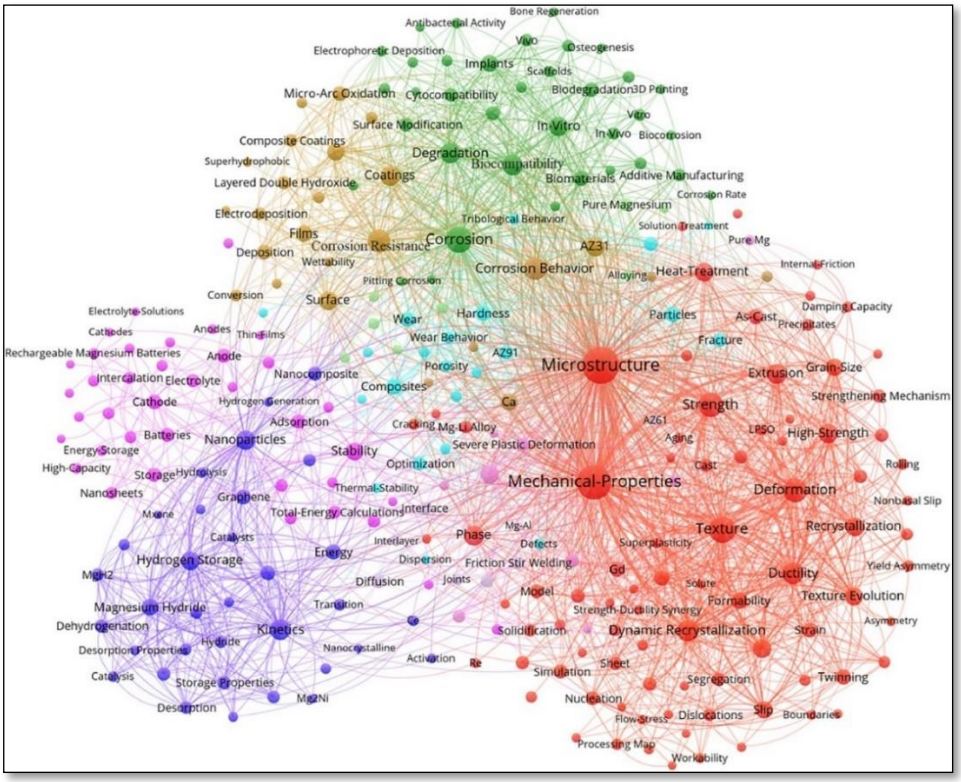

Figure 2.4 Network visualization among different keywords in Mg-related papers [124]

2.7 Summary of Literature Gaps

- Despite substantial progress in biodegradable magnesium (Mg) alloys for resorbable implant applications, clinical translation remains limited by uncontrolled surface-driven degradation and insufficient understanding of bio–interface interactions, rather than bulk material constraints. Although alloy design strategies such as grain refinement, alloying, and thermomechanical processing improve intrinsic corrosion resistance and mechanical properties,

they provide limited control over interfacial reactions governing in vivo degradation kinetics, hydrogen evolution, and cellular response.

- Surface engineering has therefore gained prominence; however, existing coating approaches suffer from critical limitations, including reliance on toxic or costly chemicals, environmentally unsustainable and energy-intensive multi-step processes, and poor scalability for biomedical deployment. So, investigation of on cost-effective, eco-friendly coating is indeed necessary. Moreover, systematic investigations on composite coatings incorporating natural biomaterials such as chitosan and hydroxyapatite (HAp) and the role of HAp doping in enhancing surface protection remain limited, restricting the development of stable, bioactive, and clinically viable Mg implant surfaces.
- Another notable gap lies in the limited integration of data-driven approaches in Mg surface engineering research. Although artificial intelligence (AI) and machine learning (ML) techniques offer powerful tools for multi-parameter optimization, their application in this field remains sparse. This limitation is primarily attributed to the lack of structured, high-quality experimental datasets, minimal use of data augmentation strategies, and insufficient adoption of hybrid or multi-stage optimization frameworks that combine statistical, metaheuristic, and physics-based models. Consequently, most optimization efforts remain confined to conventional one-factor-at-a-time or single-technique approaches, restricting predictive capability and generalizability.
- Furthermore, the majority of corrosion and degradation studies are conducted under static in vitro conditions, which do not accurately replicate the dynamic physiological environment experienced by implants in vivo. Real-time degradation behavior of Mg alloys under dynamic flow conditions, coupled with experimental–computational validation, remains inadequately explored. The absence of such integrated experimental–simulation frameworks limit the ability to predict long-term implant performance and degradation kinetics reliably.

- Post-deposition treatments, particularly heat treatment of coated Mg alloys, represent another underexplored area. While coating composition and deposition parameters have been widely studied, the influence of post-deposition thermal treatments on coating microstructure, phase stability, adhesion, corrosion behavior, and subsequent cell-surface interactions has received limited systematic attention. Given that post-deposition heat treatment can significantly alter surface chemistry and topography, its role in modulating both degradation behavior and cellular response warrants comprehensive investigation.
- Finally, although numerous studies report corrosion resistance and basic cytocompatibility, there remains a lack of holistic investigations linking surface engineering parameters, degradation behavior, mechanobiological response, and cell-material interactions in a unified framework. The absence of such integrated studies hinders the rational design of eco-friendly, multifunctional surface-modified Mg alloys with predictable degradation and enhanced biological performance.

2.8 Research Objectives

The primary aim of this research is to develop eco-friendly surface engineering strategies for magnesium alloys to enable their safe and reliable use as resorbable implant materials. Emphasis is placed on tailoring surface wettability, chemistry, and micro-/nano-scale morphology to achieve controlled degradation, enhanced corrosion resistance, and improved biological performance. The study adopts a systematic and sequential approach, integrating experimental surface modification, dynamic degradation evaluation, post-deposition treatment, and multiscale computational modeling to establish comprehensive structure–property–biological response relationships.

I. Development of Eco-Friendly Hydrophobic Coatings

To develop environmentally benign hydrophobic coatings on magnesium alloy surfaces aimed at reducing corrosion rate and enhancing surface stability for resorbable implant applications.

II. **Optimization Toward Superhydrophobic Surface States**

To optimize hydrophobic coating parameters to achieve superhydrophobic behavior by controlling surface wettability, surface roughness, and corrosion resistance using systematic and data-driven optimization approaches.

III. **Design of Bioactive Composite Coating Systems**

To design and fabricate bioactive composite coating systems incorporating natural biomaterials such as hydroxyapatite, Zn-doped hydroxyapatite, and chitosan on optimized magnesium alloy surfaces to enhance cellular response while maintaining controlled degradation behavior.

IV. **Evaluation of Dynamic Degradation Under Physiological Flow**

To investigate the degradation behavior of surface-modified magnesium alloys under physiologically relevant flow conditions, simulating in vivo environments and assessing the influence of flow-induced shear stress on corrosion kinetics.

V. **Influence of Post-Deposition Heat Treatment**

To study the effect of post-deposition heat treatment on coating microstructure, surface chemistry, crystallinity, and wettability, and to evaluate its subsequent influence on corrosion performance and cell growth.

VI. **Multiscale Simulation of Cell–Surface Interactions**

To employ multiscale computational simulations to analyze cell-surface interactions on modified magnesium alloy surfaces, enabling mechanistic understanding of stress, strain, and strain energy density at the bio–interface.

Chapter 3

Development of Hydrophobic Coatings on Magnesium Alloys

3.1 Experimental procedure

3.1.1 Materials and Pretreatment of Magnesium Alloys

In this study, the pristine samples are Mg alloy (Az31). The samples were mechanically ground by sandpapers of different grit sizes (600, 800, 1000, and 1200) and cloth polished with fine-grained abrasive powder. Then the samples were subjected to an ultrasonic cleaning process in anhydrous ethanol and deionized water. Finally, the samples were exposed to atmospheric conditions until dried properly and were cut into plates with 10 mm×10 mm×2 mm.

3.1.2 Hydrophobic coating construction process

The experimental setup for the coating has been shown in the Figure 3.1 Initially, 1 gram of zinc chloride was dissolved in 30 milliliters of deionized water, while 2 grams of stearic acid were dissolved in an equal volume of absolute ethanol. Subsequently, the zinc chloride aqueous solution was added drop by drop to the stearic acid ethanol solution, with magnetic stirring, until the mixture achieved a pH of approximately 7.2–7.3. Continuous stirring ensured uniformity in the mixture. The resulting solution was used to immerse the mixture solution and the sample, which were then placed in an incubator. The incubator was heated to different temperatures ranging from 50°C to 70°C, and the samples were kept for 2 hours. Afterward, the samples were thoroughly cleaned with ethanol and deionized water.

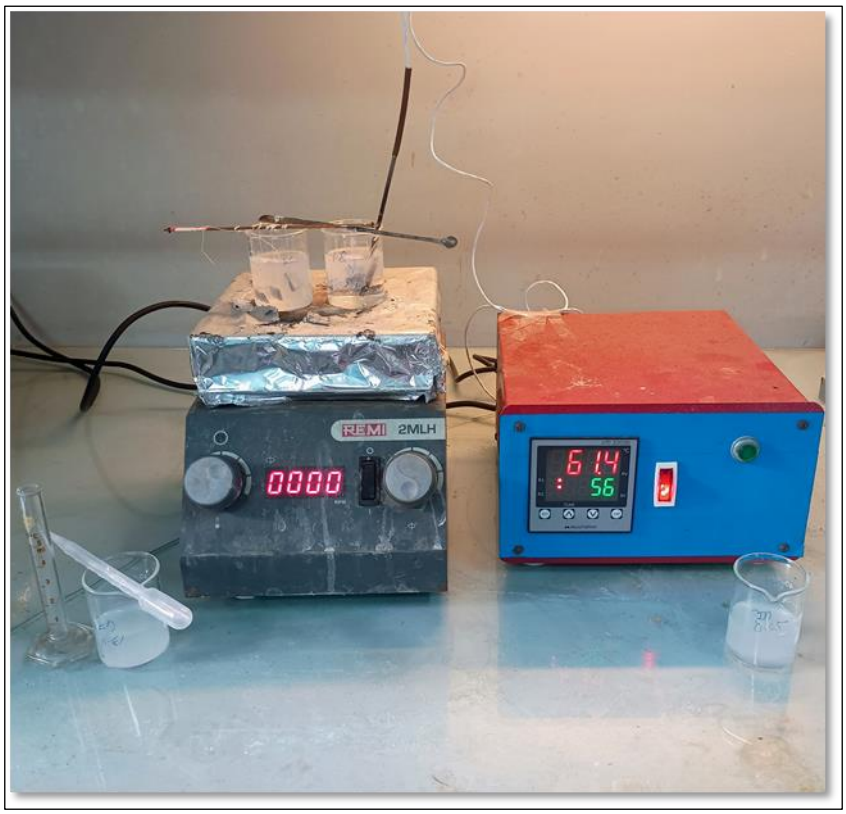

Figure 3.1 Experimental set up for coating

3.1.3 Characterization methodology

Surface wettability was determined using a contact angle goniometer (OEG GMBH, Germany). The coating structure was observed with a Field Emission Scanning Electron Microscope (FESEM, Sigma model, Carl Zeiss Microscopy Ltd.), and the elemental composition along with spatial distribution was identified using Energy-Dispersive X-ray Spectroscopy (EDX) coupled with the FESEM system. The phase compositions of both the coated and uncoated samples were identified through X-ray Diffraction (XRD) using a Rigaku Miniflex-600 system with Cu-Kα radiation ($\lambda = 1.54$ Å), scanned over a 2θ range from 10° to 90° at 0.5°/min.

3.1.4 Corrosion study (Potentiodynamic Polarization test)

To perform the Electrochemical Study, a three-electrode cell setup was used with GAMRY 620 potentiostat. The experimental configuration consisted of the coated Mg alloys as the working electrode (WE), a platinum gauze serving as the

auxiliary/counter electrode (C.E.), and a saturated calomel electrode (SCE) of Ag/AgCl functioning as the reference electrode (RE).

Before initiating each set of experiments, the working electrodes (individual samples) were immersed in the test solution (SBF) for 1 hours to achieve a stable open circuit potential (OCP). The OCP was continuously monitored for the next 30 minutes. A steady-state condition was verified when no significant potential deviation was observed during the OCP measurement.

The potential range employed for the Potentiodynamic polarization test was from -1.2 V to +0.4 V, with a scan rate of 1 mV/Sec. The Tafel Extrapolation method was applied to determine the corrosion current density (Icorr) and the corrosion potential (Ecorr). The Tafel equation is an electrochemical kinetics equation relating the electrochemical reaction rate to the overpotential. All the experiments were carried out at ambient temperature (27°C), and the open surface area to the electrolyte for each specimen was $1cm^2$; beyond that, the sample was wrapped with Teflon to avoid contact with the electrolyte. The preparation of SBF solution has been shown in APENDICES section under subsection A.1 in table A.I.

3.2 Result and analysis

3.2.1 Surface morphology and EDS analysis

Figure 3.2 (a-d) show the surfaces of hydrophobic coatings formed at different temperatures for 2 h. At 50 °C (Fig. b), the coating consists of loosely distributed and partially developed microstructures, indicating incomplete growth due to limited reaction kinetics. Increasing the temperature to 60 °C (Fig. c) results in more uniform coverage with well-developed flake-like structures and increased surface roughness. At 70 °C (Fig. d), a densely packed hierarchical micro/nanostructured morphology is clearly observed, with finer nanofeatures decorating the microscale structures. This multiscale roughness is favorable for air trapping and is characteristic of surfaces exhibiting enhanced hydrophobicity.

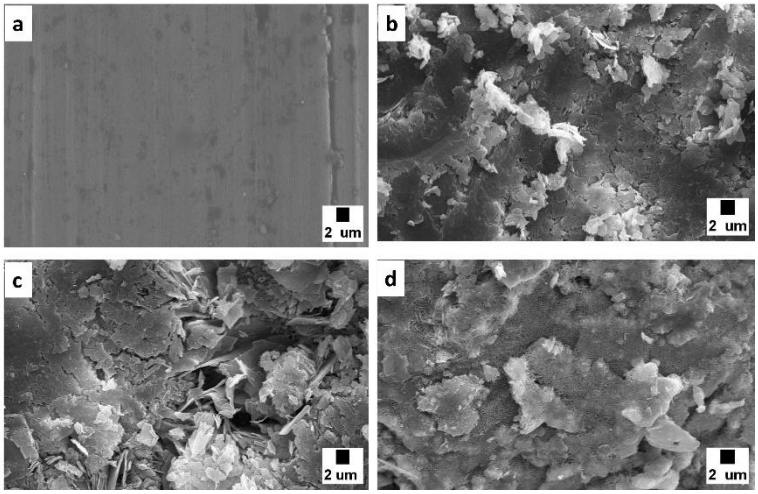

Figure 3.2 SEM images of (a) base and (b–d) coated samples at different temperatures

Figure 3.3 (a-d) shows the surface roughness profiles of the bare Mg alloy and coated samples, while the quantitative roughness parameters (Ra and Rq) are summarized in the bar chart in Figure 3.4. The bare Mg alloy exhibits a nearly flat profile with very low roughness (Ra ≈ 0.4 μm, Rq ≈ 0.5 μm), reflecting its relatively smooth surface. After coating, a significant increase in surface roughness is observed due to the formation of micro/nanostructured features. The sample coated at 50 °C (S1) shows a moderate rise in roughness (Ra ≈ 1.7 μm, Rq ≈ 2.2 μm), indicating partial development of surface asperities. The roughness further increases for the 60 °C-coated sample (S2), which exhibits the highest values (Ra ≈ 3.6 μm, Rq ≈ 4.3 μm), corresponding to pronounced height variations and deeper valleys in the roughness profile. In contrast, the 70 °C-coated sample (S3) shows an optimized and favourable roughness with Ra ≈ 2.6 μm and Rq ≈ 3.6 μm. The roughness profile of S3 reveals uniformly distributed peaks and valleys without excessive height fluctuations, indicating a well-organized hierarchical micro/nanostructure. This intermediate roughness is advantageous, as it provides sufficient multiscale texture for air entrapment while avoiding overly sharp asperities that may compromise coating stability.

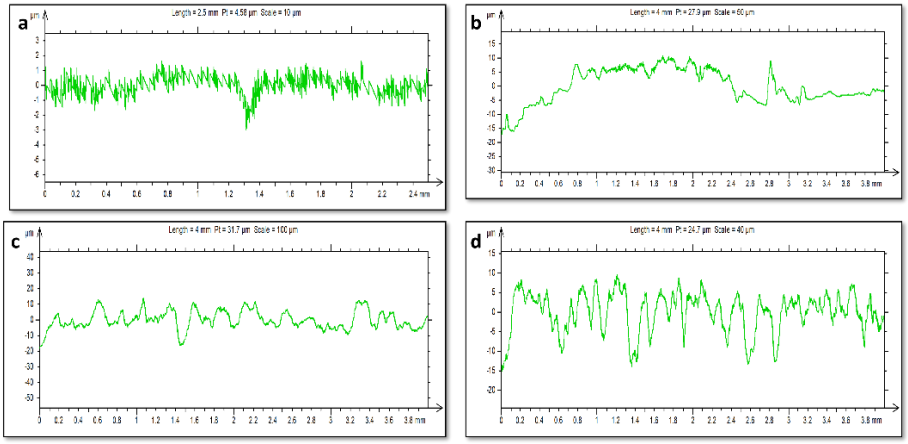

Figure 3.3 Surface profile of base and coated sample at different temperatures

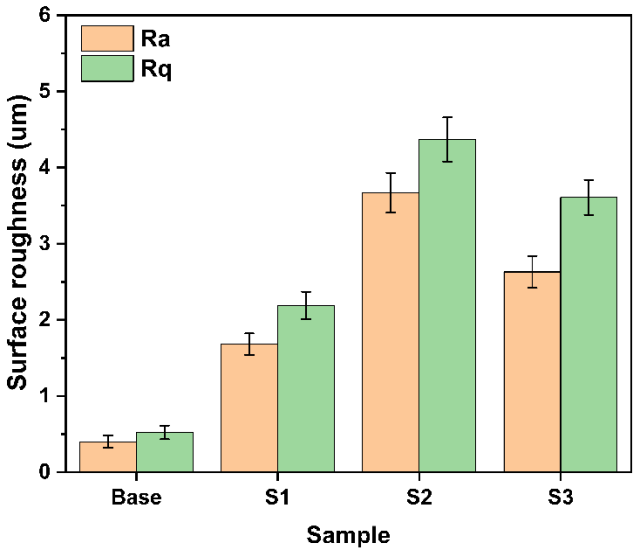

Figure 3.4 Comparison of surface roughness value of base and coated samples

3.2.2 Elemental analysis

Figure 3.5 (a) presents the EDS spectrum of the bare AZ31 magnesium alloy. The spectrum is dominated by a strong Mg peak with an atomic concentration of ≈95.2 %, confirming magnesium as the primary constituent of the alloy. Minor peaks corresponding to Al (≈2.7 %), Mn (≈0.7 %), and Zn (≈1.4 %) are also detected, which are characteristic alloying elements of AZ31. Figure 3.5 (b) shows the EDS spectrum of the hydrophobically coated AZ31 sample prepared at 70 °C. A substantial change in surface composition is observed compared to the bare alloy. The coated surface is dominated by carbon (≈76.2 %) and oxygen (≈14.4 %), confirming the formation of

an organic-rich surface layer resulting from the reaction between stearic acid and zinc species. The presence of Zn (≈2.5 %) further supports the formation of a zinc-based fatty acid compound (e.g., zinc stearate) within the coating. The significantly reduced Mg signal (≈3.7 %) indicates effective coverage of the AZ31 substrate by the coating layer. Trace amounts of Cl (≈2.6 %) are attributed to residual chloride species originating from the $ZnCl_2$ precursor, while the Pt signal (≈1.5 %) arises from the platinum sputter coating applied to improve surface conductivity during SEM-EDS analysis. Overall, the EDS results confirm the successful formation of a carbon-rich, Zn-containing hydrophobic coating on AZ31 magnesium alloy at 70 °C, providing effective surface coverage. These findings are consistent with the observed hierarchical surface morphology, optimized roughness, and enhanced hydrophobic performance demonstrated by contact angle and droplet stability measurements.

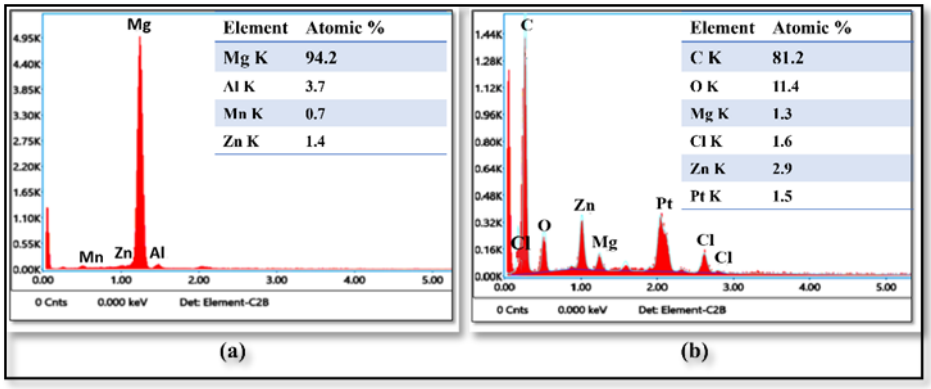

Figure 3.5 EDS spectra and corresponding atomic compositions of (a) bare magnesium alloy and (b) hydrophobically coated sample prepared at 70 °C for 2 h

3.2.3 Wettability

Figure 3.6 (a–d) shows the static water contact angle measurements of the bare Mg alloy and hydrophobically coated samples prepared at different temperatures. The bare Mg alloy (Figure 3.6 a) exhibits a low contact angle of ~82°, indicating an intrinsically hydrophilic surface, which is consistent with its smooth morphology and very low surface roughness. Upon coating, a progressive increase in contact angle is observed with increasing coating temperature. The sample coated at 50 °C (Figure 3.6 b) shows a contact angle of ~105°, reflecting the onset of hydrophobicity due to partial surface coverage and moderate roughness, as confirmed by SEM and profilometry

results. Further increasing the temperature to 60 °C (Figure 3.6 c) increases the contact angle to ~115°, corresponding to the development of more pronounced microstructures and higher surface roughness. The highest contact angle of ~139° is obtained for the 70 °C-coated sample (Figure 3.6 d). This enhanced wettability performance is attributed to the formation of well-defined hierarchical micro/nanostructures, as observed in SEM, combined with an optimized surface roughness (Ra ≈ 2.6 μm). Unlike the 60 °C sample, which exhibits higher roughness but less uniform height distribution, the 70 °C sample provides a balanced multiscale texture that effectively traps air pockets at the solid–liquid interface, promoting a Cassie–Baxter wetting state. Overall, the wettability results strongly correlate with surface morphology and roughness analyses, confirming that the hierarchical structure and optimized roughness achieved at 70 °C are primarily responsible for the superior hydrophobic behavior of the coating.

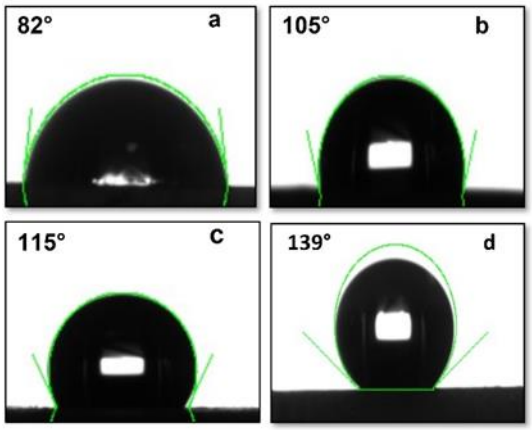

Figure 3.6 Contact angle measurements of the bare Mg alloy and coated samples

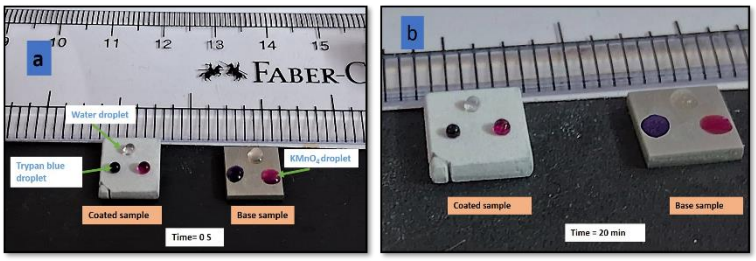

Figure 3.7 Contact angle testing with droplets of different liquid for time = 0 second and after 20 min respectively

To further validate the hydrophobic behavior, wettability tests were conducted using three different liquid droplets–water, Trypan blue, and $KMnO_4$ solutions- as shown in Figure 3.7 (a). In all cases, the droplets retained a nearly spherical shape on the coated surface, whereas rapid spreading was observed on the bare Mg alloy, indicating strong liquid–solid interactions. Figure 3.7 (b) shows the condition of the droplets after 20 minutes of exposure. The droplets on the bare Mg alloy dispersed completely due to surface wetting and absorption, while those on the coated sample remained intact and well-defined, confirming the temporal stability of the hydrophobic surface. The consistent droplet repellency across different liquid chemistries highlights the robustness of the coating and its effectiveness in minimizing liquid adhesion.

Overall, these results corroborate the contact angle measurements and demonstrate that the coating synthesized at 70 °C exhibits stable and pronounced hydrophobic behavior, attributable to its hierarchical surface morphology and optimized roughness

Chapter 4

Multi-Objective Optimization of Superhydrophobic Coatings on Magnesium Alloys

4.1 Experimental procedure

4.1.1 Design of experiment, data processing and optimization flowchart

The process flow illustrated in Figure 4.1 presents a robust multi-objective hybrid optimization framework that integrates experimental and computational techniques to achieve optimal solutions validated through experiments. The process begins with an experimental design utilizing Response Surface Methodology (RSM) with a Central Composite Design (CCD), which systematically explores parameter variations while minimizing the number of experiments. The coating process was performed based on these designed input parameters. The resulting experimental data are compiled into a datasheet containing response values, which serves as the foundation for predictive model development.

A feed-forward Neural Network (FNN) is then trained to capture complex nonlinear relationships within the data. Data augmentation methods were applied to improve the regression coefficient, robustness, and generalization of the model. The best predictive model was selected by comparing the R^2 values across multiple models to ensure the accuracy and reliability for the subsequent optimization phase.

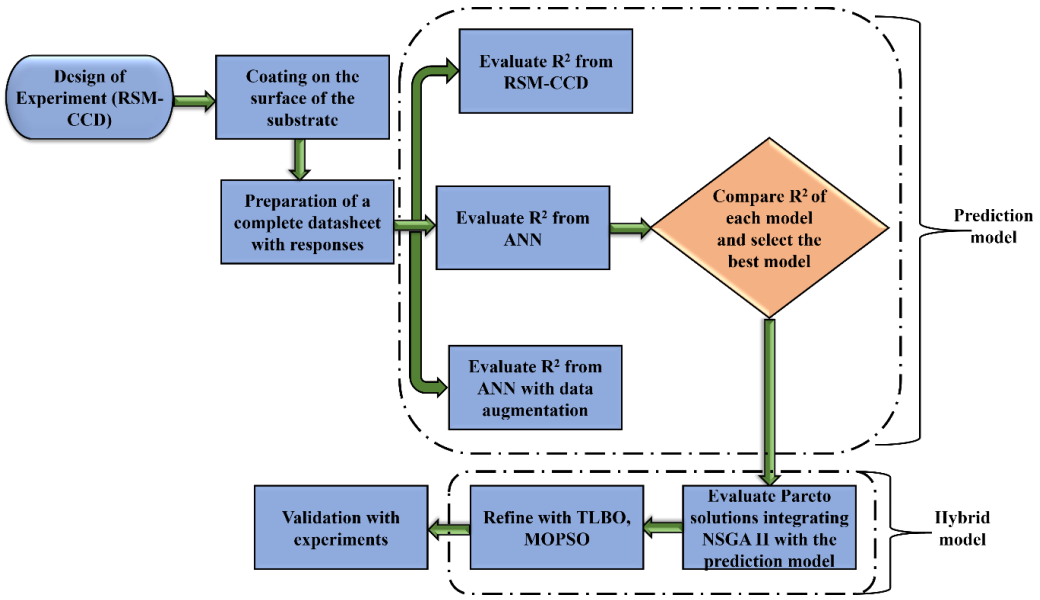

Figure 4.1. Schematic of the process flow chart from the design of the experiment to optimization and experimental validation

The optimization process consisted of two stages. In the first stage, the NSGA-II algorithm was integrated with the best predictive model, which served as the objective function for optimization. This hybrid approach generates a Pareto front that represents the trade-offs between conflicting objectives. In the second stage, the solutions obtained are further refined using Teaching-Learning-Based Optimization (TLBO) and Multiobjective Particle Swarm Optimization (MOPSO). These methods help converge the diverse regions of the Pareto front, improve optimality, and plot the convergence process for individual responses. Finally, the computationally optimized solutions were validated experimentally to assess their real-world applicability and conduct a comparative analysis of the algorithm performance. This workflow effectively integrates experimental design, predictive modelling, and advanced optimization algorithms, ensuring a thorough exploration of the design space, accurate predictions, and practical validation.

4.1.2 Experimental design through RSM-CCD

To methodically examine how the process parameters influence the functionality of hydrophobic coatings, a combination of RSM and CCD was employed. This statistical approach is well suited for analyzing multivariable systems,

allowing for predictive modeling while reducing the total number of required experiments.

Table 4.1 The range of input process parameters, including the design summary of RSM-CCD, has been represented below

Input process parameters	**Range**
Stearic acid (M)	0.18 to 0.26
Zinc Chloride (M)	0.16 to 0.24
Coating temperature (℃)	50 ℃ to 70℃
Coating Duration (hr.)	1 hour to 5 hours
Design Summary	
Factors	4
Replicates	1
Total runs	30
Total blocks	3
A	1

Table 4.1 illustrates the examination of four independent continuous variables: stearic acid concentration, zinc chloride concentration, coating temperature, and coating duration. The concentrations of stearic acid and $ZnCl_2$ were varied between 0.18 M and 0.26 M and 0.16 M to 0.24 M respectively, to evaluate the influence of hydrophobic agents and surface modifications resulting from chemical reactions.

The coating temperature was adjusted between 50 °C and 70 °C to regulate the reaction kinetics, coating formation, and deposition rate. The coating duration ranged from 1 to 5 hours to assess its effects on the coating quality. These parameter ranges were selected to satisfy the functional and chemical requirements of the coating process.

The experimental design comprised 30 runs distributed across three base blocks with one replicate per condition. A face-centered CCD was employed with an α value of 1. To improve model accuracy and assess reproducibility, the design incorporated multiple centre point replicates. These repeated runs, performed under identical input conditions in runs 1, 5, 18, 19, and 26, which are shown in Table 4.2, are standard in CCD for evaluating experimental variability and enhancing statistical robustness. The

design included factorial points to capture linear and interaction effects, axial points to detect curvature, and centre points to assess experimental stability and repeatability. This well-structured approach enables a thorough exploration of the parameter space while optimizing resource efficiency. The use of blocks helped account for variability, ensuring consistency and reproducibility across the experiments.

4.1.3 Prediction and Optimization Framework

Following the development of the data sheet and application of the RSM-CCD design, the objective was to enhance the regression coefficient value, R^2, through the use of an Artificial Neural Network (ANN). The ANN employed was a feedforward network comprising one input layer, three hidden layers, and one output layer. The first, second, and third hidden layers were composed of 50, 30, and 15 neurons, respectively [125,126]. This architecture was chosen based on experimental evaluations of multiple network configurations supported by insights drawn from prior studies. The final structure, consisting of three hidden layers with 50, 30, and 15 neurons, was found to offer an optimal trade-off between model complexity and performance. Specifically, this arrangement provides sufficient capacity to capture complex relationships in the data, while mitigating the risk of overfitting [127,128]. Other architectures, including those with fewer neurons or additional layers, resulted in poorer generalization performance and lower R^2 values.

The network was trained using the Levenberg-Marquardt algorithm (trainlm), which is particularly effective for medium-sized networks due to its optimal balance between computational efficiency and convergence speed [129]. For the activation functions, the Hyperbolic Tangent Sigmoid (tansig) function was used in the hidden layers to introduce nonlinearity and ensure that the model could handle complex relationships between inputs and outputs. The output layer employs a linear activation function (pureline) to predict continuous values [130].

Data division for training, validation, and testing was conducted using a random partitioning method (dividerand) with 70% of the data allocated for training, 15% for testing, and 15% for validation. This partitioning ensures a representative sample

across all subsets, allowing the model to be trained effectively while being validated and tested on separate data to evaluate the generalization. Network performance was assessed using the Mean Squared Error (MSE) metric, a standard method for evaluating regression errors in ANN-based models [131].

To enhance the predictive efficiency of machine learning models such as artificial neural networks (ANN), a substantial volume of data is typically necessary. The data augmentation process was implemented by introducing random noise from the gaussian distribution into the normalized input and output data. The mathematical model employed for augmentation is delineated in Equations 4.1 and 4.2 [132][133,134].

$$x_{augmented} = x + \epsilon \tag{4.1}$$

$$y_{augmented} = y + \epsilon \tag{4.2}$$

where, $x_{augmented}$, and $y_{augmented}$ represent the augmented input data points and output data points respectively and term ϵ represents a perturbation or noise term.

The mathematical equation utilized for gaussian distribution is shown in the Equation 4.3 below [135]

$$p(\epsilon) = \frac{1}{\sqrt{2\pi\sigma^2}} e^{-\frac{(\epsilon-\mu)^2}{2\sigma^2}} \tag{4.3}$$

In this study, the random variation magnitude is controlled by the standard deviation (σ) of Gaussian noise. The parameter σ governs the intensity of the noise added to the input and output data. The mean (μ) was set to zero to ensure that the noise was unbiased.

To determine the optimal value of σ, a sensitivity analysis was conducted, in which different values of σ (0.1, 0.5, and 0.9) were tested. The results of this analysis showed that σ = 0.5 yielded the best performance in terms of prediction accuracy. Specifically, σ = 0.5 produced the highest correlation coefficient (R = 0.9919) and the lowest Mean

Squared Error (MSE = 24.0896) compared to other tested values of σ. These sensitivity analysis tests reports have been provided in APPENDICES section under subsection A.2. These results indicate that σ = 0.5, which provides the best balance between the noise intensity and model performance.

Gaussian noise was selected for data augmentation because of its well-established role in the modeling of natural noise. The zero-mean property of the Gaussian distribution ensures unbiased augmentation, whereas the chosen σ value controls variability, promoting generalization and robustness during the training process [136]. The Gaussian distribution's ability to introduce smooth, unbiased perturbations is also well-suited for working with normalized data, making it a natural choice for improving the ANN model's performance [137].

NSGA-II, an advanced variant of the Genetic Algorithm (GA), incorporates significant enhancements such as rapid nondominated sorting, crowding distance calculation, and the principle of elitism [138]. The schematic of the flow chart of NSGA-II has been shown in the Figure 4.2. In this study, the NSGA-II algorithm was employed to optimize the process parameters and corresponding responses by utilizing an objective function and database derived from the outputs of an Artificial Neural Network (ANN). This integration constitutes a hybrid dynamic optimization approach. The nondominated set is required to satisfy the following conditions, as represented in the Equation 4.4 below [139]

$$M_{x\in(1,2,3\ldots n)}.\,Q = P \qquad (4.4)$$
$$\forall i,j \in (1,2,3\ldots n), i \neq j, x_i \cap x_j = \emptyset$$
$$x_1 > x_2 > x_3 \ldots . x_n$$

where, P represents the nondominated set, M denotes the overall population, Q indicates the spatial position of the offspring, and x_k refers to any decision variable

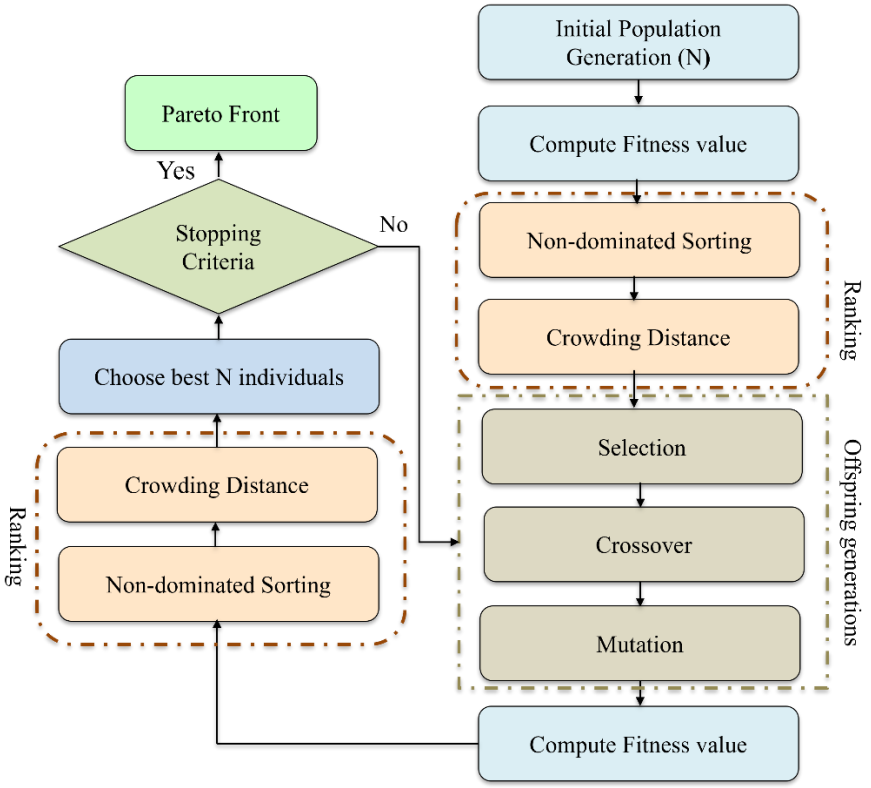

Figure 4.2 Schematic of flow chart NSGA II algorithm [140]

The NSGA-II algorithm was implemented with a population size of 200, selected to promote a diverse search across the solution space and ensure robust convergence toward the Pareto front. Each individual encoded four decision variables bounded within experimentally defined limits: 0.18–0.26, 0.16–0.24, 50–70, and 1–5 for the respective parameters. The algorithm was executed over 50 generations, allowing sufficient evolutionary progress without incurring excessive computational cost [141]. A crossover probability of 0.8 is widely accepted in multi-objective optimization literature for its effective balance between exploration and convergence, was employed to enhance genetic diversity by promoting extensive information exchange between parent solutions. A mutation probability of 0.25 was used to preserve population diversity and prevent premature convergence, particularly in complex optimization landscapes [142]. These parameter settings were not only informed by established practices, but were also validated through preliminary trial-and-error testing to ensure stability and performance in the current application. The selection process was driven by nondominated sorting and crowding distance computation to

preserve population diversity, along with tournament selection based on Pareto dominance and crowding distance values.

The Teaching-Learning-Based Optimization (TLBO) algorithm is a population-driven metaheuristic that draws inspiration from the educational dynamics of classroom environments. It comprises two principal phases: teaching and learning. During the Teaching Phase, the most knowledgeable individual within the population was designated as a teacher. The teacher's objective is to improve the average outcomes of learners by imparting knowledge, which is represented by the mean position of other learners [143]. Equation 4.5 outlines the mathematical structure of the teacher phase.

$$X_{new} = X_i + r.(X_{teacher} - (T_F.X_{mean}) \quad (4.5)$$

where X_{new}, represents the updated position of learner i, while X_i denotes the current position of learner i, and the parameter r is random within the interval [0,1]. $X_{teacher}$ indicates the position of the best learner (teacher) and X_{mean} represents the mean position of all learners in the population. T_F is the teaching factor, which is randomly assigned between 1 and 2. This random assignment enables the algorithm to adapt directly to the population, based on the comparative efficacy of the teacher solutions. This value is consistent with the typical approach used in TLBO to introduce variability and improve the search dynamics [144].

In the Learner Phase, individuals improve their understanding by interacting with one another. Each participant evaluated their fitness by comparing it to that of another randomly selected participant. Based on the comparative fitness levels, the individuals adjust their positions accordingly, moving towards the one with superior fitness. Equations 4.6 and 4.7 below illustrate the mathematical representations,

$$X_{new} = X_i + r.(X_i - X_j) \quad \text{if } f(X_i) < f(X_j), i \neq j \quad (4.6)$$

$$X_{new} = X_i + r.(X_j - X_i) \quad \text{if } f(X_i) > f(X_j), i \neq j \quad (4.7)$$

where X_{new}, is the updated position of learner i and r is a random number between [0,1]. Now, if X_i demonstrates superior performance compared to X_j then X_j moved towards X_i in accordance with Equation (4.6), otherwise X_i is moved towards X_j as

per Equation (4.7). Notably, X_i will be replaced by X_{new} only if X_{new} exhibits greater knowledge than X_i. The schematic of the flow chart of the TLBO algorithm gas been displayed in the Figure 4.3.

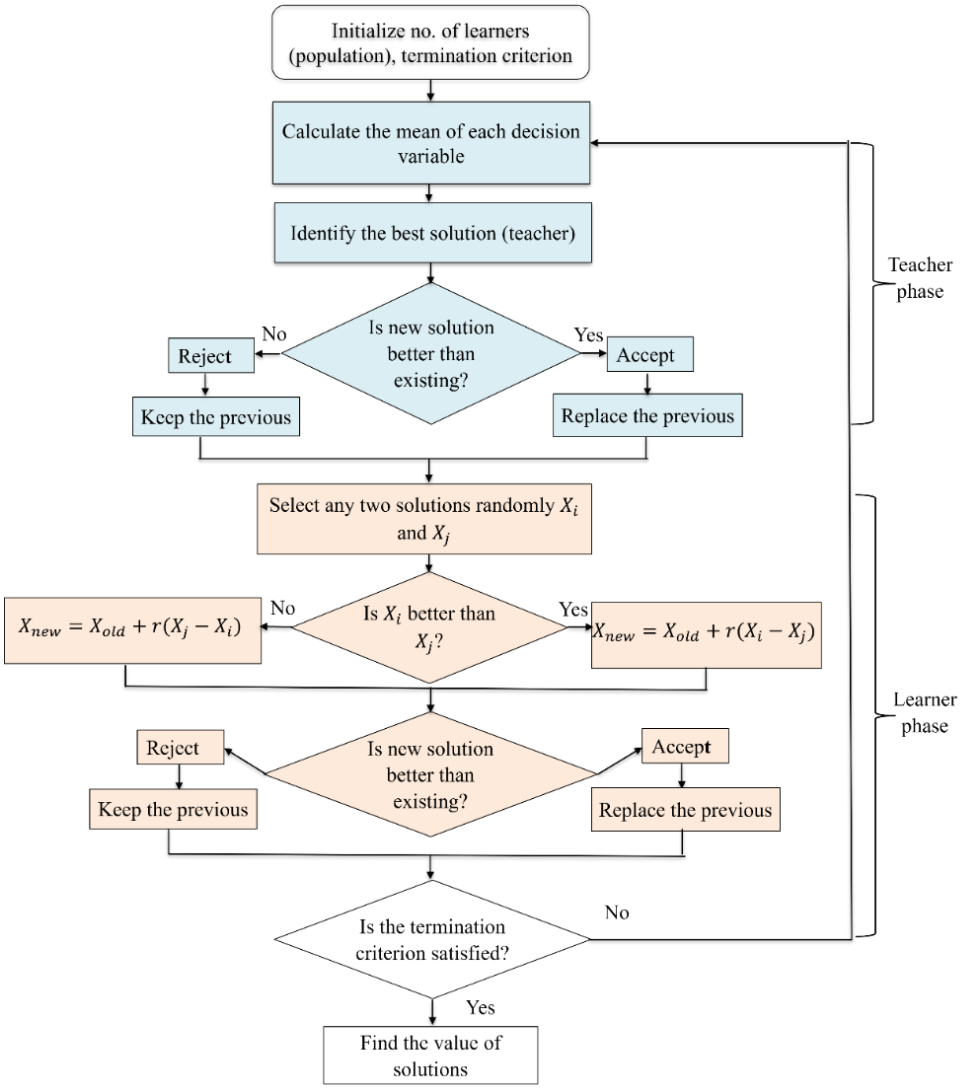

Figure 4.3 Schematic of flow chart TLBO algorithm [145]

The Multi-Objective Particle Swarm Optimization (MOPSO) algorithm adjusts the particle positions and velocities at each iteration to solve optimization problems. It uses guiding particles known as leaders and maintains a record of superior solutions in an external archive. In addition, mutation operators can be applied when required. Each particle updates its velocity and position by considering both the leader and best-known global positions, helping the swarm move efficiently toward optimal solutions

[146]. The formulas for updating particle velocities are as denoted in Equations 4.8, 4.9, and 4.10 below,

$$V_{id}^{k+1} = \omega_k V_{id}^k + c_1(P_{id}^k - X_{id}^k) + (P_{gk}^k - X_{id}^k) \quad (4.8)$$

$$X_{id}^{k+1} = X_{id}^k + V_{id}^{k+1} \quad (4.9)$$

$$V_{id} \in [-V_{max}, V_{max}] \quad (4.10)$$

where k indicates the iteration count, ω_k refers to the inertia weight and X_{id}^k signifies the position of the particle, V_{id}^k represents the velocity of the particle, P_{id}^k is the individual best of the particle, P_{gk}^k stands for the global best position of the particle at the k^{th} iteration. The coefficients c_1 and c_2 serve as the learning parameters. V_{max} represents the maximum velocity of the particle. In the MOPSO implementation, an inertia weight of 0.4 was adopted to facilitate a balanced trade-off between exploration and exploitation throughout the optimization process. This value encourages particles to gradually reduce their search radius, enabling a smoother convergence toward optimal regions without overshooting or stagnating prematurely. Additionally, the cognitive and social coefficients were both set to 1.2, representing moderate influence levels from a particle's own historical best (cognitive) and swarm's global best (social). These values were selected to ensure stable and effective search dynamics, allowing particles to benefit from both individual learning and collaborative information sharing, while avoiding overly aggressive convergence behaviors. In this study, for both TLBO and MOPSO, the population number was set to 100 and the number of generations was set to 50 [147,148]. The schematic of the flow chart of the MOPSO algorithm gas been shown in the Figure 4.4.

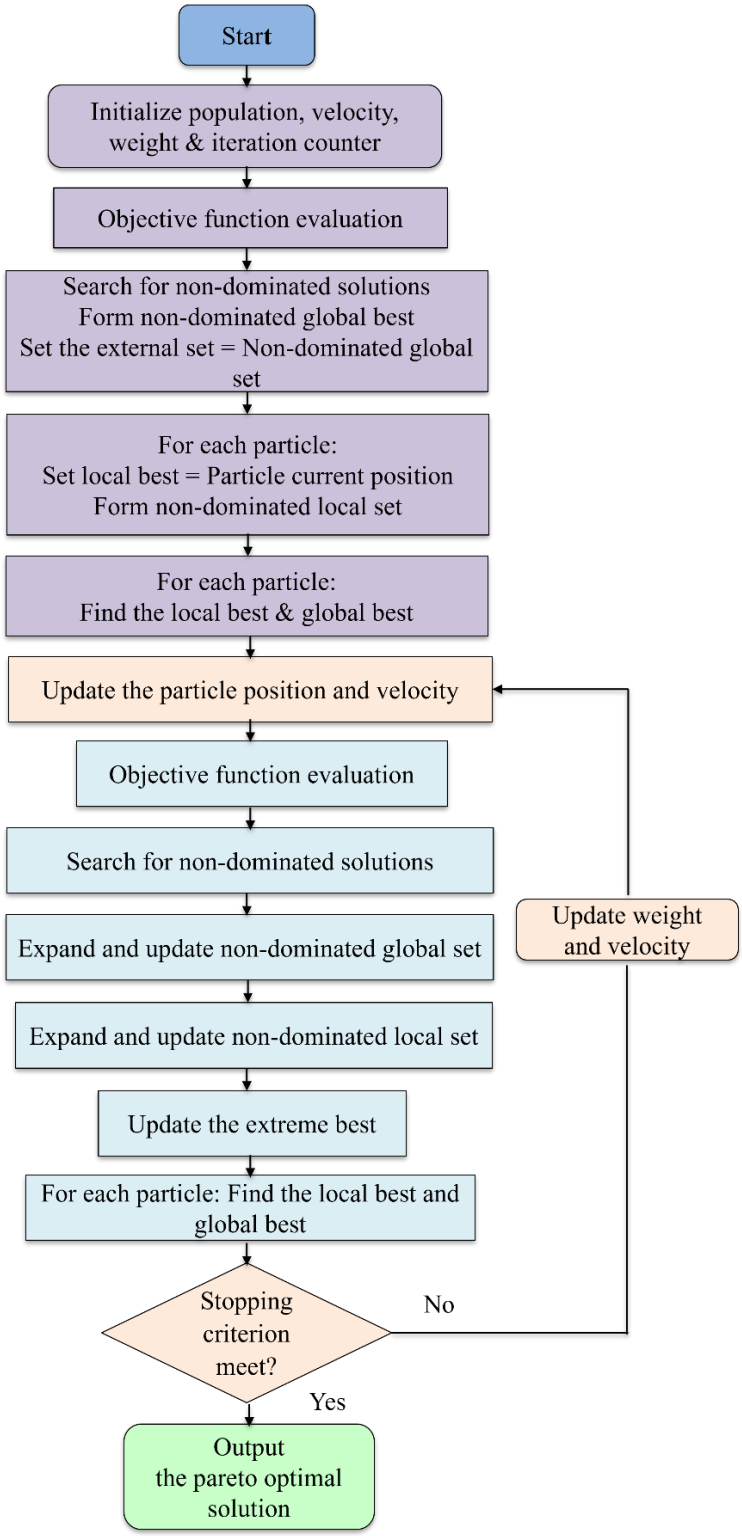

Figure 4.4 Schematic of flow chart MOPSO algorithm [149]

4.1.4 Preparation of the coated surface

In this study, cast magnesium alloy blocks were cut using wire electrical discharge machining (EDM), followed by mechanical polishing to achieve the final dimensions of 10 mm×10 mm×2 mm. The polished samples were ultrasonically cleaned in acetone for 10 min and allowed to air-dry. A solution of stearic acid (0.18–0.26 M) was prepared by dissolving the acid in 30 mL absolute ethanol (99.9%) using ultrasonication to ensure complete dissolution. The samples were then immersed in an ethanolic stearic acid solution. Separately, a $ZnCl_2$ aqueous solution (0.16–0.24 M) was prepared and introduced dropwise into the stearic acid solution under continuous magnetic stirring. The rate of $ZnCl_2$ addition was maintained at a moderate, controlled rate to avoid rapid substrate corrosion or premature precipitation. Subsequently, the reaction bath was gradually heated to 75 °C and maintained at this temperature for up to 5 h to allow complete formation of the coating. After immersion, the samples were removed, gently rinsed with ethanol, and air-dried. The schematic of the coating procedure has been shown in Figure 4.5.

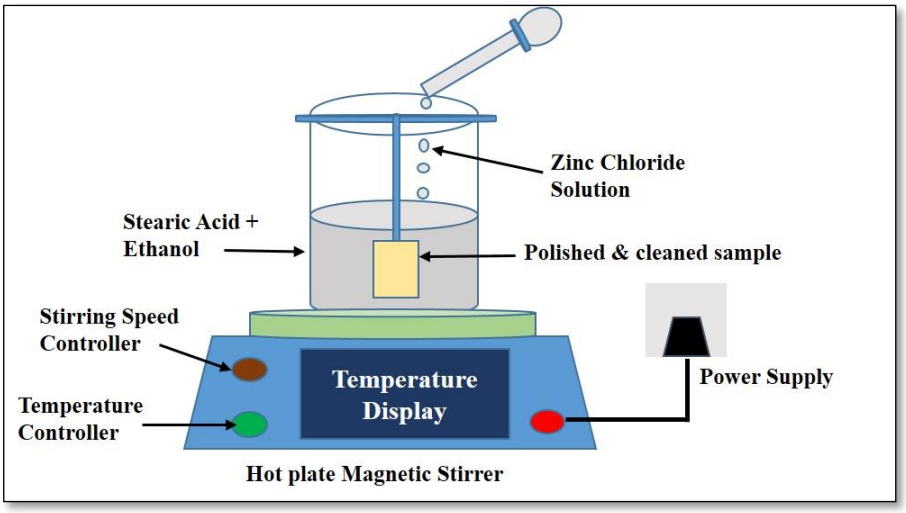

Figure 4.5 Schematic of Coating Process

4.1.5 Characterization methods

Surface wettability was determined using a contact angle goniometer (OEG GMBH, Germany). The coating structure was observed with a Field Emission Scanning Electron Microscope (FESEM, Sigma model, Carl Zeiss Microscopy Ltd.), and the elemental composition along with spatial distribution was identified using Energy-Dispersive X-ray Spectroscopy (EDX) coupled with the FESEM system.

The surface texture and roughness values were captured using an optical profilometer (Zygo NewView9000). The phase compositions of both the coated and uncoated samples were identified through X-ray Diffraction (XRD) using a Rigaku Miniflex-600 system with Cu-Kα radiation (λ = 1.54 Å), scanned over a 2θ range from 10° to 90° at 0.5°/min.

The presence of functional groups was tracked using Fourier Transform Infrared Spectroscopy (FTIR) in ATR mode with a Jasco FTIR 4700 (Japan), spanning 4000 to 70 cm^{-1}. The structural and molecular features were further probed via Raman spectroscopy using a Witec Alpha 400 R (Germany), featuring a 785 nm laser, 300 lines/mm grating, and a CCD detector (1024×127 pixels) cooled to 208 K.

4.1.6 Surface roughness and Surface-free energy measurement

The surface roughness of the samples was quantified by using an optical profilometer (Zygo NewView 9000). The surface energy was calculated employing the Owens and Wendt geometric mean method [150] as delineated in Equations (4.11) and (4.12):

$$y_L(1+\cos\theta) = 2\left(\sqrt{y_S^d y_L^d} + \sqrt{y_S^p y_L^p}\right) \tag{4.11}$$

$$y_S = y_s^d + y_s^p \tag{4.12}$$

Where y_L and y_S represent the surface tension of the test liquid and the surface free energy of the solid, respectively while $y^d$and $y^p$are the dispersion and polar

components respectively. The symbol θ denotes the measured contact angle. Contact angles were recorded for two test liquids distilled water (y_L=72.8 mN/m, y^d=21.8 mN/m, y^p=51 mN/m) and ethylene glycol (y_L==48 mN/m, y^d=29 mN/m, y^p=19 mN/m) using a goniometer (KYOWA FAMAS). The surface free energy was calculated based on the mean value obtained from three measurements taken for each sample.

4.1.7 Potentiodynamic polarization test

Electrochemical assessments were conducted utilizing a GAMRY 620 potentiostat. The experimental configuration comprised both coated and uncoated magnesium specimens as the working electrode (WE) with platinum gauze employed as the counter (auxiliary) electrode (CE). A saturated calomel electrode (SCE), specifically Ag/AgCl, was employed as the reference electrode (RE). Simulated body fluid (SBF) was selected as the electrolyte medium for corrosion studies. To ensure controlled exposure, only an 8 mm×4 mm section of each 10 mm×10 mm sample was exposed to the electrolyte, whereas the remaining portion was insulated with Teflon to prevent unintended electrochemical interactions. Electrochemical behavior was studied through techniques such as open-circuit potential (OCP), potentiodynamic polarization, and electrochemical impedance spectroscopy (EIS). For the polarization study, the potential range was set between −4.5 V and +1.5 V, with a scanning rate of 1 mV/s. EIS data were collected at the OCP using a 5 mV AC signal across a frequency spectrum ranging from 100 MHz to 100 kHz. Now, the corrosion resistance efficiency (%), CRE (%), is a quantitative metric used to evaluate the improvement in corrosion resistance provided by a protective coating relative to an uncoated (bare) substrate. The corrosion resistance efficiency (CRE) was calculated from the current density of the substrate (I_{cor}^S) and coated samples (I_{cor}^C), it has been shown in Equation 4.13 below [150],

$$CRE\ (\%) = 1 - \frac{I_{cor}^C}{I_{cor}^S} \qquad (4.13)$$

4.1.8 In vitro biocompatibility test

The cytocompatibility and cell proliferation characteristics of the samples were evaluated through extensive in vitro experiments conducted in accordance with the established protocols of ISO 10993-5, which included MTT and Live/Dead assays [151,152].

Cytotoxicity was assessed using the MTT assay. Scaffolds seeded with L929 adherent mouse fibroblast cells were incubated for 1 and 2 days. At each specified time point, 10 µL of MTT solution (EZCount MTT Assay Kit, Abcam, USA) was added to each sample, followed by a 4-hour incubation period. After incubation, the supernatant was meticulously removed, and the resultant formazan crystals were dissolved by the addition of 100 µL of isopropanol, followed by a 15-minute incubation. Cell viability was quantified employing the standard calculation method delineated in Equation 4.14 [153], based on absorbance readings at 570 nm and 670 nm obtained using a Thermo Scientific™ Multiskan™ GO Microplate Spectrophotometer (Finland).

$$Cell\ viability\ (\%) = {}^{(T-B)}\Big/_{(C-B)} \tag{4.14}$$

where T, B, and C signify the test, blank, and control results, respectively.

For the Live/Dead assay, an extract was first prepared by immersing the coated scaffold in simulated body fluid (SBF). This extract was used to culture L929 adherent mouse fibroblast cells in DMEM medium for 48 hours. After incubation, the culture medium was removed from the scaffolds, which were pre-seeded with the cells. The scaffolds were then stained with fluorescein diacetate (FDA) dye at a concentration of 10 mg/mL in serum-free DMEM for approximately 5 min. The FDA selectively stains viable cells with intact membranes. After staining, the scaffolds were gently rinsed to remove excess dye and were visualized using an inverted fluorescence microscope. Live cells appeared fluorescent under a microscope, indicating their viability and metabolic activity.

4.2 Results and dissuasion

4.2.1 Experimental data of Corrosion rate and Surface roughness according to RSM-CCD design

Table 4.2 presents the experimental results of the input parameters and their corresponding responses, specifically the surface roughness, surface free energy, and corrosion resistance efficiency (%) across 30 experimental runs. The observed range for surface roughness (μm) is from 0.69 μm to 4.12 μm, the surface free energy (mN/m) is from 6.10 mN/m to 9.09 mN/m, and the corrosion resistance efficiency (%) ranges from 39.46 % to 92.37 %.

Table 4.2 Experimental data sheet of input process parameters and corresponding responses

Sl No.	Stearic Acid (M)	$ZnCl_2$ (M)	Coating temperature (℃)	Coating duration (hour)	Surface roughness (μm)	Surface free energy (mN/m)	Corrosion resistance efficiency (%)
1	0.22	0.2	60	3	2.30	6.42	88.25
2	0.18	0.16	70	1	1.82	7.93	62.77
3	0.26	0.16	70	5	3.08	7.69	66.87
4	0.26	0.24	50	5	4.02	8.88	46.87
5	0.22	0.2	60	3	2.30	6.42	88.25
6	0.26	0.16	50	1	0.99	8.08	48.61
7	0.18	0.24	70	5	4.12	8.80	49.47
8	0.18	0.16	50	5	1.23	7.65	52.96
9	0.18	0.24	50	1	1.21	8.44	50.15
10	0.26	0.24	70	1	3.47	9.09	39.46
11	0.18	0.16	50	1	0.69	8.72	50.26
12	0.26	0.16	50	5	2.69	7.83	52.39
13	0.18	0.24	50	5	3.02	8.03	60.80
14	0.26	0.24	70	5	4.23	8.92	48.26
15	0.18	0.16	70	5	2.59	7.13	80.39

16	0.26	0.24	50	1	1.35	8.43	50.90
17	0.26	0.16	70	1	1.88	7.89	57.03
18	0.22	0.2	60	3	2.30	6.42	88.25
19	0.22	0.2	60	3	2.30	6.42	88.25
20	0.18	0.24	70	1	2.88	7.44	58.97
21	0.22	0.2	60	5	2.83	6.28	83.88
22	0.22	0.24	60	3	2.73	7.37	79.70
23	0.18	0.2	60	3	2.02	6.10	81.22
24	0.22	0.2	60	1	1.44	7.69	60.68
25	0.26	0.2	60	3	3.05	6.62	80.54
26	0.22	0.2	60	3	2.30	6.42	88.25
27	0.22	0.16	60	3	2.24	6.53	92.37
28	0.22	0.2	50	3	1.79	7.60	71.52
29	0.22	0.2	60	3	2.37	6.42	88.25
30	0.22	0.2	70	3	3.17	7.08	86.21

4.2.2 Analysis of RSM Results

4.2.2.1 Development of Regression Equations

Equations 4.15, 4.16, and 4.17 denote the relationship between the output responses (y_1, y_2, y_3) and input process parameters (x_1, x_2, x_3). The equations show that complex polynomial relations exist between the input parameters and the output responses.

$$y_1 = 7.54 - 165.5x_1 - 92.7x_2 + 0.564x_3 + 0.849x_4 + 382x_1^2 + 194x_2^2 - 0.00439x_3^2 - 0.0721x_4^2 + 12.4x_1x_2 - 0.101x_1x_3 + 1.38x_1x_4 + 0.397x_2x_3 - 0.10x_2x_4 - 0.00665x_3x_4 \quad (4.15)$$

$$y_2 = 61.69 - 60.6x_1 - 112.1x_2 - 1.160x_3 - 1.914x_4 + 102x_1^2 + 154x_2^2 + 0.000739x_3^2 - 0.0158x_4^2 + 15.1x_1x_2 + 0.223x_1x_3 + 0.72x_1x_4 + 0.774x_2x_3 + 2.09x_2x_4 + 0.02329x_3x_4 \quad (4.16)$$

$$y_3 = 55.05 - 60.6x_1 - 112.1x_2 - 1.160x_3 - 1.914x_4 + 102x_1^2 + 154x_2^2 + 0.00739x_3^2 - 0.0158x_4^2 + 15.1x_1x_2 + 0.223x_1x_3 + 0.72x_1x_4 + 0.774x_2x_3 + 2.09x_2x_4 + 0.02329x_3x_4 \quad (4.17)$$

where y_1 is the surface roughness (µm), y_2 is the surface free energy (mN/m), y_3 is the corrosion resistance efficiency (%), x_1 is stearic acid (M), x_2 is $ZnCl_2$ (M), x_3 is the coating temperature (ºC), and is the coating duration (h).

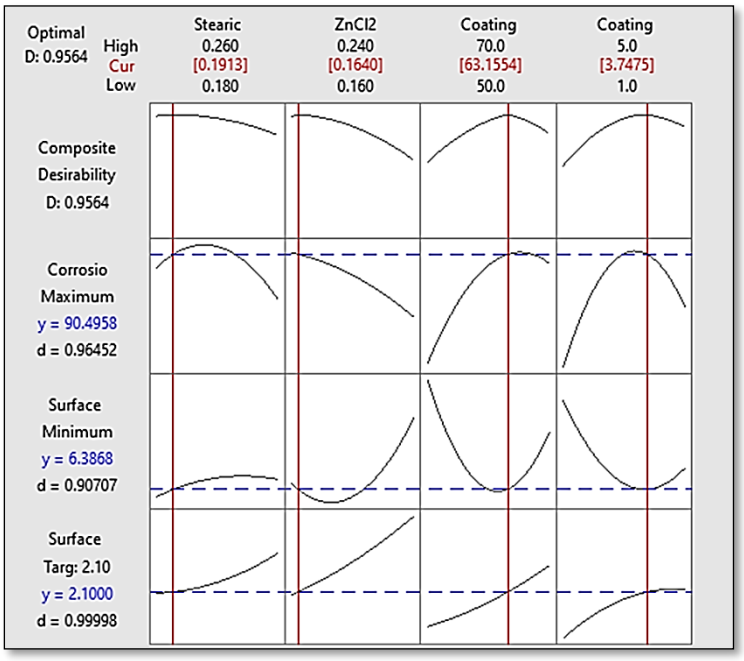

Figure 4.6 Response optimization plot obtained using Response Surface Methodology (RSM), showing the optimization of Stearic acid, $ZnCl_2$, and Coating concentrations for maximizing composite desirability (D), corrosion resistance, and surface characteristics

Table 4.3 Regression coefficient for different response

Regression coefficient (R^2)	Surface Roughness (µm)	Surface free energy (mN/m)	Corrosion resistance efficiency (%)
	90.95	85.68	90.45

Figure 4.6 illustrates the optimal settings of the input variables, such as stearic acid (M), $ZnCl_2$ (M), coating temperature (°C), and coating duration, which are necessary to achieve the desired responses while maximizing the composite desirability. An overall composite desirability (D) of 0.9564 indicates an effective optimization

process, with model predictions closely aligned with the desired outcomes [154]. The desirability functions in the plot visually demonstrate how the optimal parameter settings achieve balance across multiple responses, with red vertical lines indicating the optimal values and blue dashed lines representing the response targets. The curvature of these functions reflects the sensitivity of the responses to parameter variations, thereby underscoring the robustness and effectiveness of the experimental design and response models. Additionally, Table 4.3 presents the regression coefficients, where the regression coefficients (R^2) for the responses Surface Roughness, Surface Free Energy, and Corrosion Resistance Efficiency demonstrate the robustness and predictive accuracy of the model developed from the experimental data. The model demonstrated a strong predictive performance, with R^2 values of 90.95 % for surface roughness, 90.45 % for corrosion resistance efficiency, and 85.68 % for surface free energy. These values indicate that the model reliably explains most of the variability in the experimental data, validating its effectiveness in optimizing the input parameters and achieving targeted outcomes [155,156].

4.2.2.2 Statistical Significance and Model Evaluation Using Analysis of variance

The statistical significance of the developed regression models was comprehensively evaluated using an analysis of variance (ANOVA). For all three responses (surface roughness, surface free energy, and corrosion resistance efficiency), the models exhibited highly significant F-values of 21.82, 13.39, and 20.63, respectively, with corresponding p-values well below 0.05, confirming their robustness and reliability. Furthermore, the coefficients of determination (R^2), reported in Table 4.4, exceeded 85 % for all responses, underscoring the models' strong predictive accuracy. The statistical relevance of individual model terms including linear, quadratic, and interaction effects has been discussed separately for each response in Tables 4.4, 4.5, and 4.6, based on their respective F-values and P-values, offering a detailed insight into the contribution of each parameter[1].

[1] *Note: In the ANOVA tables, DF = Degrees of Freedom, Adj SS = Adjusted Sum of Squares, Adj MS = Adjusted Mean Square (Adj SS/DF), F-Value = Fisher's test statistic, and P-Value = Statistical*

Table 4.4 Analysis of Variance (ANOVA) for surface roughness, showing the significance of different factors on the surface texture

Source	**DF**	**Adj SS**	**Adj MS**	**F-Value**	**P-Value**
Model	14	22.4298	1.60213	21.82	0.000
Linear	4	20.8244	5.20609	70.91	0.000
Stearic acid	1	1.4999	1.49991	20.43	0.000
$ZnCl_2$	1	5.3661	5.36609	73.09	0.000
Coating temperature	1	5.8607	5.86075	79.83	0.000
Coating duration	1	8.0976	8.09763	110.30	0.000
Square	4	0.2789	0.06973	0.95	0.463
Stearic acid × Stearic acid	1	0.0614	0.06138	0.84	0.375
$ZnCl_2$ × $ZnCl_2$	1	0.0274	0.02744	0.37	0.550
Coating temperature × Coating temperature	1	0.0277	0.02771	0.38	0.548
Coating duration × Coating duration	1	0.1563	0.15627	2.13	0.165
2-Way Interaction	6	1.3265	0.22109	3.01	0.039
Stearic acid × $ZnCl_2$	1	0.0146	0.01458	0.20	0.662
Stearic acid × Coating temperature	1	0.1700	0.16995	2.31	0.149
Stearic acid × Coating duration	1	0.2428	0.24280	3.31	0.089
$ZnCl_2$ × Coating temperature	1	0.1121	0.11206	1.53	0.236
$ZnCl_2$ × Coating duration	1	0.3223	0.32234	4.39	0.054
Coating temperature × Coating duration	1	0.4648	0.46478	6.33	0.024
Error	15	1.1012	0.07341		
Pure Error	5	0.0040	0.00079		
Total	29	23.5310			

significance level. Interaction terms represent combined effects of two variables. A P-value less than 0.05 indicates statistical significance

Table 4.5 Analysis of Variance (ANOVA) for surface free energy, highlighting the contribution of various factors to the surface energy characteristics

Source	**DF**	**Adj SS**	**Adj MS**	**F-Value**	**P-Value**
Model	14	23.2502	1.66073	13.39	0.000
Linear	4	3.0532	0.76329	6.15	0.004
Stearic acid	1	0.5698	0.56981	4.59	0.049
$ZnCl_2$	1	1.9749	1.97495	15.92	0.001
Coating temperature	1	0.1597	0.15973	1.29	0.274
Coating duration	1	0.3487	0.34867	2.81	0.114
Square	4	18.3030	4.57576	36.90	0.000
Stearic acid × Stearic acid	1	0.0309	0.03087	0.25	0.625
$ZnCl_2$ × $ZnCl_2$	1	0.5787	0.57869	4.67	0.047
Coating temperature × Coating temperature	1	1.9433	1.94330	15.67	0.001
Coating duration × Coating duration	1	0.6841	0.68411	5.52	0.033
2-Way Interaction	6	1.8940	0.31567	2.55	0.067
Stearic acid × $ZnCl_2$	1	0.4055	0.40555	3.27	0.091
Stearic acid × Coating temperature	1	0.2276	0.22755	1.83	0.196
Stearic acid × Coating duration	1	0.0361	0.03615	0.29	0.597
$ZnCl_2$ × Coating temperature	1	0.2800	0.28003	2.26	0.154
$ZnCl_2$ × Coating duration	1	0.8056	0.80564	6.50	0.022
Coating temperature × Coating duration	1	0.1391	0.13911	1.12	0.306
Error	15	1.8603	0.12402		
Pure Error	5	0.0000	0.00000		
Total	29	25.1105			

ANOVA for Surface Roughness presented in Table 4.4 corroborates the presence of a highly significant model, as evidenced by an F-value of 21.82 and a p-value of 0.000. All linear terms demonstrated high significance (P<0.001), with coating duration (P=0.000) exerting the most substantial influence, followed by the coating temperature, ZnCl2 and Stearic acid. The quadratic terms, however, were collectively

non-significant (P=0.463), suggesting a minimal contribution from the curvature of the response surface. Among the two-way interactions, the interaction between coating temperature and coating duration (P=0.024) was significant, underscoring its effect on Surface Roughness.

ANOVA for Surface Free Energy shown in Table 4.5 indicates a statistically significant overall model, with an F-value of 13.39 and a P-value of 0.000. Among the linear terms, $ZnCl_2$ emerged as the most significant factor (P=0.001), whereas stearic acid demonstrated marginal significance (P=0.049). The quadratic terms collectively exhibited high significance (P=0.000), $ZnCl_2$ (P=0.047), and coating temperature (P=0.001), underscoring their pronounced nonlinear effects. Regarding two-way interactions, the interaction between $ZnCl_2$ and Coating duration was significant (P=0.022), highlighting its impact on the response. Conversely, other interaction terms had p-values exceeding 0.05, indicating weaker effects.

The ANOVA analysis for corrosion resistance efficiency, shown in Table 4.6, revealed a highly significant model with an FFF-value of 20.63 and a PPP-value of 0.000, indicating that the model effectively explains the variance in corrosion resistance. The linear terms (stearic acid, $ZnCl_2$, Coating temperature, and coating duration) showed varying levels of significance, all having PPP-values below 0.05. Notably, $ZnCl_2$ (P=0.003) exhibited the most significant linear contribution. The quadratic terms were highly significant, especially the coating duration (P=0.000), emphasizing the importance of this parameter. Among the two-way interactions, only $ZnCl_2$ × coating temperature (P=0.003) was significant, indicating a significant interaction effect.

Table 4.6 Analysis of Variance (ANOVA) for corrosion resistance efficiency, illustrating the impact of different factors on the corrosion performance

Source	**DF**	**Adj SS**	**Adj MS**	**F-Value**	**P-Value**
Model	14	7959.71	568.55	20.63	0.000
Linear	4	977.27	244.32	8.86	0.001
Stearic acid	1	174.58	174.58	6.33	0.024
$ZnCl_2$	1	347.27	347.27	12.60	0.003
Coating temperature	1	234.45	234.45	8.51	0.011

Coating duration	1	220.97	220.97	8.02	0.013
Square	4	6518.44	1629.61	59.12	0.000
Stearic acid × Stearic acid	1	125.57	125.57	4.56	0.050
$ZnCl_2$ × $ZnCl_2$	1	8.45	8.45	0.31	0.588
Coating temperature × Coating temperature	1	208.71	208.71	7.57	0.015
Coating duration × Coating duration	1	627.79	627.79	22.77	0.000
2-Way Interaction	6	464.01	77.33	2.81	0.049
Stearic acid × $ZnCl_2$	1	9.63	9.63	0.35	0.563
Stearic acid × Coating temperature	1	37.77	37.77	1.37	0.260
Stearic acid × Coating duration	1	0.60	0.60	0.02	0.885
$ZnCl_2$ × Coating temperature	1	355.27	355.27	12.89	0.003
$ZnCl_2$ × Coating duration	1	49.08	49.08	1.78	0.202
Coating temperature × Coating duration	1	11.66	11.66	0.42	0.525
Error	15	413.48	27.57		
Pure Error	5	0.00	0.00		
Total	29	8373.19			

4.2.2.3 Analysis of surface plots

Figure 4.7 depicts three-dimensional surface plots that elucidate the relationship between the response variable, Surface Roughness, and input parameters: Stearic Acid concentration (M), $ZnCl_2$ concentration (M), Coating Temperature (°C), and Coating Duration (hour). The plots indicate that an increase in both Stearic Acid and $ZnCl_2$ concentrations leads to elevated Surface Roughness. Nevertheless, the Surface Roughness value was attained within a moderate range of Stearic Acid concentration (0.20–0.22 M) and a slightly lower range of $ZnCl_2$ concentration (0.16–0.18 M). This observation suggests a synergistic interaction between Stearic Acid and $ZnCl_2$ to achieve the desired surface characteristics.

For the Coating temperature and duration, the surface roughness also increased with higher values of these parameters. A moderate value of surface roughness was attained when the Coating Temperature was in the range of 60–65 °C and the coating duration was approximately 3.5–4 hours. At lower temperatures, the chemical reaction rate is likely to be insufficient, resulting in thin-layer formation. As the temperature increased, the deposition on the substrate intensified, leading to a higher surface roughness. Similarly, increasing the coating duration allows more time for layer buildup, thereby increasing Surface Roughness [157].

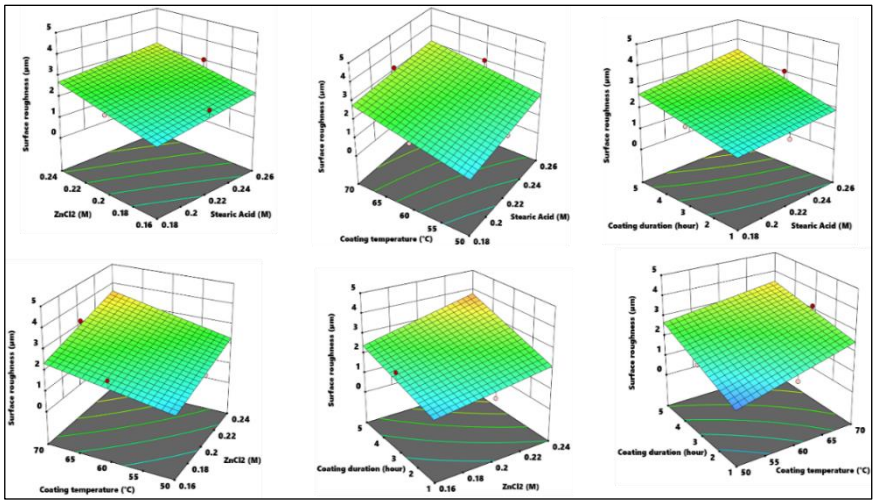

Figure 4.7 Surface plot of Surface roughness with different process parameters

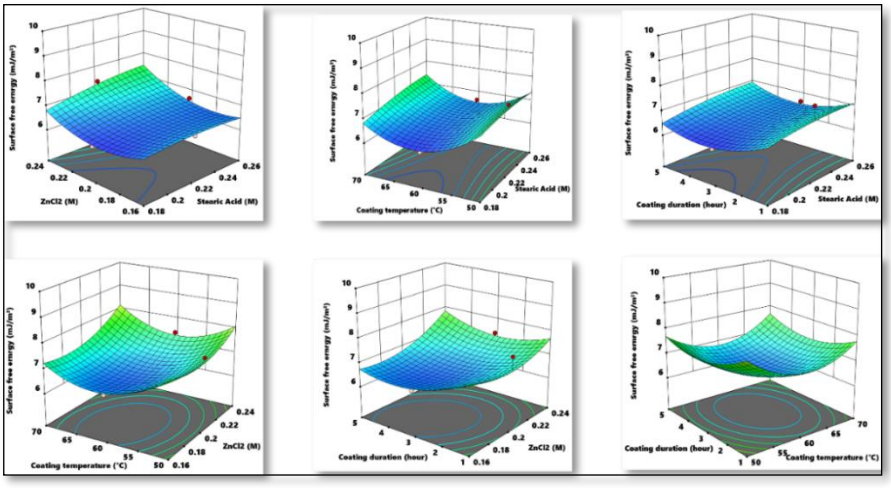

Figure 4.8 Surface plots of Surface free energy with different input parameters

Figure 4.8 shows 3D surface plots illustrating the relationship between the Surface Free Energy (mN/m) and input parameters, with the goal of minimizing the Surface Free Energy. The minimum values are achieved at low Stearic Acid concentrations (0.16–0.18 M), high $ZnCl_2$ concentrations (0.22–0.24 M), moderate Coating temperatures (55–60 °C), and moderate Coating durations (3–4 hours). Higher Stearic acid concentrations and lower $ZnCl_2$ concentrations led to increased surface free energy, while excessively high coating temperatures and long coating durations also caused deviations from the minimum. $ZnCl_2$ concentration and Coating Temperature had the most significant effects, with interactive influences observed between parameters such as $ZnCl_2$ and Coating temperature, Stearic Acid and Coating Duration. These findings highlight the importance of precise parameter optimization to achieve minimal surface free energy.

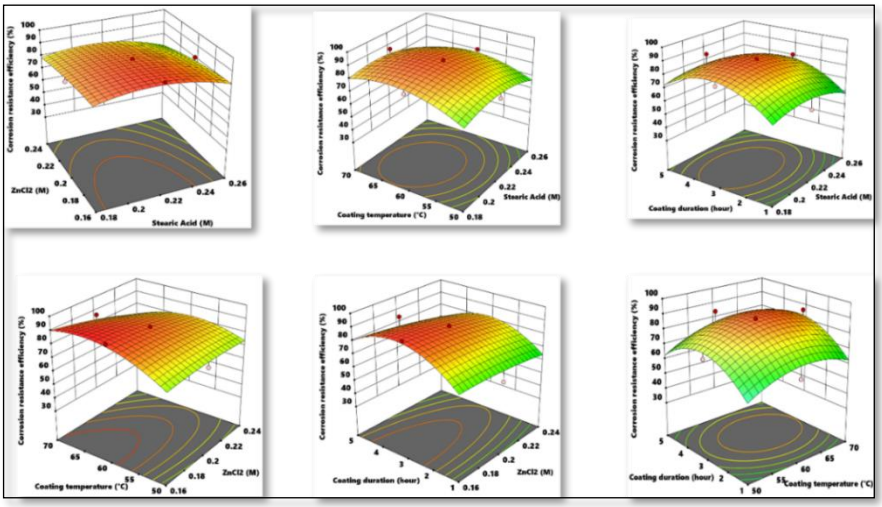

Figure 4.9 surface plots of corrosion resistance efficiency with the different input parameters

Figure 4.9 presents three-dimensional surface plots illustrating the effects of stearic acid concentration, $ZnCl_2$ concentration, coating temperature, and coating duration on the corrosion resistance efficiency, with the objective of maximizing the response. Optimal corrosion resistance is attained at Stearic acid concentrations of 0.22–0.24 M, $ZnCl_2$ concentrations of 0.22–0.24 M, coating temperatures of 60–65 °C, and coating durations of 3.5–4 hours. Elevated concentrations of stearic acid and $ZnCl_2$ significantly enhanced the corrosion resistance, whereas moderate coating

temperatures and durations facilitated uniform and effective layer formation. Deviations from these specified ranges, such as lower concentrations or extreme temperatures, lead to a diminished efficiency. These findings highlight the complexity of the system and emphasize the necessity for the precise control of multiple parameters to achieve the desired coating properties. No single parameter independently ensures the target value, underscoring the importance of collective optimization.

4.2.3 ANN results

Figure 4.10 shows the ANN results, which demonstrate strong performance and reliability in modeling a dataset consisting of input parameters and responses. The Mean Squared Error (MSE) plot shows that the training, validation, and test errors decreased consistently, with the best validation performance (MSE = 0.1) achieved at epoch 3, indicating proper convergence without overfitting. The gradient and Mu values decreased steadily, with the gradient reaching a minimal value of 7.913×10^{-12} and Mu stabilizing at 1×10^{-12} by epoch 6, thereby confirming the stability and effectiveness of the training process. The error histogram reveals a narrow distribution centered around zero, suggesting accurate predictions with minimal deviations, although a few outliers were observed. The regression plots showed high correlation coefficients across the training (R = 0.953), validation (R = 0.936), test (R = 0.969), and overall (R = 0.942) datasets, indicating good predictive accuracy and excellent generalization to unseen data.

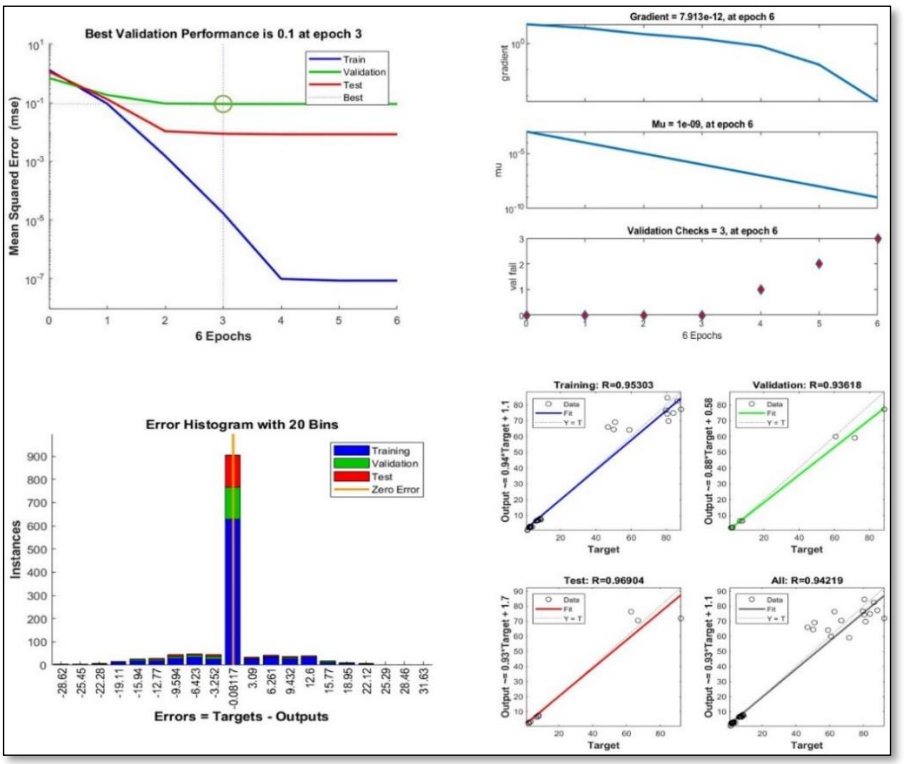

Figure 4.10 ANN results with performance plot, training state plot, error histogram, and regression plot

The results from the ANN after data augmentation demonstrated significant improvements in the model training, validation, and testing performance, as shown in Figure 4.11. The Mean Squared Error (MSE) plot shows consistent reductions across the training, validation, and testing datasets, with the best validation performance (MSE = 0.0168) achieved at epoch 23, highlighting the improved generalization of the model. The gradient decreases to 13.8788, and the Mu stabilizes at 10^{-7}, indicating efficient convergence and stability during training. The error histogram reveals a highly concentrated error distribution around zero with minimal outliers, reflecting improved prediction accuracy. Regression analysis showed near-perfect correlations, with R-values of 0.999 for training, 0.994 for validation, 0.990 for testing, and 0.997 overall, indicating the ANN's enhanced ability to accurately model data. The regression lines aligned closely with the ideal line, further demonstrating the precision of the predictions.

The introduction of data augmentation provided a more diverse dataset, enabling the ANN to better learn, generalize, and achieve superior performance metrics. Consequently, the overall value of R increased from 0.942 to 0.997, indicating its high accuracy in capturing the complex nonlinear relationships between the input process parameters and output responses. This strong correlation between the predicted and actual values underscores the excellent generalization ability of the model across unseen datasets, reinforcing its reliability as a surrogate model for multi-objective optimization. The error histograms presented for both the ANN and ANN with data augmentation models in Figures 4.10 and 4.11, respectively, display distributions tightly centered around zero, reflecting strong predictive accuracy across the training, validation, and test datasets. Nevertheless, a small number of outliers were observed in both the cases. These deviations are likely due to sparsity or noise within the experimental dataset, particularly in regions of the input space that were underrepresented during training [158,159]. In the baseline ANN model, although most prediction errors were clustered near zero, several extreme values ranging from −22.28 to +22.12 were recorded. In contrast, the ANN model enhanced with data augmentation exhibited a significantly reduced error range from −0.8517 to +1.12, with a denser concentration of instances near the zero-error line. This notable reduction in outlier magnitude indicates that the augmented dataset improved the model's ability to learn from a broader range of input variations, enhancing generalization and reducing sensitivity to rare or noisy cases. The presence of a few outliers did not compromise the reliability of the ANN model, as most prediction errors were tightly clustered around zero, demonstrating strong generalization across datasets. Additionally, high R^2 values and low mean squared errors confirmed the accuracy of the model, making the outliers negligible for practical engineering applications. Collectively, the high R^2 value not only attests to the robustness, stability, and accuracy of the ANN model, but also underscores its strong predictive capability in capturing complex relationships and intricate output behaviors across diverse experimental conditions. This ensures that the ANN model can reliably guide the optimization process, offering precise predictions that are critical for enhancing the performance of optimization algorithms (NSGA-II, TLBO, and MOPSO), as

demonstrated later in the manuscript. The high R^2 value plays a pivotal role in ensuring that these optimization algorithms converge towards optimal solutions, ultimately leading to improved outcomes in advanced coating applications [160,161].

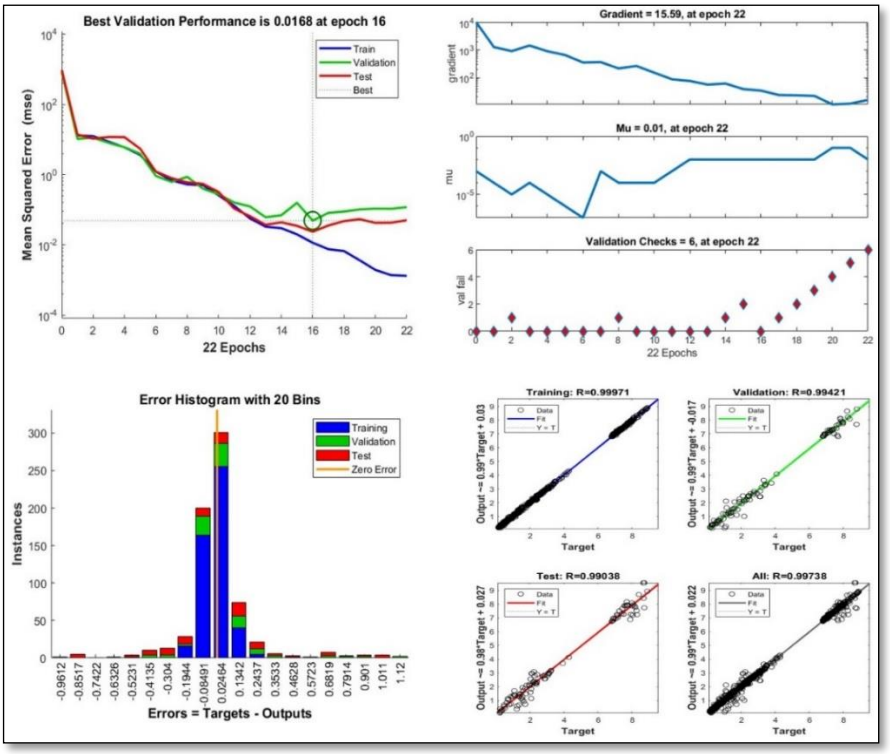

Figure 4.11 ANN results after data augmentations with performance plots, training state plots, error histograms, and regression plot

4.2.4 NSGA II results

After training, NSGA-II was applied to generate a Pareto-optimal front, as shown in Figure 4.12, effectively capturing a diverse set of trade-offs between the three response variables: corrosion resistance efficiency (%), surface free energy (mN/m), and surface roughness (µm). The non-dominated solutions from the final generation were used to construct the diverse Pareto front, effectively capturing the compromise between the three-performance metrics. From the plot, the observed ranges are approximately 0.5 µm to 4.5 µm for surface roughness, 6 mN/m to 9 mN/m for surface free energy, and 20 % to 90 % for corrosion resistance efficiency. Owing to the three-dimensional nature of the plot, it is difficult to accurately interpret the relationships when viewed only in two dimensions. For instance, while the corrosion

resistance efficiency may appear to peak near 70 % in the 2D view, the actual maximum approaches 90 % when viewed in full 3D. Therefore, the resulting Pareto front exhibits a broad solution space, meaning that multiple optimal configurations exist where varying degrees of corrosion resistance efficiency can be achieved, depending on the specific combination of surface free energy and surface roughness. The shaded Pareto region in the figure illustrates the tradeoff space, showing a wide range of feasible solutions from which, an optimal compromise can be selected based on specific application requirements. The diverse Pareto front observed in this study is also consistent with the findings reported by Siegmund and Deb [162], further validating the robustness of the multi-objective optimization approach used in this study.

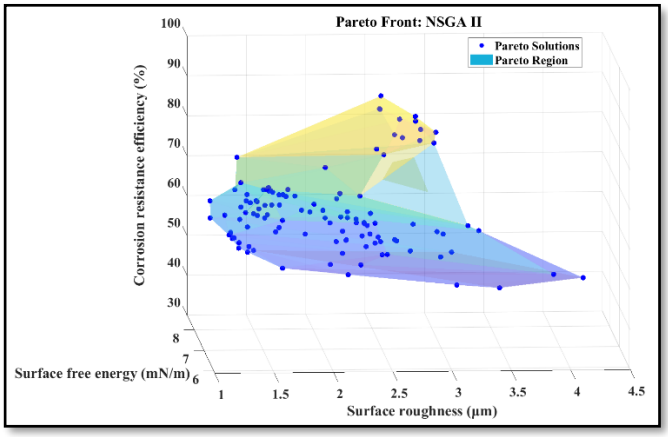

Figure 4.12 Diverse Pareto front achieved by NSGA-II, illustrating the trade-offs between multiple objectives in the optimization process

4.2.5 Refine with TLBO, and MOPSO and compare with the experimental and prediction results

In this study, TLBO and MOPSO were employed as second-stage refinement algorithms within a two-step hybrid optimization framework. The first stage utilized NSGA-II to explore the broader solution space and generate an initial diverse Pareto front (as shown in Figure 4.12). Its underlying mechanisms such as non-dominated sorting and crowding distance are designed to effectively explore trade-offs among conflicting objectives, thereby ensuring comprehensive coverage of the Pareto front, as described by Equation 4.4 [162]. The solutions produced by NSGA-II, along with

their corresponding decision variables, were then passed as inputs to TLBO and MOPSO. To enhance the local search capability during this stage, Gaussian data augmentation was reintroduced, allowing the dataset to be densified while remaining within established bounds. Now, TLBO operates through a deterministic teacher-student learning mechanism, where the population is iteratively adjusted based on the influence of the best-performing solution (the "teacher") and the mean performance of the group. As described in Equation 4.5 this approach facilitates effective local exploitation and precise fine-tuning of the candidate solutions. By contrast, MOPSO employs a swarm intelligence-based strategy, where solutions are updated through social learning and guided by both individual and global historical bests, as represented in Equation 4.6. In terms of the objective distribution, the initial Pareto front generated by the NSGA-II (Figure 4.9) spans a broad range of feasible solutions. Specifically, surface roughness varies from approximately 1.0 to 4.5 μm, surface free energy ranges from 6.0 to 8.0 mN/m, and corrosion resistance efficiency extends from 30% to 95%. In contrast, the refined Pareto fronts obtained using the TLBO and MOPSO algorithms (Figures 4.13 and 4.14) demonstrate more concentrated solution clusters. These refined results typically fall within narrower ranges: 1.5 to 2.5 μm for surface roughness, 6.0 to 7.5 mN/m for surface free energy, and 50% to 95% for corrosion resistance efficiency. This outcome demonstrates the improved convergence and local refinement achieved through second-stage optimization. The initial diversification of the Pareto front by NSGA-II, followed by its refinement through MOPSO, is consistent with the hybrid optimization strategy reported in earlier studies by Hu et al. [163].

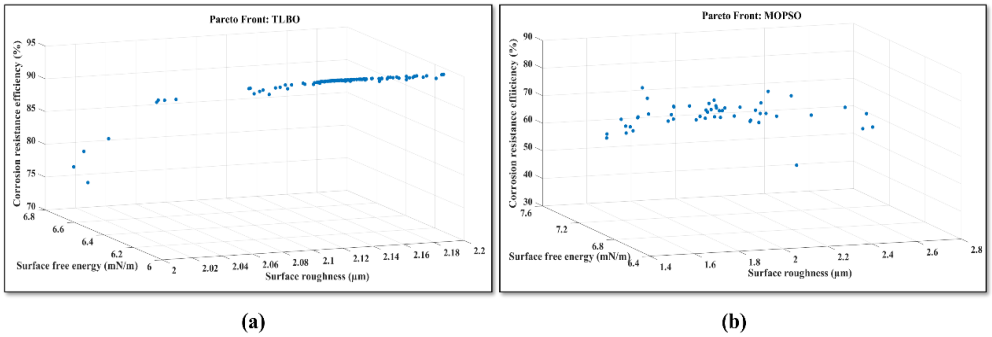

(a) (b)

Figure 4.13 Refined Pareto front: (a) TLBO optimization and (b) MOPSO optimization, demonstrating improved convergence and solution refinement compared to the initial Pareto front

The convergence plots clearly illustrate the differing optimization behaviors of TLBO and MOPSO. TLBO exhibits a smooth and stable convergence path, underscoring its robustness and efficiency in driving solutions toward the optimal regions. However, its deterministic nature can lead to premature convergence, particularly in complex or multimodal search landscapes, as noted by Fatehi et al. and Dong et al. [143,164]. In contrast, MOPSO demonstrates a more irregular and scattered convergence trend, which is a characteristic of its stochastic search strategy. This randomness, while less stable, enhances its ability to escape local optima, making it particularly effective in tackling multi-objective problems with rugged or highly nonlinear fitness landscapes, as discussed by Z et al. and Xu et al. [165,166]. Importantly, these convergence characteristics align with the distribution patterns observed in their respective refined Pareto fronts, thereby reinforcing the consistency and reliability of their optimization behaviors.

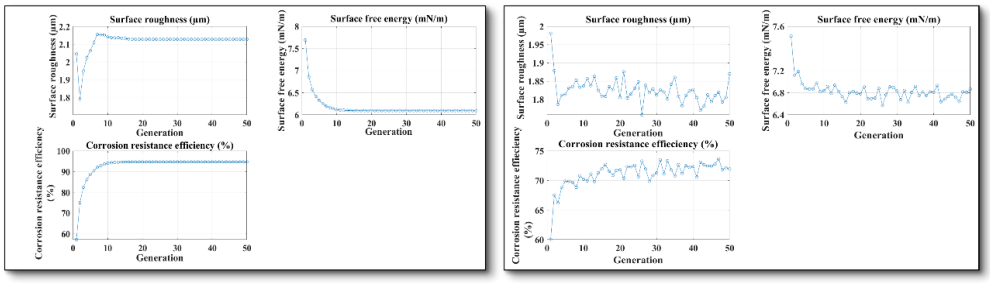

(a) (b)

Figure 4.14 Individual response convergence plot: (a) TLBO and (b) MOPSO, showing the progression of convergence for each optimization method across the responses

The best optimal solution after further refinement by TLBO and MOPSO was achieved using a compromise-based decision-making method. The non-dominated solutions of pareto front were then normalized on a scale of 0 to 1 utilizing the below mathematical Equation 4.18 and 4.19 [167],

$$Normalized\ Value = \frac{X - X_{min}}{X_{max} - X_{min}} \tag{4.18}$$

Where higher values are better.

$$Normalized\ Value = \frac{X_{max} - X}{X_{max} - X_{min}} \tag{4.19}$$

Where lower values are better.

The normalized values across all the objectives were summed. This summation provided a composite score that represented the overall performance of a solution relative to the ideal. The solution with the smallest total sum is selected as the final optimal choice, because it reflects the closest proximity to the ideal point in the normalized objective space. This approach implicitly assigns equal importance to all objectives, ensuring a balanced trade-off without bias toward any single criterion. It offers a straightforward yet effective means of identifying a well-compromised Pareto-optimal solution [168,169].

The performances of the three optimization algorithms, TLBO, MOPSO, and CCD, were evaluated by comparing the predicted and actual values of three response variables: surface roughness, surface free energy, and corrosion resistance efficiency. The comparison is illustrated in Figure 4.15, and the percentage deviations between the actual and predicted values are summarized in Table 4.7. For the surface roughness, TLBO demonstrated the highest prediction accuracy with a minimal deviation of 7.73 %, whereas CCD showed a significant overestimation, resulting in the highest deviation of 22.09 % among the three. MOPSO also performed reasonably well in this category but was slightly less accurate than TLBO. In contrast, the surface free energy was most accurately predicted by MOPSO, showing the lowest deviation of 6.27 %, followed by TLBO (6.96 %). The CCD showed a slightly higher deviation of 8.32 %, indicating moderate prediction reliability. Regarding the corrosion resistance efficiency, MOPSO again outperformed the other algorithms with the lowest deviation

of 11.46 %, while TLBO and CCD exhibited larger discrepancies of 18.84 % and 21.53 %, respectively. Notably, the CCD tended to significantly overpredict the corrosion resistance, whereas MOPSO was slightly underpredicted but remained closer to the actual value.

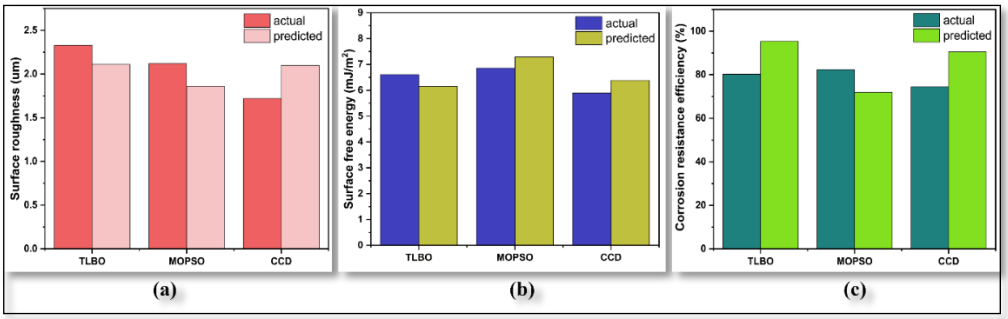

Figure 4.15 Comparison between actual and predicted values for TLBO, MOPSO, and CCD methods across key performance indicators: (a) Surface roughness (μm), (b) Surface free energy (mN/m), and (c) Corrosion resistance efficiency (%)

When evaluating the overall predictive performance, the average deviation across all three responses was the lowest for MOPSO (9.99 %), followed by TLBO (11.18 %), and CCD (17.31 %). This indicates that the MOPSO offers the most balanced and robust prediction capability across multiple performance metrics.

Table 4.7 Comparison of predicted responses from different algorithms, including TLBO, MOPSO, and CCD, highlighting the accuracy of predictions for the responses

Response	Deviation (%)		
	TLBO	MOPSO	CCD
Surface Roughness	7.73	12.26	22.09
Surface Free Energy	6.96	6.27	8.32
Corrosion Resistance Eff.	18.84	11.46	21.53
Average Deviation	11.18	9.99	17.31

In summary, while each algorithm exhibits strengths in specific response predictions, MOPSO provides the best overall prediction accuracy and consistency, making it the most suitable optimization technique for this multi-objective coating performance analysis.

4.2.6 Sensitivity analysis

The sensitivity analysis results from TLBO, as depicted in Figure 4.16, and MOPSO, as shown in Figure 4.17, revealed substantial differences in the influence of the input parameters on the output responses. In the Local Sensitivity Analysis, TLBO indicated that stearic acid significantly enhanced the corrosion resistance performance (+124.3), but diminished the surface roughness and surface free energy. Conversely, $ZnCl_2$ negatively impacted the corrosion resistance while exerting a moderate positive effect on the surface roughness. The coating temperature and duration exhibited a minimal local influence. In contrast, MOPSO demonstrates more pronounced local sensitivities, particularly concerning corrosion resistance, where $ZnCl_2$ exerts a highly negative effect (-1540) and stearic acid has a strong positive effect (+810.6), indicating a more volatile and steep input-output relationship.

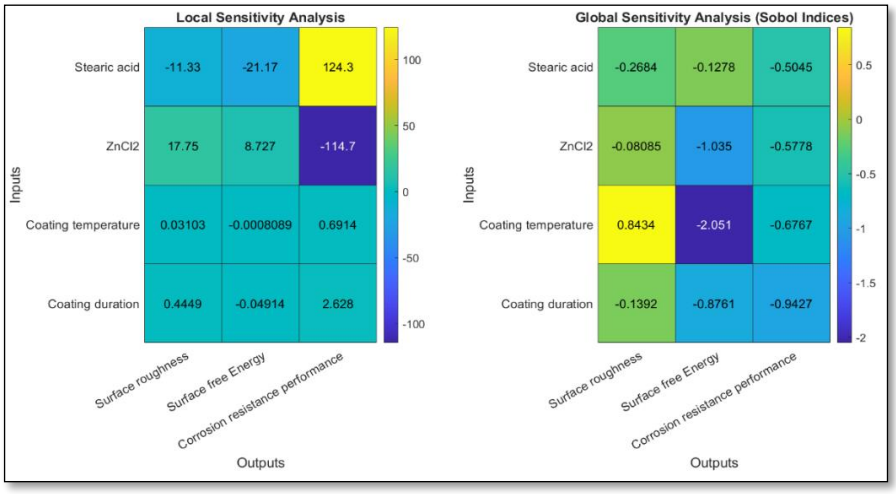

Figure 4.16 Sensitivity analysis of the optimization results using the TLBO algorithm, showing the impact of various parameters on the objective functions

The Global Sensitivity Analysis utilizing Sobol indices further highlights these distinctions. The Teaching-Learning-Based Optimization (TLBO) method identifies coating temperature as the most significant factor influencing surface roughness, with a Sobol index of 0.8434, and coating duration as the primary factor that adversely affects corrosion resistance, with a Sobol index of -0.9427. These pronounced global sensitivities suggest that TLBO reveals a more structured and interpretable optimization landscape dominated by a few critical parameters. Conversely, the multi-

objective particle swarm optimization (MOPSO) method exhibits global sensitivity indices that are notably lower and more evenly distributed across inputs, with the coating duration demonstrating the highest, albeit modest, influence on the surface roughness at 0.1538. This pattern is consistent with MOPSO's stochastic nature of MOPSO, indicating a broader but less sharply defined exploration of the input space [170]. Overall, TLBO appears to be more effective in isolating dominant factors for targeted optimization, whereas MOPSO offers a more balanced sensitivity profile, potentially mitigating overfitting and enhancing generalization in complex multiobjective problems.

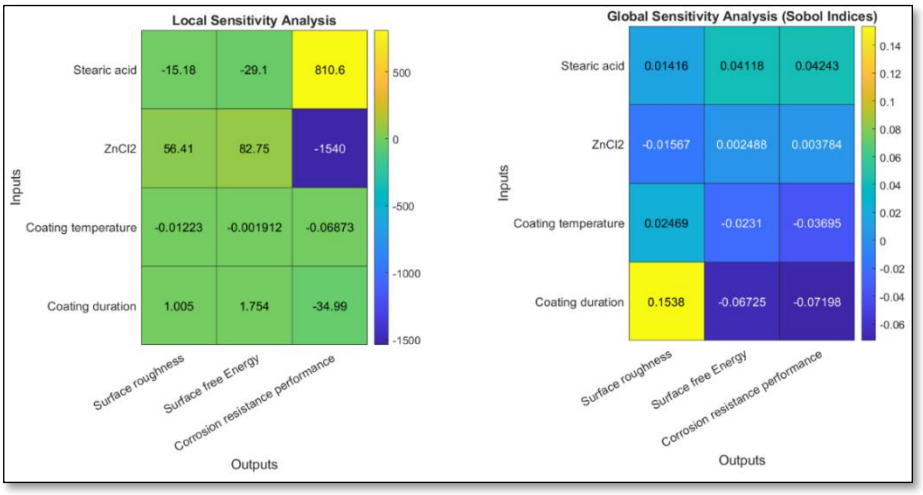

Figure 4.17 Sensitivity analysis of the optimization results using the MOPSO algorithm, illustrating the influence of different parameters on the objective functions

4.2.7 Analysis of Coating Characterizations

4.2.7.1 Wettability and Contact Angle

Figure 4.18 shows both the coated surface under the optimized parameters and the uncoated surface of the bare Mg alloy. A uniform white layer is formed on the substrate surface. Contact angle is a critical parameter for assessing the hydrophobicity and wettability of a surface. A contact angle (CA) less than 90° indicates a hydrophilic surface, whereas a CA greater than 90° indicates a hydrophobic surface [171]. However, a surface cannot be classified as superhydrophobic unless the contact angle exceeds 150° [172]. As shown in Figure 4.19, a contact angle of 152 °±1° was achieved. The contact angle of the base Mg alloy is 47°±3°. Consequently, the coating

has transformed the Mg alloy surface into a superhydrophobic one. Goniometer report of contact angle measurement has been provided in APPENDICES section under subsection A.3.

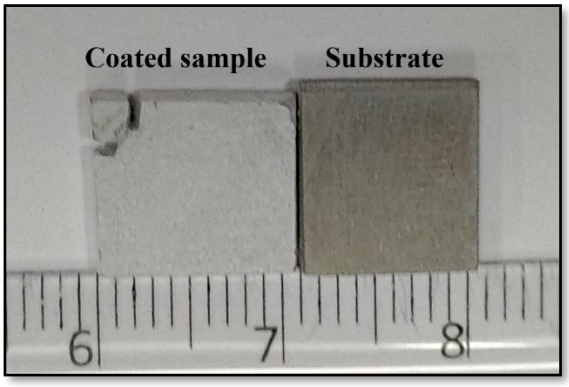

Figure 4.18 Digital images of magnesium alloy samples: (a) after superhydrophobic coating, displaying a uniformly white surface indicating the formation of Zn/Mg-stearate layer; (b) before coating, showing the bare metallic surface

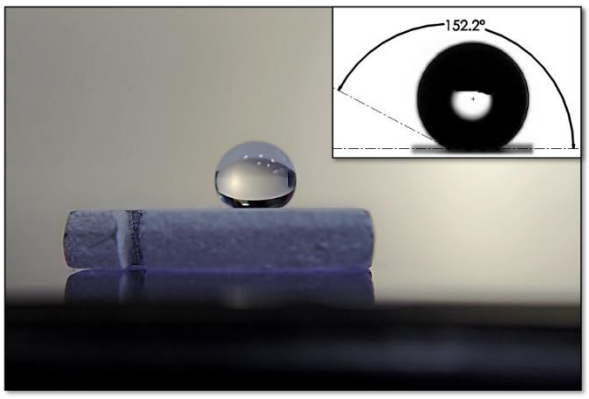

Figure 4.19 Water droplet on the coated Mg alloy surface showing super hydrophobicity. Inset: Goniometer measurement confirms a contact angle of 152.2°

4.2.7.2 Surface morphology of base and coated samples

Figure 4.20 (a) and (b) depict the SEM images of the base and coated surfaces, respectively. It is evident that the polished surface of the base Mg alloy developed a uniform nanopetal-like structure. This structural formation leads to a significant increase in the surface roughness [173]. A similar profile is observed in Figure 4.21, which presents the 3D profilometer data illustrating the variation in surface roughness. The surface roughness of the coated sample was markedly increased. The surface

roughness parameters Sa, Sq, and Sz of the base sample are 0.19, 0.27, and 7.58, respectively. In contrast, for the coated sample, the values of Sa, Sq, and Sz were 3.51 µm, 4.23 µm, and 36.78 µm, respectively. These changes in surface morphology and microstructure result in the surface acquiring hydrophobic properties [174].

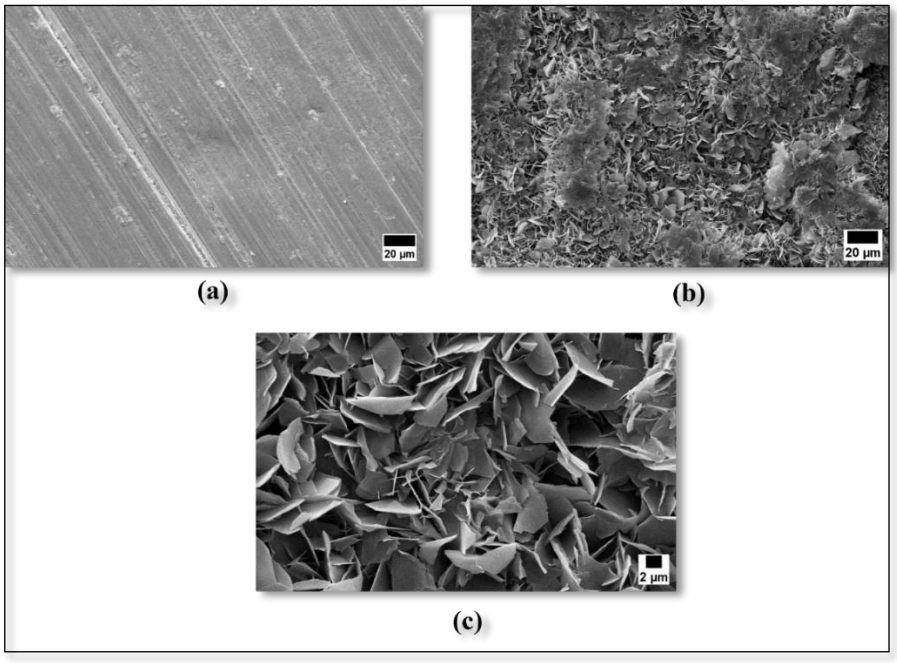

Figure 4.20 Surface morphology of (a) Bare polished Mg alloy showing linear grinding marks; (b) Coated surface at low magnification showing rough and hierarchical morphology; (c) High-magnification SEM image revealing densely packed, micro/nano flake-like structures

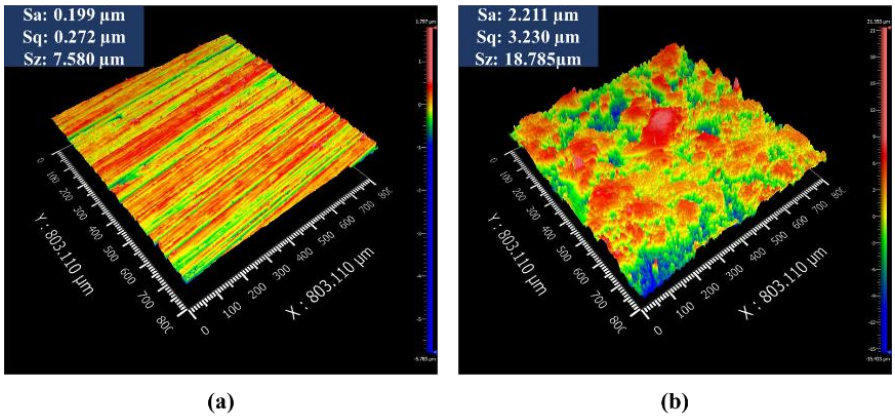

Figure 4.21 3D surface profilometry images showing surface roughness topography of (a) uncoated substrate Mg alloy and (b) coated Mg alloy. Clear contrast in surface morphology demonstrates the formation of micro/nano hierarchical structures post-coating

4.2.7.3 Analysis of Phase, Elemental Composition, and Functional Groups

Figure 4.22 illustrates the X-ray diffraction (XRD) phase angles of the Mg phase in the Mg alloy substrate, observed at 32.61°, 34.85°, 36.66°, 48.15°, 57.59°, 63.46°, 69.32°, and 70.43°, respectively [175]. Notably, the intensities of these peaks varied between those of the base and coated samples. Furthermore, the coated sample exhibits additional peaks, including those of $Mg(OH)_2$ at 27.88° and 40.02°. The peaks at 13.23° and 30.127° indicated the presence of a complex compound phase, $Mg_2Cl(OH)_3$, formed by magnesium and zinc chloride. Additionally, the peaks at 43.863° and 52.86° indicated the presence of a Zn phase [176].

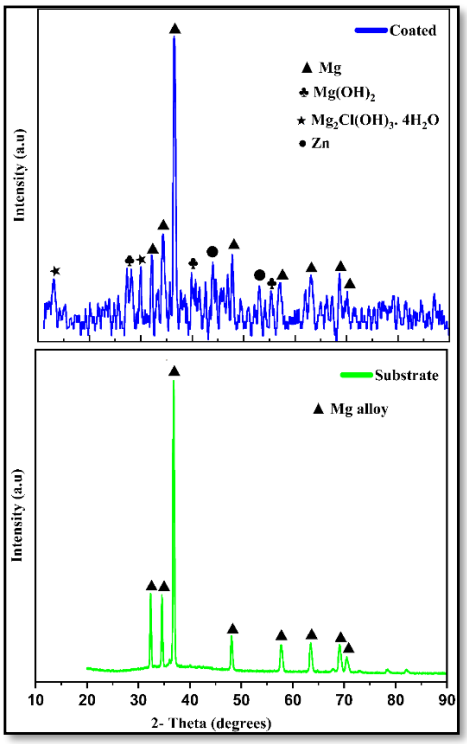

Figure 4.22 X-ray Diffraction (XRD) patterns of (a) bare Mg alloy (base) and (b) Zn stearate-coated Mg alloy, showing phase composition and crystallinity of the samples

Figure 4.23 presents the Energy Dispersive Spectroscopy (EDS) spectra for both the (a) base Mg alloy and (b) coated samples. The EDS spectrum of the base alloy, depicted in Figure 4.20 (a), confirms a predominant magnesium content (90.9 %), accompanied by minor quantities of aluminum (3.7 %), zinc (2.9 %), and manganese (0.7%). Conversely, the spectrum of the coated sample, shown in Figure 4.20 (b),

exhibited pronounced additional peaks for carbon (81.2 %) and oxygen (11.4 %), along with the presence of chlorine (1.6 %) and zinc (2.9 %), while the magnesium signal was significantly reduced to 1.3 %. This marked increase in C, O, and Cl contents, coupled with the diminished Mg signal, substantiates the successful formation of an organic-inorganic coating layer on the Mg alloy surface, indicating effective surface modification through the application of stearic acid and $ZnCl_2$ treatment.

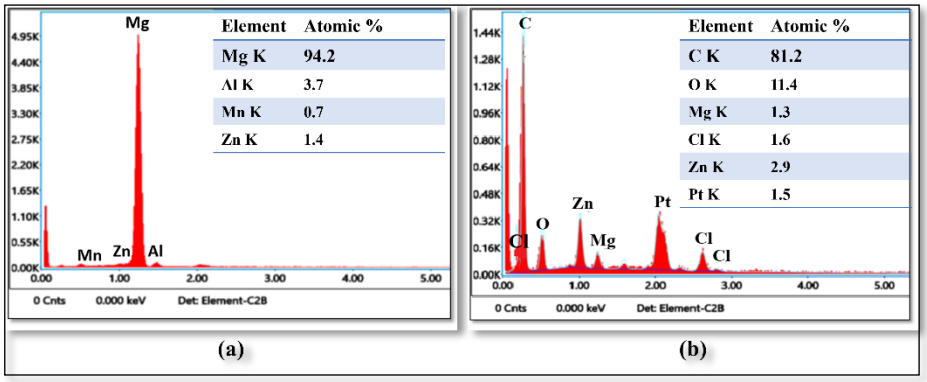

Figure 4.23 Energy Dispersive X-ray Spectroscopy (EDS) spectra of (a) bare Mg alloy and (b) Zn stearate-coated Mg alloy, illustrating the elemental composition and distribution of key elements

Figure 4.24 (a) shows the FTIR spectra of the base and coated samples, where, at 2355 cm^{-1}, the CO_2 group is basically for atmospheric carbon. In the energy bands at 1395 cm^{-1}, $–CH_3$, 1459 $–CH_2$, 1535.80 –COO, 2841, and 2917 –CH groups were present, suggesting the formation of a compound from stearic acid ($C_{18}H_{36}O_2$), magnesium, and zinc chloride [177]. A vibrational band ranging from 3545 cm^{-1} to 3876 cm^{-1} was observed for both the base and coated samples. This indicated the presence of moisture ($–OH_2$) on the surface of the sample.

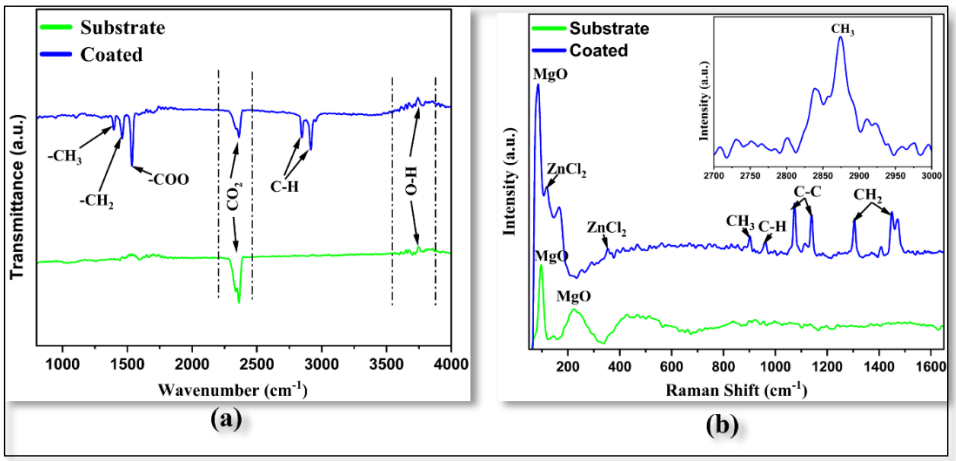

Figure 4.24 (a) Fourier Transform Infrared (FTIR) spectra of bare and coated Mg alloy, highlighting the functional groups and bonding characteristics. (b) Raman spectra of bare and coated Mg alloy, revealing insights into the chemical bonding of the samples

Figure 4.24 (b) represents the Raman spectra of the base and coated samples. For the base sample, two prominent peaks for MgO were observed at 95 cm^{-1} and 219 cm^{-1}, whereas for the coated sample, one prominent peak at 85 cm^{-1} for MgO was observed [178]. The presence of $ZnCl_2$ was observed at approximately 118 and 349 cm^{-1} [179]. The CH_3 group can be found at two positions: one is at 901 cm^{-1} and the other is in the higher band zone at 2874 cm^{-1}. The C–C bond was observed at 1076 cm^{-1} and 1138 cm^{-1}. The peak at 962 cm^{-1} shows the presence of a C–H group. The two peaks near 1304 cm^{-1} and 1449 cm^{-1} indicate the presence of the $–CH_2$ group [180]. Thus, these Raman peaks aligned with the FTIR results. All these bonds indicate the composition of the base material and prove the formation of the expected complex compound during the coating process.

4.2.7.4 Reaction mechanism

The development of superhydrophobic surfaces on Mg alloys involves a sequence of surface reactions, as supported by both experimental results and the existing literature [176,181].

Reactions corresponding to Equations 4.20 and 4.21 lead to the formation of $Zn(OH)_2$ and ZnO in the reactions with water, which precipitate and grow as nanostructured crystallites on the alloy surface.

$$ZnCl_2 + 2H_2O \leftrightarrow Zn(OH)_2 + 2H^+ + 2Cl^- \quad (4.20)$$

$$ZnCl_2 + H_2O \leftrightarrow ZnO + 2H^+ + 2Cl^- \quad (4.21)$$

Simultaneously, the generation of HCl acidifies the local environment, accelerating the corrosion of the magnesium substrate and promoting the formation of a micro/nanostructured hierarchical surface, which is an essential condition for achieving superhydrophobicity. Under these acidic conditions, Mg undergoes spontaneous redox reactions: metallic Mg reacts with H^+ ions generated during $ZnCl_2$ hydrolysis, releasing Mg^{2+} and hydrogen gas. Additionally, Mg reacts directly with water to form a porous $Mg(OH)_2$ layer and further evolves into H_2, as shown in Equations 4.22 and 4.23.

$$Mg + 2H^+ \rightarrow Mg^{2+} + H_2 \quad (4.22)$$

$$Mg + 2H_2O \rightarrow Mg(OH)_2 \quad (4.23)$$

In the same acidic environment, ZnO can also dissolve by reacting with H^+ to regenerate Zn^{2+}, as shown in the Equation 25.

$$ZnO + 2H^+ \rightarrow Zn^{2+} + H_2O \quad (4.24)$$

Furthermore, interactions among Mg^{2+}, Cl^-, and OH^- ions can result in the formation of complex salts such as $Mg_2Cl(OH)_3$, as described in Equation 26 and confirmed by XRD analysis.

$$3Mg(OH)_2 + Mg^{2+}2Cl^- \rightarrow 2Mg_2Cl(OH)_3 \quad (4.25)$$

The formation of the Zn/Mg-stearate-based coating was primarily governed by ionic interactions between divalent metal cations (Zn^{2+} and Mg^{2+}) and the carboxylate groups of stearic acid. Upon the dropwise addition of $ZnCl_2$ into the stearic acid–ethanol solution, Zn^{2+} ions promptly react with stearate anions ($CH_3(CH_2)_{16}COO^-$) to form zinc stearate, a low-solubility metal soap that precipitates out and deposits as a uniform hydrophobic layer. This morphology is clearly observed in the SEM microstructure in Figure 16. During the coating process, both the zinc and magnesium stearates contributed to the formation of the final surface layer. Upon dropwise addition of $ZnCl_2$ to the stearic acid–ethanol solution, Zn^{2+} ions readily react with

stearate anions to form zinc stearate, which precipitates as a dense, hydrophobic layer. Simultaneously, a limited amount of Mg^{2+} ions are released from the substrate due to the mildly acidic environment created by $ZnCl_2$ hydrolysis. These Mg^{2+} ions can also interact with stearate anions to form magnesium stearate. However, because Zn^{2+} is present at higher concentrations in the reaction medium and has a higher affinity for stearate, the resulting coating consists predominantly of zinc stearate with only a minor contribution from magnesium stearate. The two components are believed to either co-deposit or sequentially form a composite metal–organic layer on the magnesium surface, as illustrated in Equations 4.26 and 4.27.

$$Zn^{2+} + 2CH_3(CH_2)_{16}COOH \rightarrow Zn[CH_3(CH_2)_{16}COO]_2 + 2H^+ \quad (4.26)$$

$$Mg^{2+} + 2CH_3(CH_2)_{16}COOH \rightarrow Mg[CH_3(CH_2)_{16}COO]_2 + 2H^+ \quad (4.27)$$

During the entire reaction process, ethanol serves dual and essential functions. First, it acts as a solubilizing agent, effectively dissolving stearic acid, which is otherwise poorly soluble in water. This is made possible due to ethanol's low surface energy and amphiphilic nature, allowing it to interact with both the hydrophilic carboxylic head and hydrophobic hydrocarbon tail of the fatty acid, resulting in a stable and uniform solution [182]. Second, ethanol functions as a homogeneous reaction medium, ensuring uniform mixing and facilitating efficient ionic interactions between the Zn^{2+}, Mg^{2+}, and stearate anions. This promotes consistent nucleation and deposition of the hydrophobic layer across the etched Mg surface, leading to the formation of a uniform and effective superhydrophobic coating [181].

The remarkable chemical stability of this layer arises from two primary factors: (1) robust ionic interactions between the metal cations and carboxylate groups, which create a tightly bound network, and (2) the presence of long hydrophobic alkyl chains (from stearate), which act as barriers that hinder the penetration of water molecules. These combined effects minimize water ingress and protect the interface from degradation [183,184]. Zinc stearate further contributes by offering superior chemical and thermal inertness, reinforcing the integrity of the coating against aggressive electrolytic environments. Moreover, Zn^{2+} itself offers intrinsic corrosion-inhibiting properties, enhancing the passive protection mechanism [185,186]. Together, the

Zn/Mg-stearate composite forms a chemically robust and hydrophobic barrier that reduces the surface energy and corrosion kinetics via both physical shielding and sacrificial protection. The successful formation and chemical stability of these compounds are corroborated by FTIR and Raman spectroscopy, which display characteristic COO^- stretching and metal-oxygen bonding features [187].

Based on the observed reactions, it can be concluded that the significant by-products, including zinc stearates, magnesium stearates, $Mg(OH)_2$ and $Mg_2Cl(OH)_3$ are not toxic to the environment or the human body. The biocompatibility of the sample, which includes these by-products, has been analysed using the MTT and live-dead cell assays, as discussed in subsequent sections.

4.2.8 Assessment of electrochemical properties

Figure 4.25 illustrates the electrochemical behavior of bare and coated magnesium alloy samples in simulated body fluid (SBF), as assessed by potentiodynamic polarization and electrochemical impedance spectroscopy (EIS). The corrosion current density I_{corr} was determined via Tafel extrapolation from the polarization curves shown in Figure 4.25 (a). This method involves fitting the linear portions of the anodic and cathodic branches and identifying the intersection point from which the corrosion potential E_{corr} and I_{corr} values were obtained [155]. It can be shown from the Table 4.8 the coated sample exhibited a significant enhancement in corrosion protection, as evidenced by a positive shift in E_{corr} (from –1.409 V to –0.833 V) and a tenfold reduction in I_{corr} (from 83.49 µA/cm² to 8.03 µA/cm²). This corresponds to a reduction in corrosion rate from 2.874 mm/year to just 0.180 mm/year.

The Nyquist plots obtained from Electrochemical Impedance Spectroscopy (EIS), as shown in Figure 4.25 (b), illustrate the electrochemical behavior of both the uncoated substrate and the coated magnesium alloy. These plots were fitted using EIS analyzer software based on the equivalent electrical circuit illustrated in Figure 4.25 (c). In this circuit, R_1 denotes the solution resistance of the electrolyte, R_2 corresponds to the resistance of the surface coating or passive film, and R_3 represents the charge transfer

resistance at the electrolyte–substrate interface [188]. The circuit also includes two constant phase elements, CPE_1 and CPE_2, which capture the non-ideal capacitive behavior associated with interfacial effects. The n-values for these CPEs, ranging from 0 to 1, indicate the degree of deviation from ideal capacitive behavior, where values approaching 1 suggest more ideal behavior and better electrochemical stability. The p-value reflects the admittance of the non-ideal capacitive element [189]. The Nyquist plot shows two distinct semicircular arcs: the high-frequency semicircle corresponds to the double-layer capacitance and charge transfer resistance, while the low-frequency semicircle is associated with the film properties of the coating. From Table 4.9 it is also notable that the coated sample exhibited significantly higher R_2 and R_3 values compared to the uncoated alloy, signifying an enhanced barrier effect and reduced electrochemical reactivity. Additionally, the increase in n-values for the coated sample suggests a more homogeneous and ideal capacitive interface. Collectively, the elevated polarization resistance and reduced corrosion current density underscore the effectiveness of the superhydrophobic Zn–stearate and Mg–stearate composite layers, confirming their role as dual-barrier systems that provide both physical obstruction to electrolyte ingress and chemical passivation for corrosion inhibition.

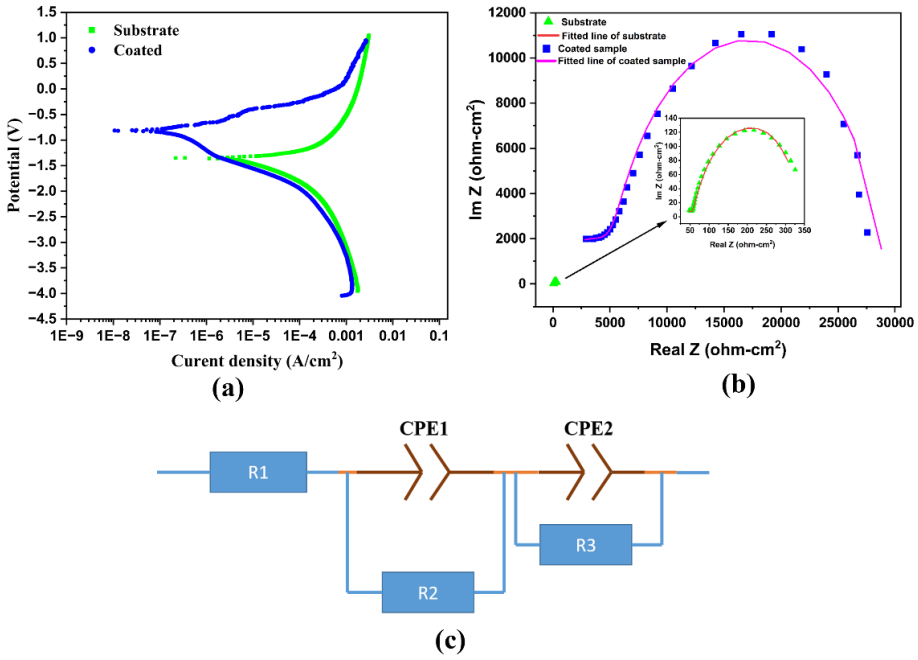

Figure 4.25 Electrochemical characterization of the coated and uncoated Mg alloys: (a) Potentiodynamic polarization curves for substrate and coated samples. (b) Nyquist plot from EIS showing impedance data with fitted curves. (c) Equivalent circuit model with R1, R2, and R3 representing solution resistance, coating resistance, and charge transfer resistance, respectively

Table 4.8 Corrosion parameters for the coated and uncoated Mg alloy samples, including corrosion current density (I_{corr}), corrosion potential (E_{corr}), and corrosion rate

Sample	E_{corr} (V)	I_{corr} (uA/cm^2)	Corrosion rate (mm/year)
Substrate	-1.409	83.49	2.874
Coated	-0.833	8.027	0.180

Table 4.9 EIS parameters, including R1, R2, R3, and constant phase elements (CPE n, CPE p), for both substrate and coated samples

Sample	R1	R2	R3	CPE 1		CPE 2	
				p_1	n_1	p_2	n_2
Substrate	48	325	60	2.68×10^{-6}	0.91	89×10^{-6}	0.41
Coated sample	2622	27545	4900	2.83×10^{-8}	0.96	5.73×10^{-6}	0.63

4.2.9 Optical after and before corrosion of the coated surface

The optical images presented in Figure 4.26 depict the surface conditions of the coated and uncoated magnesium alloy samples before and after exposure to the SBF solution. The coated sample prior to corrosion (image a) exhibited a smooth and uniform surface, indicative of the successful and continuous deposition of the stearic acid and $ZnCl_2$-based superhydrophobic layer. Post-corrosion (image b), the coated surface largely maintains its integrity, with only a few localized dark spots, suggesting minor electrolyte penetration or coating imperfections. Conversely, the uncoated substrate before corrosion (image c) displays a clean surface with visible polishing lines, characteristic of a mechanically prepared metal. However, following corrosion (image d), the substrate revealed significant surface damage, including extensive roughness and accumulation of corrosion products, indicative of active degradation in the absence of a protective barrier. Overall, the comparison clearly demonstrates that the superhydrophobic coating significantly enhances corrosion resistance by preserving surface stability, whereas the bare alloy undergoes rapid deterioration under the same conditions.

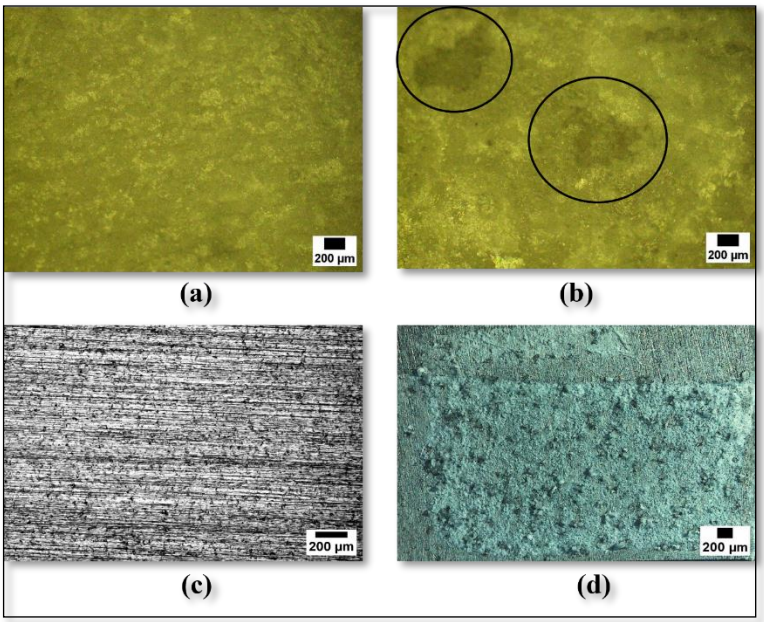

Figure 4.26 Optical images before and after corrosion of coated (a&b) and substrate (c&d)

4.2.10 Assessment of the MTT and live dead cell assay of the coated sample

The biocompatibility of the coated and uncoated magnesium (Mg) alloy samples was assessed using the MTT and live dead cell assays. The MTT assay results presented in Figure 4.27 show that after 24 h of incubation, the coated sample exhibited a cell viability of approximately 97 %, which closely matched that of the control (uncoated) group. This suggests excellent initial cytocompatibility of the $ZnCl_2$ and stearic acid hydrothermally coated Mg surfaces. At 48 h, the coated sample maintained a cell viability of nearly 86 %, whereas that of the control group remained at approximately 96 %. Despite the slight decrease, the coated sample demonstrated acceptable biocompatibility. These findings are consistent with those reported by Doskočil et al. [176] and Vishnu et al. [190], supporting the cytocompatibility of Zn-based surface-modified Mg alloys.

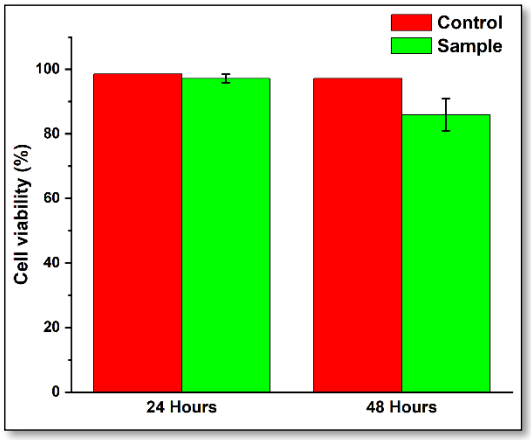

Figure 4.27 Cell viability percentage of control and coated sample after 24 hours and 48 hours

The results of the live-dead cell assay, as depicted in Figures 4.28 and 4.29 for the 24-hour and 48-hour time points, revealed a distinct pattern of biocompatibility for the hydrophobic-coated Mg alloy. Over a 48-hour period, there was a notable increase in live cell density, as evidenced by green fluorescence, indicating robust cell proliferation. Although there was a slight increase in the number of dead cells (red fluorescence), it remained minimal compared to the overall cell population, thereby reinforcing the biocompatibility of the material.

The improvement in cell proliferation can be mechanistically accounted for by the combined action of the surface chemistry and topography of the coating. Zinc stearate is a metal-organic compound that contains zinc ions and stearate ligands. It provides useful biochemical signals through the controlled release of zinc ions. Zn ions have been reported to play an essential role in cellular growth, wound repair, and regulation of enzymatic activity in mammalian systems, especially in dermal and connective tissue repair mechanisms [191,192]. Their slow release from the coating can serve as a localized proliferative signal, promoting fibroblast viability and metabolic activity without causing cytotoxicity [193].

In addition to the chemical contributions, the structured morphology and the super-hydrophobicity of the coating also enhance an ideal environment for cell growth [194]. The surface coating reduces direct fluid contact with the inner Mg substrate, which effectively minimizes hydrogen evolution and sudden pH changes that are mostly associated with Mg degradation [6]. This regulation of the corrosion environment facilitates the stable adhesion and survival of cells. In addition, intrinsic surface roughness, coupled with low surface energy, is likely to augment the formation of focal adhesions and cytoskeletal organization, both of which are essential for cell spreading and growth [195].

Electrochemically, the coating efficiently inhibits premature Mg corrosion, which tends to contribute to the high local alkalinity and gas release factors that adversely affect early tissue integration [196,197]. By stabilizing the implant–tissue interface, the zinc stearate film enables cells to experience a biofunctional, non-toxic surface during the critical initial stage of the host response. Such protective function is especially timely for biodegradable implant use, where premature degradation can degrade both structural and biological performance

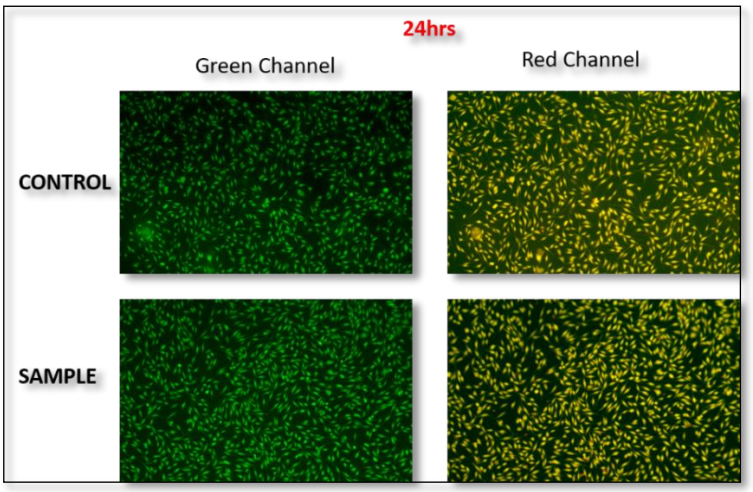

Figure 4.28 Live dead cell assay of coated sample after 24 hours

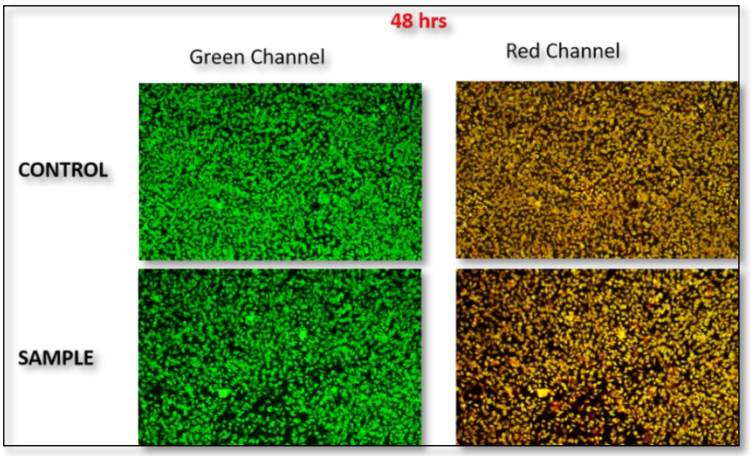

Figure 4.29 Live dead cell assay of coated sample after 48 hours

Compared with conventional coating methodologies for Mg alloys, the proposed system has several interesting advantages. Conventional coatings, such as calcium phosphate, hydroxyapatite (HA), poly(lactic-co-glycolic acid) (PLGA), polydopamine, and silica-based sol-gels, have been extensively investigated for corrosion resistance and bioactivity. However, many of these coatings have practical drawbacks. For example, HA coatings, which are highly osteoconductive, tend to be brittle and delaminate under physiological conditions [198]. Polymeric coatings such as PLGA or PCL have tunable degradation rates, but require further functionalization to achieve good corrosion resistance [199]. Inorganic coatings derived through sol-gel

can impart strong barrier properties, but might cause high pH shifts during the initial stages of degradation, which could impact cytocompatibility [200].

Chapter 5

Bioactive HA and Zn-Doped HA Coatings on Magnesium Alloys: Degradation Assessment in Simulated Physiological Conditions

5.1 Materials and methodology

5.1.1 Preparation of coating materials and substrate

The wet chemical process, as described in earlier research, was carried out to produce pure hydroxyapatite (HA) and zinc-doped hydroxyapatite (ZnHA) powders [201,202]. Briefly, the reaction between calcium hydroxide and orthophosphoric acid produced a Ca/P ratio of 1.67, which is the stoichiometric ratio of HA [203]. Zinc oxide was used for zinc doping. The reaction took place at 80 °C with a pH of 11-12. The calcium hydroxide solution was mixed with 5-wt% ZnO prior to the addition of orthophosphoric acid. Powders were then made from this solution through precipitation and filtering processes. Following an 800 °C calcination, these powders were mechanically ball-milled in ethanol for four hours to produce finely ground particles. The ethanol was then removed by drying the mixture for six hours at 50 °C [201].

To prepare a dispersion of HA particles, a chitosan gel was first prepared. For the chitosan gel, 0.5 grams of chitosan were mixed with 50 ml of distilled water and 0.5 ml of acetic acid was combined with the mixture. This dispersion was stirred with a magnetic stirrer for 10 hours. After the gel was successfully prepared, the pure and the zinc-doped HA particles were introduced into the gel. The mixture was then magnetically stirred for 1 hour, followed by vortexing for 20 minutes to achieve a uniform coating gel. Prior to coating, care was taken to ensure no bubbles were present.

To prepare the substrate, the magnesium (Mg) alloy was first sliced into 10 mm×10 mm×2 mm dimensions using wire Electrical Discharge Machining (EDM). The samples then underwent mechanical grinding with emery paper graded from 600 to

2000 to attain a uniform surface. After grinding, acetone was used for ten minutes to thoroughly clean the sample's surfaces. Following the acetone cleaning, the samples were immersed in deionized (DI) water and then carefully desiccated to further ensure the removal of any remaining impurities or particles. Once completely dry, the samples were treated in a 1 mL 1 M HCl solution for 50 seconds to activate the surface and produce a porous and rough texture.

5.1.2 Dip coating process

The diagram in Figure 5.1 illustrates the sequential process of substrate pretreatment and the subsequent steps involved in dip coating. During this process, the activated samples were immersed for a total of 20 cycles. The immersion speed of the samples was maintained at 400 mm/sec, and a drying time of 5 seconds was allowed between each immersion cycle. Following the coating procedure, the coated samples were subjected to air-drying at room temperature for a day.

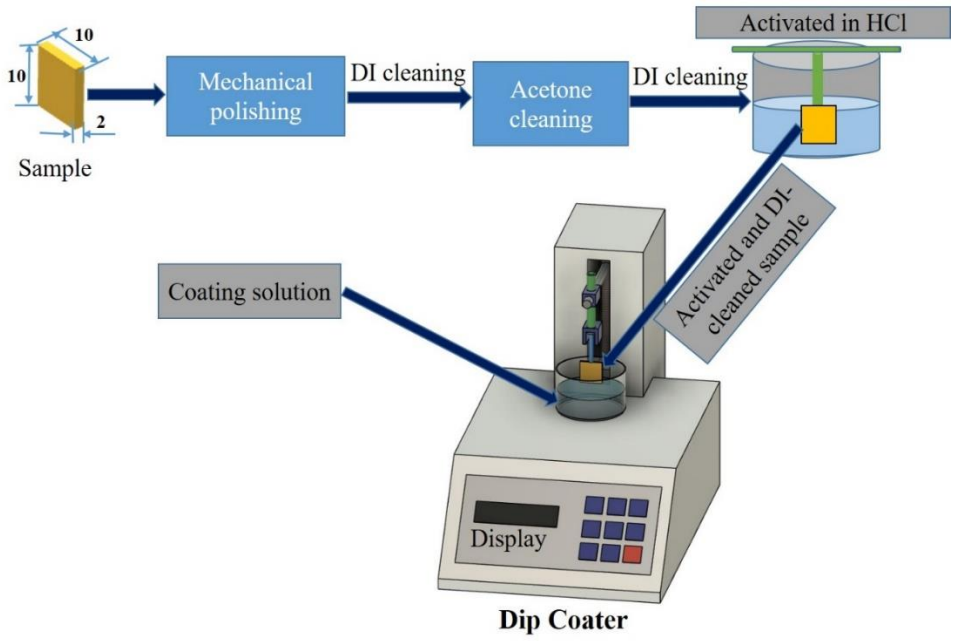

Figure 5.1 Schematic of flow process of dip coating

5.1.3 Computational Framework

This work employs a three-dimensional approach, to analyze stress profiles on the top surface of all the samples, under varying velocities and coating-based mechanical properties. The simulation geometry is designed to mimic an experimental immersion test setup in a physiological environment. Within the fluid-solid interaction module, the Navier-Stokes equations describe the motion of the fluid, while the solid mechanics equations account for any deformation or displacement of the solid. Inlet and outlet functions define the direction and velocity of the fluid. The fixed constraint function ensures that the bottom surface of the solid sample remains fixed, so deformation and displacement are zero, with linear elasticity and inertia being neglected.

$u_{solid} = 0$; where u is the velocity of the solid

$\nabla . \sigma = 0$; where σ is the stress tensor in the solid

The fluid is presumed to be incompressible and isotropic Newtonian. The subject of interest here is to study the shear stress profile on the upper surface of the specimens. Hence, FISS on the surface can be estimated by Equation 5.1 [204],

$$\tau_{ij} = \eta\,(\partial v_i/\partial x_j + \partial v_j/\partial x_i) \quad (5.1)$$

Where the fluid's shear viscosity is represented by η, the spatial coordinate is by x_i, the fluid's velocity is by v_i along axis i, and the component of stress in the j direction acting on the fluid's surface perpendicular to the axis i is by τ_{ij}. The following characteristics of SBF were utilized in the simulation: temperature of 37 °C, viscosity of 0.001 Pa·s, and density of 1000 kg.m^{-3}. The flow rates of 2 ml/min, 5 ml/min, and 9 ml/min were selected to align with previous studies and represent physiological conditions. For instance, R. Putra et al. [205] examined the fatigue life of porous magnesium scaffolds through dynamic immersion testing at a flow rate of 0.025 ml/min, Koo et al. [206] studied dynamic loading in both in vitro and in vivo at 1.5 ml/min flow rate, Wang et al. [97] developed a model to simulate flow-induced stress at 10 ml/min flow rate, A. Putra et al. [98] studied dynamic degradation behavior under simulated environment

at flow rate ranging from 0.025 ml/min to 0.8 ml/min, Wang et al. [96] has also observed corrosion behavior of absorbable magnesium-based stents at 40 ml/min flow rate. These flow rates aim to replicate the fluid dynamics around implants under different conditions, like for bone tissue cells low flow rate is required as lower flow rates can enhance cell attachment and proliferation on biomaterial surfaces, particularly in bone and soft tissue environments, the medium flow rate is required for normal blood flow in capillaries and microcirculatory systems where nutrient and oxygen exchange occurs, the higher flow rate is taken to check the stress-bearing capacity in higher flow stress like at larger vessels or arteries [207]. The properties of the substrate Mg alloy and the coated samples are mentioned in Table 5.1 [208,209].

Table 5.1. The physical attributes of the Mg alloy base material and the coated specimens

Property	Bare Mg Alloy	MgHA[2]	MgZnHA[3]
Youngs Modulus	45 GPa	106.554 GPa	107.249 GPa
Poisson's Ratio	0.35	0.277	0.276
Density	1810 Kg/m^3	3060 Kg/m^3	3080 Kg/m^3

5.1.4 Structural Characterization

An X-ray diffractometer (Rigaku Miniflex-600, Cu-K alpha radiation) was employed to determine the phases in the coated and base samples. The wavelength of the X-ray diffractometer was 1.54 Å, operating at a scanning rate of 1° per minute, and the scan covered a range of 10°–90° (2θ). The identification of phases was facilitated by the Xpert High-Score Plus software. Fourier Transform Infrared Spectroscopy (FTIR) combined with Attenuated Total Reflectance (ATR) was conducted using a Jasco FTIR 4700 instrument from Japan, over a scanning range of

[2] MgHA: Hydroxyapatite coated sample
[3] MgZnHA: Zn doped Hydroxyapatite coated sample

4000–70 cm^{-1}, to detect functional groups within the samples. An Alpha 400 R spectrometer from Witec (Germany) was utilized for the Raman spectroscopy analysis. The apparatus featured a 300 lines/mm grating, a 785 nm excitation laser, and a 1024 ×127-pixel CCD camera that was chilled to 208 K. The study's spectral range was 50–1800 cm^{-1}. Data were obtained with a 10 × objective (NA 0.25, Nikon) at 4 accumulations and 10 seconds of exposure time for each spectrum. The samples were subjected to XPS analysis utilizing the Thermo Fisher Nexsa XPS apparatus, which was equipped with a 100 μm beam size and monochromatic Al Kα radiation as the X-ray source. Surface roughness measurements of the samples were taken using an optical profilometer (Zygo Newview9000). A Field Emission Scanning Electron Microscope (FESEM, Sigma model from Carl Zeiss Microscopy Ltd) was used to investigate the microstructural morphology of all the samples. Using the FESEM in conjunction with EDX, elemental percentage analysis, and mapping were carried out.

5.1.5 Potentiodynamic Polarization

A GAMRY 620 potentiostat was used for the electrochemical analyses. In the experimental arrangement, the working electrode (WE) comprised coated and uncoated magnesium samples, while a platinum gauze was employed as the auxiliary or counter electrode (C.E.). The reference electrode (RE) used was a saturated calomel electrode (SCE) of Ag/AgCl [132]. The electrolyte in the corrosion test was Hank's solution. For the electrochemical tests, a 7 mm × 3 mm area of the 10 mm × 10 mm sample was in contact with the electrolyte, while the rest of the sample was protected with Teflon to prevent any electrolytic reactions. Open circuit potential (OCP), potentiodynamic polarization, and electrochemical impedance spectroscopy (EIS) studies were utilized to evaluate the electrochemical behavior. In the potentiodynamic polarization test, the potential range was scanned at a rate of 1 mV/sec, ranging from -1.5V to +1.5V. Electrochemical impedance tests spanning a frequency of 100 MHz and 100 kHz were conducted at open circuit voltage with an amplitude of 5 mV [210].

5.1.6 Dynamic immersion test

The immersion test was conducted in a pH 7.4 SBF solution. Four different flow conditions were applied during this immersion test, including static conditions (0 ml/min) and varying flow rates of 2 ml/min, 5 ml/min, and 9 ml/min. The pH was consistently maintained at 7.0 throughout the test. After 24 hours, 48 hours, and 72 hours, the samples were weighed, and the corresponding loss in weight was recorded. The corrosion rate was then calculated for each flow condition using Equation 5.2 [211].

$$CR = KW/AtD \quad (5.2)$$

Here, CR represents the corrosion rate in mm/year, k is a unit constant valued at 8.76 $\times 10^4$, W denotes the weight loss, A represents the exposed surface area in cm^2, t indicates the immersion time, and D signifies the density in g/cm^3 [212].

5.1.7 Biological characterization

5.1.7.1 In vitro hemocompatibility test

The bare Mg, MgHA, and MgZnHA samples were first submerged in 10 mL of saline water at 37 °C for 7 hours. After this duration, the samples were withdrawn from the solution, and the liquid solution was centrifuged at 2000 rpm for 10 minutes. Subsequently, the solution was sonicated for 10 minutes. Three sets of solutions for each sample type (bare Mg, MgHA, and MgZnHA) were prepared using a 10 µL sonicated solution. After diluting each produced solution with 1 mL of saline solution, the mixture went through incubation at 37 °C for an hour. Following the mixing with a 3.8% w/v sodium citrate solution at a ratio of 10:1, normal saline was added at a ratio of 4:1 to dilute the blood. Now, 20 µL of the diluted blood was taken and mixed with the previously prepared sample solution. This mixture was then incubated for another hour at 37 °C. Following incubation, all of the samples were centrifuged at 2000 rpm for five minutes. The supernatant fluid was then meticulously collected and subjected to an optical density (O.D.) analysis at a wavelength of 545 nm using a UV-vis spectrophotometer. The positive control was diluted blood mixed with sodium

bicarbonate, while the negative control was diluted blood mixed with saline, with no specimens included. The subsequent Equation 5.3 was utilized to calculate the level of hemolysis [213],

$$\% \, hemolysis = O.D.(test) - O.D\,(negative)/O.D.(positive) - O.D.(negative) \times 100 \quad (5.3)$$

5.1.7.2 Antimicrobial test

The agar disk diffusion method was utilized to assess the in vitro antibacterial activity of bare Mg, MgHA, and MgZnHA samples against the Gram-positive bacterial strain S. aureus. Initially, each sample was degraded in 5 ml of saline solution (0.9% NaCl) at 37 °C for 6 hours. After degradation, the resulting solution was thoroughly mixed by sonication for 10 minutes. Luria Bertani agar plates were prepared under sterile conditions for this experiment [214]. Small disks were then immersed in the sonicated solution used for the antibacterial test. Meanwhile, after being inoculated with Luria-Bertani agar, Staphylococcus aureus (S.A.) strains were allowed to grow for 24 hours at 37 °C. Finally, Using ImageJ software, the breadth of the inhibition zones surrounding the disks was measured to determine the antibacterial activity of the samples after the incubation period. The size of these inhibition zones provided a quantitative measure of the antibacterial efficacy of the Mg, MgHA, and MgZnHA samples, with larger zones indicating stronger antibacterial activity.

5.1.7.3 Cell culture

Extract preparation

The sample extracts were prepared according to the protocols specified in the International Standard Organization (ISO 10993-12) [215]. In short, the coated samples MgHA and MgZnHA, as well as the substrate Mg, were submerged in α-MEM at 37 °C for 6 hours, after which they were discarded. Following a centrifugation of the mixture, the supernatant was collected. A 220 mm membrane filter was used to

filter this supernatant in order to sterilize it. The resulting extracts were subsequently used for cell culture.

Cell viability assay

An MTT (3-(4,5-dimethylthiazol-2-yl)-2-5-diphenyl tetrazolium bromide) experiment was carried out to evaluate the viability of the cells. Initially, 1.0×10^5 cells/mL of MC3T3 cells were plated into a 96-well plate and incubated for 12 hours at 37 °C. Subsequently, the cells were subjected to the extracts at a concentration of 100 μg/mL for five days. Now, 100 μL of serum-free medium and 10 μL of MTT solution were added to each well. The cells were then incubated for an additional 4 hours at 37 °C. Following the incubation period, 100 μL of isopropanol was introduced to each well after the extracts were removed. After that, the plates were incubated for a further fifteen minutes. Finally, a Multi-Scan Go spectrophotometer manufactured by Thermo Fisher, Finland, was utilized to determine the absorbance at 570 and 670 nm [216,217]. The cell viability percentage was determined by applying Equation 5.4 [218]

$$\%\ cell\ viability = (T - B)/(C - B)\ \times 100 \qquad (5.4)$$

Where T represents the test data, B is the blank data, and C is the control data.

DAPI staining of MC3T3 cells

DAPI staining of MC3T3 cells was done to confirm cell viability. For this experiment, cells with a concentration of 2×10^5 cells/mL were mixed with extracts at 100 μg/L in a 24-well plate and then cultured for five days under standard conditions (37 °C, 5% CO2). Following the 5-day culture period, the cells were treated with 4% paraformaldehyde for twenty minutes at room temperature.

To observe cell morphology and viability, the fixed cells were stained with 50 μg/ml TRITC-phalloidin (Invitrogen, CA, USA) for 90 minutes, which allowed for visualization of actin filaments and cell structure [216]. After TRITC staining, the cells were stained again with 1 μg/ml 2-(4-Amidinophenyl)-6-indolecarbamidine dihydrochloride (DAPI, Invitrogen) for one minute to visualize the cell nuclei, with

excitation occurring at 340–380 nm and emission at 435–485 nm. Images of the stained cells were subsequently captured using a Nikon Eclipse TiU fluorescence microscope (Japan). Finally, Image J software was used to quantify the number of cells adhered to the cell culture well-plate surface. Analysis was conducted using three representative images of the fluorescent cell structure for each sample group [216].

5.2 Results and discussion

5.2.1 Simulation of FISS distribution

Figure 5.2 illustrates the stress profiles of coated/uncoated samples along the bisector in the flow direction with varying flow rates. The bisector was chosen to avoid edge effects and accurately represent the stress distribution in the flow path. Shear stress increased with flow rate, peaking around the x coordinate -0.3. The variation in stress along the bisector might be a result of fluid velocity variation across the sample surface and an increase in fluid-solid interaction area (impact area of fluid on solid). The slope of the peak increased with the flow rate. The central region experienced the lowest shear stress for all cases, followed by a proportional increase as a function of flow rate.

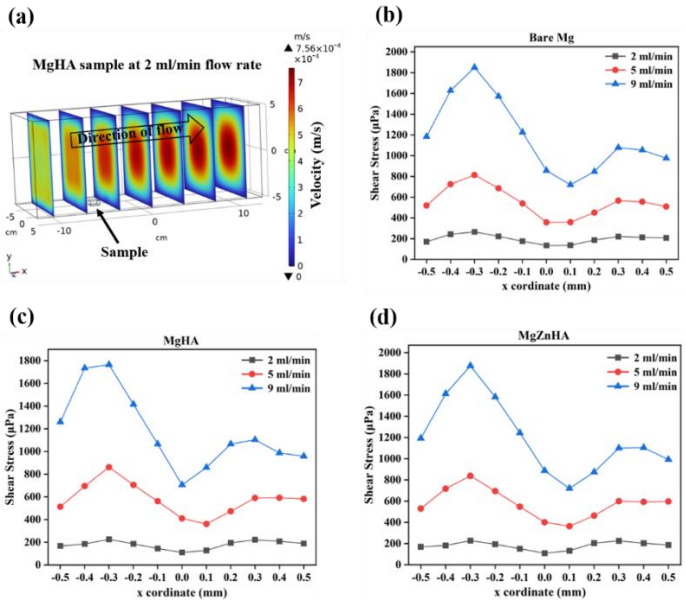

Figure 5.2. (a) Velocity profile of MgHA sample at 2 ml/min flow rate. (b), (c), (d) Shear Stress profiles along the bisector of the top surface in the flow direction for bare Mg, MgHA, and MgZnHA samples respectively

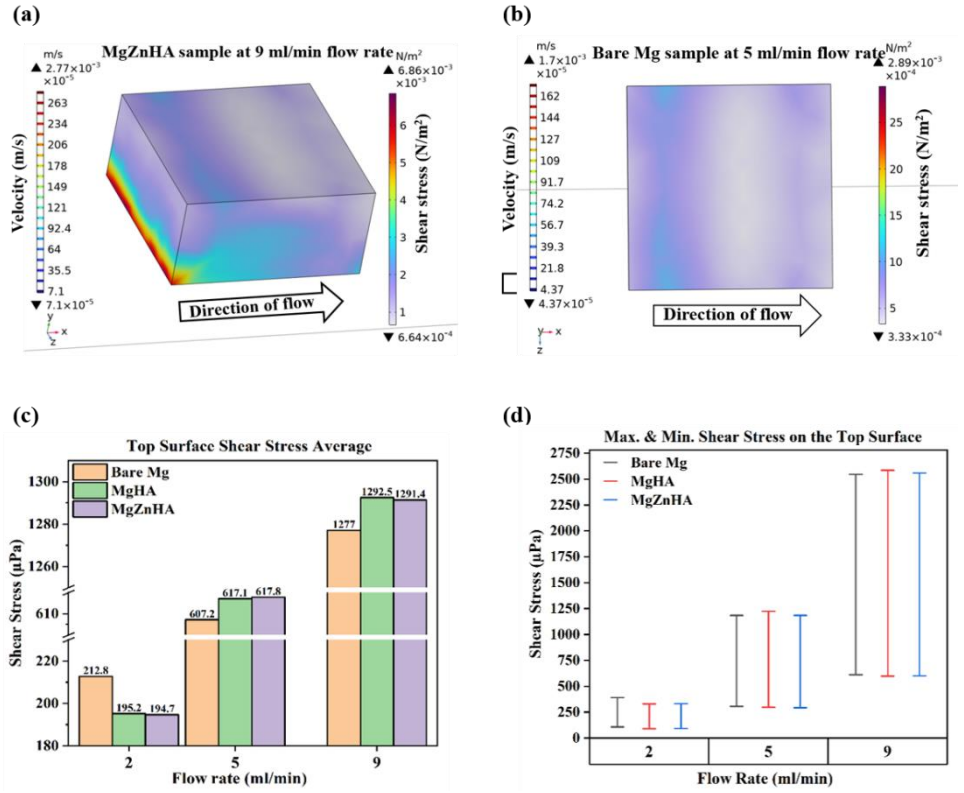

Figure 5.3. (a) Body shear stress profile of the MgZnHA sample at 9 ml/min flow rate, (b) Top surface shear stress profile of bare Mg sample at 5 ml/min, (c) Top surface shear stress average for the three samples w.r.t. flow rate, (d) Range of shear stress on the top surface for the three samples as a function of flow rate.

As the bottom of the sample is fixed, the bottom edge facing the flow experienced the highest shear stress in all cases. The bare sample top surface initially endured higher shear stress than the coated samples at a flow rate of 2 ml/min. As the flow rate increased, MgHA and MgZnHA- experienced higher shear stress than the bare Mg sample. At 5 ml/min MgZnHA experienced higher shear stress than MgHA, while at 9 ml/min MgHA showed higher shear stress. The similar shear stress values of the coated samples can be attributed to the comparable mechanical properties of MgZnHA and MgHA.

Figures 5.3 (a) and 5.3 (b) depict the body shear stress of the MgZnHA coating and the top surface shear stress of the bare Mg substrate respectively. Figure 5.3 (c) illustrates the increment in top surface average shear stress with flow rate for the bare Mg and coated samples. Shear stress increased with flow rate (2–9 ml/min): from 212 μPa to 1277 μPa for bare Mg, 195 μPa to 1292.5 μPa for MgHA, and 194.7 μPa to

1291.4 µPa for MgZnHA. From 5.3 (d), it is noticeable that the minimum value, maximum value, and range of shear stress increased with the flow rate for the three samples. These results indicate that the FISS values for all samples increased with the rise in flow rate, which aligns with findings by Wang et al. and Putra et al. [96–98].

5.2.2 Dynamic Immersion test and assessment of degraded surface

The corrosion rates of the MgZnHA sample under four distinct flow conditions: 0 ml/min, 2 ml/min, 5 ml/min, and 9 ml/min during the immersion test are presented in Figure 5.4. The data reveals a clear trend of increasing corrosion rates with flow rate, reaching a maximum of 9 ml/min. Specifically, after 72 hours of immersion, the corrosion rate reaches 8.17 mm/year, representing a 177% increase from the 0 ml/min to the 9 ml/min flow condition. While the corrosion rate continues to rise over time, the rate of increase slows down. This deceleration is likely due to the formation of a passivation layer and a layer of corrosion products on the sample surface after about 48 hours, which acts to inhibit further corrosion. However, at the highest flow rate of 9 ml/min, the slope of the curve does not decrease between 48 and 72 hours as it does for other flow rates. This is because the higher flow rate likely removes the corrosion products, consequently exposing fresh surfaces to the solution, and continuing the corrosion process.

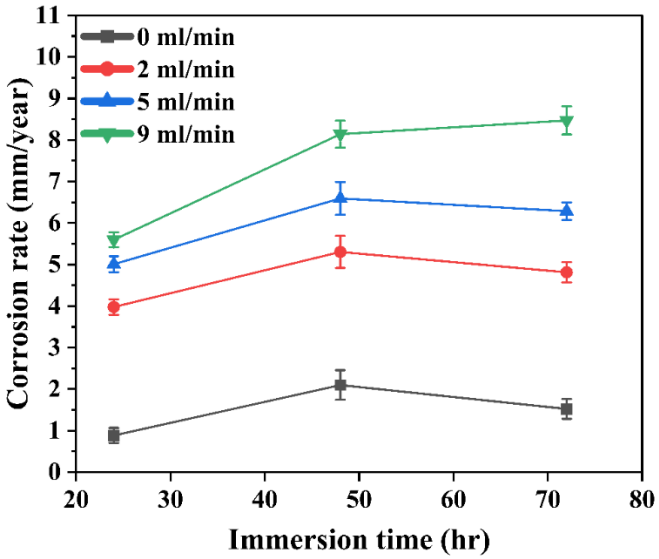

Figure 5.4. Corrosion rate of MgZnHA sample under varying flow rates

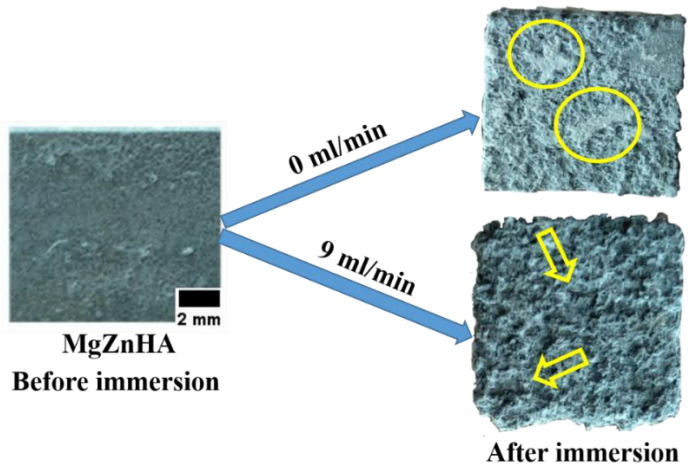

Figure 5.5. Image of immersion test of the MgZnHA coated sample in two different flow conditions

Figure 5.5 shows the pre-immersion and post-immersion conditions of the MgZnHA sample under static conditions (0 ml/min) and a flow rate of 9 ml/min. Figure 5.6 presents SEM images (a) to (d) depicting the surface conditions after immersion under different flow rates: 0 ml/min, 2 ml/min, 5 ml/min, and 9 ml/min. In both figures 5.5 and 5.6, it is evident that corroded products adhere to the sample surface under static conditions. These corroded products and pits are marked in both figures. Additionally, as the flow rate increases, the corroded products are gradually detached from the surface. This removal is due to the higher fluid-induced shear stress (FISS) on the sample surfaces at higher flow rates, as observed in FISS simulations. Consequently, as the corroded products are removed, new surfaces are exposed to the solution, leading to localized corrosion and an increase in the corrosion rate. Under static conditions, ion diffusion constraints cause a higher local pH microenvironment to gradually rise, which inhibits the dissolution of Mg and decreases the corrosion rate. However, at higher flow rates, the removal of degradation products accelerates ion and mass transfer at the Mg surface-SBF solution interface, resulting in localized corrosion, larger pits, and an increase in overall corrosion rate [96,97]. Figures 5.6 (e) and (f) illustrate the surface morphology at higher magnification of the MgZnHA sample subjected to a flow rate of 9 ml/min. In this image, the microstructure of the corroded product is clearly visible, appearing as rod and needle-like shapes.

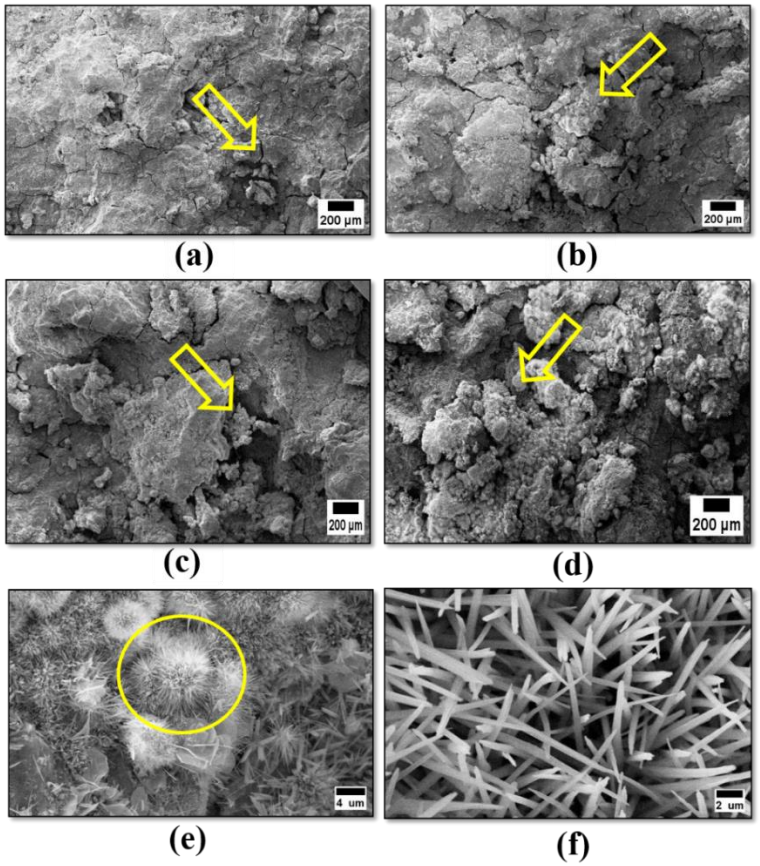

Figure 5.6. Image of SEM micrograph of MgZnHA sample after immersion test in (a) static flow condition, (b) 2 ml/min flow rate, (c) 5 ml/min flow rate, (d) 9 ml/min flow rate, and (e), (f) higher magnification image at 9 ml/min flow rate

5.2.3 Assessment of Potentiodynamic Polarization

The potentiodynamic polarization curves for the substrate Mg sample, MgHA sample, and MgZnHA sample are shown in Figure 5.7 Equilibrium corrosion current density (I_{corr}) and equilibrium corrosion potential (E_{corr}) were derived from the graphs utilizing Tafel extrapolation. Subsequently, corrosion rates for the different samples were calculated based on the corrosion current density. It has been noticed that the I_{corr} value shifts towards the left for the coated samples. This leftward shift indicates a reduction in corrosion current density and, consequently, a decrease in the corrosion rate. Additionally, the E_{corr} value shifts to a more positive value in the case of the coated specimens, with the highest value recorded for the MgZnHA sample. It is known that active dissolution and hydrogen evolution govern the cathodic and anodic

reactions. Additionally, previous studies have shown that the mechanism of hydrogen evolution is dependent on coating morphology and their net-like microstructures [219]. Here in this study, the MgHA and the MgZnHA samples may have affected the hydrogen evolution rate, leading to a higher cathodic current. Table 5.2 provides the electrochemical parameters, E_{corr} (corrosion potential) and I_{corr} (corrosion current density), together with the corrosion rate (mm/year). It is apparent that the corrosion potential (E_{corr}) increased to 117 mV for MgHA compared to the Mg alloy substrate and further increased by 166 mV for MgZnHA. The corrosion current density (I_{corr}) showed a significant decrease of 119.28 µA/cm² for MgHA compared to Mg and 134.15 µA/cm² for MgZnHA. Consequently, the corrosion rates for all the samples indicate a reduction, with MgHA showing a decrease to 4.72 mm/year from 17.71 mm/year for Mg, and MgZnHA further reducing the rate to 3.10 mm/year.

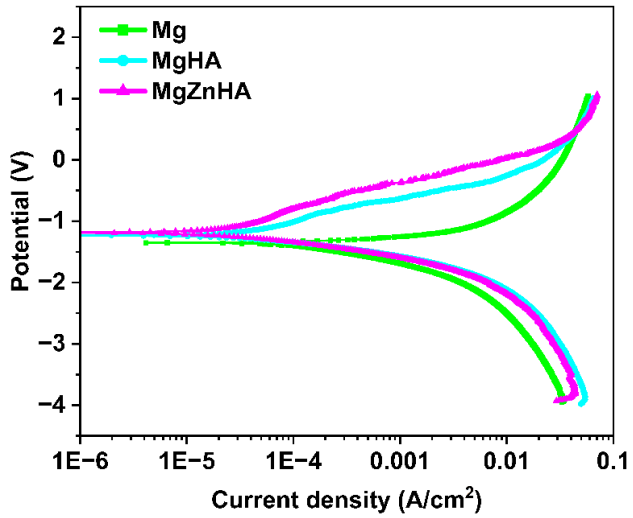

Figure 5.7. Potentiodynamic polarization curve of Mg, MgHA, and MgZnHA samples

Table 5.2. Parameter's summary computed from potentiodynamic polarization observations for different samples

Sample name	E_{Corr} (V)	I_{Corr} (µA/cm^2)	Corrosion rate (mm/Year)
Mg	-1.351	162.70	17.71
MgHA	-1.234	43.42	4.72
MgZnHA	-1.185	28.55	3.10

5.2.4 Evaluation of Electrochemical Impedance Spectroscopy

The EIS spectrum analyzer application was used to fit the impedance data using an equivalent circuit, as shown in Figure 5.8. The electrolysis resistance associated with the working electrode (WE) and the reference electrode is indicated by R_1 in this equivalent circuit. At the contact surface of the electrolysis and electrode, R_2 denotes the polarization resistance or charge migration resistance. To accurately model the electrode's capacitive behavior under real-world conditions, two constant phase elements (CPE) are utilized. CPEs are employed to account for non-ideal capacitive responses resulting from a variety of causes, including non-uniform current and potential distributions during mass-transport processes, and electrode porosity. This can often be caused by structural flaws in the samples, such as surface inhomogeneity, uneven surface reactivity, and roughness or fractal shapes [97]. The CPE's impedance has been evaluated by Equation 5.5 [97],

$$Z_{CPE} = Q^{-1}(j\omega)^{-n} \quad (5.5)$$

Where n is a constant without dimensions ranging from -1 to 1, Z is the CPE impedance ($\Omega.cm^2$), Q is a constant with units $s^n\Omega^{-1}cm^{-2}$, j is the imaginary unit $j = \sqrt{-1}$, and ω stands for the angular frequency, defined as $\omega = 2\pi f$, where f denotes the frequency in Hertz. For an ideal capacitor, n equals 1; for a resistor, n equals 0; for an inductor, n equals -1 and, it shows mass-transport behaviors when n equals 0.5 [189].

In Figure 5.9, the Nyquist plot along with a fitted solid line for the base and coated substrate are presented. The two notable sections of this Nyquist spectrum are the low-frequency R-C loop and the high-frequency R-C loop. The double-layer creation is described by the high-frequency loop, while the film production process is represented by the low-frequency loop [188]. It can be observed that the diameter of both capacitive arcs increased when HA and ZnHA coatings were applied to the Mg substrate surface. This is due to the creation of a resistive corrosion product film and the stabilization of electrochemical reactions at the sample's surface.

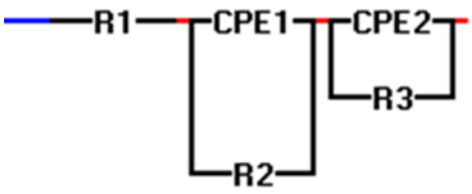

Figure 5.8. Equivalent circuit for EIS data fitting

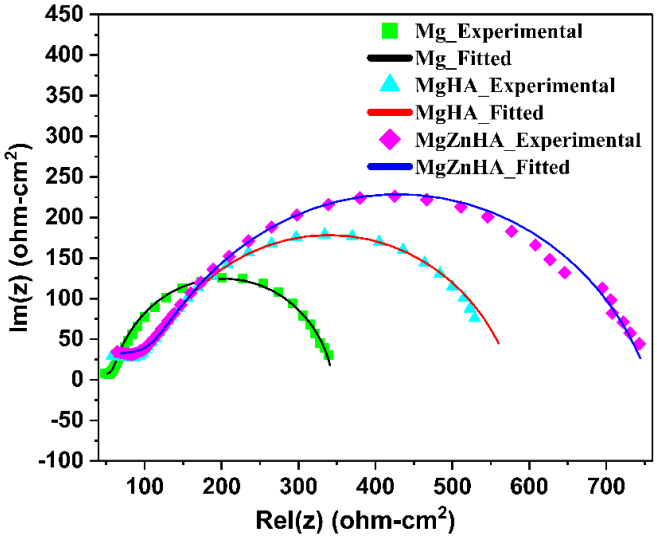

Figure 5.9. Nyquist plot of Mg, MgHA, and MgZnHA samples

Table 5.3. Impedance parameters for different samples

Sample	R_1 (ohm-cm^2)	R_2 (ohm-cm^2)	R_3 (ohm-cm^2)	CPE-1		CPE-2	
				P	n	P	n
Mg	25	280	40	2.55×10^{-6}	0.92	9×10^{-5}	0.38
MgHA	8	472	101	6.47×10^{-6}	0.81	2.59×10^{-6}	0.60
MgZnHA	10	646	107	4.22×10^{-6}	0.78	2.01×10^{-6}	0.62

Table 5.3 presents the EIS parameters R_1, R_2, R_3, CPE-p, and CPE-n. The p-value and n-value indicate the non-ideal behavior of the capacitor and its deviation from ideal behavior, respectively. Notably, the values of R_1 and R_2, R_3 are higher for the coated samples compared to the base samples. As a result, the coated samples demonstrate

enhanced corrosion resistance [220,221]. The results of the potentiodynamic polarization test and the EIS test indicate that the formation of a barrier composite film consisting of HA, ZnHA, and chitosan restricts the solution's interaction with the bulk substrate [219]. This prevents chloride ions from affecting the surface of the magnesium substrate in the coated samples. In addition, chitosan's positively charged amino groups facilitate the association with anions and prevent their invasive corrosion [222]. Among the coated samples, MgZnHA demonstrates slightly superior corrosion resistance due to the inclusion of Zn^{2+} ions into the HA lattice. The pH decreases partially following Zn^{2+} doping in the HA group. In addition, Zn^{2+} can protect the sample surfaces from Cl^- -induced galvanic corrosion. For these additional reasons, the Zn-doped sample exhibits more significant corrosion resistance than the HA-coated sample [223].

5.2.5 Surface morphology after Potentiodynamic Polarization

In Figure 5.10 (a) and (b), SEM images of MgHA and MgZnHA after potentiodynamic testing are displayed. It is evident that larger pits have formed on the surface of the MgHA sample in comparison to the MgZnHA sample. This difference can be attributed to the doping of Zn^{2+} ions in the HA lattice, as illustrated in the EDS spectra in Figure 5.10 (c) and 5.10 (d).

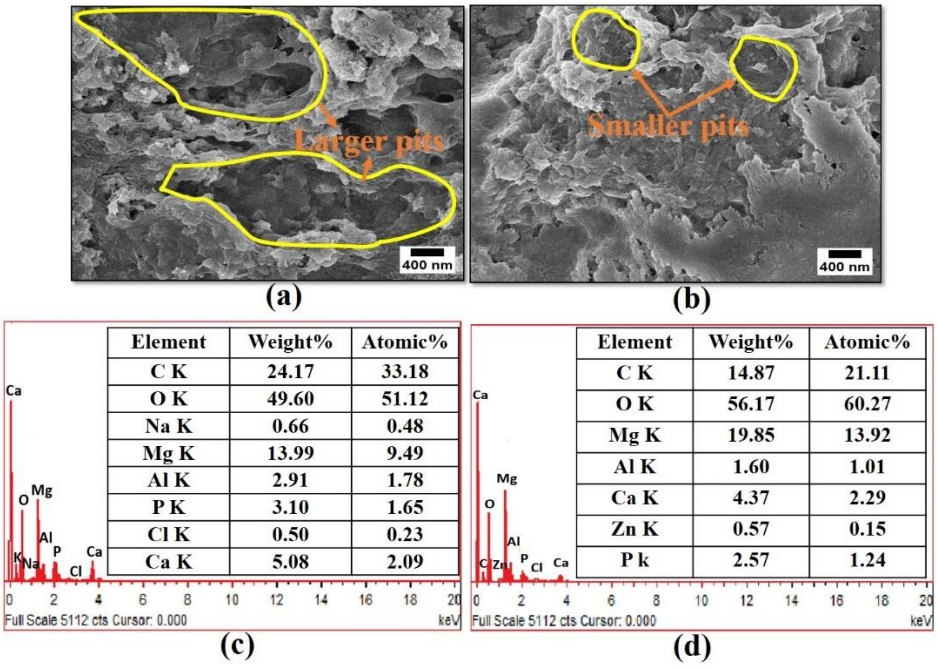

Figure 5.10. SEM and EDS image of (a), (c) MgHA and, (b), (d) MgZnHA

5.2.6 Analysis of Structural Characterization

Figure 5.11 displays X-ray diffraction patterns for bare Mg, MgHA, and MgZnHA samples. The bare Mg exhibits distinct peaks at 32.46°, 34.56°, 36.82°, 48.16°, 57.82°, 63.42°, 69.1°, and 70.52° [224]. In contrast, all three samples show Mg-containing phase peaks at 32.46°, 48.16°, and 63.42°, albeit with reduced intensity in the coated samples. This reduction is likely due to the absorption properties of a thick coating layer covering the bare substrate. Additionally, the coated samples exhibit prominent peaks corresponding to HA at 25.96°, 28.97°, 31.75°, 34.03°, 39.63°, 46.37°, 49.03°, and 52.79° as established by the previous literature [225]. No additional peaks are observed in the MgZnHA samples as expected [226].

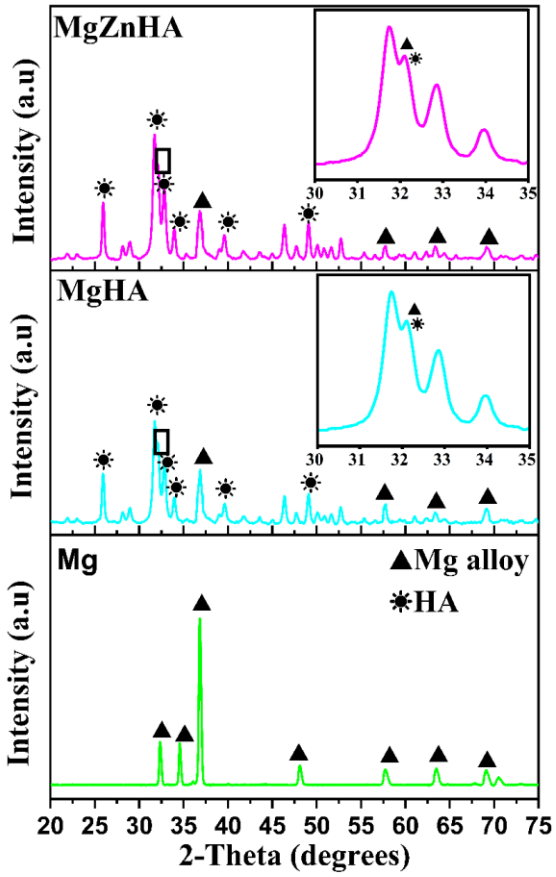

Figure 5.11 XRD pattern of substrate Mg, MgHA, and MgZnHA samples

Figure 5.12 (a) shows the FTIR spectrum for all three samples. The functional group presents in substrate Mg, MgHA, and MgZnHA samples is confirmed by FTIR. The strong vibrational group ranging from 520 cm^{-1} to 670^{-1} indicates a strong Mg-O bond which is present in the substrate and in both coated samples. Similarly, for all three samples, the stretching band of the O–H group, observed in the 3672 cm^{-1} to 3842 cm^{-1} range, indicates atmospheric absorbance on the sample surface [227]. At 2364 cm^{-1} a strong band has been found, it exhibits a C=O bond present in the atmosphere [228]. At 1580 cm^{-1} and 1020 cm^{-1} indicate the bending mode of $–NH_2$ and PO_4^{3-} group which is normally associated with Chitosan and HA [222]. The absorption band around 1435 cm^{-1} is assigned to CO_3^{2-} which implies that some portions of the PO_4^{3-} group have been replaced by CO_3^{2-}, which normally comes from the reaction of HA with atmospheric CO_2 [229].

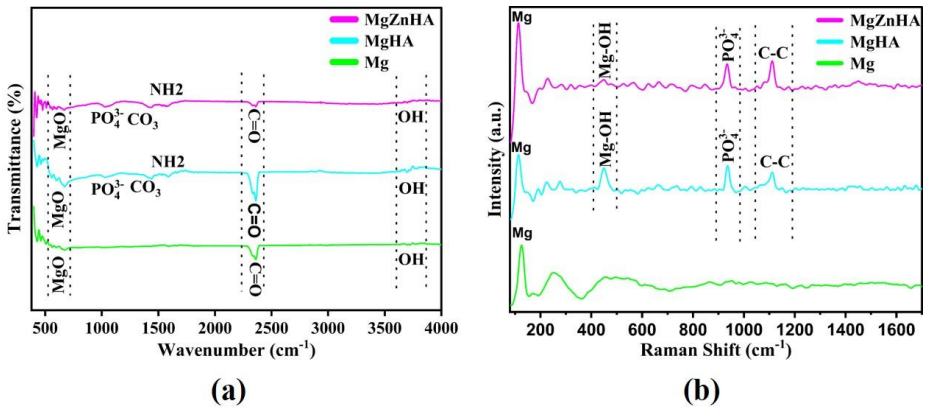

Figure 5.12. (a) FTIR and (b) Raman spectrum of substrate Mg, MgHA, and MgZnHA samples

In Figure 5.12 (b) the Raman spectra of the substrate Mg and the coated samples are presented. It is observed that all samples exhibit a prominent peak between 110 cm^{-1} and 125 cm^{-1}, characteristic of metallic magnesium [230]. In the case of the coated samples, an additional peak at 936 cm^{-1} is observed, attributed to the PO_4^{3-} group, confirming the presence of Hydroxyapatite (HA) [231]. Furthermore, a notable peak near 1110 cm^{-1} indicates the presence of C–C groups originating from chitosan [232]. In the MgHA samples, a strong peak at 450 cm^{-1} signifies the Mg-OH bond. However, in the MgZnHA samples, the intensity of this peak is significantly reduced. This reduction suggests enhanced corrosion resistance in the Zn-doped HA, as discussed in the preceding sections. Therefore, the Raman spectrum reconfirms the formation of HA, as revealed by XRD and FTIR techniques.

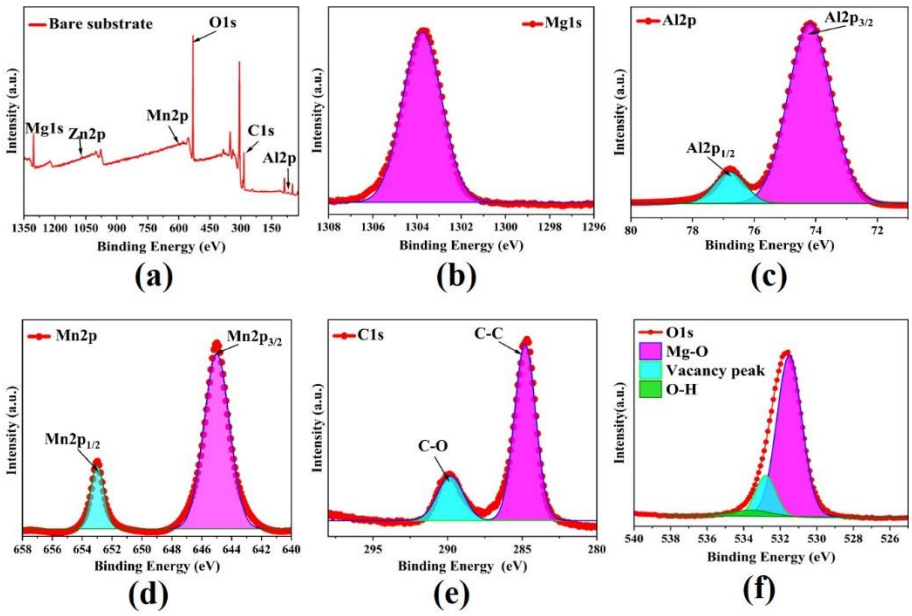

Figure 5.13. XPS analysis of base Mg alloy showing (a) survey spectra, (b) Mg 1s, (c) Al 2p, (d) Mn 2p, (e) C 1s, and (f) O1s peaks

Figure 5.13 illustrates the XPS analysis of the substrate Mg, offering insights into its elemental composition and chemical nature. In Figure 5.13 (a), a survey spectrum reveals the presence of Mg, Al, Mn, Zn, C, and O in the bare alloy. Figure 5.13 (b) displays an XPS peak at a binding energy of 1303.78 eV, corresponding to a typical Mg1s peak indicative of Mg^{2+}, suggesting the presence of MgO bonding. This finding aligns with observations by Haider et al. [233] and Alam et al. [234] in their respective studies. Furthermore, Figure 5.13 (c) exhibits the spectra of Al2p, which is deconvoluted into $Al2p_{3/2}$ and $Al2p_{1/2}$ peaks at binding energies of 74.19 eV and 76.82 eV, respectively. This suggests the coexistence of both Aluminum Oxide and Aluminum Hydroxide, with the intensity of Al_xO_y greater than that of $Al_x(OH)_y$, Similar binding energies for Al have also been reported in the literature by Wang et al. [235]. In Figure 5.13 (d), the deconvoluted peaks of Mn2p are presented, indicating oxidation states of Mn, with peaks observed at binding energies of 644.9 eV ($Mn2p_{3/2}$) and 652.97 eV ($Mn2p_{1/2}$) [236]. The presence of Al and Mn oxides can influence the stability, corrosion resistance, and biocompatibility of bare Mg to some extent, as confirmed by Ding et al. [237] and Agarwal et al. [238]. The O1s spectra, deconvoluted into OI, OII, and OIII components at 531.50 eV, 532.780 eV, and 533.56

eV respectively, are presented in Figure 5.13 (e). OI signifies O^{2-} ions forming MgO bonds on the surface of the Mg, while OII suggests oxygen defects within the metal oxide matrix, possibly related to oxygen vacancies. OIII bonds are attributed to hydroxyl groups (OH) that can form $Mg(OH)_2$ [239,240]. Peng et al. observed that $Mg(OH)_2$ bonding forms a protective layer in the physiological environment, offering protection to the Mg surface up to a certain extent; this is consistent with our detection of MgO and $Mg(OH)_2$ on the Mg surface before coating [241]. In Figure 5.13 (f), the deconvoluted C1s XPS spectra are shown, with C-C and C-O bonds observed at binding energies of 284.80 eV and 289.87 eV respectively [242] This presence of C1s spectra is attributed to atmospheric carbon, further confirmed by FTIR spectra in Figure 5.12 (a).

In Figure 5.14 (a), the survey spectra of the MgZnHA sample are presented, confirming the presence of Mg Zn, O, N, C, Ca, and P. This outcome corroborates the formation of the target materials. Figure 5.14 (b) exhibits the high-resolution spectra of C1s. The peak at a binding energy of 284.6 eV indicates the presence of the C–C group, affirming the aliphatic nature. Additionally, a prominent peak at 285.97 eV suggests the presence of C–N and C–O bonds, indicating strong interactions between carbon and nitrogen. Furthermore, a sub-peak recorded at 287.46 eV can be attributed to the C=O bond, which suggests the presence of an organic component such as chitosan on the coating surface matching previous results by Wang et al. precisely [243]. In the N1s XPS spectra, a strong peak is observed at 399.3 eV, indicative of the $–NH_2$ group. The existence of C-C, C-N, and $–NH_2$ bonds confirms the presence of chitosan on the surface of the MgZnHA sample, as described by Li et al. [244]. The C–C and $–NH_2$ groups in chitosan can enhance hydrophilicity, absorptivity, and adhesion strength in the coating, thereby improving corrosion resistance and promoting cell proliferation, as documented by Hsu et al. [245] and Farrokhi-Rad et al. [246]. The Ca2p spectrum displays peaks at 351.05 eV and 347.13 eV for $Ca2p_{3/2}$ and $Ca2p_{1/2}$, respectively, suggesting that Ca^{2+} ions are bound to PO_4^{3-} groups. In the deconvoluted spectrum of P2p, peaks are observed at 132.97 eV and 133.93 eV, assigned as $P2p_{3/2}$ and $P2p_{1/2,}$ respectively, with a ΔE of 0.9 eV, consistent with the article as noted by Catalin Constantin Negrila et al. [242]. With the two components

linked to phosphate groups and P–O–Ca bonds at the surface of the biomaterial, this asymmetric peak is typical of phosphate compounds like HA. Figure 5.14 (f) displays the high-resolution deconvoluted spectra of Zn2p. The $Zn2p_{3/2}$ spectra, where a peak at a binding energy of 1021.52 eV corresponds to Zn metal (Zn^{2+}), while a lower intensity peak at 1045.54 eV indicates the presence of Zn^{0} [247]. The difference in spin-orbit energy (ΔE) of 24.02 eV suggests that Zn^{2+} is predominant in the MgZnHA sample, confirming successful Zn^{2+}/Ca^{2+} substitution in the HA lattice. Sprio et al. [248] elucidated that the substitution of Ca^{2+} ions with Zn^{2+} ions in the HA lattice results in a reduction of lattice structure and grain sizes, consequently enhancing mechanical properties such as flexural strength and elasticity. Furthermore, Zn^{2+} ions demonstrate minimal degradation in a physiochemical environment, indicating their stability within the HA lattice, which may contribute to improved corrosion resistance and bioactivity. These findings align with our observed results. In Figure 5.14 (g), the O1s XPS spectra of the MgZnHA sample are presented. These spectra have been deconvoluted into three distinct peaks. The first peak at 530.9 eV indicates the presence of C=O and O–H groups, while the other two peaks at 531.56 eV and 532.25 eV indicate P–O and P–O–P groups, aligning well with previous literature [249,250]. So, all the structural characterization i.e., XRD, FTIR, RAMAN, XPS confirms the presence of corresponding phases, groups, and elements. Therefore, it confirms the target coating material has been formed on the surface of the Mg substrate.

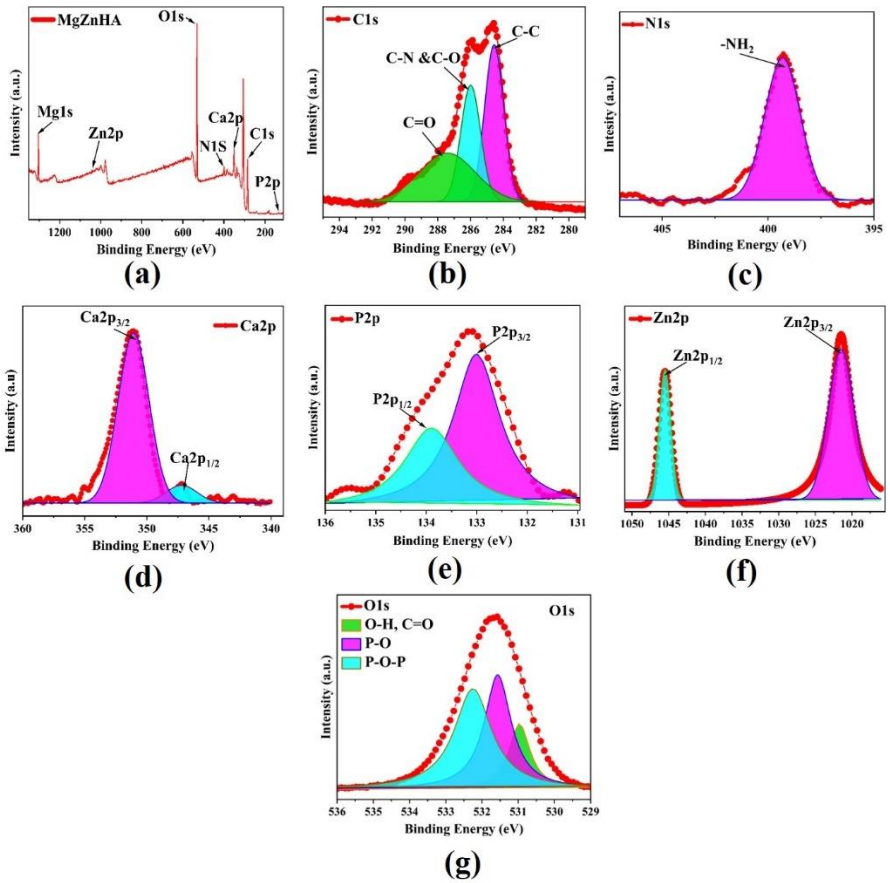

Figure 5.14 XPS analysis of Zn-doped HA coated Mg alloy (MgZnHA) showing (a) survey peak, (b) C1s, (c) N1s, (d) Ca2p, (e) P2p, (f) Zn2p, (g) O1s

5.2.7 Assessment of Surface roughness

The surface roughness characteristics of all the samples are depicted in Figure 5.15, where 5.15 (a) shows the polished bare Mg surface without any chemical etching, and 5.15 (b) illustrates the surface after etching with HCl. Figures 5.15 (c) and 5.15 (d) present the surfaces of the MgHA and MgZnHA samples, respectively. It is clear from the figure that the surface roughness of the initially polished sample has significantly increased following the etching process, consistent with observations from the SEM images [150]. The increased surface roughness observed aligns with previous literature by Shi et al., which demonstrates that etching with HCl creates a textured, rough surface on Mg that enhances adhesion. [251]. In our studies, this increased rough surface also facilitated the binding of HA and ZnHA particles through mechanical interlocking, which is essential for the long-term stability of the coating in

the biological environment. For the MgHA sample, the average surface roughness (Sa) is 3.158 µm, with a root mean square height (Sq) of 4.242 µm. Similarly, for the MgZnHA sample, the average surface roughness (Sa) is 3.376 µm, with a root mean square height (Sq) of 4.599 µm. Therefore, the surface roughness has significantly increased for the coated samples especially for the MgZnHA sample, aligning with the findings observed in the SEM images. This increase in surface roughness is advantageous for bio-integration [252]. Previous studies by Begam et al. [253] and Ding et al. [254] have shown that higher surface roughness in coated samples enhances cell adhesion and proliferation by providing greater surface area and micro-topographical features that facilitate cell attachment.

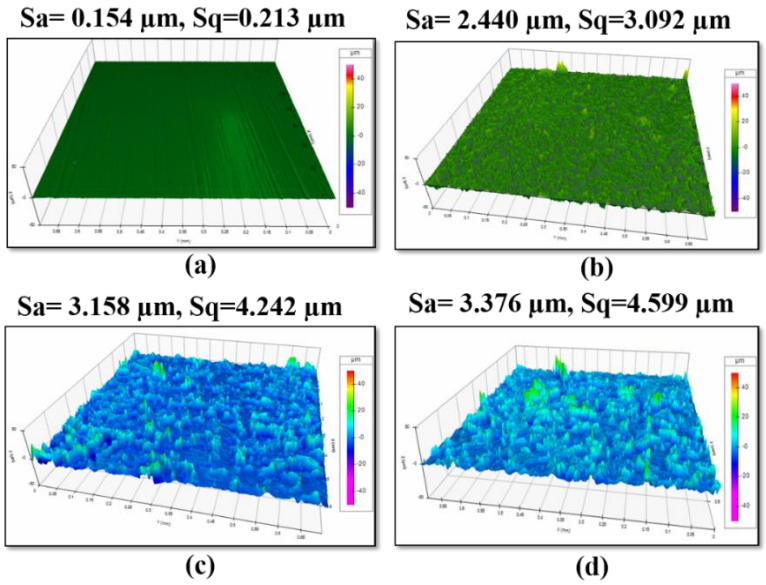

Figure 5.15. Surface morphology by 3d profilometer: (a) Bare Mg, (b) Mg after etching, (c) MgHA sample, and (d) MgZnHA sample

5.2.8 Surface morphology and Elemental analysis of substrate and coated samples

The SEM micrograph presented in Figure 5.16 depicts the microstructure variations among the bare Mg sample, etched sample, MgHA sample, and MgZnHA sample. The purpose of etching the bare sample is to induce porosity and roughness on its surface, facilitating the deposition and strong binding of HA and Zn-doped HA particles by chitosan. Figure 5.16 (b) clearly illustrates the transformation from a

uniformly smooth surface of the unetched polished sample to a rough and porous surface after etching. In the case of HA coating, a uniform and dense structure is evident, with nano HA particles embedded within. Conversely, for Zn-doped HA coating, a surface adorned with petal or needle-like structures with more porosity is observed [219]. Upon closer examination, particularly at higher magnifications akin to those depicted in Figure 5.16 (e), the microstructure of the HA-coated surface reveals the presence of net and flower-like formations. This detailed observation underscores the intricacies of the surface morphology, offering valuable insights into the coating process and resulting structures.

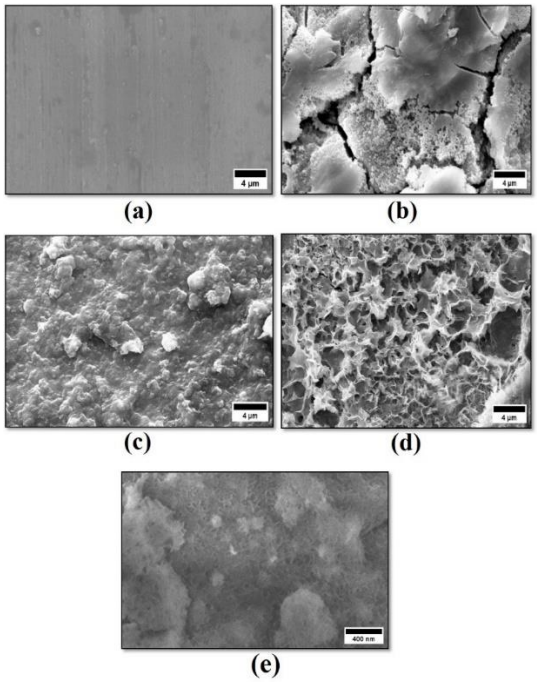

Figure 5.16. SEM image of (a) base (b) etched (c) HA, (d) Zn HA, (e) HA in higher magnification

Figure 5.17 displays the EDS spectra along with the quantitative analysis of the elements present on the surface of the samples. For the bare Mg sample, peaks corresponding to Mg, Al, Mn, and Zn are identified. Additionally, a small amount of Cl is detected on the etched surface, attributed to the treatment with HCl. Notably, there is a reduction in the weight percentage and atomic percentage of magnesium, accompanied by a significant rise in the presence of oxygen. In the MgHA sample, the presence of calcium (Ca) and phosphorus (P) is discernible. The ratio of Ca to P is

calculated as 1.75 (1.4/0.8), closely approximating the standard ratio of Ca to P in HA, which is 1.67 [203]. Similarly, for the Zn-doped HA sample, the Ca/P ratio is determined as 1.625 (1.3/0.8), again closely aligning with the standard ratio of Ca to P in HA. Notably, an increase in the quantity of zinc (Zn) is also evident from the EDS analysis. These observations highlight the elemental composition variations across the different samples, providing valuable insights into the surface characteristics and elemental distribution, particularly regarding the incorporation of calcium phosphate and zinc in the coatings [201]

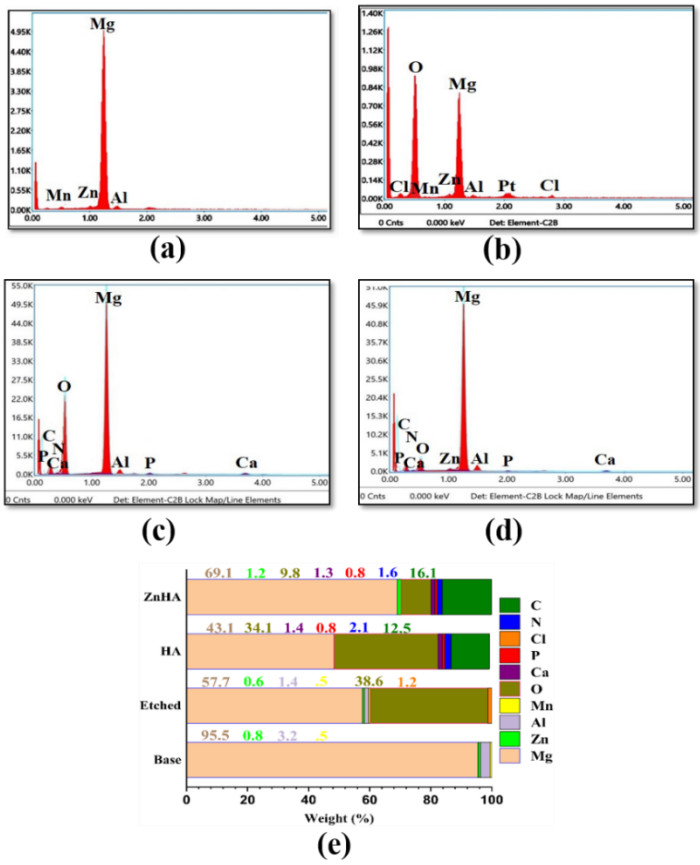

Figure 5.17. EDS spectra of (a) Base, (b) Etched, (c)HA coated, (d) Zn doped HA-coated, and, (e) their Corresponding EDS spectra plot

5.2.9 Cross-sectional view and Elemental Mapping of MgZnHA

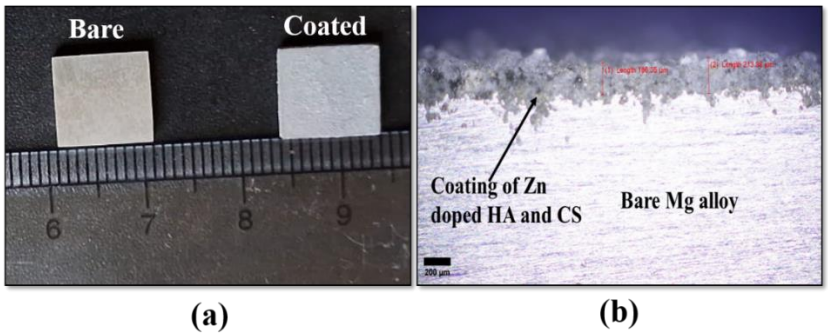

Figure 5.18. (a) Bare sample before coating and after coating, (b) optical cross-sectional view of the coated sample

Figure 5.18 (a) presents images of the bare Mg sample and the MgZnHA sample. Figure 5.18 (b) displays a cross-sectional image of the MgZnHA sample, revealing an average coating thickness of nearly 190 µm. Figure 5.19 illustrates the cross-sectional elemental mapping of the MgZnHA sample. This mapping enables the confirmation of the presence and spatial distribution of elements. Notably, the results closely resemble the EDS findings of MgZnHA presented in Figure 5.17. These figures collectively provide comprehensive visual and analytical insights into the coating process, coating thickness, and elemental distribution, thereby contributing to a deeper understanding of the material's characteristics and performance.

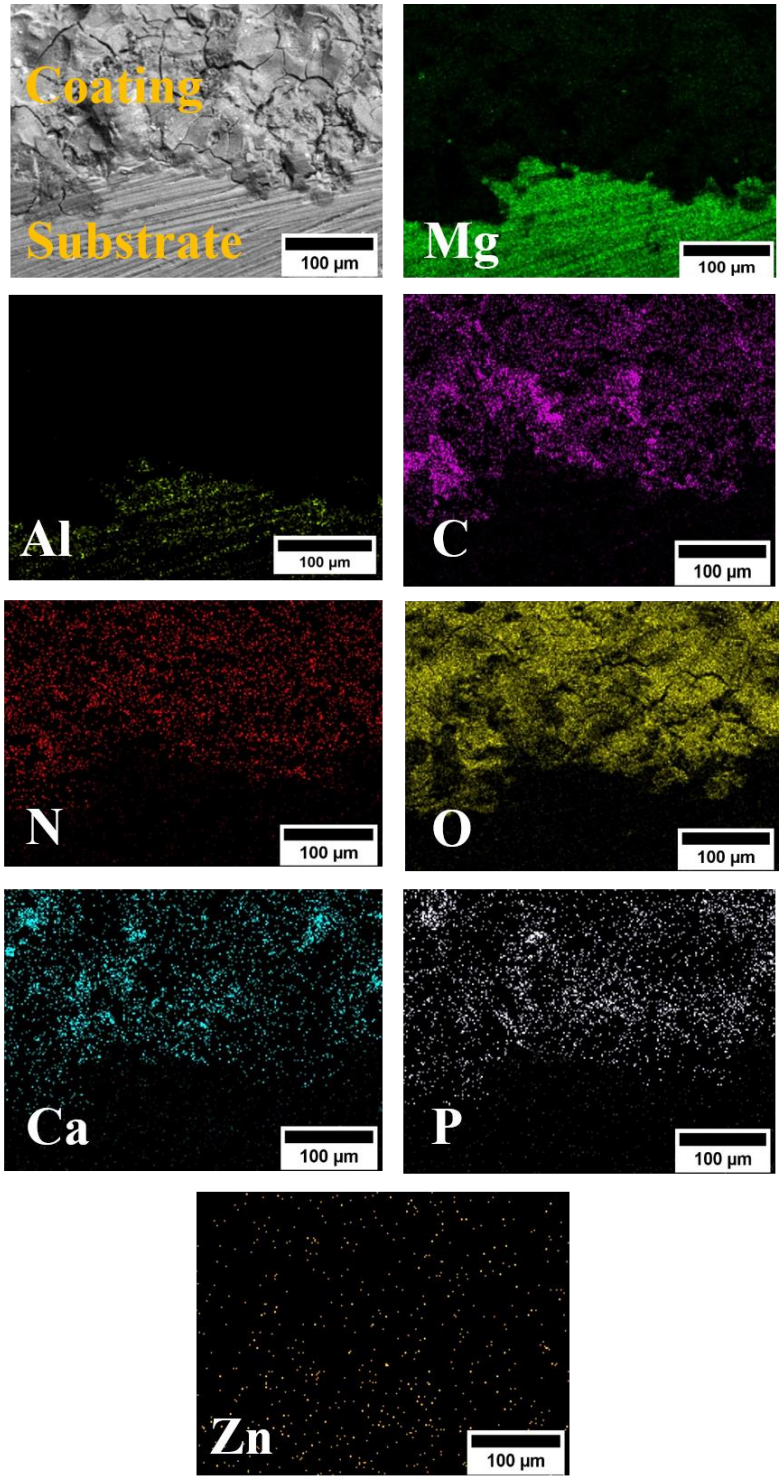

Figure 5.19 Elemental mapping of MgZnHA

5.2.10 Adhesion strength of coated sample

Figure 5.20 illustrates the results of the tape scratch test conducted to assess the adhesion strength of the ZnHA coating on the surface of the Mg substrate. Figure 5.20 (a) depicts the sample before the scratch test, whereas Figures 20 (b) and 5.20 (c) present the sample after the pull-off test. This test adhered to the ASTM D3359-22 standards (Methods A and B), and the coating exhibited excellent adhesion, with only minimal coating removal observed after tape pull-off. Based on these results, the adhesion strength is classified as 4A and 4B, according to ASTM standards [255,256]. Critical steps such as etching and drying post-coating are essential for achieving a strong bond between the coating and Mg substrate. Etching generated a rough, porous surface that facilitated the adherence of the chitosan and ZnHA coating while drying further increased the compactness and strength of the coating on the Mg surface [257,258].

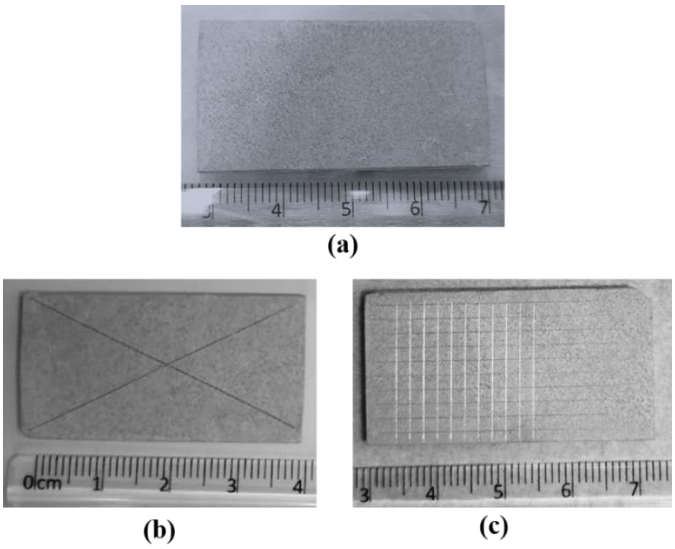

Figure 5.20 Tape scratch test to evaluate bonding strength between coating and substrate: (a) sample before scratch test, (b) and (c) samples after scratch test

5.2.11 Assessment of biological characteristics

5.2.12 Hemocompatibility

Figure 5.21 illustrates the hemolysis results for all samples. According to ISO 10993-5, a material with a hemolysis ratio ≤ 5% is considered hemocompatible [259]. Based on the results, all samples meet this criterion, though the hemolysis percentage varies among them. The substrate Mg exhibited the highest hemolysis percentage, which is consistent with previous literature findings, including those reported by Sandeep Singh et al. [260]. This increased hemolysis is primarily due to the physiological behavior of Mg, which includes high local pH changes and hydrogen evolution that can cause significant damage to red blood cells [261]. In contrast, the MgHA sample showed a significantly reduced hemolysis percentage. The bioactive layer of chitosan and hydroxyapatite inhibits direct contact between the Mg substrate and blood cells, stabilizing the surface and reducing degradation and hemolysis. The MgZnHA sample demonstrated the lowest hemolysis percentage. The addition of Zn^{2+} ions enhances the bioactive and antibacterial properties of the coating, maintaining a more stable physiological environment by moderating pH levels and providing additional protection against bacterial contamination, thus further decreasing hemolysis [261,262]. In conclusion, while all tested samples are hemocompatible, the substrate Mg alloy shows the highest hemolysis due to its inherent physiological reactions. Coating the Mg alloy with chitosan and HA significantly improves hemocompatibility, with the ZnHA providing the most effective reduction in hemolysis due to its enhanced bioactive properties.

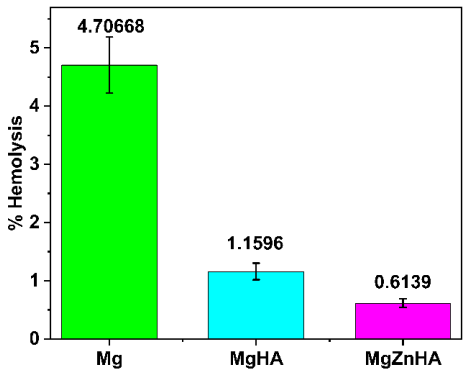

Figure 5.21. Hemolysis analysis of Bare, MgHA, and MgZnHA samples

5.2.13 Antimicrobial Activity

Figure 5.22 depicts the growth of Staphylococcus aureus (S.A.) bacteria over 48 hours. All three samples - bare Mg, MgHA, and MgZnHA - demonstrate inhibition zones against S.A. growth. Magnesium alloys are known for their biocompatibility and biodegradability. However, the lack of significant antibacterial properties in the bare Mg can be attributed to the absence of active antimicrobial agents in its composition. Magnesium alone does not possess strong antibacterial activity [263].

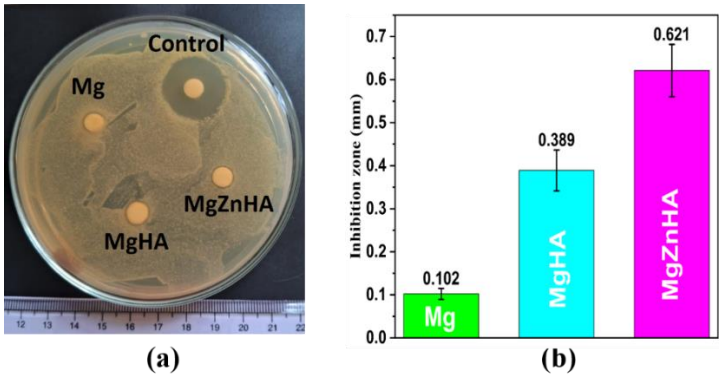

Figure 5.22. Images of (a) Antimicrobial test results, and (b) corresponding inhibition zone

As a result, the Mg sample showed a very minimal inhibition zone. Now, the coating of chitosan and hydroxyapatite (HA) on the magnesium alloy provides a slight improvement in antibacterial properties. Chitosan, a natural polysaccharide, is known for its antimicrobial properties. However, the antibacterial effect may not be strong enough to create a significant inhibition zone. The inhibition zone has been increased but not significantly [213,264]. Zinc is known for its strong antibacterial properties [265]. The incorporation of Zinc into the Hydroxyapatite coating enhances the antimicrobial activity of the Mg alloy. Zinc ions can disrupt bacterial cell membranes, interfere with enzyme function, and induce oxidative stress within bacterial cells, leading to effective inhibition of bacterial growth [266]. This results in a larger and clearer inhibition zone around the MgZnHA sample, demonstrating its potent antibacterial properties.

5.2.14 MTT Assay and DAPI Imaging

The average percentage of cell viability for all three samples is presented in Figure 5.23, along with their respective standard deviations. It is evident that all samples are non-cytotoxic, with cell viability over 100%. However, the coated samples showed higher cell viability compared to the base substrate. The percentage of cell viability for the MgHA sample increased by 4.93% and 16.02% for the MgZnHA sample. Figure 5.24 (a), (b), and (c) present DAPI staining illustrating cell growth and proliferation across all samples. It is evident that MC3T3 cells successfully adhered to all samples. Following a 5-day cell culture period, the highest cell count was observed in the Zn-doped HA-coated samples. Approximately 210 ± 7 cells were present on the bare Mg, which increased to 439 ± 9 in the MgHA and further rose to 602 ± 14 in the MgZnHA samples. So clearly, the DAPI imaging results also support the MTT assay trends.

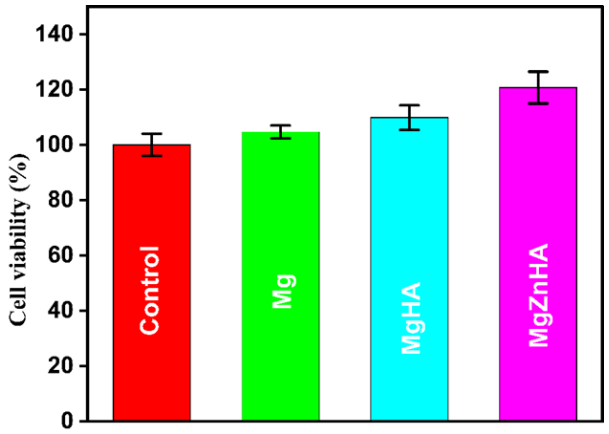

Figure 5.23. Comparison of cell viability percentages among control, base Mg, MgHA, and MgZnHA samples

Hydroxyapatite (HA) is highly valued for its osteoconductive properties, meaning it promotes the attachment and growth of bone cells [267]. When applied as a coating, HA facilitates the Mg alloy surface to create a layer of apatite that resembles bone, which enhances the interaction between the implant and surrounding tissue. [268]. Chitosan, known for its excellent biocompatibility and biodegradability, creates a non-toxic interface that encourages cell adhesion and proliferation, facilitating a supportive environment for cell growth on the bare Mg surface [269]. In the case of MgHA

samples, the complex coating layer containing both chitosan and HA enhances cell viability compared to the uncoated substrate. For MgZnHA samples, the addition of Zn^{2+} ions decreases the crystallinity of HA, making it slightly amorphous [270]. Moreover, the incorporation of Zn^{2+} ions can alter the surface energy and binding energy, which in turn increases the wettability of the sample. This improved wettability stimulates cellular activities, promoting cell proliferation and differentiation, ultimately leading to higher cell viability in the MgZnHA samples [271,272].

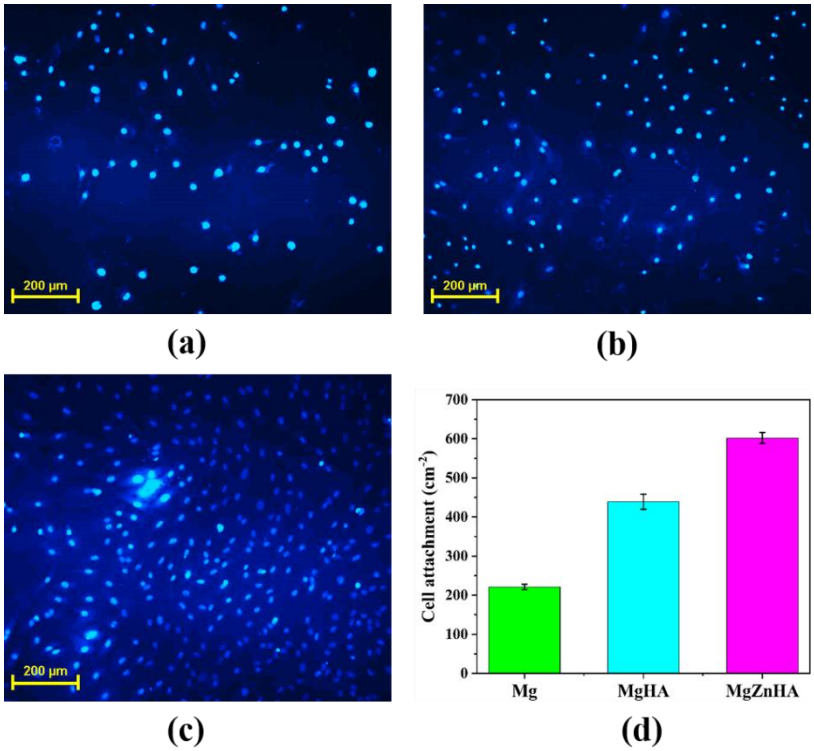

Figure 5.24. (a), (b), (c) Image of MC3T3 cell nucleus after 5 days of culture of Mg, MgHA, MgZnHA, and, (d) Quantitative cell attachment results for different samples

Chapter 6

Post-Deposition Heat Treatment of Chitosan/Zn-HA Coatings on Mg Alloys: Experimental and Modeling Study

6.1 Experimental procedure

6.1.1 Sample preparation

The preparation of coated sample was done similarly to our previous work [153]. In brief, at first the Mg alloy, sample cut into 10 mm×10 mm dimension. Then the sample was polished with emery paper upto grade 2000. Then the sample was cleaned by acetone. Now the sample was etched by HCl for 50 seconds. This etched sample was dipped for 20 cycles in the chitosan and HAp composite gel to get the coated surface. Then the sample was gone for post heat treatment process for three different temperature 120 ºC, 240 ºC, and 360 ºC.

6.1.2 Coating Characterization

The thermal stability of the coatings was investigated by TGA that was carried out using a PerkinElmer TGA 4000 system in nitrogen flow (atmosphere rate), to heat up at 15 ℃/min until it reaches 800 ℃ optical micrographs and coating thickness measurements were acquired by an optical microscope (Olympus BX53M, Japan) with Stream Basic software. The surface morphology and element composition of the coatings were investigated by scanning electron microscope (SEM) equipped with energy dispersive X-ray spectroscope (EDS) (Sigma Model, Carl Zeiss Microscopy Ltd., Germany). Phase analysis was carried out by X-ray diffraction (XRD) on a Rigaku, Miniflex-600 machine with Cu-Kα radiation (λ = 1.54 Å) in the 2θ range of 10°–90° at a step speed of 0.5°/min. The surface roughness of films was measured by optical profilometer (Zygo NewView 9000). The functional groups in the coatings were further characterized by Fourier Transform Infrared Spectroscopy (FTIR) and Attenuated Total Reflectance (ATR), where the FTIR-4700 (Jasco, Japan).

6.1.3 Electrochemical Corrosion Characterization

Electrochemical assessments were performed using a GAMRY Reference 620 potentiostat to evaluate the corrosion behavior of both coated and uncoated magnesium alloy specimens. In the three-electrode cell configuration, the specimen served as the working electrode (WE), platinum gauze was used as the counter electrode (CE), and an Ag/AgCl (in saturated KCl) electrode functioned as the reference electrode (RE). Simulated Body Fluid (SBF) was employed as the electrolyte medium to replicate the physiological environment, and its composition details are provided in the. To ensure controlled exposure, only a 6 mm × 3 mm area of each 10 mm × 10 mm sample was exposed to the electrolyte, while the remaining surface was insulated with Teflon tape to prevent undesired electrochemical interactions. Prior to electrochemical testing, samples were stabilized under open circuit potential (OCP) conditions for approximately 30 minutes to reach a steady-state potential. Subsequently, Electrochemical Impedance Spectroscopy (EIS) measurements were conducted at OCP using a 5 mV AC perturbation over a frequency range of 100 kHz to 100 mHz. The resulting Nyquist and Bode plots were analyzed to evaluate coating resistance and charge-transfer characteristics. Following EIS, Potentiodynamic Polarization (PDP) tests were performed at a scan rate of 1 mV/s to determine the corrosion potential (Ecorr), corrosion current density (icorr), and corresponding corrosion rate through Tafel extrapolation.

6.1.4 Biological characterization

6.1.4.1 MTT (cell assay)

The cytocompatibility of both coated samples, prior to and following heat treatment, was evaluated using an ISO 10993-12 MTT (3-(4,5-dimethylthiazol-2-yl)-2,5-diphenyl tetrazolium bromide) assay [216]. Initially, extracts were prepared by immersing the samples in α-MEM medium at 37 °C for 6 hours. Subsequently, the samples were centrifuged, and the resulting supernatants were filter-sterilized using a 0.22 µm membrane. MC3T3 pre-osteoblast cells (1×10^5 cells/mL) were plated in 96-well plates and incubated for adhesion during at least 12 h and treated with extracts

(100 µg/mL) for 4 days at 37 °C in a 5% CO_2 atmosphere. After incubation, 10 µL MTT reagent and 100 µL serum-free medium were added into each well followed by additional incubation for 4 h; then the formazan crystals were dissolved in 100 µL isopropanol and absorbance was measured at a wavelength of 570 nm (reference at 670 nm) with a Multi-Scan Go spectrophotometer (Thermo Fisher Scientific, Finland). The cell viability (%) was determined as follows Equation (6.1) [153]

$$Cell\ viability\ (\%) = \frac{(T - B)}{(C - B)} \times 100 \qquad (6.1)$$

Where T is the test data, B is the blank data and C is the control data.

6.1.4.2 DAPI test

Cell attachment and morphology were assessed using DAPI staining. MC3T3 cells (2×10^5 cells/mL) were cultured with the sample extracts (100 µg/mL) in 24-well plates for 4 days under standard incubation conditions (37 °C, 5% CO_2). The cells were then fixed with 4% paraformaldehyde for 20 min at room temperature. To visualize the cytoskeletal structure, cells were stained with 50 µg/mL TRITC–phalloidin (Invitrogen, USA) for 90 min, followed by nuclear staining with 1 µg/mL DAPI for 1 min (excitation: 340–380 nm; emission: 435–485 nm). Fluorescence images were captured using a Nikon Eclipse TiU microscope (Japan), and the number of adhered cells was quantified using ImageJ software from three representative fields for each sample [216].

6.1.5 Finite element (FE) analysis

Finite element (FE) simulations were conducted to evaluate how heat treatment of substrates influences the mechanical stimulation experienced by an adhered cell. The cell geometry was constructed from a microscopic image, and the modelling procedures for both the cell and substrates are explained in the subsequent sections. Here, static cell culture conditions were analyzed by applying a static pressure on the cell model in ANSYS.

6.1.6 FE modelling of cell and substrate

A cell image of the dental pulp MSC, isolated from the extracted human teeth, was chosen to mimic the cell model. The detailed incubation and image capturing process of cell are described in the article written by Das et al. [273]. Using the microscopic image of the stem cell, a 3D cell model was created in ANSYS APDL, as shown in Figure 6.1 (a) and 6.1 (b). The geometric configuration used in the cell model is presented in Figure 6.1 (d). To determine the cell height, the same height-to-maximum-width ratio reported by Slomka and Gefen [274] was adopted. Based on the observed morphology in the microscopic image (Figure 6.1 c), the nucleus was represented as an ellipsoid with major and minor axes of 34 μm and 5 μm, respectively. It was positioned slightly above the substrate surface, with its centre set 1 μm from the cell base and 15 μm inward from the widest point of the cell boundary. Both the cytoplasm and nucleus were modelled as isotropic, compressible hyperelastic materials using a Neo-Hookean strain energy formulation [275]. Cytoskeletal filaments were introduced as two-node beam elements oriented along the direction of the applied loading, reflecting the organization typically seen in living cells during mechanical activity [276]. Following the discretization of the cytoplasmic region with 10-node tetrahedral solid elements (Solid187), the nodal coordinates were extracted via ANSYS APDL. Vertical nodes within 0.1 μm tolerance were identified using a Python® script and grouped to enable beam element creation in APDL. In accordance with values reported by Katti and Katti [277] the total volume of cytoskeletal filaments was set to 0.24% of the entire cell volume.

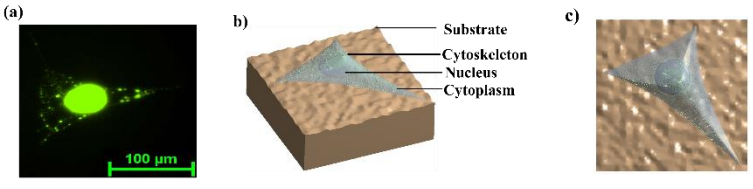

(d)

Geometrical Properties	Value
Height (µm)	2.20
Maximum width at base (µm)	22.13
Total cell volume (µm^3)	67.17
Nuclear Volume (µm^3)	5.43
Cell surface area (µm^2)	201.16
Area of the cell at base (µm^2)	93.06
Nucleus surface area (µm^2)	32.83
Diameter of cytoskeletons (nm)	7

Figure 6.1. (a) Microscopic image of transfected mesenchymal stem cell; (b) 3D FE model and internal components of the cell model; (c) Top view of cell model; (d) Geometric properties used for designing the cell model.

Table 6.1. Number of elements used for substrate models.

Substrate Model	**7.67 µm**	**6.44 µm**	**8.96 µm**	**4.22 µm**
Elements	45379	43973	47373	35830

The substrate geometry was defined as a 150 µm × 150 µm × 30 µm rectangular block [Figure 6. 2 (a)]. Surface roughness was incorporated in ANSYS APDL using the ASPDENS command, following the procedure outlined in Gupta et al. [276]. Roughness values (Ra) of 7.67 µm, 6.44 µm, 8.96 µm and 4.22 µm were assigned to represent the without heat treated and coated surfaces heat treated at temperatures 120 ºC, 240 ºC and 360 ºC respectively [Fig. 2(a)]. Each substrate model was meshed with Solid187 elements, with the corresponding element numbers provided in Table 6.1.

Table 6.2 summarizes the material properties used for both the cell and substrate components.

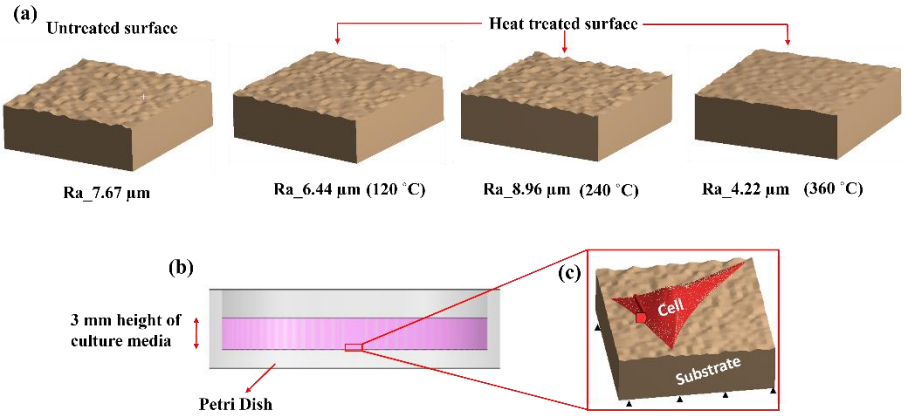

Figure 6.2. (a) Average roughness of untreated and heat-treated substrates; (b) Schematic of static cell culture condition indicating cell position on petri dish; (c) Boundary condition on cellular model by applying hydrostatic pressure on cell face (red contour) and keeping bottom face of substrate fixed

Table 6.2. Material parameters of cellular components.

Cellular components	Material parameters	Value	Reference
Cytoplasm	Elastic modulus	4.47 KPa	[275]
	Poisson ratio	0.4	
Nucleus	Elastic modulus	17.88 KPa	
	Poisson ratio	0.4	
Cytoskeleton	Elastic modulus	1 GPa	[277]
	Poisson ratio	0.3	
Substrate (Zn doped HAP)	Elastic modulus	105.786 GPa	[278]
	Poisson ratio	0.3	

6.1.7 Boundary condition and solution method

In this work, static cell culture conditions were modelled by assuming the cell seeded substrate remained submerged in a 3 mm layer of culture medium (saline water) inside a petri dish, as shown in Figure 6.2 (b). The hydrostatic pressure at the base of the medium was computed and applied as a uniform static pressure load on the cell surface [Figure 6.2 (c)]. All cell substrate interfaces were defined using a surface-to-surface contact formulation with a no-separation condition. The bottom surfaces of the substrates were fully constrained. FE simulations were performed using the ANSYS Static Structural solver, where rotational degrees of freedom of the beam element nodes were restricted. Large-deflection effects were enabled for all analyses. Number of elements for the FE models were determined through a mesh convergence study, refining the element size until the difference in results between successive refinements was below 2%.

6.2 Result and discussion

6.2.1 TGA analysis

Thermogravimetric analysis of the coated samples shown in Figure 6.3 reveals three main mass-loss stages. The initial mass loss of about ~ 5.92% occurring near 130 °C corresponds to the release of both adsorbed water molecules on the surface and absorbed residual solvents trapped within the coating matrix [279]. The mass loss observed between 150 °C and 300 °C (~4.91%) is attributed to the release of strongly bound or chemically associated water still desorbing in this temperature range and the initial decomposition of thermally labile organic components in the composite coating. The major mass loss around ~ 24 % occurs between 300 °C and 520 °C and is assigned to the bulk thermal decomposition of the chitosan backbone that is glycosidic bond scission, dehydration and volatilization of carbonaceous fragments, as also previously reported by ámiz-gonzález et al. [280]. So, the incorporation of HAp actually increased the thermal stability of compared to only chitosan [281]. These observations agree with prior reports on HAp-reinforced chitosan systems such as Al-Shanqiti et al. [282] reported that incorporation of hydroxyapatite increases the thermal stability of

chitosan, results in lower weight loss and higher residual amounts. Dosić et al. [283] observed analogous TG/DTG features for HAP/CS and HAP/CS/Gr coatings initial water loss below 170 °C, chitosan decomposition as a broad DTG peak around 270 °C, and additional high-temperature losses related to filler/nanosheet decomposition and HAp dehydroxylation. Together, these data indicate that HAp addition stabilizes the composite against thermal degradation by both physically restricting polymer chain motion and increasing inorganic residue.

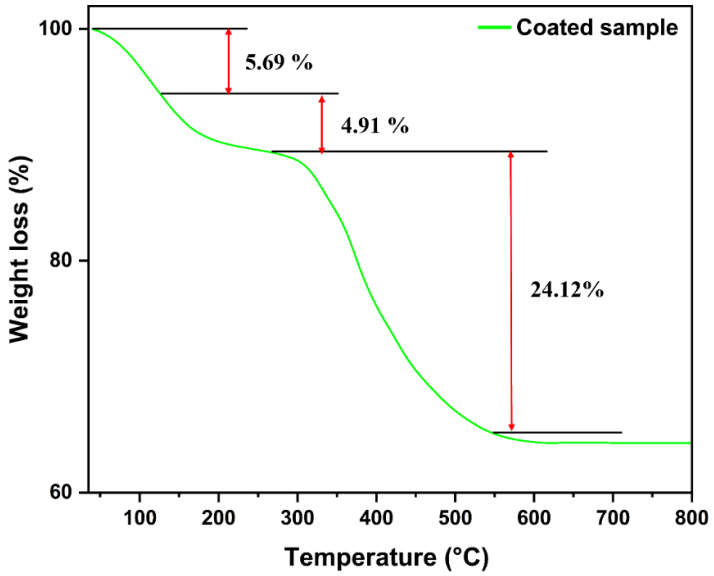

Figure 6.3. Thermogravimetric analysis (TGA) curve of the Zn-doped hydroxyapatite (HAp) and chitosan composite coated sample.

6.2.2 Optical microscopy and coating thickness

The optical microscopic image and cross-sectional images of the chitosan/Zn-doped HAp composite coatings on Mg alloy before and after heat treatment are presented in Figure 6.4 and Figure 6.5, respectively. Distinct changes in both surface morphology and coating thickness are evident with increasing temperature. In the as-coated condition Figure 6.4 (a), the coating shows a relatively smooth and uniform surface. The coating thickness is approximately 190 µm, representing the initial as-deposited composite layer formed through dip coating, shown in Figure 6.5 (a). The smooth surface morphology and substantial thickness again confirm effective adherence and homogeneous deposition of the polymer–ceramic composite prior to

any thermal modification. After heat treatment at 120 °C, as shown in Figure 6.4 (b), the surface remains largely continuous but displays signs of partial dehydration. The coating thickness, as shown in Figure 6.5 (b), decreases significantly to approximately 76 µm, indicating initial compaction and partial removal of volatile components, including absorbed moisture and loosely bound organic species, which is consistent with the TGA results [284]. At 240 °C Figure 6.4 (c), the coating shows a more heterogeneous morphology with increased darkness contrast. These features arise from partial degradation of chitosan of the coating. The coating thickness decrease slightly to 72 µm as shown in Figure 6.5 (c). Upon heating to 360 °C Figure 6.4 (d), the coating becomes distinctly darker in color, corresponding to the major decomposition of the organic matrix and dominance of the ceramic phase. The coating thickness further decreases to nearly 65 µm, reflecting pronounced shrinkage associated with major polymer decomposition and removal of residual organics, Figure 6.5 (d).

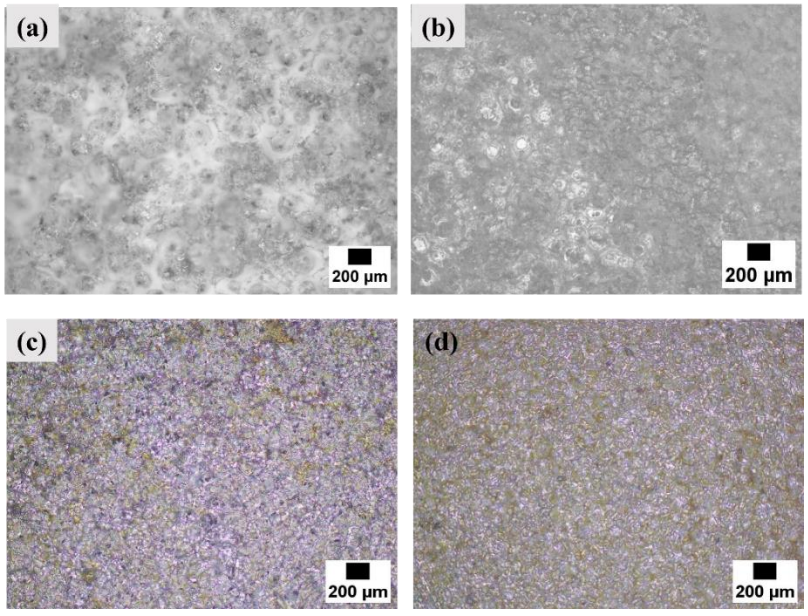

Figure 6.4. Optical micrographs of Zn-doped hydroxyapatite (HAp) and chitosan composite coatings on Mg alloy: (a) as-coated (before heat treatment), and after heat treatment at (b) 120 °C, (c) 240 °C, and (d) 360 °C.

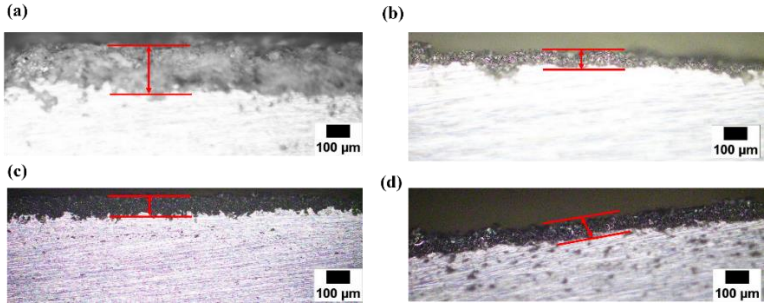

Figure 6.5. Cross-sectional optical micrographs of Zn-doped hydroxyapatite (HAp) and chitosan composite coatings on Mg alloy: (a) as-coated (before heat treatment), and after heat treatment at (b) 120 °C, (c) 240 °C, and (d) 360 °C

6.2.3 Surface morphology and roughness analysis

The surface morphologies of the chitosan/Zn-doped HAp coatings on Mg alloy before and after heat treatment are presented in Figure 6.6 (a–d). Figure 6.6 (a) shows the as-coated sample with a relatively compact and continuous surface, within which agglomerated bright particles are dispersed. These features are most likely hydroxyapatite (HAp) particle agglomerates embedded in the chitosan matrix. The surface can be seen uniform, homogenous and dense. After heat treatment (120 °C) as seen in Figure 6.6 (b), the surface images start to show micro-cracks and small surface roughening, which is attributed to partial dehydration and contraction of the chitosan matrix. At 240 °C [Figure 6.6 (c)], the coating is more granular and inhomogeneous, showing a well-developed rough surface with clustered HAp particles and evident porous areas. The increased granule size observed may coincide with partial degradation of chitosan and enhanced crystallization of HAp particles, representing an intermediate microstructural state characterized by maximum surface formation and increased roughness, as also similar trends observed by A. Jankovi et al. [283]. With further heating to 360 °C [Figure 6.6 (d)], the coating exhibits a highly porous and fractured morphology, attributed to extensive chitosan decomposition and carbonization. At this temperature, the polymer phase is majorly eliminated, leaving behind a brittle, mineral-rich structure dominated by Zn-doped HAp. The surface becomes noticeably coarser and less compact, consistent with the major decomposition of the organic binder and the corresponding loss of cohesive strength at elevated temperatures.

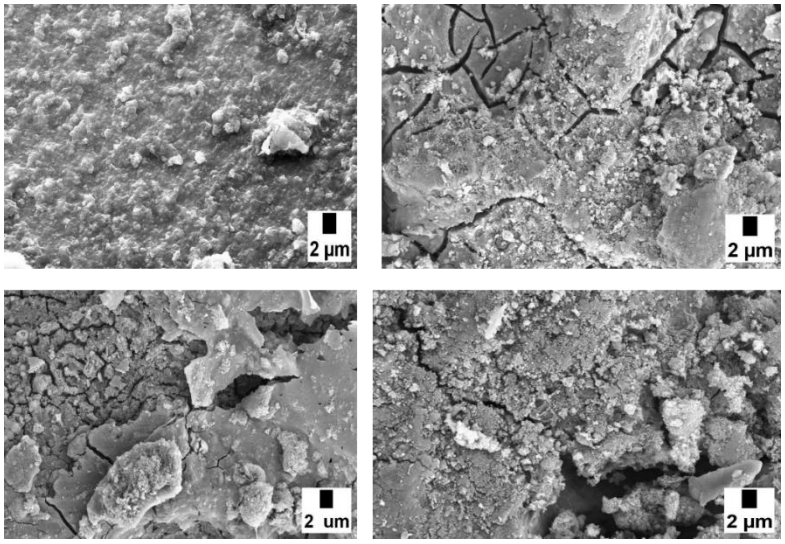

Figure 6.6. SEM micrographs of Zn-doped hydroxyapatite (HAp) and chitosan composite coatings on Mg alloy: (a) as-coated (before heat treatment), and after heat treatment at (b) 120 °C, (c) 240 °C, and (d) 360 °C

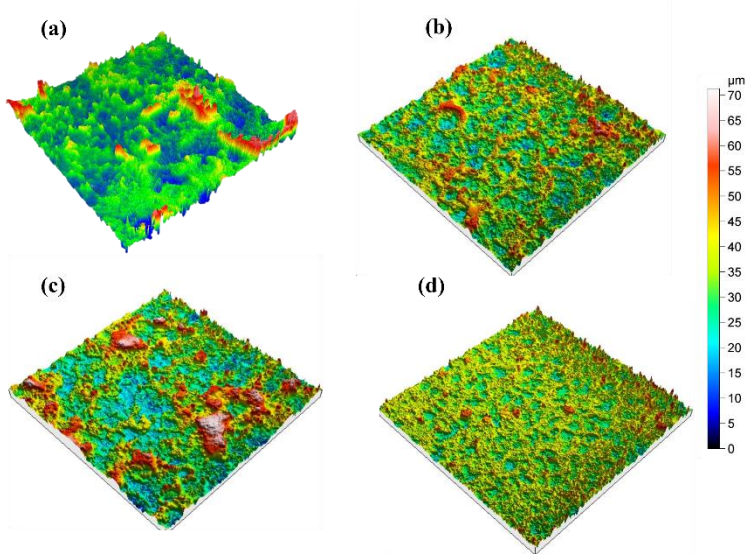

Figure 6.7. 3D surface profilometry images of Zn-doped hydroxyapatite (HAp) and chitosan composite coatings on Mg alloy: (a) as-coated (before heat treatment), and after heat treatment at (b) 120 °C, (c) 240 °C, and (d) 360 °C

The 3D surface roughness profiles of the coatings before and after heat treatment are shown in Figure 6.7 (a–d). The as-coated surface [Figure 6.7 (a)] displays an average roughness (Sa) of 7.2 µm, reflecting a moderately rough and uniform morphology typical of polymer–ceramic composite layers. After heating to 120 °C [Figure 6.7 (b)],

the roughness slightly decreases to 6.8 µm, likely due to densification associated with dehydration, while the coating remains continuous and adherent. At 240 °C [Figure 6.7 (c)], the roughness increases significantly to 9.2 µm. Partial degradation of chitosan and increased exposure of HAp particles result in a more heterogeneous surface with pronounced peak-to-valley features, as evident from the figure. This increased roughness enhances surface area which may promote improved biological interactions. Upon further heating to 360 °C [Figure 6.7 (d)], the roughness drops significantly to 4.5 µm, indicating structural collapse and densification resulting from substantial decomposition of the organic phase. The diminished surface relief is attributed to porous and compaction of the remaining ceramic component, producing a flatter, mineral-dominated surface. Overall, the evolution of surface roughness is consistent with the SEM findings: the initially polymer-rich and relatively smooth surface becomes progressively rougher at 240 °C, and then undergoes partial densification while becoming porous at 360 °C as the chitosan degrades and the ceramic phase begins to consolidate.

6.2.4 Phase and elemental analysis by XRD, EDS and FTIR

Figure 6.8 presents the X-ray diffraction (XRD) patterns of the as-coated sample and those heat-treated at 120 °C, 240 °C, and 360 °C. The XRD pattern of the Zn-doped hydroxyapatite (HAp)/chitosan composite coating on the Mg alloy substrate prior to heat treatment exhibits distinct HAp reflections at 2θ values of 25.87°, 28.96°, 31.82°, 32.24°, and 39.90°, along with a minor chitosan peak at 19.89° [281,285]. Intense reflections corresponding to the Mg substrate appear at 32.85°, 34.3°, and 47.1°, owing to X-ray penetration through the coating layer [281]. The as-deposited coating shows broad and weak HAp peaks, together with a low-intensity amorphous hump at low angles attributed to the polymeric chitosan matrix. These characteristics suggest low crystallinity, small apatite crystallite size, and a significant amorphous or organic phase content.

Upon mild heat treatment at 120 °C (S|120), the chitosan peak at 19.69° remains visible, and low-intensity peaks corresponding to HAp and Mg appear around 32.30° and 34.1°, indicating limited thermal ordering and partial removal of organics. A

strong crystalline Mg peak also emerges at 36.6°. At 240 °C (S|240), the chitosan peak disappears, while the HAp and Mg peaks become sharper and more intense, signifying improved crystallinity and partial decomposition or densification of the polymer phase, which enhances exposure and consolidation of the apatite domains. The most significant structural evolution occurs at 360 °C (S3), where HAp peaks are sharpest and most intense, reflecting substantial grain growth and the highest level of crystallographic ordering among all samples. The absence of the amorphous/chitosan feature beyond 240 °C further indicates that the organic binder undergoes major decomposition or carbonization at higher temperatures, resulting in a predominantly crystalline, mineral-rich coating.

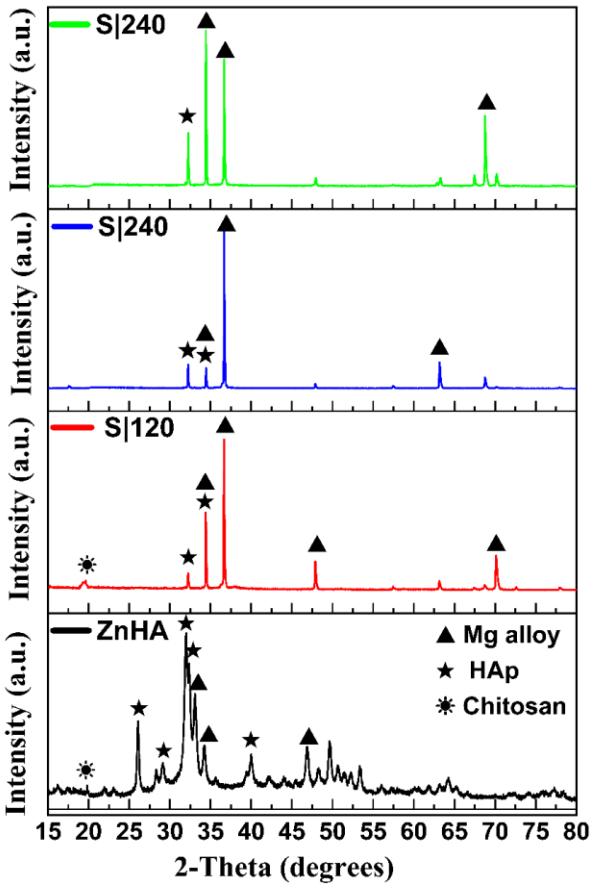

Figure 6.8. X-ray diffraction (XRD) patterns of Zn-doped hydroxyapatite (HAp) and chitosan composite coatings on Mg alloy: as-coated (ZnHA) and heat-treated samples at 120 °C (S|120), 240 °C (S|240), and 360 °C (S|360)

Figure 6.9 shows the FTIR spectra of the coated and heat-treated samples. In the as-coated condition (black line), the ZnHA spectrum confirms the successful formation of the composite, exhibiting the characteristic peaks of its main constituents. The strong stretching vibration of the phosphate group (PO_4^{3-}) in hydroxyapatite appears at 1025 cm^{-1}, while the chitosan component contributes distinct bands C–H stretching from its polymer backbone at 2950 cm^{-1}, N–H bending from primary amine (NH_2) groups at 1550 cm^{-1}, and C–C stretching in aromatic rings at 1410 cm^{-1}, These features are consistent with previous reports [286,287]. A broad absorption band centered near 3400 cm^{-1} corresponds to O–H stretching vibrations arising from both the materials and adsorbed moisture [288]. Upon mild heat treatment at 120°C (S|120, red line), the overall spectral features remain largely unchanged, indicating that the composite retains good thermal stability at this temperature. However, a slight decrease in the intensity of the broad O–H band is observed, which is attributed to the evaporation of physically adsorbed water from the coating surface. The fundamental structures of both hydroxyapatite and chitosan remain unaffected. When the temperature is increased to 240°C (S|240, blue line), a noticeable transformation occurs the band at 1590 cm^{-1}, corresponding to the amine (NH_2) groups of chitosan, disappears completely, signifying the onset of polymer decomposition as these groups are among the first to degrade. After heating to 360°C (S|360, green line), significant degradation is evident. The C–H stretching peaks around 2920 cm^{-1} vanish entirely, while only a weak band near 1400 cm^{-1}, associated with C=C bonds, persists. This confirms the complete burnout of the organic chitosan phase, leaving behind a predominantly inorganic, thermally stable hydroxyapatite coating on the magnesium substrate, as evidenced by the strong retained PO_4^{3-} peak.

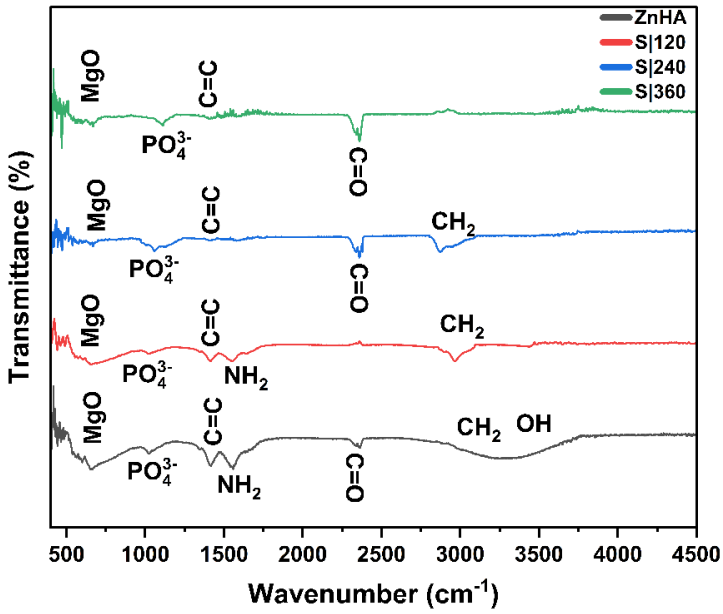

Figure 6.9. FTIR spectra of Zn-doped hydroxyapatite (HAp) and chitosan composite coatings on Mg alloy: as-coated (ZnHA) and heat-treated samples at 120 °C (S|120), 240 °C (S2|240), and 360 °C (S|360)

The EDS analysis shown in Figure 6.10 clearly illustrates the thermal evolution of the ZnHA–chitosan coatings. In the as-deposited condition, the high contents of N (11.91 wt%) and C (33.14 wt%) indicate a substantial presence of chitosan, while the detection of Ca and P confirms the presence of HAp. At 120 °C, partial degradation of chitosan begins, reflected by a decrease in N to 7.25 wt%, whereas the HA phase remains stable. At 240 °C, further reductions in N (5.1 wt%) and C (9.4 wt%) signify progressive chitosan decomposition. By 360 °C, there is substantial decomposition of chitosan, with N dropping to 1.8 wt% and C to 2.21 wt%. This thermal burnout exposes more of the underlying surface, as indicated by a rise in O to 16.4 wt%. With the gradual removal of the organic component, the relative concentrations of Ca and P increase, confirming HA enrichment and its stability at elevated temperatures. These EDS findings are consistent with the trends observed in other characterization results, including TGA, SEM, and 3D profilometry.

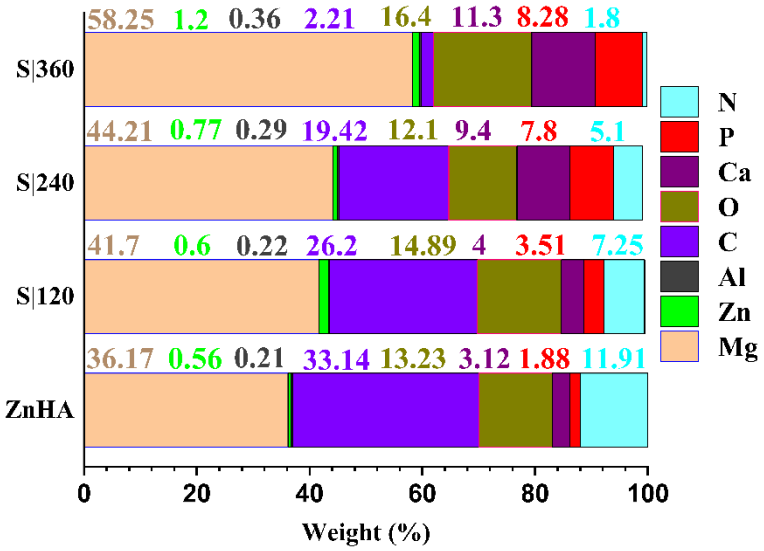

Figure 6.10. Elemental composition (EDS analysis) of Zn-doped hydroxyapatite (HAp) and chitosan composite coatings on Mg alloy: as-coated (ZnHA) and heat-treated samples at 120 °C (S|120), 240 °C (S|240), and 360 °C (S|360)

6.2.5 Adhesion strength of coated sample (relation with degradation and surface energy, interface energy)

As shown in Figure 6.11 (a–b), the tape scratch test was performed to evaluate the adhesion strength of the coatings before and after heat treatment according to ASTM D3359-22 (Method A). Figure 6.11 (c) presents the optical image of the as-deposited coating corresponding to Figure 6.11 (b). The groove is observed to be shallow with little edge lifting, suggesting moderate (as-formed) adhesion characteristic of a porous composite coating. Heat-treated sample at 120 °C [Figure 6.11 (d)], the wear scar is progressively enlarged with increasing size, becoming broader and more sectioned, showing alternate edge chipping and micro-debonding. This reduction of adhesion is ascribed to dehydration induced residual stresses in the coating. At 240 °C [Figure 6.11(e)] and the groove is clear, well-defined and no spallation, or edge lift has been observed which shows it exhibits excellent adhesion compared to all other samples. At moderate heat-treatment temperatures (~240 °C), chitosan does not undergo significant backbone degradation as shown in the TGA results and also evident in the study by Georgieva et al.[289]. In this temperature range near 240 °C, physically adsorbed and weakly bound moisture is removed from the

chitosan matrix. This dehydration facilitates closer packing and rearrangement of chitosan chains and embedded HAp particles, thereby strengthening non-covalent interactions–primarily hydrogen bonding between chitosan functional groups (–NH_2/–OH) and HAp surface groups (–PO_4^{3-}/–OH). These enhanced interfacial interactions promote mechanical interlocking and densification of the composite coating matrix; these similar observations also done the study by E.M. Al et al [282] and M. Đo et al. [283]. By 360 °C [Figure 6.13 (f)], pronounced edge chipping and localized spallation reappear, associated with significant chitosan degradation, resulting in reduced adhesion relative to the 240 °C sample. Overall, the coating heat-treated at 240 °C exhibits the highest adhesion, although all samples show generally good adhesion performance.

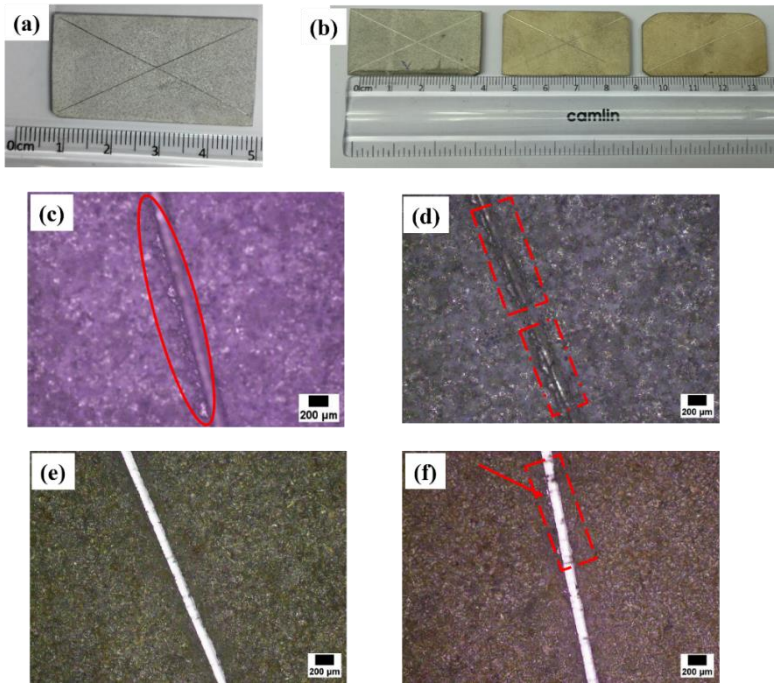

Figure 6.11 Scratch test images of Zn-doped hydroxyapatite (HAp) and chitosan composite coatings on Mg alloy for adhesion analysis: (a) as-coated (before heat treatment) sample and (b) heat-treated samples at 120 °C, 240 °C, and 360 °C. Optical micrographs of the scratch regions are shown for (c) the as-coated surface and (d–f) coatings after heat treatment at 120 °C, 240 °C, and 360 °C, respectively

6.2.6 Assessment of potentiodynamic test

Potentiodynamic polarization and EIS responses are presented in Figure 6.12. From the Tafel plot [Figure 6.12 (a)], the corrosion parameters E_{corr} and I_{corr} were extracted and are summarized in Table 6.3. For the as-coated ZnHA sample, E_{corr} is −1.172 V, which shifts positively to −1.114 V after heat treatment at 120 °C (S1|120) and further to −0.958 V at 240 °C (S2|240). However, a negative shift is observed at 360 °C (S3|360), where E_{corr} decreases to −1.240 V. A similar trend is reflected in the corrosion current density: I_{corr} decreases from 14.75 μA cm^{-2} (ZnHA) to 9.09 μA cm^{-2} (S1|120), reaching its minimum value of 2.82 μA cm^{-2} at 240 °C, but sharply increases to 28.58 μA cm^{-2} for S3|360. In Fig. 12(b), Nyquist fitting further clarifies the corrosion behavior. The as-deposited coating requires two-time constants, whereas the heat-treated samples are adequately described by a single capacitive loop, and these results have been quantified in the Table 6.4 and the circuit used to fit as deposited coating and heat-treated samples have been shown in Figure 6.12 (c) and (d) respectively. The largest semicircle diameter and highest charge-transfer resistance observed for S2 corroborate its lowest I_{corr}. Improvements in the CPE exponent (n), increasing from 0.74/0.64 (ZnHA) to 0.80–0.86 after thermal treatment, indicate enhanced interfacial uniformity and reduced surface heterogeneity. When the coated samples are heat-treated at a moderate temperature in the range of approximately 220–250 °C, bound water is removed, as evidenced by the TGA mass loss of less than 6%. This dehydration leads to physical consolidation of the coating, resulting in a denser and more compact matrix with improved incorporation of HAp particles, thereby minimizing micro-pathways for the penetration of corrosive ions. Importantly, this densification occurs without major degradation of the chitosan backbone, effectively sealing the coating and contributing to a reduced corrosion current density, a behavior typical of dense organic–inorganic hybrid coatings and consistent with the observations reported by Li et al [290] and Wang et al. [291]. Simultaneously, dehydration lowers the coating–substrate interfacial energy by strengthening hydrogen bonding between chitosan and HAp and by improving wetting of the magnesium surface. This promotes conformal adhesion and suppresses coating delamination under

corrosive conditions. Similar effects have been reported by Gnedenkov et al. [292], who demonstrated that boiling an initial plasma electrolytic oxidation (PEO) coating in $Na_2SiO_3 \cdot H_2O$ solution increased the surface density of chemisorption-active −OH groups, thereby enhancing chemical bonding capability and improving the adhesion of subsequent coatings. These findings are also consistent with the adhesion measurements, which show that the maximum adhesion strength is achieved at 240 °C. In contrast, excessive heating to 360 °C leads to partial degradation of the polymer binder, promotes crack formation, and results in partial exposure of the substrate surface, thereby significantly accelerating the corrosion process.

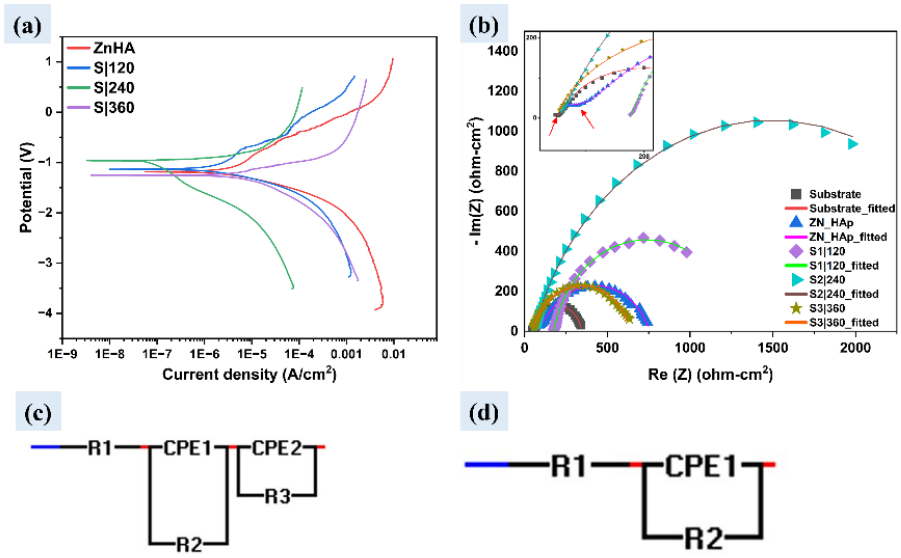

Figure 6.12. Corrosion test results: (a) Tafel plot, (b) Nyquist plot, (c) & (d) Equivalent circuits

Table 6.3 Corrosion parameters from Tafel plot

Sample	E_corr (V)	I_corr (µA)
Zn doped HAp	-1.172	14.75
S1|120	-1.114	9.09
S2|240	-0.958	2.82
S3|360	-1.2402	28.58

Table 6.4 EIS parameters from Nyquist plot

Sample	R1	R2	R3	CPE1		CPE2	
				p	n	p	n
MgZnHA	64	672	98	1.12×10^{-5}	0.74	1.76×10^{-6}	0.64
S1|120	176	1128	--	1.42×10^{-5}	0.86	--	--
S2|240	58	2869	--	7.77×10^{-6}	0.80	--	--
S3|360	50	600	--	4.98×10^{-6}	0.83	--	--

6.2.7 Invitro biocompatibility test

The MTT test in Figure 6.13 shows that all Zn-doped HAp/chitosan-coated samples possess favorable biocompatibility and cytocompatible (cell viability above 90.0%), indicating that the coatings are non-cytotoxic. The as-coated sample (ZnHA) exhibits a cell viability close to that of the control, showing that the as-deposited chitosan and Zn-doped HAp matrix allows metabolic activity and proliferation of cells. On mild heat treatment at 120 °C (S1), cell viability slightly goes up indicating the better surface stability and lower residual solvents/un- reacted organics that might hinder the cell growth in the initial stage. The highest cell viability is obtained with the 240 °C treated sample (S2) cell viability up to 110%, implying that mild temperature treatment could optimize on surface structure, including roughness, hydrophilicity and crystallinity for improved cell metabolism and growth. This increase is also consistent with the enhanced surface roughness and crystalline quality demonstrated by SEM and XRD characterizations. Upon additional heat treatment at 360 °C (S3), detection of a minimal decrease in cell viability below ca. 90% was observed, which can be attributed to an over decomposition of the chitosan matrix and higher brittleness or surface densification that would cause a decrease in surface functionality and bioactivity. However, all the samples remain above the cytotoxic threshold, thus here we demonstrate these samples are applicable to biological applications.

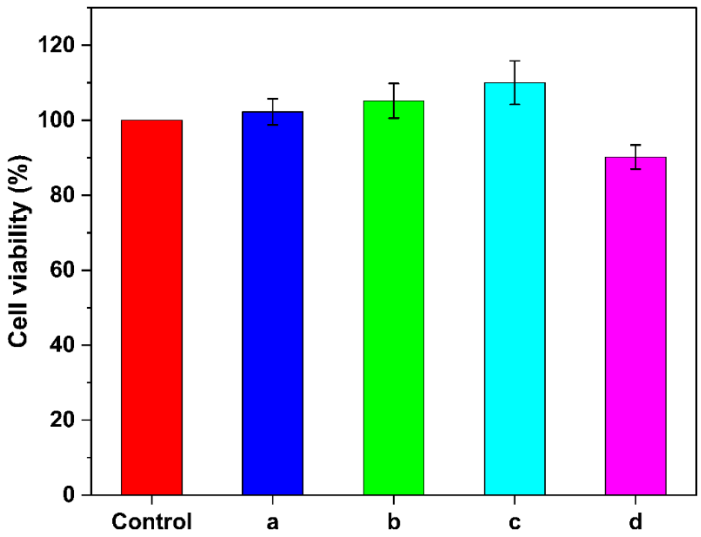

Figure 6.13. Cell viability results by MTT test for (a) as-coated (before heat treatment), and after heat treatment at (b) 120 °C, (c) 240 °C, and (d) 360 °C

These DAPI fluorescence images (Figure 6.14) and the corresponding quantitative analysis demonstrate profound differences in cell attachment between all of the samples. The as-coated ZnHA/chitosan [Figure 6.14 (a)] sample shows an intermediate quantity of attached cells. After treatment at 120 °C[Figure 6.14 (b)], a greater amount of cells, distributed in an ordered manner, is observed indicating that gentle modification improves surface affinity. The greatest number of adhered cells is observed for coating treated at 240 °C [Figure 6.14 (c)]. This observation can be ascribed to the enhanced surface roughness and increased crystallinity of the coating at this temperature, thus providing a beneficial form of micro/nano-topographical cues for cells attachment [293]. Conversely, the 360 °C processed coating [Figure 6.14 (d)] presents a decrease in cell number and attachment that can be attributed to the loss of hydrophilic groups and lower polymeric content resulting from a considerable chitosan decomposition.

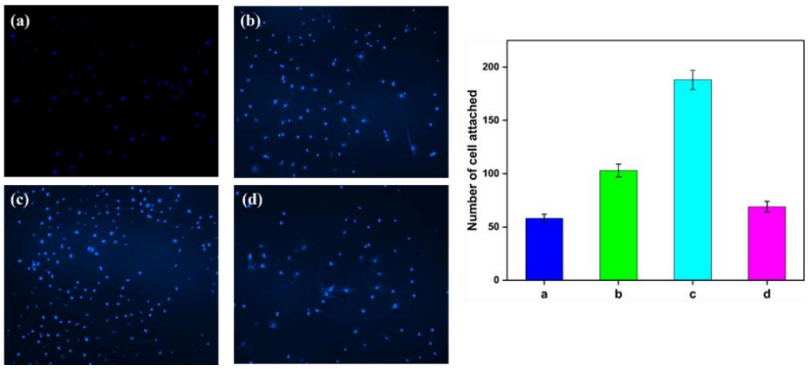

Figure 6.14. Cell attachment results by DAPI for (a) as-coated (before heat treatment), and after heat treatment at (b) 120 °C, (c) 240 °C, and (d) 360 °C

Overall, both MTT and DAPI analyses consistently indicate that moderate heat treatment at 240 °C provides the most favorable surface environment for cell adhesion and proliferation. This enhancement can be attributed to a synergistic effect of increased crystallinity, optimal surface roughness, and the balanced retention of organic functional groups within the Zn-doped HAp/chitosan matrix. In contrast, excessive heat treatment at 360 °C, though improving crystalline purity, reduces the polymeric contribution necessary for optimal bioactivity.

6.2.8 Evaluation of Cellular responses through FE simulation

In this study, the FE analysis revealed variations in mechanical strain and strain energy density (SED) on cell at the cell–substrate interface across different surface conditions, including both untreated and heat-treated substrates at different temperatures. The maximum principal strain contours [Figure 6.15] and quantitative data (Table 6.5) show that both strain and SED increased with surface roughness, reaching their highest values for the sample with an 8.96 µm roughness (average strain = 0.140; SED = 2.98×10^{-4} mJ/mm³). These findings suggest that surface morphology significantly influences local mechanical cues at the cell interface. Strain and SED, as forms of mechano-stimulation, are known to regulate critical cellular functions such as proliferation, differentiation, migration, and extracellular matrix (ECM) synthesis [294,295]. Mechanical strain replicates the physiological forces experienced by cells in vivo, activating mechanostimulation pathways involving integrins, focal adhesions, and cytoskeletal remodeling [296]. According to previous studies, strain magnitudes

exceeding 10,000 με are necessary to effectively stimulate osteogenic responses in bone cells [297,298]. Whereas, Kashani and Packirisamy [295] reported a positive correlation between SED at the cell interface and the migration behavior of adherent cells, demonstrating that increased substrate roughness enhances cell migration. The present results indicate that substrates with higher surface roughness can enhance strain concentration and SED near the cell interface, thereby promoting favourable mechanical environments for bone cell activation and tissue regeneration.

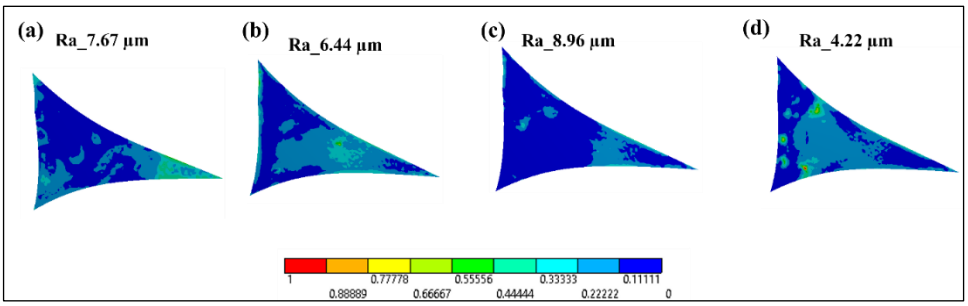

Figure 6.15. Maximum principle strain contours at cell interface for (a) untreated coated sample surface and (b), (C), (d) coated sample surface heat treated at 120 °C, 240 °C and 360 °C respectively

Table 6.5. Average Strain and Strain energy density (SED) oberved at cell interace for different substrate roughness

Substrate roughness	**7.67 µm**	**6.44 µm**	**8.96 µm**	**4.22 µm**
Avg strain	0.128	0.114	0.140	0.078
Avg SED (mJ/mm^3)	2.34×10^{-04}	1.82×10^{-04}	2.98×10^{-04}	1.22×10^{-04}

Chapter 7

Conclusions and Future Perspectives

7.1 Conclusion

This thesis addresses the critical challenge of rapid degradation and limited biological performance of magnesium (Mg)-based bioresorbable implants. A multidisciplinary approach integrating surface engineering, bioactive coating development, computational modeling, and data-driven optimization has been employed to design and optimize multifunctional coatings capable of enhancing corrosion resistance and biocompatibility under physiological conditions. The work systematically progresses from fundamental surface modification to advanced hybrid optimization and mechanistic understanding, establishing a coherent pathway for the development of next-generation Mg-based implant systems.

7.1.1 Evolution of Surface Functionalization: From Hydrophobicity to Bioactivity

The initial phase of the research demonstrated the successful fabrication of hydrophobic coatings on Mg alloys via a facile hydrothermal method. The development of hierarchical micro/nano-scale surface structures, combined with low surface energy modification, resulted in significant water repellency, achieving contact angles of ~130°. These surfaces exhibited markedly improved corrosion resistance in simulated body fluid (SBF), primarily by limiting electrolyte penetration and chloride ion ingress, as evidenced by reduced corrosion current density and a positive shift in corrosion potential.

While this study established the effectiveness of wettability control in mitigating corrosion, it also highlighted the need for further functionalization to meet biological requirements. Building upon this foundation, the research progressed toward the development of superhydrophobic and biofunctional coatings tailored specifically for biomedical applications.

7.1.2 Rational Design through Hybrid Data-Driven Optimization

To overcome the limitations of empirical coating design, a hybrid multi-objective optimization framework was developed. Response Surface Methodology using Central Composite Design (RSM-CCD) enabled systematic investigation of process parameters, while Artificial Neural Networks (ANN), enhanced through data augmentation, provided highly accurate predictive capability ($R^2 \approx 0.99$).

Coupling the ANN model with advanced optimization algorithms such as NSGA-II, Teaching-Learning-Based Optimization (TLBO), and Multi-Objective Particle Swarm Optimization (MOPSO) enabled simultaneous optimization of multiple performance parameters, including corrosion resistance, surface free energy, and surface roughness. The resulting Pareto fronts revealed a wide and tunable design space, achieving corrosion resistance efficiencies up to ~90% with controlled surface characteristics.

Importantly, the optimized parameter combinations facilitated a transition from hydrophobic to superhydrophobic behavior, yielding coatings with water contact angles exceeding 150°, thereby significantly enhancing surface functionality and corrosion protection.

This approach represents a significant advancement over conventional trial-and-error methodologies, offering a scalable and intelligent framework for the design of multifunctional coatings in biomedical and engineering applications.

7.1.3 Synergistic Role of Bioactive and Polymeric Components: HA, Zn, and Chitosan

A key contribution of this thesis lies in the development of composite bioactive coatings incorporating hydroxyapatite (HA), Zn-doped HA, and chitosan, thereby integrating corrosion protection with biological functionality.

HA coatings, owing to their chemical similarity to bone mineral, significantly reduced corrosion rates (~73.33%) by forming a protective and bioactive barrier. The incorporation of Zn^{2+} ions further enhanced performance (~82.45% reduction in

corrosion rate) by modifying crystallinity, surface energy, and providing antimicrobial effects, while also promoting cellular activity.

The introduction of chitosan as a polymeric matrix played a crucial role in achieving multifunctionality. Chitosan contributed to:

- Improved coating uniformity and adhesion by acting as an effective binder between ceramic particles and the Mg substrate,
- Enhanced corrosion resistance through its barrier properties,
- Increased bioactivity and antibacterial behavior due to its intrinsic biological functionality,
- Promotion of cell adhesion and proliferation via favorable surface chemistry and biocompatibility.
- Importantly, chitosan also mitigates the inherent brittleness of ceramic coatings such as HA, providing mechanical compliance and structural integrity to the composite system. The synergistic combination of HA (bioactivity), Zn (functional ion release), and chitosan (polymeric support) resulted in coatings that effectively balance electrochemical stability and biological performance.

7.1.4 Performance under Dynamic Physiological Conditions

Moving beyond conventional static evaluations, this work incorporated flow-induced shear stress (FISS) simulations and dynamic immersion experiments to better replicate physiological conditions. The results demonstrated that while material composition has a relatively minor influence on shear stress distribution, flow rate plays a dominant role in governing corrosion behavior.

Higher flow rates resulted in increased degradation due to elevated shear stress and enhanced mass transport of corrosive species. These findings highlight the limitations of static corrosion testing and emphasize the importance of evaluating biomaterials under realistic fluid flow environments.

The strong agreement between simulation and experimental observations validates the multiphysics approach adopted in this study and provides deeper insights into the interaction between fluid dynamics and material degradation.

7.1.5 Tailoring Coating Performance through Post-Deposition Heat Treatment

The final phase of the research established post-deposition heat treatment as a decisive parameter in controlling the microstructure and performance of chitosan/Zn-doped HA composite coatings. Controlled thermal processing induced a transition from a polymer-rich structure to a more crystalline ceramic-dominated architecture, significantly influencing coating adhesion, phase composition, and interfacial integrity.

An optimal heat treatment temperature of 240 °C was identified, achieving:

- Significant reduction in corrosion current density (~80.8%),
- Enhanced coating adhesion and phase purity,
- Improved structural stability and interfacial bonding,
- Superior biological performance, with cell viability exceeding 110%.

At this condition, an optimal balance was achieved between chitosan consolidation and hydroxyapatite crystallization. While chitosan provided initial flexibility and bioactivity, controlled heat treatment ensured structural refinement without complete degradation of the polymeric phase.

Finite element analysis further corroborated these findings by demonstrating enhanced strain and strain energy density at the cell-material interface, indicating improved mechanobiological stimulation, which is critical for tissue regeneration and implant integration.

7.1.6 Key Achievements of the Thesis

- Development of hydrophobic and superhydrophobic coatings with significantly improved corrosion resistance.

- Establishment of a hybrid optimization framework integrating RSM, ANN, and evolutionary algorithms (NSGA-II, TLBO, MOPSO).
- Achievement of high predictive accuracy ($R^2 \approx 0.99$) for coating performance modeling.
- Demonstration of up to ~90% corrosion resistance efficiency through optimized coatings.
- Successful integration of HA, Zn, and chitosan for multifunctional bioactive coatings.
- Elucidation of flow-induced corrosion behavior under dynamic physiological conditions.
- Identification of optimal post-deposition heat treatment (240 °C) for enhanced electrochemical and biological performance.

7.1.7 Limitations of the Present Study

Despite the significant advancements, certain limitations remain:

- The study is primarily limited to in vitro investigations, and in vivo validation is required to confirm long-term biological performance and degradation behavior.
- Long-term degradation kinetics and their interaction with tissue regeneration were not fully explored.
- Flow simulations and experiments were conducted under simplified conditions and may not fully capture the complexity of physiological environments.
- The predictive models, particularly ANN, are dependent on dataset size and quality, which may limit generalization beyond the studied parameter space.

7.2 Future Perspectives

Building upon the findings of this thesis, several directions for future research are identified:

- **In vivo validation:** Long-term animal and clinical studies to assess degradation behavior, tissue response, and implant safety.

- **Controlled ion release:** Optimization of Mg^{2+} and Zn^{2+} ion release to balance bioactivity and cytotoxicity.
- **Advanced optimization strategies:** Integration of multi-criteria decision-making tools such as TOPSIS, fuzzy logic, and weighted optimization.
- **Coupled multiphysics modeling:** Development of comprehensive models integrating corrosion, mechanical loading, and biological interactions.
- **Process scalability and translation:** Ensuring reproducibility, scalability, and regulatory compliance for clinical and industrial implementation.

Final Remark

This thesis advances the fundamental understanding of coating design, degradation mechanisms, and biological interactions in magnesium-based biomaterials. By integrating surface engineering, bioactive materials (HA, Zn, and chitosan), multiphysics modeling, and artificial intelligence-driven optimization, it establishes a robust and scalable framework for the rational design of high-performance bioresorbable implants. The outcomes of this work contribute significantly toward bridging the gap between laboratory-scale research and clinically viable magnesium-based implant technologies, positioning this approach at the forefront of next-generation biomaterials development.

References

[1] R. Li, G. Wilde, Y. Zhang, Synergizing mechanical properties and damping capacities in a lightweight Al-Zn-Li-Mg-Cu alloy, J. Alloys Compd. 886 (2021) 161285. https://doi.org/10.1016/j.jallcom.2021.161285.

[2] J. Zhang, J. Miao, N. Balasubramani, D.H. Cho, T. Avey, C.-Y. Chang, A.A. Luo, Magnesium research and applications: Past, present and future, J. Magnes. Alloy. 11 (2023) 3867–3895. https://doi.org/10.1016/j.jma.2023.11.007.

[3] B. Liu, J. Yang, X. Zhang, Q. Yang, J. Zhang, X. Li, Development and application of magnesium alloy parts for automotive OEMs: A review, J. Magnes. Alloy. 11 (2023) 15–47. https://doi.org/10.1016/j.jma.2022.12.015.

[4] J. Wang, Y. Zou, C. Dang, Z. Wan, J. Wang, F. Pan, Research Progress and the Prospect of Damping Magnesium Alloys, Materials (Basel). 17 (2024). https://doi.org/10.3390/ma17061285.

[5] S.V.S. Prasad, S.B. Prasad, K. Verma, R.K. Mishra, V. Kumar, S. Singh, The role and significance of Magnesium in modern day research-A review, J. Magnes. Alloy. 10 (2022) 1–61. https://doi.org/https://doi.org/10.1016/j.jma.2021.05.012.

[6] M. Rahman, N.K. Dutta, N. Roy Choudhury, Magnesium Alloys With Tunable Interfaces as Bone Implant Materials, Front. Bioeng. Biotechnol. 8 (2020). https://doi.org/10.3389/fbioe.2020.00564.

[7] M. Aikin, V. Shalomeev, V. Kukhar, A. Kostryzhev, I. Kuziev, V. Kulynych, O. Dykha, V. Dytyniuk, O. Shapoval, A. Zagorskis, V. Burko, O. Khliestova, V. Titov, O. Hrushko, Recent Advances in Biodegradable Magnesium Alloys for Medical Implants: Evolution, Innovations, and Clinical Translation, Crystals 15 (2025). https://doi.org/10.3390/cryst15080671.

[8] N. Singh, U. Batra, K. Kumar, N. Ahuja, A. Mahapatro, Progress in bioactive surface coatings on biodegradable Mg alloys: A critical review towards clinical translation, Bioact. Mater. 19 (2023) 717–757.

https://doi.org/10.1016/j.bioactmat.2022.05.009.

[9] A.W. Hashmi, Y. Tian, C. Wang, D. Wang, B. Sagbas, A.P.V. Puerta, M.R. Sankar, Adapted interfaces in magnesium alloys for biomedical applications: Synthesis, properties, and performance enhancement, J. Alloys Compd. 1048 (2025) 185179. https://doi.org/https://doi.org/10.1016/j.jallcom.2025.185179.

[10] P.C. Banerjee, S. Al-saadi, L. Choudhary, Magnesium Implants : Prospects and Challenges, 2 (2019) 1–21. https://doi.org/10.3390/ma12010136.

[11] F. Amerstorfer, S.F. Fischerauer, L. Fischer, J. Eichler, J. Draxler, A. Zitek, M. Meischel, E. Martinelli, T. Kraus, S. Hann, S.E. Stanzl-tschegg, P.J. Uggowitzer, J.F. Löffler, A.M. Weinberg, T. Prohaska, Acta Biomaterialia Long-term in vivo degradation behavior and near-implant distribution of resorbed elements for magnesium alloys WZ21 and ZX50, Acta Biomater. 42 (2016) 440–450. https://doi.org/10.1016/j.actbio.2016.06.025.

[12] L. Wei, Z. Gao, RSC Advances and protection , and novel coating materials of, (2023) 8427–8463. https://doi.org/10.1039/d2ra07829e.

[13] A.K. Vaqif, Review of degradation behaviour biodegradable magne- sium MgZnCa alloys, 7 (2025) 1–11.

[14] F. Peng, H. Li, D. Wang, P. Tian, Y. Tian, G. Yuan, D. Xu, X. Liu, Enhanced Corrosion Resistance and Biocompatibility of Magnesium Alloy by Mg − Al-Layered Double Hydroxide, (2016). https://doi.org/10.1021/acsami.6b12974.

[15] K.X. Kuah, S. Wijesinghe, D.J. Blackwood, Toward understanding in vivo corrosion : Influence of interfacial hydrogen gas build-up on degradation of magnesium alloy implants, (2023) 5–8. https://doi.org/10.1002/jbm.a.37446.

[16] B. Zeller-plumhoff, A.R. Akkineni, M. Mosshammer, Oxygen-sensitive nanoparticles reveal the spatiotemporal dynamics of oxygen reduction during magnesium implant biodegradation, (n.d.). https://doi.org/10.1038/s41529-022-00302-9.

[17] O. Jung, R. Smeets, P. Hartjen, R. Schnettler, F. Feyerabend, M. Klein, N. Wegner, F. Walther, D. Stangier, A. Henningsen, C. Rendenbach, M. Heiland, M. Barbeck, A. Kopp, Improved In Vitro Test Procedure for Full Assessment of the Cytocompatibility of Degradable Magnesium Based on ISO 10993-5/-12, Int. J. Mol. Sci. 20 (2019). https://doi.org/10.3390/ijms20020255.

[18] L. Xu, X. Liu, K. Sun, R. Fu, G. Wang, Corrosion Behavior in Magnesium-Based Alloys for Biomedical Applications, Materials (Basel). 15 (2022). https://doi.org/10.3390/ma15072613.

[19] H. Chen, B. Yuan, R. Zhao, X. Yang, Z. Xiao, A. Aurora, B. Ana, X. Zhu, A. Vasile, X. Zhang, Evaluation on the corrosion resistance , antibacterial property and osteogenic activity of biodegradable Mg-Ca and Mg-Ca-Zn-Ag alloys, J. Magnes. Alloy. 10 (2022) 3380–3396. https://doi.org/10.1016/j.jma.2021.05.013.

[20] L. Choudhary, J. Szmerling, R. Goldwasser, R.K.S. Raman, Investigations into stress corrosion cracking behaviour of AZ91D magnesium alloy in physiological environment, Procedia Eng. 10 (2011) 518–523. https://doi.org/10.1016/j.proeng.2011.04.087.

[21] H. Jia, Y. Li, S. Xu, L. Wang, Y. Xi, The strain rate-dependent stress corrosion cracking behavior of a biodegradable Mg-Zn-Cu alloy, Sci. Rep. 16 (2026) 3449. https://doi.org/10.1038/s41598-025-33420-w.

[22] H. Muhammad, R. Tariq, M. Ishtiaq, H. Kang, U.M. Chaudry, T. Jun, A Critical Review on the Comparative Assessment of Rare-Earth and Non-Rare-Earth Alloying in Magnesium Alloys, (2025) 1–21.

[23] J. Li, X. Zhang, W. Fan, Novel Al-Ce-C-O-Mg Grain Refiners with Superior Efficiency and Mechanical Properties Enhancement for AZ91 Alloys, (2025) 1–13.

[24] H. Zhao, J. Cheng, C. Zhao, M. Wen, R. Wang, D. Wu, Z. Wu, F. Yang, L. Sheng, The Recent Developments of Thermomechanical Processing for

Biomedical Mg Alloys and Their Clinical Applications, (2025) 9–11.

[25] M. L., S. Kar, N. B., S.S. Dhilip Kumar, M. Nagai, T.S. Santra, Formation of nanostructures on magnesium alloy by anodization for potential biomedical applications, Mater. Today Commun. 25 (2020) 101403. https://doi.org/10.1016/j.mtcomm.2020.101403.

[26] V.S. Simi, V.S. Vineeth, S. Arun Kumar, A. Srinivasan, Corrosion performance of electrochemically anodized and calcium phosphate coated AZ31 magnesium alloy, Mater. Chem. Phys. 343 (2025) 131066. https://doi.org/10.1016/j.matchemphys.2025.131066.

[27] H. Gerengi, M. Cabrini, M.M. Solomon, E. Kaya, L. Gritti, M.L. Yola, Chemical, Electrochemical, and Surface Morphological Studies of the Corrosion Behavior of the AZ31 Alloy in Simulated Body Fluid: Effect of NaOH and H2O2 Surface Pretreatments on the Corrosion Resistance Property, ACS Omega 7 (2022) 26687–26700. https://doi.org/10.1021/acsomega.2c02998.

[28] S. Zhang, J. Jiang, X. Zou, N. Liu, C. Liang, Progress of laser surface treatment on magnesium alloy, (2022) 1–16. https://doi.org/10.3389/fchem.2022.999630.

[29] Y. Zhang, H. Wang, Novel Phosphate Conversion Coating with Superior Corrosion Resistance on the Mg-Al-RE Alloy Based on the Introduction of Silane, ACS Omega 8 (2023) 29374–29387. https://doi.org/10.1021/acsomega.3c02824.

[30] B. Vaghefinazari, E. Wierzbicka, P. Visser, R. Posner, R. Arrabal, E. Matykina, M. Mohedano, C. Blawert, M. Zheludkevich, S. Lamaka, Chromate-Free Corrosion Protection Strategies for Magnesium Alloys—A Review: PART I—Pre-Treatment and Conversion Coating, Materials (Basel). 15 (2022). https://doi.org/10.3390/ma15238676.

[31] K. Cesarz-Andraczke, K. Pałka, M. Skonieczna, A new method of applying PLA coatings on the surface of magnesium alloy using the FDM technique,

Surf. Coatings Technol. 479 (2024) 130462. https://doi.org/10.1016/j.surfcoat.2024.130462.

[32] N. Fiedler, M. Teske, S.-C. Nelz, J.W. Flügge, V. Senz, D. Bajer, N. Grabow, S. Oschatz, In Vitro Corrosion of Polyester-Coated Magnesium Alloy under pH-Static Conditions, ACS Biomater. Sci. Eng. 10 (2024) 5844–5855. https://doi.org/10.1021/acsbiomaterials.4c00835.

[33] L. Qian, M. Sun, N. Huang, P. Yang, F. Jing, A. Zhao, B. Akhavan, Biodegradable PTMC-MAO composite coatings on AZ31 Mg-alloys for enhanced corrosion-resistance, J. Alloys Compd. 998 (2024) 175017. https://doi.org/https://doi.org/10.1016/j.jallcom.2024.175017.

[34] S. Mahmud, M.M. Rahman, H. Khatun, M.O. Ali, M.R. Ali, M. Rahaman, S. Islam, Y. Ali, Ceramic coating on Mg alloy for enhanced degradation resistance as implant material, Surf. Coatings Technol. 479 (2024) 130544. https://doi.org/10.1016/j.surfcoat.2024.130544.

[35] H. Khatun, M. Rahman, S. Mahmud, M.O. Ali, M. Akter, Current advancements of hybrid coating on Mg alloys for medical applications, Results Eng. 18 (2023) 101162. https://doi.org/10.1016/j.rineng.2023.101162.

[36] A. You, M. Be, I. In, Hydrothermal preparation of magnesium alloy surface composite coatings and its performance research, (2025). https://doi.org/10.1063/5.0221930.

[37] S. Kunjukunju, A. Roy, J. Ohodnicki, B. Lee, J.E. Candiello, M. Patil, P.N. Kumta, Bioactive Synthetic Polymer-Based Polyelectrolyte LbL Coating Assembly on Surface Treated AZ31-Mg Alloys, (2023).

[38] M.T. Selvan, M. Somasundaram, A.R. Annamalai, Optimizing dry milling of stir- cast and heat-treated AZ80 magnesium alloy using multiple criteria optimization technique : an experimental study, (2024) 1–16.

[39] J. Kim, D. Gun, K. Kyung, H. Ryu, Piecewise Response Surface Methodology for Enhanced Modeling and Optimization of Complex Systems, Korean J.

Chem. Eng. 42 (2025) 537–545. https://doi.org/10.1007/s11814-024-00362-4.

[40] M.A. Bezerra, R.E. Santelli, E.P. Oliveira, L.S. Villar, L.A. Escaleira, Response surface methodology (RSM) as a tool for optimization in analytical chemistry, Talanta 76 (2008) 965–977. https://doi.org/10.1016/j.talanta.2008.05.019.

[41] S. Amukarimi, Biodegradable magnesium-based biomaterials : An overview of challenges and opportunities, (2021) 123–144. https://doi.org/10.1002/mco2.59.

[42] Y.S. Chaudhari, M.Y. Chaudhari, A.D. Gholap, M.I. Alam, T.J. Webster, Surface engineering of nano magnesium alloys for orthopedic implants : a systematic review of strategies to mitigate corrosion and promote bone regeneration, (2025) 1–18. https://doi.org/10.3389/fbioe.2025.1617585.

[43] G. Dhanuskar, A. Kuthe, D. Bhiogade, B. Sarode, Investigating microstructural and mechanical properties evolution in biomedical AZ31 magnesium alloy under different casting conditions, (2025) 1–20.

[44] M.G. Jiru, E.A. Esleman, Effect of powder metallurgy parameters on microstructure , mechanical , and bio-corrosion properties of Mg-alloys for biodegradable orthopedic implants, (2026) 1–18.

[45] S. Ali, M. Irfan, U.M. Niazi, A. Majdi, A. Rani, A. Rashedi, S. Rahman, M. Kamal, A. Khan, M.A. Alsaiari, S. Legutko, J. Petr, A. Trefil, Microstructure and Mechanical Properties of Modified 316L Stainless Steel Alloy for Biomedical Applications Using Powder Metallurgy, (2022).

[46] B. Baufeld, O. Van Der Biest, Mechanical properties of Ti-6Al-4V specimens produced by shaped metal deposition, 6996 (2009). https://doi.org/10.1088/1468-6996/10/1/015008.

[47] T. Odaira, S. Xu, K. Hirata, X. Xu, T. Omori, K. Ueki, K. Ueda, T. Narushima, M. Nagasako, S. Harjo, T. Kawasaki, L. Bodnárová, P. Sedlák, H. Seiner, R. Kainuma, Flexible and Tough Superelastic Co – Cr Alloys for Biomedical Applications, (2022). https://doi.org/10.1002/adma.202202305.

[48] H. Yang, B. Jia, Z. Zhang, X. Qu, G. Li, W. Lin, D. Zhu, K. Dai, Y. Zheng, Alloying design of biodegradable zinc as promising bone implants for load-bearing applications, Nat. Commun. 11 (2020) 401. https://doi.org/10.1038/s41467-019-14153-7.

[49] M. Salama, F. Maria, C. Santos, Biodegradable Iron and Porous Iron : Mechanical Properties , Degradation Behaviour , Manufacturing Routes and Biomedical Applications, (2022).

[50] S. El-khatib, Critical Review on Polylactic Acid : Properties , Structure , (2022).

[51] L. Dong, G. Zhang, Z. Shen, X. Hong, Y. Xing, Y. Wu, W. Yang, B. Zhang, Z. Shi, Degradation of WE43 Magnesium Alloy in Vivo and Its Degradation Products on Macrophages, (2025). https://doi.org/10.1021/acsomega.4c09349.

[52] S.K. Sharma, K.K. Saxena, V. Malik, K.A. Mohammed, C. Prakash, D. Buddhi, S. Dixit, Significance of Alloying Elements on the Mechanical Characteristics of Mg-Based Materials for Biomedical Applications, (2022).

[53] L. Del, C. Gutie, Biomaterials for orthopedic applications and techniques to improve corrosion resistance and mechanical properties for magnesium alloy : a review, (n.d.). https://doi.org/10.1007/s10853-023-08237-5.

[54] S.R. Kim, K.M. Lee, J.H. Kim, Y.J. Choi, H.I. Park, H.C. Jung, H.J. Roh, J. Hye, L. Han, J.R. Kim, B.K. Lee, Biocompatibility evaluation of peo - treated magnesium alloy implants placed in rabbit femur condyle notches and paravertebral muscles, Biomater. Res. (2022) 1–19. https://doi.org/10.1186/s40824-022-00279-1.

[55] T. Approach, Engineering Corrosion Resistance in Magnesium Alloys for Biomedical Applications : A Synergy of Zn / Ca Atomic Ratio and, (2024).

[56] J. Pan, J. Zhang, Y. Li, F. Yang, Y. Yu, S. Wang, Jie Pan, Jinling Zhang, * Yelei Li, Fanxi Yang, Yanchong Yu, * and Shebin Wang, (2024). https://doi.org/10.1021/acs.langmuir.4c01715.

[57] S. Torii, A. Yamamoto, A. Yoshikawa, L. Lu, M. Sasaki, S. Obuchi, A. Wada, Degradation of a novel magnesium alloy - based bioresorbable coronary scaffold in a swine coronary artery model, Cardiovasc. Interv. Ther. 39 (2024) 428–437. https://doi.org/10.1007/s12928-024-01023-3.

[58] A. Drobyshev, A. Komissarov, N. Redko, Z. Gurganchova, E.S. Statnik, V. Bazhenov, I. Sadykova, A. Miterev, I. Romanenko, O. Yanushevich, Bone Remodeling Interaction with Magnesium Alloy Implants Studied by SEM and EDX, Materials (Basel). 15 (2022). https://doi.org/10.3390/ma15217529.

[59] A. Motaharinia, J.W. Drelich, S. Sharif, A.F. Ismail, Overview of porous magnesium-based scaffolds : development , properties and biomedical applications, (2025).

[60] J. Cheng, Q. Deng, W. Wu, X. Feng, Q. Pang, Study on the effect and mechanism of gold nanocoated magnesium bone scaffolds for bone repair, BMC Musculoskelet. Disord. 27 (2025) 13. https://doi.org/10.1186/s12891-025-09375-4.

[61] G. Giavaresi, D. Bellavia, A. De Luca, V. Costa, L. Raimondi, A. Cordaro, M. Sartori, S. Terrando, A. Toscano, G. Pignatti, M. Fini, Magnesium Alloys in Orthopedics : A Systematic Review on Approaches , Coatings and Strategies to Improve Biocompatibility , Osteogenic Properties and Osteointegration Capabilities, (2024).

[62] J. Xie, T. Zhang, J. Jiang, W. Xue, W. Wang, J. Ni, X. Zhang, X. Liu, Advances in magnesium-based implants for biomedical applications : A comprehensive review and future perspectives ☆, J. Magnes. Alloy. 13 (2025) 2978–3003. https://doi.org/10.1016/j.jma.2025.05.009.

[63] J. Seitz, A. Lucas, M. Kirschner, Magnesium-Based Compression Screws : A Novelty in the Clinical Use of Implants, 68 (2016) 1177–1182. https://doi.org/10.1007/s11837-015-1773-1.

[64] M. Haude, A. Wlodarczak, R.J. van der Schaaf, J. Torzewski, B. Ferdinande, J.

Escaned, J.F. Iglesias, J. Bennett, G. Toth, M. Joner, R. Toelg, M. Wiemer, G. Olivecrona, P. Vermeersch, H.M. Garcia-Garcia, R. Waksman, Safety and performance of the third-generation drug-eluting resorbable coronary magnesium scaffold system in the treatment of subjects with de novo coronary artery lesions: 6-month results of the prospective, multicenter BIOMAG-I first-in-human study, EClinicalMedicine 59 (2023). https://doi.org/10.1016/j.eclinm.2023.101940.

[65] H.M. Garcia-Garcia, M. Haude, K. Kuku, A. Hideo-Kajita, H. Ince, A. Abizaid, R. Tölg, P.A. Lemos, C. von Birgelen, E.H. Christiansen, W. Wijns, J. Escaned, J. Dijkstra, R. Waksman, In vivo serial invasive imaging of the second-generation drug-eluting absorbable metal scaffold (Magmaris — DREAMS 2G) in de novo coronary lesions: Insights from the BIOSOLVE-II First-In-Man Trial, Int. J. Cardiol. 255 (2018) 22–28. https://doi.org/10.1016/j.ijcard.2017.12.053.

[66] L. Mao, L. shen, J. Chen, X. Zhang, M. Kwak, Y. Wu, R. Fan, L. Zhang, J. Pei, G. Yuan, C. Song, J. Ge, W. Ding, A promising biodegradable magnesium alloy suitable for clinical vascular stent application, Sci. Rep. 7 (2017) 46343. https://doi.org/10.1038/srep46343.

[67] R. Waksman, Current state of the absorbable metallic (magnesium) stent Magnesium alloy composition , design evolution and future developments, (2026) 1–15.

[68] D.L. Merson, S. Physics, Mechanical and corrosion anisotropy of magnesium single crystal, (2025) 39–52.

[69] S.A.M. Magnesium, Corrosion and Mechanical Behavior of the As-Cast and, (2023).

[70] B. Applications, L. Xu, X. Liu, K. Sun, R. Fu, G. Wang, Corrosion Behavior in Magnesium-Based Alloys for, (2022).

[71] H. Zhang, X. Li, Z. Qu, W. Zhang, Q. Wang, D. Cao, Y. Wang, X. Wang, Y.

Wang, L. Yu, J. Ding, Effects of serum proteins on corrosion rates and product bioabsorbability of biodegradable metals, (2024).

[72] R. Academy, R. Federation, Triazoles as a class of multifunctional corrosion inhibitors ., (2021) 29–53. https://doi.org/10.17675/2305-6894-2021-10-1-2.

[73] A.S. Gnedenkov, S.L. Sinebryukhov, V.S. Filonina, V.S. Egorkin, A.Y. Ustinov, V.I. Sergienko, S. V Gnedenkov, The detailed corrosion performance of bioresorbable Mg-0 . 8Ca alloy in physiological solutions, 10 (2022) 1326–1350. https://doi.org/10.1016/j.jma.2021.11.027.

[74] X. Li, B. Ma, Study on the mechanism of grain size and residual stress coupling distribution on the intergranular corrosion susceptibility of AZ31B magnesium alloy, (2024) 38832–38854. https://doi.org/10.1039/d4ra07164f.

[75] J. Jiang, X. Geng, X. Zhang, Stress corrosion cracking of magnesium alloys : A review, J. Magnes. Alloy. 11 (2023) 1906–1930. https://doi.org/10.1016/j.jma.2023.05.011.

[76] K. An, W. Tong, Y. Wang, Y. Qing, Y. Sui, Y. Xu, C. Ni, Eco-Friendly Superhydrophobic Coupling Conversion Coating with Corrosion Resistance on Magnesium Alloy, (2023). https://doi.org/10.1021/acs.langmuir.3c00025.

[77] J.J. Kalmoni, F.L. Heale, C.S. Blackman, I.P. Parkin, C.J. Carmalt, A Single-Step Route to Robust and Fluorine-Free Superhydrophobic Coatings via Aerosol-Assisted Chemical Vapor Deposition, (2023). https://doi.org/10.1021/acs.langmuir.3c00554.

[78] V. Diniz, S. Rath, C.R. Crick, Optimizing Superhydrophobic Coatings: The Role of Catalysts, Additives, and Composition on UV and Thermal Stability of Inverse Vulcanization Polymers, (2025) 0–5. https://doi.org/10.1021/acsapm.4c02634.

[79] L. Ch, L. Veleva, S. Diana, R. Ram, Hybrid Coating of Polystyrene – ZrO 2 for Corrosion Protection of AM Magnesium Alloys, (2023).

[80] C.S. Rauta, G. Majumdar, S. Mukherjee, S. Sarkar, An eco-friendly one-step pretreatment method for the synthesis of electroless coating on magnesium alloy, Phys. Scr. 99 (2024) 105934. https://doi.org/10.1088/1402-4896/ad733c.

[81] A. Groza, M.E. Hurjui, S.A. Yehia-Alexe, C. Staicu, C. Bleotu, S.L. Iconaru, C.S. Ciobanu, L. Ghegoiu, D. Predoi, Influence of Electron Beam Irradiation and RPMI Immersion on the Development of Magnesium-Doped Hydroxyapatite/Chitosan Composite Bioactive Layers for Biomedical Applications, Polymers (Basel). 17 (2025). https://doi.org/10.3390/polym17040533.

[82] J. He, X. Cheng, S. Zhang, Y. Tao, H. Shi, Fabrication and characterization of an anti-corrosion / infection VAN @ PLGA / HA / CMCS composite coating on magnesium alloy, J. Mater. Sci. Mater. Med. (2025). https://doi.org/10.1007/s10856-025-06956-6.

[83] I. Ullah, S. Ali, Z. Ahmad, A. Khan, M.A. Siddiqui, Y. Jiang, H. Li, I. Shawish, M. Bououdina, W. Zuo, Physicochemical Properties and Simulation of Magnesium/Zinc Binary-Substituted Hydroxyapatite with Enhanced Biocompatibility and Antibacterial Ability, ACS Appl. Bio Mater. 6 (2023) 5349–5359. https://doi.org/10.1021/acsabm.3c00599.

[84] H.-H. Hou, B.-S. Lee, Y.-C. Liu, Y.-P. Wang, W.-T. Kuo, I.-H. Chen, A.-C. He, C.-H. Lai, K.-L. Tung, Y.-W. Chen, Vapor-Induced Pore-Forming Atmospheric-Plasma-Sprayed Zinc-, Strontium-, and Magnesium-Doped Hydroxyapatite Coatings on Titanium Implants Enhance New Bone Formation—An In Vivo and In Vitro Investigation, Int. J. Mol. Sci. 24 (2023). https://doi.org/10.3390/ijms24054933.

[85] M. Hamza, Q. Kanwal, Z. Ali, S. Zargar, A.H. Alshammari, T.A. Wani, M. Rizwan, K. Rohm, M.A. Mushtaq, Exploring the molecular biology of zinc-doped hydroxyapatite nanocomposites as fillers for dental materials : a self-defensive approach targeting bacterial DNA Exploring the molecular biology of zinc-doped hydroxyapatite nanocomposites as fi llers for dental materials : a

self-defensive approach targeting bacterial DNA, (n.d.).

[86] O.C. Activity, Phenolic Modified Ceramic Coating on Biodegradable Mg Alloy : The Improved Corrosion Resistance and, (2017). https://doi.org/10.3390/ma10070696.

[87] D. V Mashtalyar, K. V Nadaraia, I.M. Imshinetskiy, S.L. Sinebryukhov, S. V Gnedenkov, New approach to formation of coatings on Mg – Mn – Ce alloy using a combination of plasma treatment and spraying of fluoropolymers, J. Magnes. Alloy. 10 (2022) 1033–1050. https://doi.org/10.1016/j.jma.2021.07.020.

[88] H. Li, Z. Qin, Y. Ouyang, B. Zheng, H. Wei, J. Ou, C. Shen, Hydroxyapatite/chitosan-metformin composite coating enhances the biocompatibility and osteogenic activity of AZ31 magnesium alloy, J. Alloys Compd. 909 (2022) 164694. https://doi.org/10.1016/j.jallcom.2022.164694.

[89] S. Mahmud, M. Rahman, H. Khatun, O. Ali, R. Ali, M. Rahaman, S. Islam, Y. Ali, Surface & Coatings Technology Ceramic coating on Mg alloy for enhanced degradation resistance as implant material, Surf. Coat. Technol. 479 (2024) 130544. https://doi.org/10.1016/j.surfcoat.2024.130544.

[90] I. Kozina, H. Krawiec, M. Starowicz, M. Kawalec, Corrosion Resistance of MgZn Alloy Covered by Chitosan-Based Coatings, (2021).

[91] M. Ferroni, F. De Gaetano, D. Gastaldi, M.G. Cereda, F. Boschetti, Investigating Flow-Induced Corrosion of Magnesium in Ophthalmological Milieu, Materials (Basel). 17 (2024). https://doi.org/10.3390/ma17174404.

[92] X. Zhang, L. Zhang, L. Han, J. Bai, Z. Huang, C. Guo, F. Xue, P.K. Chu, C. Chu, Effects of Dynamic Flow Rates on the In Vitro Bio-Corrosion Behavior of Zn-Cu Alloy, Coatings 14 (2024). https://doi.org/10.3390/coatings14060711.

[93] J. Ren, Z. Zhao, H. Li, D. Wang, C. Shuai, Y. Yang, Surface Coatings on Biomedical Magnesium Alloys, Materials (Basel). 18 (2025).

https://doi.org/10.3390/ma18143411.

[94] T. Shang, K. Wang, S. Tang, Y. Shen, L. Zhou, L. Zhang, The Flow-Induced Degradation and Vascular Cellular Response Study of Magnesium-Based Materials, 10 (2022) 1–14. https://doi.org/10.3389/fbioe.2022.940172.

[95] J. Wang, Y. Jang, G. Wan, V. Giridharan, G.-L. Song, Z. Xu, Y. Koo, P. Qi, J. Sankar, N. Huang, Y. Yun, Flow-induced corrosion of absorbable magnesium alloy: In-situ and real-time electrochemical study, Corros. Sci. 104 (2016) 277–289. https://doi.org/10.1016/j.corsci.2015.12.020.

[96] J. Wang, V. Giridharan, V. Shanov, Z. Xu, B. Collins, L. White, Y. Jang, J. Sankar, N. Huang, Y. Yun, Acta Biomaterialia Flow-induced corrosion behavior of absorbable magnesium-based stents, Acta Biomater. 10 (2014) 5213–5223. https://doi.org/10.1016/j.actbio.2014.08.034.

[97] J. Wang, Y. Jang, G. Wan, V. Giridharan, G. Song, Z. Xu, Y. Koo, P. Qi, J. Sankar, N. Huang, Y. Yun, Flow-induced corrosion of absorbable magnesium alloy : In-situ and real-time electrochemical study, Eval. Program Plann. 104 (2016) 277–289. https://doi.org/10.1016/j.corsci.2015.12.020.

[98] A. Putra, R. Adibah, A. Rahim, M. Noor, H. Basri, J. Abdullah, M. Ra, A. Kadir, A. Syahrom, The in fl uence of fl ow rates on the dynamic degradation behaviour of porous magnesium under a simulated environment of human cancellous bone, 122 (2017) 268–279. https://doi.org/10.1016/j.matdes.2017.03.029.

[99] B.Z. Alloy, X. Zhang, L. Zhang, L. Han, J. Bai, Z. Huang, C. Guo, F. Xue, Effects of Dynamic Flow Rates on the In Vitro Bio-Corrosion, (2024).

[100] R. Sathiyamoorthy, K. Shanmugam, V. Balasubramanian, Establishing an empirical relationship to predict porosity and hardness of Titanium Oxide (TiO 2) coating deposited by High Velocity Oxy Fuel (HVOF) spraying, 2 (2015) 90–97.

[101] S.M.A. Bukhari, R. Qurashi, N. Husnain, M.A. Sadiq, M.Q. Zafar, M.T. Anwar,

S. Abbas, F.A. Siddiqui, S. Sarfraz, Response Surface Methodology-Based Optimization of Coating Material, Coating Thickness, and Diameter of Dental Implant for Enhanced Mechanical Behavior Using Finite Element Method, Adv. Eng. Mater. 26 (2024) 2401729. https://doi.org/10.1002/adem.202401729.

[102] L.W. Hernández, Y. Seid Ahmed, D.A. Curra, R. Pérez, Multi-Response Optimization of Milling Parameters of AISI D2 Steel Using Response Surface Methodology and Desirability Function, J. Manuf. Mater. Process. 9 (2025). https://doi.org/10.3390/jmmp9090314.

[103] ChemistryOpen - 2024 - Aristizábal-Alzate - Integration of Design of Experiments Analysis of Variance and Response Surface.pdf, (n.d.).

[104] F. You, Materials Horizons, 13 (2026). https://doi.org/10.1039/d5mh01525a.

[105] Y. Sun, X. Chen, J. Gao, W. Zhu, M. Pan, Rationally Design Thermoelectric Materials Based on Ingenious Machine Learning Methods, 2500210 (2025) 1–10. https://doi.org/10.1002/aelm.202500210.

[106] L.-T. Wu, M. Zdravković, D. Milosavljević, K. Köster, O. Guillon, J.-C. Jiang, P. Kaghazchi, Prediction of Structural Stability of Layered Oxide Cathode Materials: Combination of Machine Learning and Ab Initio Thermodynamics, Adv. Energy Mater. n/a (2025) e05470. https://doi.org/10.1002/aenm.202505470.

[107] H. Fu, X. Zhou, P. Xu, D. Sun, Prediction of Compressive Strength of Concrete Using Explainable Machine Learning Models, Materials (Basel). 18 (2025). https://doi.org/10.3390/ma18215009.

[108] B.P. Nandurkar, J.M. Raut, P.K. Hinge, B. V Bahoria, Optimization and predictive performance of fly ash-based sustainable concrete using integrated multitask deep learning framework with interpretable machine learning techniques SHapley Additive exPlanations, (2025) 1–20.

[109] T. Chen, X. Mi, S. Zhou, S. Tong, Y. Zhou, Y. Zhang, Y. Yuan, Machine

Learning Prediction of Density for Binary Mg-Containing Phases, (2025). https://doi.org/10.32604/cmc.2025.070649.

[110] A. Mohankumar, T. Duraisamy, V. Packkirisamy, Optimizing cold spray process parameters for AA2024/Al2O3 coatings to minimize wear loss via response surface methodology and particle swarm optimization, J. Adhes. Sci. Technol. 39 (2025) 2686–2709. https://doi.org/10.1080/01694243.2025.2512167.

[111] Y.W.U. Iheng, H.A.C. Hen, T.F.U. Ingzhao, J.I.Z. Hang, Z.H.Z. Hu, S.H.J. In, Flat broadband frequency upconversion within a thin-film lithium niobate waveguide achieved by multi-objective genetic algorithm particle swarm optimization, 33 (2025) 7126–7133. https://doi.org/10.1364/OE.550626.

[112] J. Shao, Y. Lu, Y. Sun, L. Zhao, An improved multi-objective particle swarm optimization algorithm for the design of foundation pit of rail transit upper cover project, (2025) 1–25.

[113] W. Hu, Y. Zhang, L. Liu, P. Zhang, J. Qin, B. Nie, Study on Multi-Objective Optimization of Construction Project Based on Improved Genetic Algorithm and Particle Swarm Optimization, Processes 12 (2024). https://doi.org/10.3390/pr12081737.

[114] A.K. Shrivastav, S. Dutta, Multi-objective optimization of hybrid microgrid for energy trilemma goals using slime mould algorithm, (2025) 1–22.

[115] M. Danish, S. Rubaiee, H. Ijaz, Predictive Modelling and Multi-Objective Optimization of Surface Integrity Parameters in Sustainable Machining, (2021).

[116] S. Chaurasiya, M.N. Pandey, A.K. Chaurasia, Experimental investigation of surface roughness reduction of biomaterial (Co-Cr-Mo) alloys using MFAFP and RSM-based optimization, (2026). https://doi.org/10.1177/25165984261417765.

[117] R.E. Hammam, A.A.A. Solyman, M.H. Alsharif, P. Uthansakul, M.A. Deif, Design of Biodegradable Mg Alloy for Abdominal Aortic Aneurysm Repair (

AAAR) Using ANFIS Regression Model, IEEE Access 10 (2022) 28579–28589. https://doi.org/10.1109/ACCESS.2022.3155645.

[118] C.K.D.N. Senthilkumar, K.P.B. Deepanraj, Machinability evaluation of magnesium composite using response surface methodology and nature-inspired metaheuristic algorithms, Int. J. Interact. Des. Manuf. 19 (2025) 2607–2627. https://doi.org/10.1007/s12008-024-01866-3.

[119] N. Usmaniya, S. R., P. V., R.K. L., R. N., Development of hydroxyapatite/bioactive glass incorporated chitosan layer on plasma electrolytic oxidised ZM21 alloy for temporary implant applications, J. Alloys Compd. 1004 (2024) 175723. https://doi.org/10.1016/j.jallcom.2024.175723.

[120] Q. Wang, Q. Liu, J. Gao, J. He, H. Zhang, J. Ding, Stereo Coverage and Overall Stiffness of Biomaterial Arrays Underly Parts of Topography Effects on Cell Adhesion, (2023). https://doi.org/10.1021/acsami.2c19742.

[121] D.E. Ingber, Cellular mechanotransduction: putting all the pieces together again, FASEB J. 20 (2006) 811–827. https://doi.org/10.1096/fj.05-5424rev.

[122] C.S. Chen, Mechanotransduction – a field pulling together?, J. Cell Sci. 121 (2008) 3285–3292. https://doi.org/10.1242/jcs.023507.

[123] A. Gupta, A. Das, A. Barui, A. Das, A. Roy Chowdhury, Evaluating the cell migration potential of TiO2 nanorods incorporated in a Ti6Al4V scaffold: A multiscale approach, J. Mech. Behav. Biomed. Mater. 144 (2023) 105940. https://doi.org/10.1016/j.jmbbm.2023.105940.

[124] J. She, J. Chen, X. Xiong, Y. Yang, X. Peng, D. Chen, F. Pan, Research advances of magnesium and magnesium alloys globally in 2023, J. Magnes. Alloy. 12 (2024) 3441–3475. https://doi.org/10.1016/j.jma.2024.10.001.

[125] J. Moon, S. Park, S. Rho, E. Hwang, A comparative analysis of artificial neural network architectures for building energy consumption forecasting, Int. J. Distrib. Sens. Networks 15 (2019). https://doi.org/10.1177/1550147719877616.

[126] I. Shaft, J. Ahmad, S.I. Shah, F.M. Kashif, Impact of varying neurons and hidden layers in neural network architecture for a time frequency application, 10th IEEE Int. Multitopic Conf. 2006, INMIC (2006) 188–193. https://doi.org/10.1109/INMIC.2006.358160.

[127] A. Hou, S. Jin, D. Gruber, H. Harmuth, Influence of variation/response space complexity and variable completeness on BP-ANN model establishment: Case study of steel ladle lining, Appl. Sci. 9 (2019). https://doi.org/10.3390/app9142835.

[128] M.Y. Otache, J.J. Musa, I.A. Kuti, M. Mohammed, L.E. Pam, Effects of Model Structural Complexity and Data Pre-Processing on Artificial Neural Network (ANN) Forecast Performance for Hydrological Process Modelling, Open J. Mod. Hydrol. 11 (2021) 1–18. https://doi.org/10.4236/ojmh.2021.111001.

[129] H. Mustafidah, C.P. Putri, H. Harjono, S. Suwarsito, The most optimal performance of the Levenberg-Marquardt algorithm based on neurons in the hidden layer, J. Phys. Conf. Ser. 1402 (2019). https://doi.org/10.1088/1742-6596/1402/6/066099.

[130] Z. Yan, S. Zhong, L. Lin, Z. Cui, Adaptive levenberg–marquardt algorithm: A new optimization strategy for levenberg–marquardt neural networks, Mathematics 9 (2021). https://doi.org/10.3390/math9172176.

[131] H. Liu, M. Cocea, Semi-random partitioning of data into training and test sets in granular computing context, Granul. Comput. 2 (2017) 357–386. https://doi.org/10.1007/s41066-017-0049-2.

[132] B. Barai, A. Ojha, S. Sarkar, S. Kundu, B. Oraon, T. Mandal, Enhancing Corrosion Resistance of Biodegradable Magnesium Alloys through Hydrophobic Surface Modification: Experimental Analysis and ANN Modeling, Surf. Rev. Lett. (2024). https://doi.org/10.1142/s0218625x24500938.

[133] F.J. Moreno-Barea, F. Strazzera, J.M. Jerez, D. Urda, L. Franco, Forward Noise

Adjustment Scheme for Data Augmentation, Proc. 2018 IEEE Symp. Ser. Comput. Intell. SSCI 2018 (2018) 728–734. https://doi.org/10.1109/SSCI.2018.8628917.

[134] P. Panda, K. Roy, Implicit adversarial data augmentation and robustness with Noise-based Learning, Neural Networks 141 (2021) 120–132. https://doi.org/10.1016/j.neunet.2021.04.008.

[135] H. Dong, J. Wang, X. Wu, M. Zhou, J. Lu, Gaussian Noise Data Augmentation-Based Delay Prediction for High-Speed Railways, IEEE Intell. Transp. Syst. Mag. 15 (2023) 8–18. https://doi.org/10.1109/MITS.2023.3274787.

[136] Y. Yu, D. Ma, M. Yang, X. Yang, H. Guan, Surrogate modeling with non-stationary-noise based Gaussian process regression and K-Fold ANN for systems featuring uneven sensitivity distribution, Aerosp. Sci. Technol. 150 (2024) 109157. https://doi.org/10.1016/j.ast.2024.109157.

[137] J. Tumpach, J. Koza, M. Holeňa, Neural-network-based estimation of normal distributions in black-box optimization, (2022) 187–192. https://doi.org/10.14428/esann/2022.es2022-113.

[138] M. Tian, X. Gong, L. Yin, H. Li, W. Ming, Z. Zhang, J. Chen, Multi-objective optimization of injection molding process parameters in two stages for multiple quality characteristics and energy efficiency using Taguchi method and NSGA-II, Int. J. Adv. Manuf. Technol. 89 (2017) 241–254. https://doi.org/10.1007/s00170-016-9065-7.

[139] D. Luo, C. Liu, C. Wang, Y. Wang, X. Wang, J. Zhao, S. Jiang, Optimization of multilayer laser cladding process parameters based on NSGA-II-MOPSO algorithm, Opt. Laser Technol. 176 (2024) 111025. https://doi.org/10.1016/j.optlastec.2024.111025.

[140] M. Ahmad, R. Alkanhel, W. El-Shafai, A.D. Algarni, F.E.A. El-Samie, N.F. Soliman, Multi-Objective Evolution of Strong S-Boxes Using Non-Dominated Sorting Genetic Algorithm-II and Chaos for Secure Telemedicine, IEEE Access

10 (2022) 112757–112775. https://doi.org/10.1109/ACCESS.2022.3209202.

[141] M. Hort, F. Sarro, The effect of offspring population size on NSGA-II: A preliminary study, GECCO 2021 Companion - Proc. 2021 Genet. Evol. Comput. Conf. Companion (2021) 179–180. https://doi.org/10.1145/3449726.3459479.

[142] P. Vijai, P. Bagavathi Sivakumar, A hybrid multi-objective optimization approach with NSGA-II for feature selection, Decis. Anal. J. 14 (2025) 100550. https://doi.org/10.1016/j.dajour.2025.100550.

[143] M. Fatehi, A. Toloei, S.T.A. Niaki, E. Zio, An advanced teaching-learning-based algorithm to solve unconstrained optimization problems, Intell. Syst. with Appl. 17 (2023) 200163. https://doi.org/10.1016/j.iswa.2022.200163.

[144] S.J. Patel, A. Toshniwal, V. Kheraj, A novel teaching-learning based optimization approach for design of broad-band anti-reflection coatings, Swarm Evol. Comput. 34 (2017) 68–74. https://doi.org/10.1016/j.swevo.2016.12.003.

[145] L.R. Rodrigues, TEACHING-LEARNING BASED OPTIMIZATION FOR JOB SHOP SCHEDULING PROBLEMS BY ELIMINATING UNNECESSARY OBJECTIVE FUNCTION CALLS, (n.d.).

[146] R. Nshimirimana, A. Abraham, G. Nothnagel, A multi-objective particle swarm for constraint and unconstrained problems, Springer London, 2021. https://doi.org/10.1007/s00521-020-05555-6.

[147] A. Kumar, C. Upadhyay, Shashikant, Experimental investigation on WEDM performance analysis using grey-fuzzy integrated with TLBO algorithm for Inconel 625: comparison with GA and SA, World J. Eng. 18 (2021) 720–733. https://doi.org/10.1108/WJE-12-2020-0643.

[148] J. Wang, Y. Zhang, S. Zhu, J. Wang, A Novel Multi-Objective Trajectory Planning Method for Robots Based on the Multi-Objective Particle Swarm Optimization Algorithm, Sensors 24 (2024). https://doi.org/10.3390/s24237663.

[149] H. Saheban, A multi-objective optimization of sensitivity and bandwidth of a 3-D MEMS bionic vector hydrophone, Analog Integr. Circuits Signal Process. 110 (2022) 455–467. https://doi.org/10.1007/s10470-021-01975-z.

[150] V. Kumar, B. Baran, S. Das, B. Oraon, S. Mukherjee, Surface & Coatings Technology Tailoring electroless Ni-W-P polyalloy coatings : Unveiling the synergistic impact of cerium addition and annealing on surface functional properties, Surf. Coat. Technol. 485 (2024) 130874. https://doi.org/10.1016/j.surfcoat.2024.130874.

[151] W. LI, J. ZHOU, Y. XU, Study of the in vitro cytotoxicity testing of medical devices, Biomed. Reports 3 (2015) 617–620. https://doi.org/10.3892/br.2015.481.

[152] S.H. Bae, J.H. Che, J.M. Seo, J. Jeong, E.T. Kim, S.W. Lee, K.I. Koo, G.J. Suaning, N.H. Lovell, D. Il Dan Cho, S.J. Kim, H. Chung, In vitro biocompatibility of various polymer-based microelectrode arrays for retinal prosthesis, Investig. Ophthalmol. Vis. Sci. 53 (2012) 2653–2657. https://doi.org/10.1167/iovs.11-9341.

[153] B. Barai, K. Boorgula, H. Begam, S. Sarkar, A. Barui, S. Kundu, B. Oraon, T. Mandal, Multiphysics simulation and experimental investigation of HA and Zn-doped HA coatings on magnesium alloys for resorbable implant applications, Mater. Today Commun. 42 (2025). https://doi.org/10.1016/j.mtcomm.2024.111241.

[154] S. Bose, T. Nandi, Statistical and experimental investigation using a novel multi-objective optimization algorithm on a novel titanium hybrid composite developed by lens process, Proc. Inst. Mech. Eng. Part C J. Mech. Eng. Sci. 235 (2021) 2911–2933. https://doi.org/10.1177/0954406220959101.

[155] U. Sajjad, A. Abbas, A. Sadeghianjahromi, N. Abbas, J.S. Liaw, C.C. Wang, Enhancing corrosion resistance of Al 5050 alloy based on surface roughness and its fabrication methods; an experimental investigation, J. Mater. Res.

Technol. 11 (2021) 1859–1867. https://doi.org/10.1016/j.jmrt.2021.01.096.

[156] C. Feng, E. Qin, W. Li, M. Li, J. Su, X. Xu, Energy consumption and surface roughness modelling for multi-objective optimisation of machining processes, Int. J. Adv. Manuf. Technol. 133 (2024) 5065–5087. https://doi.org/10.1007/s00170-024-14043-3.

[157] M. Bi, J. Zhu, Y. Luo, H. Cai, X. Li, X. Wang, Y. Wei, X. Wang, C. Hu, J. Hu, G. Zhang, X. Wang, X. Zhang, Effect of Deposition Temperature on the Surface, Structural, and Mechanical Properties of HfO2 Using Chemical Vapor Deposition (CVD), Coatings 12 (2022). https://doi.org/10.3390/coatings12111731.

[158] K. Zhang, K. Yang, S. Li, D. Jing, H.-B. Chen, ANN-Based Outlier Detection for Wireless Sensor Networks in Smart Buildings, IEEE Access 7 (2019) 95987–95997. https://api.semanticscholar.org/CorpusID:199440374.

[159] T. Singh, Entropy Feature Based Outlier Detection using ANN for WSN Application, Int. J. Adv. Trends Comput. Sci. Eng. 9 (2020) 6043–6047. https://doi.org/10.30534/ijatcse/2020/273942020.

[160] M. Adjeisah, X. Zhu, H. Xu, T.A. Ayall, Towards data augmentation in graph neural network: An overview and evaluation, Comput. Sci. Rev. 47 (2023) 100527. https://doi.org/10.1016/j.cosrev.2022.100527.

[161] M. Nagaraju, P. Chawla, N. Kumar, Performance improvement of Deep Learning Models using image augmentation techniques, Multimed. Tools Appl. 81 (2022) 9177–9200. https://doi.org/10.1007/s11042-021-11869-x.

[162] F. Siegmund, A.H.C. Ng, K. Deb, Finding a preferred diverse set of Pareto-optimal solutions for a limited number of function calls, 2012 IEEE Congr. Evol. Comput. CEC 2012 (2012). https://doi.org/10.1109/CEC.2012.6256654.

[163] M. Hu, Y. Wang, W. Tian, Adaptive hybrid optimization for integrated project scheduling and staffing problem with time/resource trade-offs, Oper. Res. Perspect. 15 (2025) 100346. https://doi.org/10.1016/j.orp.2025.100346.

[164] H. Dong, Y. Xu, D. Cao, W. Zhang, Z. Yang, X. Li, An improved teaching–learning-based optimization algorithm with a modified learner phase and a new mutation-restarting phase, Knowledge-Based Syst. 258 (2022) 109989. https://doi.org/10.1016/j.knosys.2022.109989.

[165] Y. Yi, Z. Wang, Y. Shi, Z. Song, B. Zhao, Convergence-Driven Adaptive Many-Objective Particle Swarm Optimization, IEEE Access 13 (2025) 5129–5144. https://doi.org/10.1109/ACCESS.2025.3525850.

[166] G. Xu, K. Luo, G. Jing, X. Yu, X. Ruan, J. Song, On convergence analysis of multi-objective particle swarm optimization algorithm, Eur. J. Oper. Res. 286 (2020) 32–38. https://doi.org/10.1016/j.ejor.2020.03.035.

[167] M. Yazdani, P. Zarate, E.K. Zavadskas, Z. Turskis, A combined compromise solution (CoCoSo) method for multi-criteria decision-making problems, Manag. Decis. 57 (2019) 2501–2519. https://doi.org/10.1108/MD-05-2017-0458.

[168] B. Malekmohammadi, B. Zahraie, R. Kerachian, Ranking solutions of multi-objective reservoir operation optimization models using multi-criteria decision analysis, Expert Syst. Appl. 38 (2011) 7851–7863. https://doi.org/10.1016/j.eswa.2010.12.119.

[169] N. Jaini, S. Utyuzhnikov, Trade-off ranking method for multi-criteria decision analysis, J. Multi-Criteria Decis. Anal. 24 (2017) 121–132. https://doi.org/10.1002/mcda.1600.

[170] B. Li, H. Wang, Multi-objective sparrow search algorithm: A novel algorithm for solving complex multi-objective optimisation problems, Expert Syst. Appl. 210 (2022) 118414. https://doi.org/10.1016/j.eswa.2022.118414.

[171] H. Kabir, N. Garg, Machine learning enabled orthogonal camera goniometry for accurate and robust contact angle measurements, Sci. Rep. 13 (2023) 1–13. https://doi.org/10.1038/s41598-023-28763-1.

[172] C. Yang, P. Li, Y. Wei, J. Li, J. Zhang, S. Wang, Superhydrophobic

Nanocoatings Fabricated by Materials with Low Young's Contact Angle, Langmuir (2025). https://doi.org/10.1021/acs.langmuir.4c05143.

[173] J.H. Chu, G.X. Sun, L.B. Tong, Z.H. Jiang, Facile one-step hydrothermal fabrication of Allium giganteum-like superhydrophobic coating on Mg alloy with self-cleaning and anti-corrosion properties, Colloids Surfaces A Physicochem. Eng. Asp. 617 (2021) 126370. https://doi.org/10.1016/j.colsurfa.2021.126370.

[174] G. Wang, J. Jiang, Y. Qiao, L. Gu, E.E. Klu, X. Gong, A. Ma, D. Song, Enhanced super-hydrophobicity and corrosion resistance of the one-step hydrothermal synthesized coating on the Mg-9Li alloy: Role of the solid-solution treated substrate, J. Alloys Compd. 921 (2022) 166044. https://doi.org/10.1016/j.jallcom.2022.166044.

[175] Y. Zhang, J. Yao, Fabrication of biodegradable superhydrophobic Zn-Fe coating on ultra-light Mg-Li alloy, Surf. Coatings Technol. 486 (2024) 130677. https://doi.org/10.1016/j.surfcoat.2024.130677.

[176] L. Doskoˇcil, P. Šomanová, J. Másilko, M. Buchtík, M. Haso ˇnová, L. Kalina, J. Wasserbauer, Characterization of Prepared Superhydrophobic Surfaces on, (2022). https://doi.org/10.3390/coatings12101414.

[177] Q. Li, X. Bao, J. Sun, S. Cai, Y. Xie, Y. Liu, J. Liu, G. Xu, Fabrication of superhydrophobic composite coating of hydroxyapatite/stearic acid on magnesium alloy and its corrosion resistance, antibacterial adhesion, J. Mater. Sci. 56 (2021) 5233–5249. https://doi.org/10.1007/s10853-020-05592-5.

[178] M. Dekermenjian, A.P. Ruediger, A. Merlen, Raman spectroscopy investigation of magnesium oxide nanoparticles, RSC Adv. 13 (2023) 26683–26689. https://doi.org/10.1039/d3ra04492k.

[179] P. Lucas, G.J. Coleman, M. Venkateswara Rao, A.N. Edwards, C. Devaadithya, S. Wei, A.Q. Alsayoud, B.G. Potter, K. Muralidharan, P.A. Deymier, Structure of ZnCl2 Melt. Part II: Fragile-to-Strong Transition in a Tetrahedral Liquid, J.

Phys. Chem. B 121 (2017) 11210–11218. https://doi.org/10.1021/acs.jpcb.7b10857.

[180] K.I. Hadjiivanov, D.A. Panayotov, M.Y. Mihaylov, E.Z. Ivanova, K.K. Chakarova, S.M. Andonova, N.L. Drenchev, Power of Infrared and Raman Spectroscopies to Characterize Metal-Organic Frameworks and Investigate Their Interaction with Guest Molecules, Chem. Rev. 121 (2021) 1286–1424. https://doi.org/10.1021/acs.chemrev.0c00487.

[181] X. Zhang, J. Shen, D. Hu, B. Duan, C. Wang, A rapid approach to manufacture superhydrophobic coating on magnesium alloy by one-step method, Surf. Coatings Technol. 334 (2018) 90–97. https://doi.org/10.1016/j.surfcoat.2017.11.029.

[182] D.A. Setyawardhani, D.A. Majid, R.S.S. Plawi, Solid-Liquid Equilibrium Study of Binary System Saturated Fatty Acid in Short Chain Alcohols, Equilib. J. Chem. Eng. 8 (2024) 8. https://doi.org/10.20961/equilibrium.v8i1.80577.

[183] D. Yang, B.C. Gates, Analyzing Stabilities of Metal-Organic Frameworks: Correlation of Stability with Node Coordination to Linkers and Degree of Node Metal Hydrolysis, J. Phys. Chem. C 128 (2024) 8551–8559. https://doi.org/10.1021/acs.jpcc.4c02105.

[184] M. Kim, Y. Lee, H.R. Moon, Carboxylate-Based Metal–Organic Framework and Coordination Polymer Glasses: Progress and Perspectives, Acc. Chem. Res. 57 (2024) 2347–2357. https://doi.org/10.1021/acs.accounts.4c00290.

[185] Z. Liu, J. Zhao, M. Li, Y. Hu, J. Wu, F. Feng, Enhanced the Thermal Stability of Polyvinyl Chloride via Synergistic Effects of Basic Lanthanum Tartrate with Zinc Stearate and Pentaerythritol, Polym. Sci. Ser. B 63 (2021) 182–190. https://doi.org/10.1134/S156009042102007X.

[186] W. Zhang, Y. Zhu, R. Zhao, S. Zhang, X. Lai, Y. Wang, Z. Yan, W. Liu, R. Zhang, Investigation on Influencing Mechanism of Processing Parameters on Corrosion Resistance and Zinc Content of Anodic Coatings Developed on

Magnesium Alloys in Near-Neutral Solutions, Coatings 12 (2022). https://doi.org/10.3390/coatings12091286.

[187] I.S. Bayer, Superhydrophobic Coatings from Ecofriendly Materials and Processes: A Review, Adv. Mater. Interfaces 7 (2020) 1–25. https://doi.org/10.1002/admi.202000095.

[188] T. Mandal, S. Dasgupta, A. Barui, S. Kundu, Effect of strontium on microstructure , mechanical , and biological responses of Mg – Al – Zn – Sr alloys, (2022). https://doi.org/10.1080/02670836.2022.2072071.

[189] T. Zhu, Y. Yu, J. Yang, Y. Shen, L. He, Y. Xiong, Dynamic corrosion behavior of AZ80 magnesium alloy with different orientations in simulated body fluid, 259 (2021). https://doi.org/10.1016/j.matchemphys.2020.124039.

[190] J. Vishnu, K. Praveenkumar, A. Anil Kumar, A. Nair, R. Arjun, V. Gopakumar Pillai, B. Shankar, K. V Shankar, Multifunctional zinc oxide loaded stearic acid surfaces on biodegradable magnesium WE43 alloy with hydrophobic, self-cleaning and biocompatible attributes, Appl. Surf. Sci. 680 (2025) 161455. https://doi.org/10.1016/j.apsusc.2024.161455.

[191] P.H. Lin, M. Sermersheim, H. Li, P.H.U. Lee, S.M. Steinberg, J. Ma, Zinc in wound healing modulation, Nutrients 10 (2018) 1–20. https://doi.org/10.3390/nu10010016.

[192] S.A. Lebedeva, P.A. Galenko-Yaroshevsky, M.Y. Samsonov, A.B. Erlich, A.G. Margaryan, M.Y. Materenchuk, I.R. Arshinov, Y. V. Zharov, A. V. Zelenskaya, O. V. Shelemekh, I.G. Lomsadze, T.A. Demura, Molecular mechanisms of wound healing: the role of zinc as an essential microelement, Res. Results Pharmacol. 9 (2023) 25–39. https://doi.org/10.18413/rrpharmacology.9.10003.

[193] J. Han, L. Andrée, D. Deng, B.A.J.A. van Oirschot, A.S. Plachokova, S.C.G. Leeuwenburgh, F. Yang, Biofunctionalization of dental abutments by a zinc/chitosan/gelatin coating to optimize fibroblast behavior and antibacterial properties, J. Biomed. Mater. Res. - Part A 112 (2024) 1873–1892.

https://doi.org/10.1002/jbm.a.37734.

[194] M.C. Morán, G. Ruano, F. Cirisano, M. Ferrari, Mammalian cell viability on hydrophobic and superhydrophobic fabrics, Mater. Sci. Eng. C 99 (2019) 241–247. https://doi.org/10.1016/j.msec.2019.01.088.

[195] S. Cai, C. Wu, W. Yang, W. Liang, H. Yu, L. Liu, Recent advance in surface modification for regulating cell adhesion and behaviors, Nanotechnol. Rev. 9 (2020) 971–989. https://doi.org/10.1515/ntrev-2020-0076.

[196] M.S. Uddin, C. Hall, P. Murphy, Surface treatments for controlling corrosion rate of biodegradable Mg and Mg-based alloy implants, Sci. Technol. Adv. Mater. 16 (2015). https://doi.org/10.1088/1468-6996/16/5/053501.

[197] S. Zhao, M. Tayyebi, Mahdireza Yarigarravesh, G. Hu, A review of magnesium corrosion in bio-applications: mechanism, classification, modeling, in-vitro, and in-vivo experimental testing, and tailoring Mg corrosion rate, J. Mater. Sci. 58 (2023) 12158–12181. https://doi.org/10.1007/s10853-023-08782-z.

[198] L. Sun, C.C. Berndt, K.A. Gross, A. Kucuk, Material fundamentals and clinical performance of plasma-sprayed hydroxyapatite coatings: A review, J. Biomed. Mater. Res. 58 (2001) 570–592. https://doi.org/10.1002/jbm.1056.

[199] W. Xu, K. Yagoshi, Y. Koga, M. Sasaki, T. Niidome, Optimized polymer coating for magnesium alloy-based bioresorbable scaffolds for long-lasting drug release and corrosion resistance, Colloids Surfaces B Biointerfaces 163 (2018) 100–106. https://doi.org/10.1016/j.colsurfb.2017.12.032.

[200] L. V. Parfenova, Z.R. Galimshina, E. V. Parfenov, Organic-Inorganic Biocompatible Coatings for Temporary and Permanent Metal Implants, Int. J. Mol. Sci. 25 (2024). https://doi.org/10.3390/ijms252111623.

[201] H. Begam, Preparation and characterization of zinc doped biphasic-calcium phopshate for biomedical application, 2022 IEEE Conf. Interdiscip. Approaches Technol. Manag. Soc. Innov. (2022) 1–5. https://doi.org/10.1109/IATMSI56455.2022.10119318.

[202] H. Begam, S. Mandal, A. Chanda, J. Mukherjee, H. Begam, S. Mandal, A. Chanda, J. Mukherjee, S.K. Nandi, Transactions of the Indian Ceramic Society Effect of Zinc Doping on Biological Properties of Biphasic Calcium Phosphate Ceramics in Orthopaedic Animal Model Effect of Zinc Doping on Biological Properties of Biphasic Calcium Phosphate Ceramics, 5456 (2014). https://doi.org/10.1080/0371750X.2014.929509.

[203] T. Tsuchida, J. Kubo, T. Yoshioka, S. Sakuma, T. Takeguchi, W. Ueda, Reaction of ethanol over hydroxyapatite affected by Ca / P ratio of catalyst, J. Catal. 259 (2008) 183–189. https://doi.org/10.1016/j.jcat.2008.08.005.

[204] R.L. Ferziger, J. H., Perić, M., & Street, Computational Methods for Fluid Dynamics, Springers, 2019. https://doi.org/10.1007/978-3-319-99693-6.

[205] R.U. Putra, H. Basri, A.T. Prakoso, H. Chandra, M.I. Ammarullah, I. Akbar, A. Syahrom, T. Kamarul, Level of Activity Changes Increases the Fatigue Life of the Porous Magnesium Scaffold, as Observed in Dynamic Immersion Tests, over Time, Sustain. 15 (2023). https://doi.org/10.3390/su15010823.

[206] Y. Koo, H.B. Lee, Z. Dong, R. Kotoka, J. Sankar, N. Huang, Y. Yun, The Effects of Static and Dynamic Loading on Biodegradable Magnesium Pins in Vitro and in Vivo, Sci. Rep. 7 (2017) 1–9. https://doi.org/10.1038/s41598-017-14836-5.

[207] H. Liu, L. Lan, J. Abrigo, H.L. Ip, Y. Soo, D. Zheng, K.S. Wong, D. Wang, L. Shi, T.W. Leung, X. Leng, Comparison of Newtonian and Non-newtonian Fluid Models in Blood Flow Simulation in Patients With Intracranial Arterial Stenosis, Front. Physiol. 12 (2021) 1–11. https://doi.org/10.3389/fphys.2021.718540.

[208] H. Shi, C. Xu, X. Hu, W. Gan, K. Wu, X. Wang, Improving the Young ' s modulus of Mg via alloying and compositing – A short review, J. Magnes. Alloy. 10 (2024) 2009–2024. https://doi.org/10.1016/j.jma.2022.07.011.

[209] S. Aryal, K. Matsunaga, W. Ching, Ab initio simulation of elastic and

mechanical properties of Zn- and Mg-doped hydroxyapatite (HAP), J. Mech. Behav. Biomed. Mater. 47 (2015) 135–146. https://doi.org/10.1016/j.jmbbm.2015.03.018.

[210] D. Lopes, R.B. Soares, M.M. Castro, R.B. Figueiredo, T.G. Langdon, V.F.C. Lins, Corrosion Behavior in Hank ' s Solution of a Magnesium – Hydroxyapatite Composite Processed by High-Pressure Torsion, 2000765 (2020) 1–11. https://doi.org/10.1002/adem.202000765.

[211] F. Witte, J. Fischer, J. Nellesen, H. Crostack, V. Kaese, A. Pisch, F. Beckmann, H. Windhagen, In vitro and in vivo corrosion measurements of magnesium alloys, 27 (2006) 1013–1018. https://doi.org/10.1016/j.biomaterials.2005.07.037.

[212] A. Kasha, K. V Srinivasan, S.O. Obadimu, K.I. Kourousis, Immersion corrosion of material extrusion steel 316 L : Influence of immersion time and surface roughness, Mater. Today Commun. 35 (2023) 106394. https://doi.org/10.1016/j.mtcomm.2023.106394.

[213] D. Acharjee, S. Mandal, S.K. Samanta, M. Roy, B. Kundu, S. Roy, P. Basak, S.K. Nandi, In Vitro and In Vivo Bone Regeneration Assessment of Titanium-Doped Waste Eggshell-Derived Hydroxyapatite in the Animal Model, (2023). https://doi.org/10.1021/acsbiomaterials.3c00060.

[214] Z. Wang, Y. Fang, X. Zhou, Z. Li, H. Zhu, F. Du, X. Yuan, Q. Yao, J. Xie, Embedding ultrasmall Ag nanoclusters in Luria-Bertani extract via light irradiation for enhanced antibacterial activity, Nano Res. 13 (2020) 203–208. https://doi.org/10.1007/s12274-019-2598-y.

[215] S.N. Garcia, L. Gutierrez, A. Mcnulty, Real-time cellular analysis as a novel approach for in vitro cytotoxicity testing of medical device extracts, 2012 (2013) 2097–2106. https://doi.org/10.1002/jbm.a.34507.

[216] H. Begam, S. Dasgupta, S. Bodhak, A. Barui, Cobalt doped biphasic calcium phosphate ceramics for bone regeneration applications : Assessment of in vitro

antibacterial activity , biocompatibility , osteogenic and angiogenic properties, Ceram. Int. 50 (2024) 13276–13285. https://doi.org/10.1016/j.ceramint.2024.01.240.

[217] S. Dasgupta, A. Gope, A. Mukhopadhyay, P. Kumar, J. Chatterjee, A. Barui, Chitosan-collagen-fibrinogen uncrosslinked scaffolds possessing skin regeneration and vascularization potential., J. Biomed. Mater. Res. A 111 (2023) 725–739. https://doi.org/10.1002/jbm.a.37488.

[218] S. Dasgupta, K. Prashanth, P. Datta, A. Barui, International Journal of Biological Macromolecules Vitamin D3-incorporated chitosan / collagen / fibrinogen scaffolds promote angiogenesis and endothelial transition via HIF-1 / IGF-1 / VEGF pathways in dental pulp stem cells, Int. J. Biol. Macromol. 253 (2023) 127325. https://doi.org/10.1016/j.ijbiomac.2023.127325.

[219] Y. Huang, H. Zhang, H. Qiao, X. Nian, X. Zhang, Applied Surface Science Anticorrosive effects and in vitro cytocompatibility of calcium silicate / zinc-doped hydroxyapatite composite coatings on titanium, Appl. Surf. Sci. 357 (2015) 1776–1784. https://doi.org/10.1016/j.apsusc.2015.10.034.

[220] I. Antoniac, F. Miculescu, C. Cotrut, A. Ficai, J. V Rau, E. Grosu, A. Antoniac, C. Tecu, I. Cristescu, Controlling the Degradation Rate of Biodegradable Mg – Zn-Mn Alloys for Orthopedic Applications by Electrophoretic Deposition of Hydroxyapatite Coating, Materials (Basel). 13 (2020). https://doi.org/10.3390/ma13020263.

[221] C.F. Dunne, G. Katarivas, O. Hakimi, E. Aghion, B. Twomey, K.T. Stanton, Surface & Coatings Technology Corrosion behaviour of biodegradable magnesium alloys with hydroxyapatite coatings, Surf. Coat. Technol. 289 (2016) 37–44. https://doi.org/10.1016/j.surfcoat.2016.01.045.

[222] Q. Zhang, L. Zhang, M. Yang, Q. Hong, Z. Yang, S. Liu, Q. Xiong, C. Pan, Construction of Chi (Zn / BMP2) / HA composite coating on AZ31B magnesium alloy surface to improve the corrosion resistance and

biocompatibility, Nanotechnol. Rev. 10 (2021) 870–882. https://doi.org/10.1515/ntrev-2021-0063.

[223] W. Zhou, Z. Hu, T. Wang, G. Yang, W. Xi, Y. Gan, W. Lu, J. Hu, Enhanced corrosion resistance and bioactivity of Mg alloy modified by Zndoped nanowhisker hydroxyapatite coatings, Colloids Surfaces B Biointerfaces (2019). https://doi.org/10.1016/j.colsurfb.2019.110710.

[224] J. Li, L. Cao, Y. Song, S. Zhang, C. Zhao, F. Zhang, X. Zhang, The Bioactivated Interfacial Behavior of the Fluoridated Hydroxyapatite-Coated Mg-Zn Alloy in Cell Culture Environments, 2011 (2011). https://doi.org/10.1155/2011/192671.

[225] S. Hiromoto, M. Tomozawa, Surface & Coatings Technology Hydroxyapatite coating of AZ31 magnesium alloy by a solution treatment and its corrosion behavior in NaCl solution, Surf. Coat. Technol. 205 (2011) 4711–4719. https://doi.org/10.1016/j.surfcoat.2011.04.036.

[226] S. Gomes, J. Nedelec, G. Renaudin, Acta Biomaterialia On the effect of temperature on the insertion of zinc into hydroxyapatite, Acta Biomater. 8 (2012) 1180–1189. https://doi.org/10.1016/j.actbio.2011.12.003.

[227] Q. Yuan, J. Wu, C. Qin, A. Xu, Z. Zhang, Y. Lin, Z. Chen, S. Lin, Z. Yuan, X. Ren, P. Zhang, One-pot synthesis and characterization of Zn-doped hydroxyapatite nanocomposites, Mater. Chem. Phys. 199 (2017) 122–130. https://doi.org/10.1016/j.matchemphys.2017.06.047.

[228] D. Durgalakshmi, R.A. Rakkesh, S. Kamil, S.K.S. Balakumar, Rapid Dilapidation of Alcohol Using Magnesium Oxide and Magnesium Aspartate based Nanostructures : A Raman Spectroscopic and Molecular Simulation Approach, J. Inorg. Organomet. Polym. Mater. 29 (2019) 1390–1399. https://doi.org/10.1007/s10904-019-01105-3.

[229] D. Bhakta, L. Wu, J. Dong, X. Wei, Journal of Materials Science & Technology Effect of D-fructose on the in-vitro corrosion behavior of AZ31 magnesium alloy in simulated body fluid, J. Mater. Sci. Technol. 66 (2021) 202–212.

https://doi.org/10.1016/j.jmst.2020.03.080.

[230] S.A. Omar, J. Ballarre, W.H. Schreiner, S.M. Cer, Micro Raman and XPS surface analysis to understand the electrochemical behaviour of AZ31 and AZ91 magnesium alloys as temporary implant materials ., 31 (2022). https://doi.org/10.1016/j.mtcomm.2022.103557.

[231] J. Zhang, C. Dai, J. Wei, Z. Wen, Applied Surface Science Study on the bonding strength between calcium phosphate / chitosan composite coatings and a Mg alloy substrate, Appl. Surf. Sci. 261 (2012) 276–286. https://doi.org/10.1016/j.apsusc.2012.08.001.

[232] R. Nirmala, B.W. Il, R. Navamathavan, M.H. El-newehy, H.Y. Kim, Preparation and Characterizations of Anisotropic Chitosan Nanofibers via Electrospinning, 19 (2011) 345–350. https://doi.org/10.1007/s13233-011-0402-2.

[233] N.C. Haider, J. Alonso, Valence and Core Electron Spectra of Mg in MgO in Evoporated Thin Films, Zeitschrift Für Naturforsch. A 30 (1975) 1485–1490. https://doi.org/10.1515/zna-1975-1119.

[234] A.E. Alam, A.A. Ojo, Magnesium Incorporation in n-CdTe to Produce Wide Bandgap p-Type CdTe : Mg Window Layers, (2018) 1–13. https://doi.org/10.3390/chemengineering2040059.

[235] L. Wang, T. Shinohara, B. Zhang, Applied Surface Science XPS study of the surface chemistry on AZ31 and AZ91 magnesium alloys in dilute NaCl solution, Appl. Surf. Sci. 256 (2010) 5807–5812. https://doi.org/10.1016/j.apsusc.2010.02.058.

[236] M. Driess, Boosting electrochemical water oxidation through replacement of O h Co sites in cobalt oxide spinel with manganese †, (2017) 8018–8021. https://doi.org/10.1039/c7cc03749j.

[237] Y. Ding, C. Wen, P. Hodgson, Y. Li, Effects of alloying elements on the corrosion behavior and biocompatibility of biodegradable magnesium alloys: A

review, J. Mater. Chem. B 2 (2014) 1912–1933. https://doi.org/10.1039/c3tb21746a.

[238] S. Agarwal, J. Curtin, B. Duffy, S. Jaiswal, Biodegradable magnesium alloys for orthopaedic applications: A review on corrosion, biocompatibility and surface modifications, Mater. Sci. Eng. C 68 (2016) 948–963. https://doi.org/10.1016/j.msec.2016.06.020.

[239] S. Jain, J. Shah, N. Singh, N. Chhemendra, Significance of interface barrier at electrode of hematite hydroelectric cell for generating ecopower by water splitting, (2019) 4743–4755. https://doi.org/10.1002/er.4613.

[240] F. Sarcan, H. Rahal, R. Kihal, A. Arif, O. Belahssen, Influence of anneal temperature in air on surface morphology and photoluminescence of ZnO thin films Influence of anneal temperature in air on surface morphology and photoluminescence of ZnO thin films, (n.d.). https://doi.org/10.1088/1757-899X/522/1/012004.

[241] F. Peng, H. Li, D. Wang, P. Tian, Y. Tian, G. Yuan, D. Xu, X. Liu, Enhanced Corrosion Resistance and Biocompatibility of Magnesium Alloy by Mg-Al-Layered Double Hydroxide, ACS Appl. Mater. Interfaces 8 (2016) 35033–35044. https://doi.org/10.1021/acsami.6b12974.

[242] C.C. Negrila, M.V. Predoi, S.L. Iconaru, D. Predoi, Development of Zinc-Doped Hydroxyapatite by Sol-Gel Method for Medical Applications, (2018) 1–15. https://doi.org/10.3390/molecules23112986.

[243] L. Wang, T. Shinohara, B.-P. Zhang, XPS study of the surface chemistry on AZ31 and AZ91 magnesium alloys in dilute NaCl solution, Appl. Surf. Sci. Volume 256 (2010). https://doi.org/10.1016/j.apsusc.2010.02.058.

[244] P. Li, G. Ming, S.R. Kumar, C. Shih, C. Yang, D. Wang, S. Jessie, Electrochimica Acta Fabrication and Characterization of Chitosan Nanoparticle-Incorporated Quaternized Poly (Vinyl Alcohol) Composite Membranes as Solid Electrolytes for Direct Methanol Alkaline Fuel Cells,

Electrochim. Acta 187 (2016) 616–628. https://doi.org/10.1016/j.electacta.2015.11.117.

[245] M. Farrokhi-Rad, T. Shahrabi, S. Mahmoodi, S. Khanmohammadi, Electrophoretic deposition of hydroxyapatite-chitosan-CNTs nanocomposite coatings, Ceram. Int. 43 (2017) 4663–4669. https://doi.org/10.1016/j.ceramint.2016.12.139.

[246] H.C. Hsu, S.C. Wu, C.Y. Lin, W.F. Ho, Characterization of Hydroxyapatite/Chitosan Composite Coating Obtained from Crab Shells on Low-Modulus Ti–25Nb–8Sn Alloy through Hydrothermal Treatment, Coatings 13 (2023). https://doi.org/10.3390/coatings13020228.

[247] E. Diler, B. Lescop, S. Rioual, G.N. Vien, D. Thierry, B. Rouvellou, Initial formation of corrosion products on pure zinc and MgZn 2 examinated by XPS, Corros. Sci. 79 (2014) 83–88. https://doi.org/10.1016/j.corsci.2013.10.029.

[248] S. Sprio, M. Dapporto, L. Preti, E. Mazzoni, M.R. Iaquinta, F. Martini, M. Tognon, N.M. Pugno, E. Restivo, L. Visai, A. Tampieri, Enhancement of the Biological and Mechanical Performances of Sintered Hydroxyapatite by Multiple Ions Doping, Front. Mater. 7 (2020) 1–18. https://doi.org/10.3389/fmats.2020.00224.

[249] C. Oliveira, D. Lima, E.C.S. Filho, M. Jaber, M. Gard, Colloids and Surfaces B : Biointerfaces Zn-doped mesoporous hydroxyapatites and their antimicrobial properties, 198 (2021). https://doi.org/10.1016/j.colsurfb.2020.111471.

[250] Z. He, C. Jiao, J. Wu, J. Gu, H. Liang, Zn-doped chitosan / alginate multilayer coatings on porous hydroxyapatite scaffold with osteogenic and antibacterial properties, Int. J. Bioprinting Res. 9 (2023). https://doi.org/10.18063/ijb.v9i2.668.

[251] T. Shi, J. Kong, X. Wang, X. Li, Preparation of multifunctional Al-Mg alloy surface with hierarchical micro/nanostructures by selective chemical etching

processes, Appl. Surf. Sci. 389 (2016) 335–343. https://doi.org/10.1016/j.apsusc.2016.07.125.

[252] E.M. Lee, K. Smith, K. Gall, B.D. Boyan, Z. Schwartz, Change in surface roughness by dynamic shape-memory acrylate networks enhances osteoblast differentiation, Biomaterials 110 (2016) 34–44. https://doi.org/10.1016/j.biomaterials.2016.08.004.

[253] H. Begam, B. Kundu, A. Chanda, S. Kumar, MG63 osteoblast cell response on Zn doped hydroxyapatite (HAp) with various surface features, Ceram. Int. 43 (2017) 3752–3760. https://doi.org/10.1016/j.ceramint.2016.12.010.

[254] R. Ding, N.C. Miller, K.M. Woeppel, X.T. Cui, T.D.B. Jacobs, Surface Area and Local Curvature: Why Roughness Improves the Bioactivity of Neural Implants, Langmuir 38 (2022) 7512–7521. https://doi.org/10.1021/acs.langmuir.2c00473.

[255] C.S. Rauta, G. Majumdar, S. Mukherjee, S. Sarkar, An eco-friendly one-step pretreatment method for the synthesis of electroless coating on magnesium alloy, Phys. Scr. 99 (2024) 105934. https://doi.org/10.1088/1402-4896/ad733c.

[256] J. Xie, J. Hu, L. Fang, X. Liao, R. Du, F. Wu, L. Wu, Facile fabrication and biological properties of super-hydrophobic coating on magnesium alloy used as potential implant materials, Surf. Coatings Technol. 384 (2020). https://doi.org/10.1016/j.surfcoat.2019.125223.

[257] A. Abdal-hay, M. Dewidar, J.K. Lim, Biocorrosion behavior and cell viability of adhesive polymer coated magnesium based alloys for medical implants, Appl. Surf. Sci. 261 (2012) 536–546. https://doi.org/10.1016/j.apsusc.2012.08.051.

[258] W.S.W. Harun, R.I.M. Asri, J. Alias, F.H. Zulkifli, K. Kadirgama, S.A.C. Ghani, J.H.M. Shariffuddin, A comprehensive review of hydroxyapatite-based coatings adhesion on metallic biomaterials, Ceram. Int. 44 (2018) 1250–1268. https://doi.org/10.1016/j.ceramint.2017.10.162.

[259] S. Zhang, J. Li, Y. Song, C. Zhao, X. Zhang, C. Xie, Y. Zhang, In vitro degradation , hemolysis and MC3T3-E1 cell adhesion of biodegradable Mg – Zn alloy, Mater. Sci. Eng. C 29 (2009) 1907–1912. https://doi.org/10.1016/j.msec.2009.03.001.

[260] S. Singh, G. Singh, N. Bala, Electrophoretic deposition of Fe 3 O 4 nanoparticles incorporated hydroxyapatite-bioglass-chitosan nanocomposite coating on AZ91 Mg alloy, Mater. Today Commun. 26 (2021) 101870. https://doi.org/10.1016/j.mtcomm.2020.101870.

[261] Z. Zhen, X. Liu, T. Huang, T. Xi, Y. Zheng, Hemolysis and cytotoxicity mechanisms of biodegradable magnesium and its alloys, Mater. Sci. Eng. C 46 (2015) 202–206. https://doi.org/10.1016/j.msec.2014.08.038.

[262] X. Fan, M. Hu, Z. Qin, J. Wang, X. Chen, Bactericidal and Hemocompatible Coating via the Mixed-charged Copolymer, (2018). https://doi.org/10.1021/acsami.7b18889.

[263] Y. Zou, J. Wang, L. Cui, R. Zeng, Q. Wang, Q. Han, J. Qiu, X. Chen, D. Chen, S. Guan, Y. Zheng, Acta Biomaterialia Corrosion resistance and antibacterial activity of zinc-loaded montmorillonite coatings on biodegradable magnesium alloy AZ31 q, Acta Biomater. 98 (2019) 196–214. https://doi.org/10.1016/j.actbio.2019.05.069.

[264] E. Mena-morcillo, L. Veleva, M. Cerda-zorrilla, J.C. Castro-alcántara, R.C. Canul-puc, Development and assessment of a multifunctional chitosan-based coating applied on AZ31 magnesium alloy : Corrosion resistance and antibacterial performance against Klebsiella Pneumoniae, 9 (2021) 2133–2144. https://doi.org/10.1016/j.jma.2021.03.033.

[265] Y. Wang, A. Cao, Y. Jiang, X. Zhang, J. Liu, Y. Liu, Superior Antibacterial Activity of Zinc Oxide/Graphene Oxide Composites Originating from High Zinc Concentration Localized around Bacteria, ACS Appl. Mater. Interfaces 6 (2014). https://doi.org/10.1021/am4053317.

[266] N. IQBAL, S. IQBAL, T. IQBAL, H.R. BAKHSHESHI-RAD, A. ALSAKKAF, A. KAMIL, M.R. ABDUL KADIR, M.H. IDRIS, H.B. RAGHAV, Zinc-doped hydroxyapatite—zeolite/polycaprolactone composites coating on magnesium substrate for enhancing in-vitro corrosion and antibacterial performance, Trans. Nonferrous Met. Soc. China (English Ed. 30 (2020) 123–133. https://doi.org/10.1016/S1003-6326(19)65185-X.

[267] A. Polini, J. Wang, H. Bai, Y. Zhu, A.P. Tomsia, C. Mao, Biomaterials Science surfaces by HA-binding / osteogenic modular, (2014) 1779–1786. https://doi.org/10.1039/c4bm00164h.

[268] D. Ke, A.A. Vu, A. Bandyopadhyay, S. Bose, Acta Biomaterialia Compositionally graded doped hydroxyapatite coating on titanium using laser and plasma spray deposition for bone implants, Acta Biomater. 84 (2019) 414–423. https://doi.org/10.1016/j.actbio.2018.11.041.

[269] S. Sathiyavimal, S. Vasantharaj, F. Lewisoscar, A. Pugazhendhi, R. Subashkumar, International Journal of Biological Macromolecules Biosynthesis and characterization of hydroxyapatite and its composite (hydroxyapatite-gelatin-chitosan- fi brin-bone ash) for bone tissue engineering applications, Int. J. Biol. Macromol. 129 (2019) 844–852. https://doi.org/10.1016/j.ijbiomac.2019.02.058.

[270] E. Andrew, A. Idowu, M. Abidemi, S. Olateju, Heliyon Synthesis and characterization of Zn-Doped hydroxyapatite : scaffold application , antibacterial and bioactivity studies, Heliyon 5 (2019) e01716. https://doi.org/10.1016/j.heliyon.2019.e01716.

[271] S. Shang, Q. Zhao, D. Zhang, R. Sun, Y. Tang, Materials Science & Engineering C Molecular dynamics simulation of the adsorption behavior of two di ff erent drugs on hydroxyapatite and Zn-doped hydroxyapatite, Mater. Sci. Eng. C 105 (2019) 110017. https://doi.org/10.1016/j.msec.2019.110017.

[272] N. Al-azzam, A.A. Id, Micropatterning of cells via adjusting surface wettability

using plasma treatment and graphene oxide deposition, (2022) 1–14. https://doi.org/10.1371/journal.pone.0269914.

[273] A. Das, S. Adhikary, A.R. Chowdhury, A. Barui, Substrate-dependent control of the chiral orientation of mesenchymal stem cells : image- based quantitative profiling Substrate-dependent control of the chiral orientation of mesenchymal stem cells : image-based quantitative profiling, (n.d.).

[274] N. Slomka, A. Gefen, Confocal microscopy-based three-dimensional cell-specific modeling for large deformation analyses in cellular mechanics, J. Biomech. 43 (2010) 1806–1816. https://doi.org/10.1016/j.jbiomech.2010.02.011.

[275] T.J. Vaughan, M.G. Haugh, L.M. Mcnamara, A fluid – structure interaction model to characterize bone cell stimulation in parallel-plate flow chamber systems, (2013) 6–10.

[276] A. Gupta, A. Barui, A.R. Chowdhury, A. Das, RESEARCH ARTICLE A multiscale modeling to determine in vitro mechanical responses of different cells at the cell-substrate interface under fluid perfusion, (2024) 1–16. https://doi.org/10.1002/jbm.b.35462.

[277] D.R. Katti, K.S. Katti, Journal of the Mechanical Behavior of Biomedical Materials Cancer cell mechanics with altered cytoskeletal behavior and substrate e ff ects : A 3D fi nite element modeling study, J. Mech. Behav. Biomed. Mater. 76 (2017) 125–134. https://doi.org/10.1016/j.jmbbm.2017.05.030.

[278] S. Aryal, K. Matsunaga, W. Ching, Ab initio Simulation of Elastic and Mechanical Properties of Zn- and Mg- Doped Hydroxyapatite (HAP), (n.d.) 1–25.

[279] R. El, K. Billah, M.A. Khan, Y. Park, A. Am, H. Majdoubi, Y. Haddaji, B. Jeon, A Comparative Study on Hexavalent Chromium Adsorption onto Chitosan and Chitosan-Based Composites, (2021) 1–15.

[280] M.A. Gámiz-gonzález, D.M. Correia, S. Lanceros-mendez, V. Sencadas, Kinetic study of thermal degradation of chitosan as a function of deacetylation degree, Carbohydr. Polym. 167 (2017) 52–58. https://doi.org/10.1016/j.carbpol.2017.03.020.

[281] A. Saadati, B. Nourmohammadi, A. Asaadi, A. Nourbakhsh, H. Mohammadzadeh, Electrochemical characterization of electrophoretically deposited hydroxyapatite / chitosan / graphene oxide composite coating on Mg substrate, Surfaces and Interfaces 25 (2021) 101290. https://doi.org/10.1016/j.surfin.2021.101290.

[282] E.M. Al, K.O. Alfooty, M.Y. Abdelaal, International Journal of Biological Macromolecules Synthesis of chitosan nanocomposites for controlled release applications, Int. J. Biol. Macromol. 168 (2021) 769–774. https://doi.org/10.1016/j.ijbiomac.2020.11.134.

[283] M. Đo, A. Jankovi, J. Stojanovi, S. Park, In vitro investigation of electrophoretically deposited bioactive hydroxyapatite / chitosan coatings reinforced by graphene, 47 (2017) 336–347. https://doi.org/10.1016/j.jiec.2016.12.004.

[284] J. Dong, D. Yu, Z. Yu, L. Zhang, W. Xia, Thermally-induced crosslinking altering the properties of chitosan films : Structure , physicochemical characteristics and antioxidant activity, Food Packag. Shelf Life 34 (2022) 100948. https://doi.org/10.1016/j.fpsl.2022.100948.

[285] Z.H. Mahmoud, A. Hamrouni, A.B. Kareem, M. Ahmed, Z. Jalil, A.H. Majeed, Synthesis and characterization of chitosan sheet modi fi ed by varied weight ratio of anatase (TiO 2) nano mixture with Cr (VI) adsorbing, Kuwait J. Sci. 50 (2023) 290–299. https://doi.org/10.1016/j.kjs.2023.05.006.

[286] A.S. Neamah, R. Ghorbani, M.M. Ahadian, S. Hosseinzadeh, Targeting Heat Shock Proteins for Enhanced Apoptosis in Hyperthermic Breast Cancer Therapy Using Nanoquercetin and Nanocobalt Ferrite, 11 (2025) 55–64.

[287] S. Hossain, S. Ahmed, FTIR spectrum analysis to predict the crystalline and amorphous phases of hydroxyapatite : a comparison of vibrational motion to re fl ection †, (2023) 14625–14630. https://doi.org/10.1039/d3ra02580b.

[288] F.A. Azaman, K. Zhou, M. Blanes-mart, M.B. Fournet, D.M. Devine, Bioresorbable Chitosan-Based Bone Regeneration Scaffold Using Various Bioceramics and the Alteration of Photoinitiator Concentration in an Extended UV Photocrosslinking Reaction, (2022).

[289] V. Georgieva, D. Zvezdova, L. Vlaev, Non-isothermal kinetics of thermal degradation of chitosan, (2012) 1–10.

[290] B. Li, Z. Zhang, T. Liu, Z. Qiu, Y. Su, J. Zhang, C. Lin, L. Wang, Recent Progress in Functionalized Coatings for Corrosion Protection of Magnesium Alloys — A Review, (2022).

[291] G. Wang, Y. Wei, J. Hong, J. Lv, Spray-synthesized organic composite/hydroxyapatite coating on magnesium alloys with enhanced corrosion resistance, Front. Chem. 13 (2025) 1–11. https://doi.org/10.3389/fchem.2025.1566676.

[292] S. V Gnedenkov, V.S. Egorkin, S.L. Sinebryukhov, I.E. Vyaliy, A.S. Pashinin, A.M. Emelyanenko, L.B. Boinovich, Surface & Coatings Technology Formation and electrochemical properties of the superhydrophobic nanocomposite coating on PEO pretreated Mg – Mn – Ce magnesium alloy, Surf. Coat. Technol. 232 (2013) 240–246. https://doi.org/10.1016/j.surfcoat.2013.05.020.

[293] Z. Habli, R. Lahoud, A. Zantout, W. Abou-Kheir, M.L. Khraiche, Single-cell fluid-based force spectroscopy reveals near lipid size nano-topography effects on neural cell adhesion, Lab Chip 24 (2024) 707–718. https://doi.org/10.1039/D3LC00984J.

[294] D.E. Ingber, Cellular mechanotransduction : putting all the pieces together again, (n.d.) 811–827. https://doi.org/10.1096/fj.05.

[295] A.S. Kashani, Cancer cells optimize elasticity for efficient migration, (2020).

[296] C.S. Chen, Mechanotransduction – a field pulling together ?, (2008). https://doi.org/10.1242/jcs.023507.

[297] H.J. Donahue, Y. Zhang, Q. Chen, C.R. Jacobs, Associated With Routine Physical Activity Are Less Stimulatory to Bone Cells Relative to, (2000).

[298] L. Duncan, Mechanotransduction responsive to fluid in bone : osteoblasts forces than mechanical are more strain, (1997). https://doi.org/10.1152/ajpcell.1997.273.3.C810.

[299] A. Srinivasan, N. Rajendran, Surface characteristics, corrosion resistance and MG63 osteoblast-like cells attachment behaviour of nano SiO2-ZrO2 coated 316L stainless steel, RSC Adv. 5 (2015) 26007–26016. https://doi.org/10.1039/c5ra01881a.

APPENDICES

A.1. Preparation of Simulated body fluid (SBF)

Simulated Body Fluid (SBF) is typically prepared by dissolving reagent-grade chemicals (e.g., NaCl, KCl, $CaCl_2$, $MgCl_2 \cdot 6H_2O$, $NaHCO_3$, Na_2SO_4, and $K_2HPO_4 \cdot 3H_2O$) in distilled water in a specific sequence to avoid precipitation. The solution is buffered with Tris(hydroxymethyl)aminomethane (Tris) and its pH is adjusted to 7.4 using 1 M HCl at 36.5 °C, simulating the ionic concentration and physiological conditions of human blood plasma.

Table. A-I. Chemical composition and concentrations of constituents in Simulated Body Fluid (SBF) [299]

Sl. No.	Compound	Concentration (mM)
1	NaCl	142.0
2	$NaHCO_3$	4.2
3	KCl	5.0
4	$K_2HPO_4 \cdot 3H_2O$	1.0
5	$MgCl_2 \cdot 6H_2O$	1.5
6	$CaCl_2$	2.5
7	Na_2SO_4	0.5
8	$(CH_2OH)_3CNH_2$ (Tris buffer)	50.0
9	0.1 HCl (to adjust pH to 7.4)	

A.2 Sensitivity analysis for selecting the standard deviations (σ)

Initially, data augmentation was performed using a Gaussian noise distribution with σ values chosen at two extreme points, 0.1 and 0.9, as well as a middle value of 0.5. These augmented datasets were then fed into the ANN to evaluate the resulting R values. The augmented data can be accessed through the link below:

https://drive.google.com/drive/folders/14ZGO1nQhEuex4t_vNcscsVer1BrCOQRY?usp=sharing

For σ = 0.1:

The R^2 values for the training, validation, and test sets are moderately high (0.98903 for training, 0.98739 for validation, and 0.98365 for test), which shows that the model is performing well. However, the MSE (Mean Squared Error) value is 25.5322, which indicates that the model's predictions are relatively less accurate compared to the other sigma values.

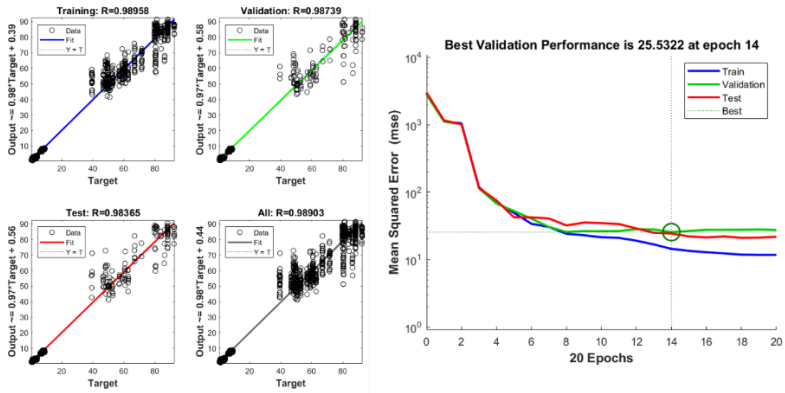

Figure A-I. Coefficient of determination (R^2) shown in the regression plots and Mean Squared Error (MSE) in the performance curve for σ = 0.1

For σ = 0.5:

This configuration gives the highest R^2 values across all sets (0.9919 for training, 0.98772 for validation, and 0.98303 for test), suggesting better generalization and predictive performance. The MSE value is also lower (24.0896), showing that the model has better accuracy.

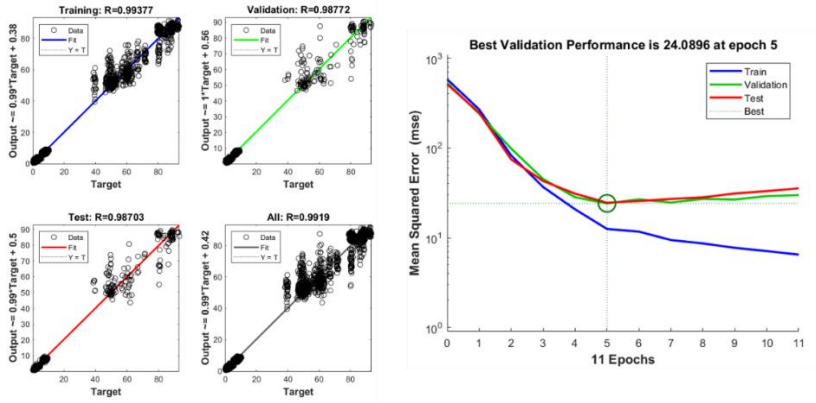

Figure A-II. Coefficient of determination (R^2) shown in the regression plots and Mean Squared Error (MSE) in the performance curve for $\sigma = 0.1$

For $\sigma = 0.9$:

While the R^2 values are still good (0.98144 for training, 0.98299 for validation, and 0.96829 for test), the MSE value increases significantly (30.9854). This higher MSE indicates that the model's performance has degraded compared to sigma = 0.5. The higher sigma introduces more noise, which can lead to overfitting or a less stable model.

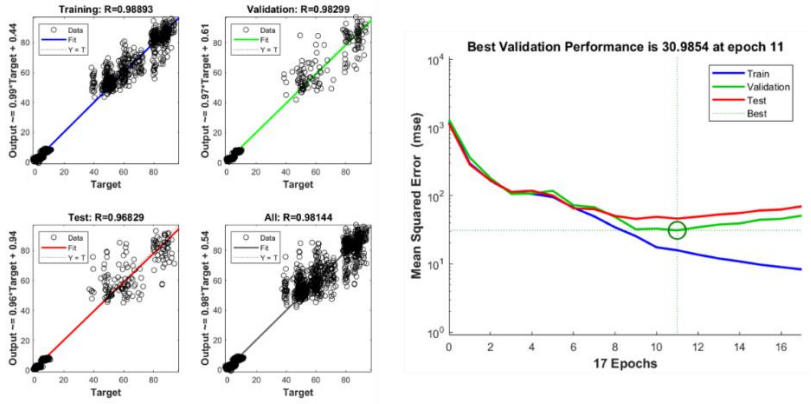

Figure A-III. Coefficient of determination (R^2) shown in the regression plots and Mean Squared Error (MSE) in the performance curve for $\sigma = 0.1$

Based on these results, sigma = 0.5 is the optimal choice because it provides a balance between model complexity and accuracy. This sigma value yields the highest R^2 values and the lowest MSE, indicating that the model generalizes well and provides accurate predictions. While sigma = 0.1 gives relatively good performance, the

model's accuracy is slightly lower than that of sigma = 0.5. On the other hand, sigma = 0.9 introduces excessive noise, resulting in a higher MSE and slightly worse performance. Therefore, sigma = 0.5 strikes the best balance for the task, ensuring robustness and minimizing errors while maintaining high predictive accuracy.

A.3 Goniometer report for Contact angle

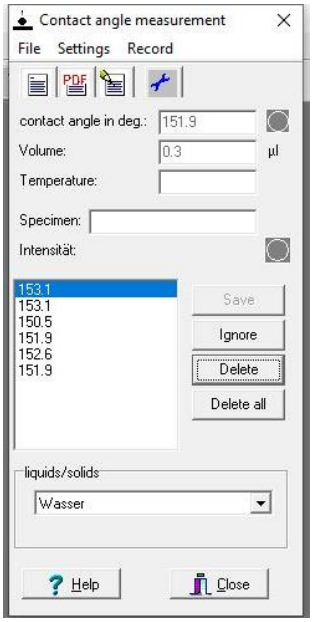

Figure A-IV. Contact angle measurement using a goniometer, showing the recorded values over six repetitions. The measurement values are consistently around 152°, indicating the super hydrophobicity of the coated surface.

In the link below the original Goniometer report have been uploaded

https://drive.google.com/file/d/1hutbiEJkWl2ENZymtjHlUx3KeBPY-ePh/view?usp=sharing

Signature of Candidate: Binod Barai

BINOD BARAI

Date: 06.04.2026

1. 06/4/2026

Dr. Buddhadeb Oraon

Professor
Dept. of Mechanical Engineering
Jadavpur University, Kolkata-32

2. 06.04.2026

Dr. Tapendu Mandal

Tapendu Mandal
Assistant Professor
Metallurgy and Materials Engineering
IIEST Shibpur

3. Subhasish Sarkar 06/04/2026

Dr. Subhasish Sarkar

Dr. SUBHASISH SARKAR
Assistant Engineer-I
Electrical Division, PHE Dte.
Govt. of West Bengal